Soft magnetic FeHfO films with high resistivity

Structural investigations and high frequency permeability calculations

J.M. Huijbregtse

August 1996

Supervisors:
prof.dr.ir. A. Van den Beukel
dr. F. Roozeboom (Philips Research)
dr.ir. J. Sietsma

Delft University of Technology
faculty: Chemical Technology and Materials Science
group: Chemical and Physical Materials Science
section: Physical Metallurgy

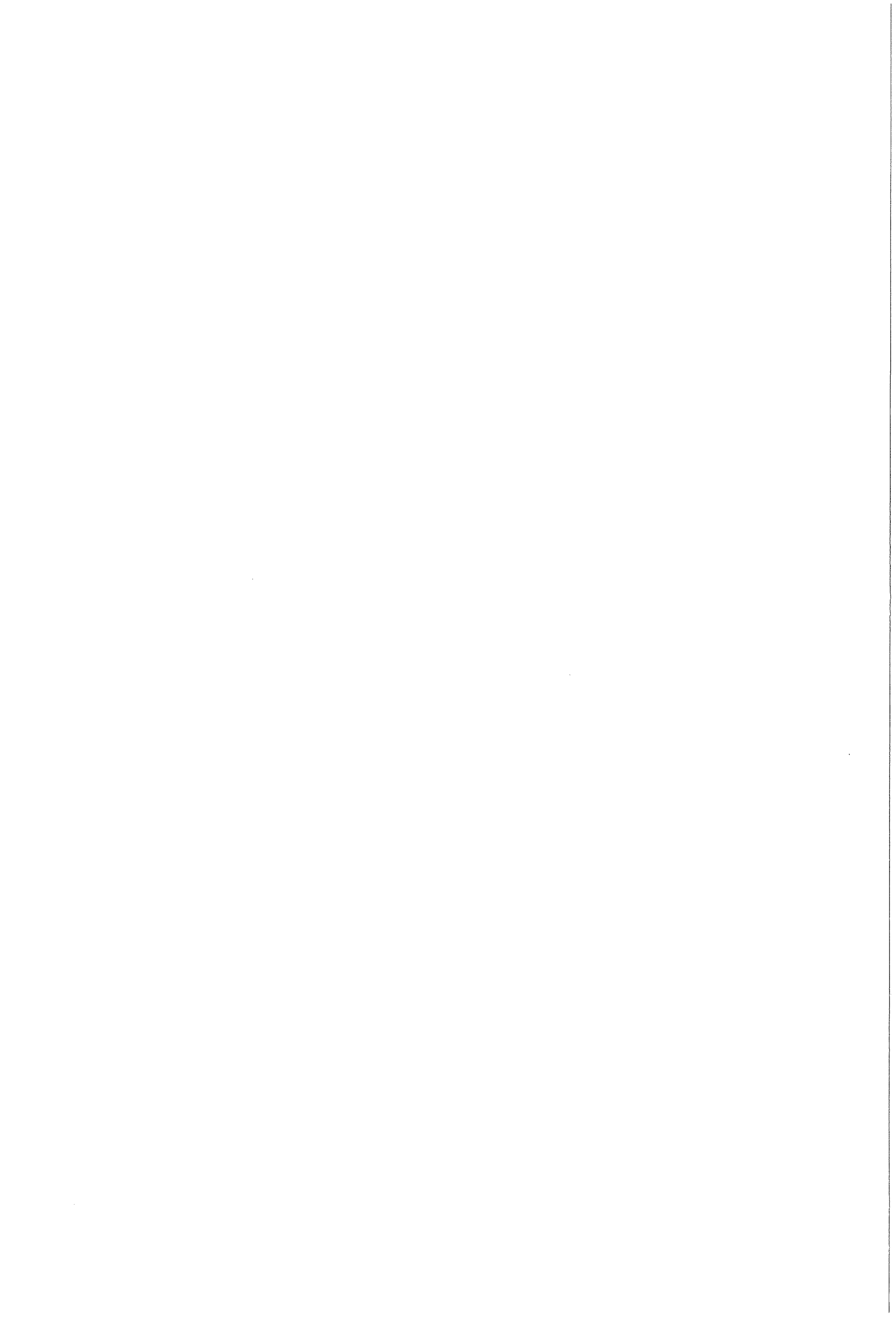

Contents

Summary 4

Samenvatting 6

Acknowledgements 8

1. Introduction 9

2. Theory 11
   2.1 Soft magnetic materials 11
      2.1.1 Introduction 12
      2.1.2 Magnetic anisotropy 12
      2.1.3 Applications 14
   2.2 Literature survey on FeHfO films 15
   2.3 The magnetic permeability 16
      2.3.1 Definition of the magnetic permeability 16
      2.3.2 The complex magnetic permeability 17
      2.3.3 Loss mechanisms 18
   2.4 Crystallisation kinetics 22
      2.4.1 Introduction 22
      2.4.2 Nucleation and growth 22
      2.4.3 Overall crystallisation kinetics 23
      2.4.4 Activation energy spectra 27
      2.4.5 Observation of the crystallisation process by means of electrical resistivity 28

3. Experimental methods 30
   3.1 Sputter deposition 30
      3.1.1 Introduction 30
      3.1.2 The sputtering process 30
      3.1.3 The experimental RF reactive sputtering set-up 31
   3.2 Annealing 33
      3.2.1 Classical thermal processing 33
      3.2.2 Rapid thermal processing 33
   3.3 Structural characterisation 34
      3.3.1 X-ray diffraction........ 34
      3.3.2 Transmission electron microscopy 35
   3.4 Auger electron spectroscopy 36
   3.5 Electrical resistivity measurements 37
   3.6 Magnetic characterisation 38
      3.6.1 Measuring the complex magnetic permeability 38
      3.6.2 Measuring BH-loops 41
      3.6.3 Measuring the saturation magnetostriction coefficient 42

4. Results 44
4.1 Optimisation procedure 44
4.1.1 Sputter conditions and uniformity 44
4.1.2 Optimising the oxygen content 45
4.1.3 Optimising the annealing procedure 45
4.1.4 Reproducibility 46
4.2 Structure of the films 46
4.2.1 X-ray diffraction results 47
4.2.2 Transmission electron microscopy results 47
4.3 Electrical resistivity measurements 48
4.4 High frequency permeability measurements 49

5. Discussion 51
5.1 Structure and structural changes upon annealing 51
5.2 Interpretation of the resistivity measurements 54
5.2.1 Calculation of the fraction transformed 54
5.2.2 Interpretation of the fraction transformed curves in terms of the JMA equation 57
5.2.3 Interpretation of the fraction transformed curves in terms of activation energy spectra 59
5.3 Comparing the measured and calculated high frequency permeability 61

6. Conclusions and recommendations 65
6.1 Conclusions 65
6.2 Recommendations 66

References 67

Appendices 71
A. Equations for eddy current and resonance loss 71
A.1 Eddy current loss in ferromagnetic thin films 71
A.2 Resonance in ferromagnetic thin films 72
A.3 Eddy current and resonance loss in ferromagnetic thin films 75
B. The non-isothermal fraction transformed 77
C. Corrections for the magnetic permeability measurement 79
D. Results of the optimisation procedure 81
D.1 Optimising the oxygen flow 81
D.2 Optimising the annealing treatment 81
E. High frequency permeability measurements 83

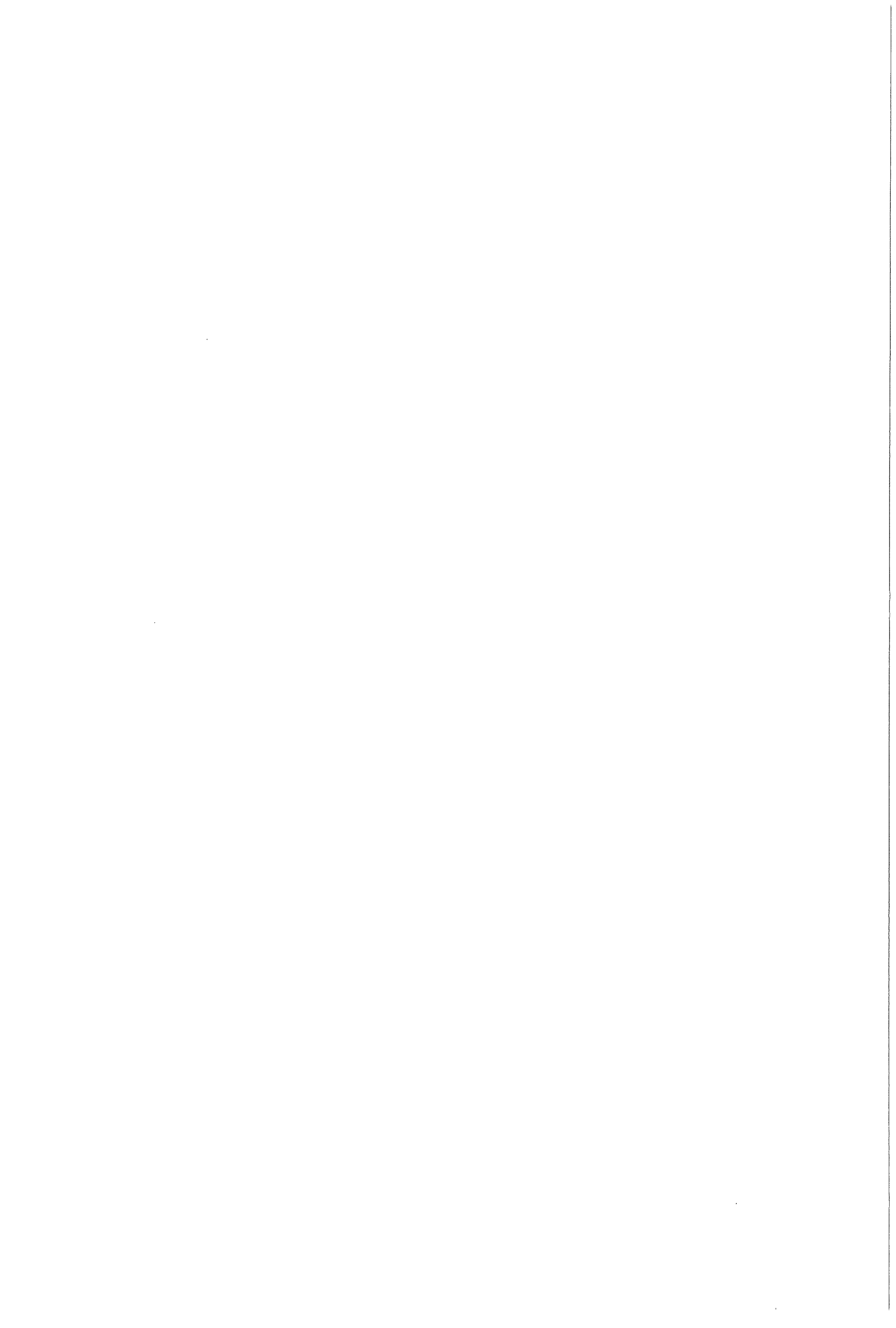

Summary

The possibility to make FeHfO films with good soft magnetic properties and a high resistivity is investigated. The films are deposited by means of RF reactive sputtering on several substrates (glass, GGG and silicon). Subsequently they are annealed to induce a uniaxial anisotropy and to reduce the saturation magnetostriction coefficient. Two experimental annealing set-ups were used: a conventional resistively heated furnace (vacuum) and a rapid process based on heating by means of radiation (inert atmosphere). It appeared that 0.70 μm thick films of composition $Fe_{55}Hf_{17}O_{28}$ that are rapid thermal processed for 5 seconds at 400°C show the best combination of good soft magnetic behaviour (relative permeability at 10 MHz of more than 10^3 and a coercivity below 50 A/m) and high resistivities of the order 10^3 μΩcm. The saturation magnetic induction is rather small (1.1 T), because of the large amounts of non-magnetic atoms. The saturation magnetostriction coefficient is large ($+5\cdot10^{-6}$) and does not change significantly upon annealing.

The structure of $Fe_{55}Hf_{17}O_{28}$ films was investigated by means of X-ray diffraction (XRD) and transmission electron microscopy (TEM). It was found that the as deposited films consist of nanocrystalline body centred cubic iron particles that are randomly dispersed in an amorphous matrix. Although some hafnium and oxygen atoms might be dissolved in the crystalline iron, it is believed that most of the oxygen and hafnium are present in the amorphous matrix, causing the high resistivity.
Upon annealing, further crystallisation of b.c.c. iron is induced and corresponding reductions in resistivity are observed. High temperature annealing induces a second crystallisation process forming hafnium oxide in two crystal structures. In the temperature range from 450 to 700°C mainly face centred cubic crystal structure is found, whereas at 900°C large amounts of monoclinic hafnium oxide are observed.

Low temperature crystallisation of iron was monitored by measuring the electrical resistance during annealing. Reductions in resistivity up to 30% are found upon annealing at temperatures between 225 and 300°C (for long periods of time). This reduction is believed to be caused by crystallisation of b.c.c. iron. The total reduction in resistivity depends on the annealing temperature and may also be related to transfer of dissolved atom from the b.c.c. iron to the amorphous matrix, as indicated by a peak shift in XRD measurements.
The resistance measurements are interpreted in terms of the JMA-equation using a single activation energy an in terms of a first order transition with an activation energy spectrum. The heating stage is included in these descriptions. An (average) activation energy of approximately approximately 157 kJ/mole is found for all situations, taking the time constant in accordance with the Debye frequency. Interpretation in terms of an Avrami exponent yields unrealistically small exponents. Therefore this description is replaced by the description based on activation energy spectra. Fitting the experiments resulted in a standard deviation of 12 kJ/mole for the situations of both a normal and a unifrom distributed energy spectrum. Crystallisation during heating is described well by this theory; larger deviation are observed in the isothermal part of the annealing treatments. The kinetic parameters strongly depend on the choice of the time constant.

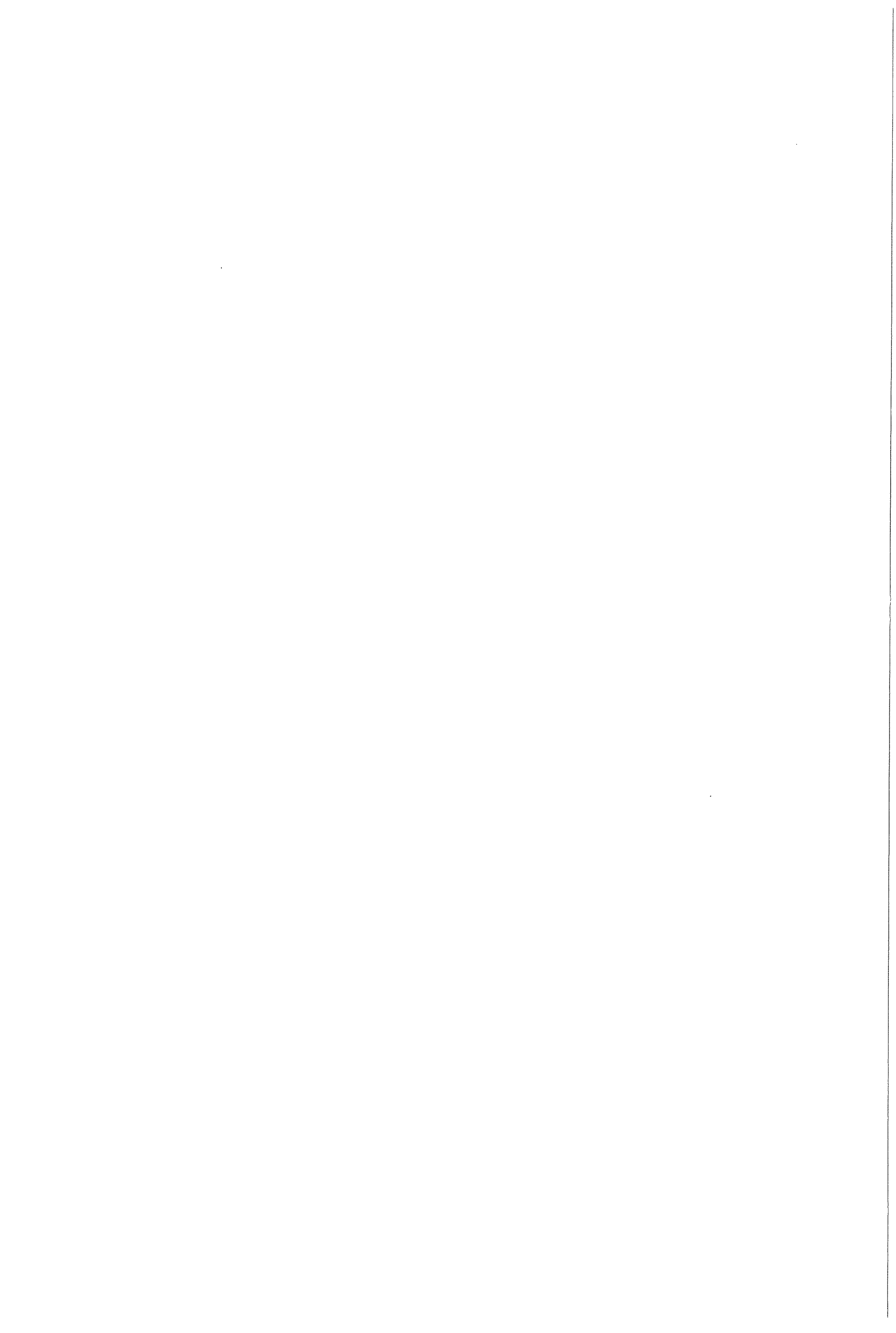

It was found that the properties of $Fe_{55}Hf_{17}O_{28}$ films do not manifest a strong thickness dependence. Then, because of their high resistivity, 10.9 μm thick FeHfO films are expected to exhibit a permeability of 10^3 up to 100 MHz, assuming eddy currents to be the only loss mechanism. However, the measured permeability (up to 200 MHz) decreases to values below 10^3 at lower frequencies. Using a phenomenological model of Landau and Lifshitz it was found that ferromagnetic resonance has to be added to explain the observed reduction in permeability. The parameters in this model are in agreement with experimental uniaxial anisotropies and reported damping constants.

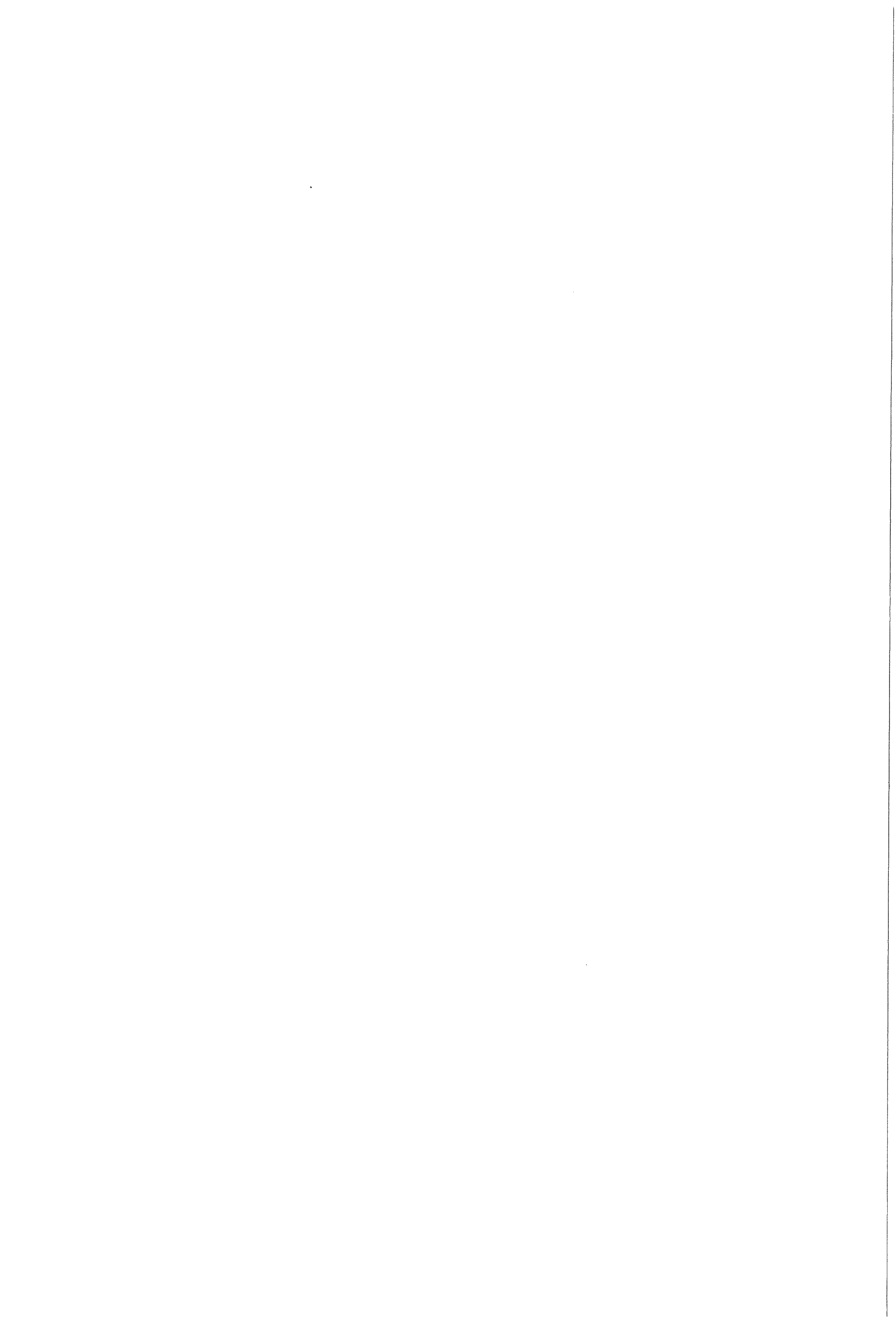

Samenvatting

Er is onderzocht of het mogelijk is om FeHfO lagen te deponeren door middel van RF reaktief sputteren die een combinatie van goede magnetische eigenschappen en een grote soortelijke weerstand vertonen. Na depostie worden de films gegloeid om een uniaxiale anisotropie te induceren en om de magnetostriktie te verkleinen. Er zijn twee gloei processen gebruikt: een gewone (resistieve) vacuümoven en een oven gebaseerd op zeer snelle verhitting door middel van straling (in inerte gassen). Het is gebleken dat 0.70 μm dikke $Fe_{55}Hf_{17}O_{28}$ films na een warmtebehandeling gedurende 5 seconden op een temperatuur van 400°C met de laatstgenoemde methode de beste combinatie van goede zachtmagnetische eigenschappen (relatieve permeabiliteit groter dan 10^3 bij 10 MHz en een coercitiefkracht kleiner dan 50 A/m) en grote soortelijke weerstanden van meer dan 10^3 μΩcm vertonen. Zoals verwacht mag worden op grond van de grote hoeveelheid niet magnetische atomen, is de verzadigings induktie laag (1.1 T). The magnetostriktie van de films is groot ($+5 \cdot 10^{-6}$) en wordt nauwelijks beïnvloed door enige gloeibehandeling.

De struktuur van $Fe_{55}Hf_{17}O_{28}$ films is onderzocht door middel van röntgendiffractie (XRD) en transmissie electronen microscopie. Het is gebleken dat de struktuur van de films direkt na depositie bestaat uit willekeurig georiënteerde kubisch ruimtelijk gecentreerde ijzer deeltjes geprecipiteerd in een amorfe matrix. Hoewel er wellicht enige hafnium en zuurstof atomen in de nanokristallijne ijzer fase zijn opgelost, is het waarschijnlijk dat de amorfe matrix verreweg de meeste van deze atomen (hetgeen de grote soortelijke weerstand zou kunnen veroorzaken). Door de films te gloeien vindt er verdere kristallisatie van b.c.c. ijzer plaats, hetgeen gepaard gaat met een afname van de soortelijke weerstand. Een tweede kristallisatie proces treedt op bij hogere gloeitemperaturen. Er werd hafniumoxide aangetroffen in twee kristalstrukturen. Bij temperaturen tussen 450 en 700°C werd hoofdzakelijk kubisch vlakken gecentreerd HfO_2 gevonden, terwijl zich bij hogere gloei temperaturen praktisch alleen monoklien HfO_2 vormde.

De kristallisatie van b.c.c. ijzer bij relatief lage temperaturen is gevolgd door middel van elektrische weerstandsmetingen. Weerstandsafnamen van zo'n 30% werden gevonden tijdens langduring gloeien bij temperaturen tussen de 225 en 300°C. Men denkt dat deze weerstandsafname veroorzaakt wordt door kristallisatie van b.c.c. ijzer. De totale weerstandsafname na afloop van het experiment hangt af van de gloeitemperatuur en is waarschijnlijk ook gerelateerd aan segregatie van opgeloste atomen uit de b.c.c. ijzer fase. Dit effekt komt tot uiting in peakverschuivingen in de XRD metingen.
De weerstandsmeting zijn geïntepreteerd in termen van de JMA vergelijking (één activerings energie) en een eerste orde overgang met een activerings energie spectrum. In de theoretische beschrijvingen is ook het opwarmgedeelte in rekening gebracht. Een (gemiddelde) activeringsenergie van ongeveer 157 kJ/mol werd gevonden voor beide modellen indien the tijdsconstante in overeenstemming wordt gekozen met de Debye frequentie. Het JMA model met de enkele activeringsenergie leverde onrealistische kleine Avrami exponenten. Daarom werd de tweede beschrijving gebruikt. Aanpassing van dit model op de experimentele resultaten gaf een standaarddeviatie van 12 kJ/mol voor zowel een uniform als een normaal verdeeld spectrum van activeringsenergieën. Het blijkt dat de kristallisatie die plaatsvindt tijdens het opwarmen goed beschreven kan worden. Dit gaat echter in veel mindere mate op voor het isotherme gedeelte. Bovendien blijken de gevonden kinetische parameter ook sterk van de keuze van de tijdsconstante af te hangen.

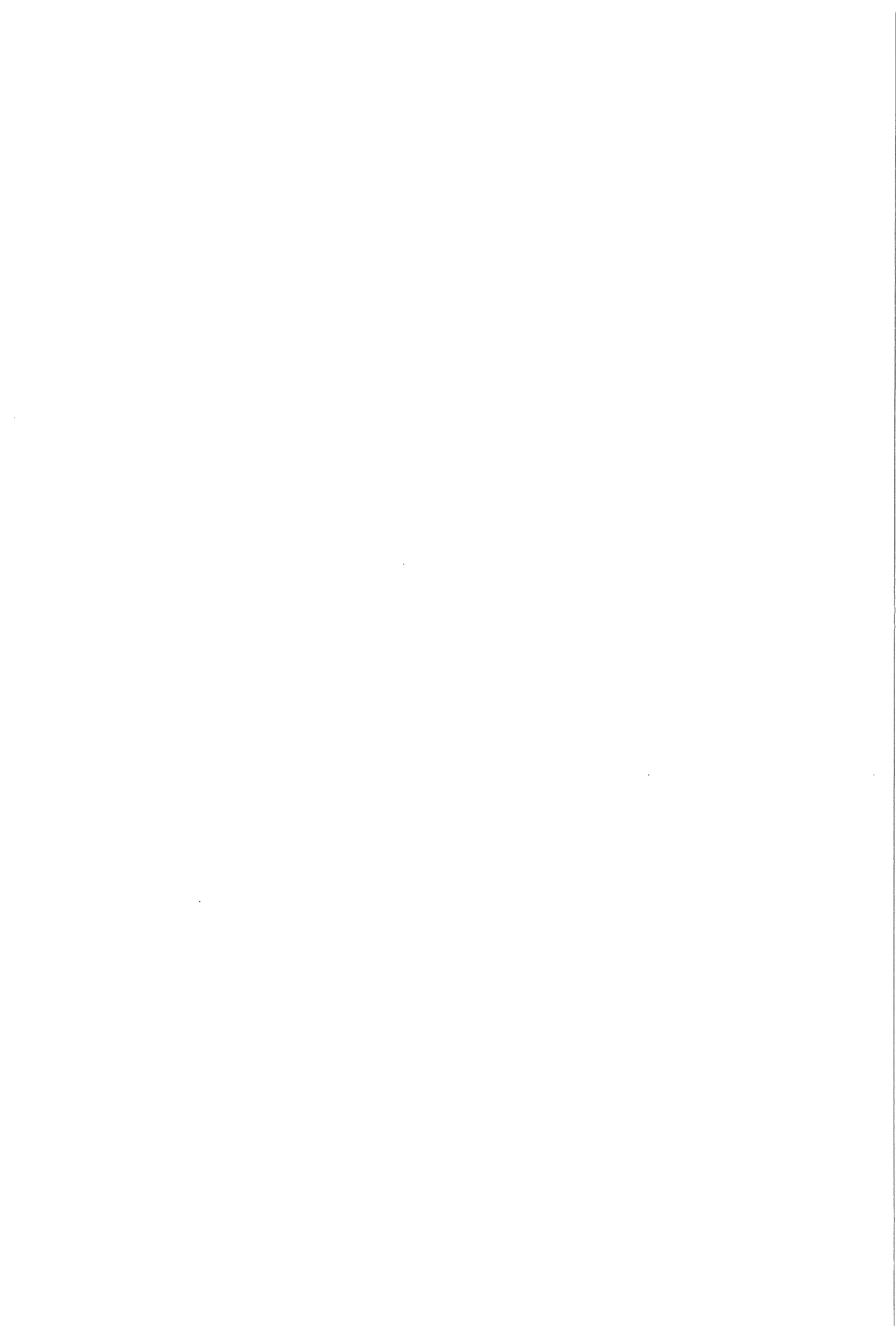

Het is gebleken dat de eigenschappen van de $Fe_{55}Hf_{17}O_{28}$ lagen nauwelijks van de dikte van de laag afhangen. Op grond van de hoge specfieke weerstand zou men verwachten dat 10.9 μm dikke films een relatieve permeabiliteiten van meer dan 10^3 tot frequenties boven 100 MHz vertonen (indien men aanneemt dat wervelstromen de verstorende faktor zijn). De gemeten frequentie afhankelijkheid (tot 200 MHz) van de permeabiliteit blijkt echter eerder af te vallen, hetgeen verklaard is door naast wervelstromen ook ferromagnetische resonantie in rekening te brengen. Hiertoe is gebruik gemaakt van een fenomenologisch model van Landau en Lifshitz. De gevonden model parameters stemmen goed overeen met in de literatuur gevonden waarden voor de dempings konstante en uit andersoortige metingen bepaalde uniaxiale anistropie konstanten.

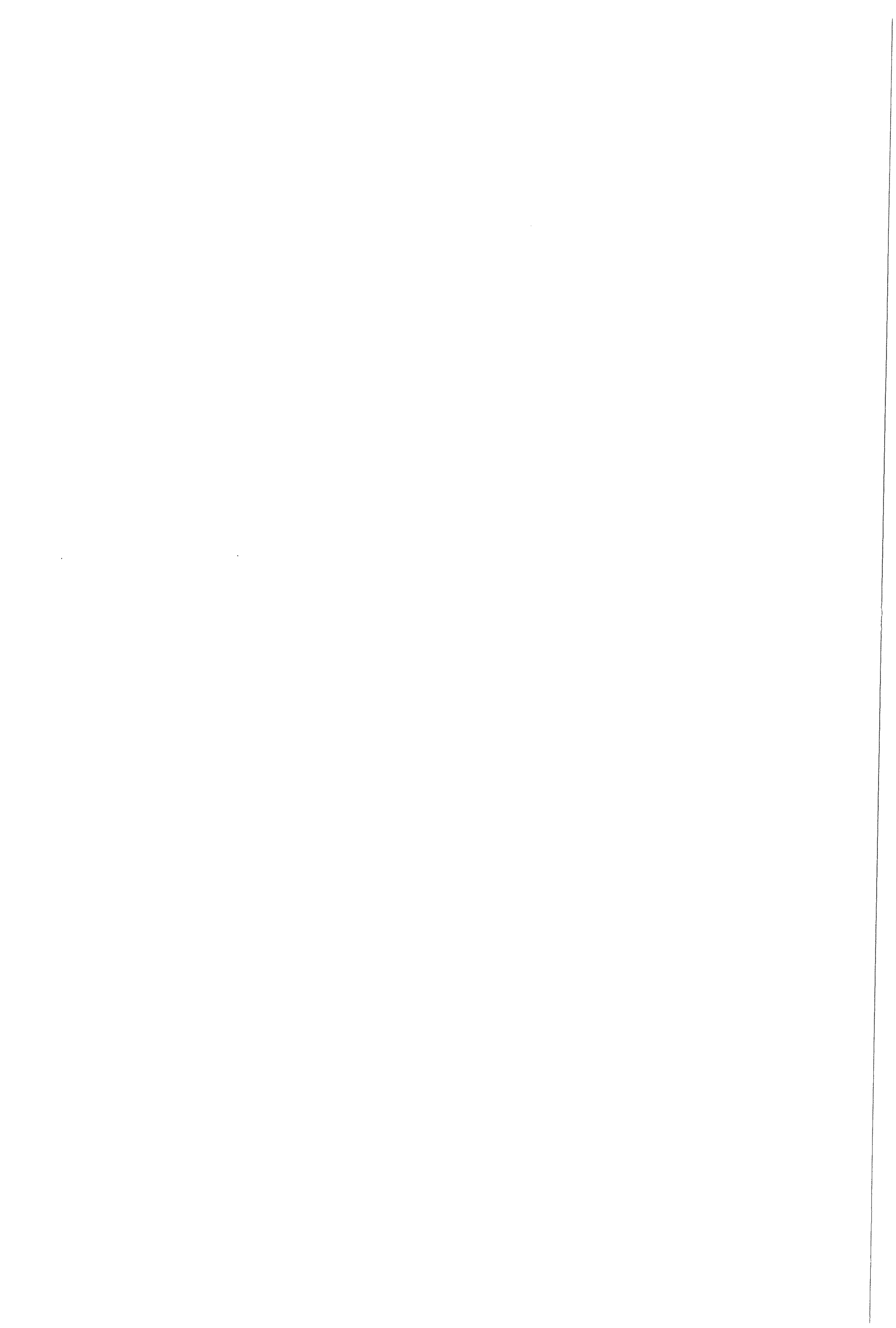

Acknowledgements

Before I went to the Natuurkundig Laboratorium in Eindhoven to join the research group Magnetism, I performed a literature study on the subject "magnetic anisotropy in soft magnetic materials". During this study I became familiar with the phenomena accompanying magnetic recording in general and soft magnetic materials in particular. Therefore, when I arrived in Eindhoven I could pay full attention to the experimental procedures from the start.

First I had to learn all about the technique of sputter deposition. In this Hans van Zon was a great help. Thereafter, Wilco Klaassens taught me how to use the magnetic characterisation techniques and Fred Roozeboom, my tutor at Philips Research, introduced me to rapid thermal processing. Now all ingredients for making soft magnetic FeHfO films were present and I spent the first months in adjusting the sputter equipment and finding the optimal sputter and annealing conditions.
Ton Kuiper determined the composition of the films by means Auger electron microscopy.

The next stage in the research project was the identification of the various crystal structures that are formed in the films upon annealing. Jo Daams performed several XRD measurement and Johan Donkers obtained transmission electron microscopy images. Thanks to their expertise the structure of the films could be revealed.

Contact with the group in Delft was maintained by Jilt Sietsma, whose suggestions strongly contributed to the investigations. It was his idea to monitor structural changes by means of electrical resistance measurements. The (numerous) resistance measurements were patiently performed by Richard van der Rijt, even though most of the experiments failed.

I'm also indebted to Pascal Bloemen, who performed some high frequency permeability calculations and adjusted the experimental equipment to measure the permeability up to 200 MHz.

I gratefully acknowledge all the people who carried out experiments and helped me with the interpretation of the numerous results. Special thanks to Fred Roozeboom for his enthusiastic support during my stay in Einhoven.

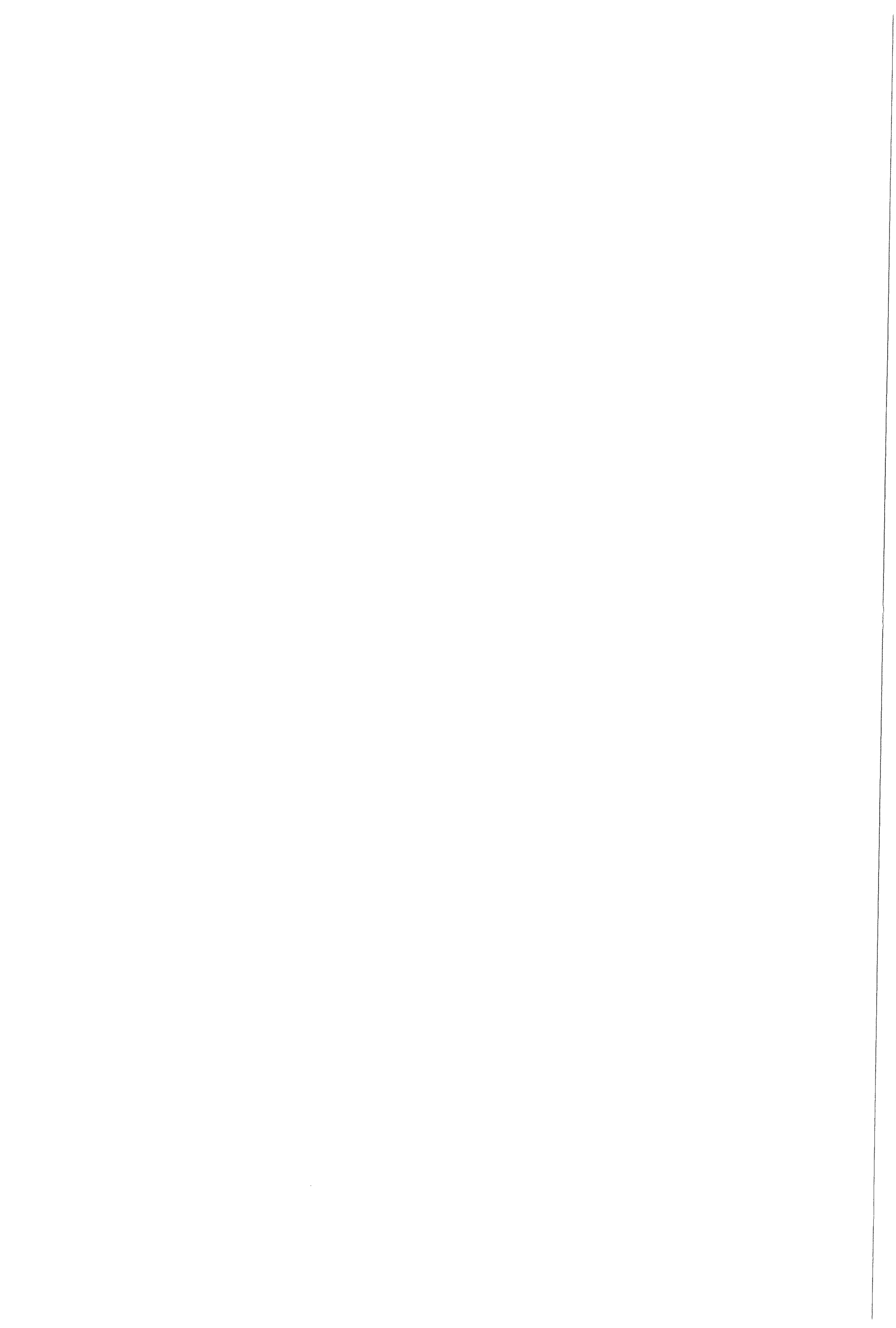

1. Introduction

Over the years sceptics predicted that magnetic data storage would soon be outperformed by solid state data storage. However, it turned out that magnetic data storage is far more cost effective than semi conductor memory. Therefore, the world-wide magnetic data storage industry (magnetic tapes and disks) is almost as large as the semiconductor industry [1]. General trends towards smaller devices and higher operating frequencies have led to very severe requirements for the materials used in magnetic recording. Both the hard magnetic storage medium itself and the soft magnetic materials in magnetic recording heads need to fulfil numerous requirements. Unfortunately, the soft magnetic materials and the hard magnetic medium are not independent.
Research [2] has shown that it is possible to obtain hard magnetic materials with very high coercivities (i.e. high recording densities). In magnetic devices, the soft magnetic materials must be able to saturate this medium. Consequently, the saturation magnetisation of the soft magnetic material needs to be high. Several other requirements that these materials have to fulfil are [3]:

- high relative permeability at high frequencies,
- small coercivity and
- low saturation magnetostriction coefficient.

A high saturation magnetisation can be obtained by using a material with a high atomic magnetic moment. Iron has the largest atomic moment, but it also has a very large (crystal) anisotropy resulting in poor soft magnetic behaviour. Recently a new class of soft-magnetic materials, known as nanocrystalline materials and having iron as the main constituent, was found to combine a high magnetisation and good soft magnetic properties. Examples are FeNbSiN and FeTaN [3].
However, the resistivity of these material is rather low, thereby limiting the operating frequency. A material that combines reasonable soft magnetic properties and a high specific resistivity is expected to perform better at high frequencies. One of the most promising materials reported in the literature is FeHfO [4]. This type of materials, partly amorphous partly nanocrystalline, is relatively unknown and is fundamentally different from the mentioned nanocrystalline alloys, which formed the reasons to start this research project.

At Philips Research in Eindhoven in the group Magnetism research is carried out on soft magnetic materials for application in magnetic heads. However, there was no experience with materials like FeHfO that show reasonable soft magnetic properties and a high resistivity. Therefore it was agreed to perform a research project in this group on this particular material.

The goal of the research project was:
- to find out if it is possible to make FeHfO that indeed shows this combination of reasonable soft magnetic properties and a high resistivity;
- subsequently, if one is able to make the optimal material reproducibly, to investigate the structure of the films and
- to elucidate, if possible, the origin of the high resistivity and to determine its influence on the high frequency magnetic properties.

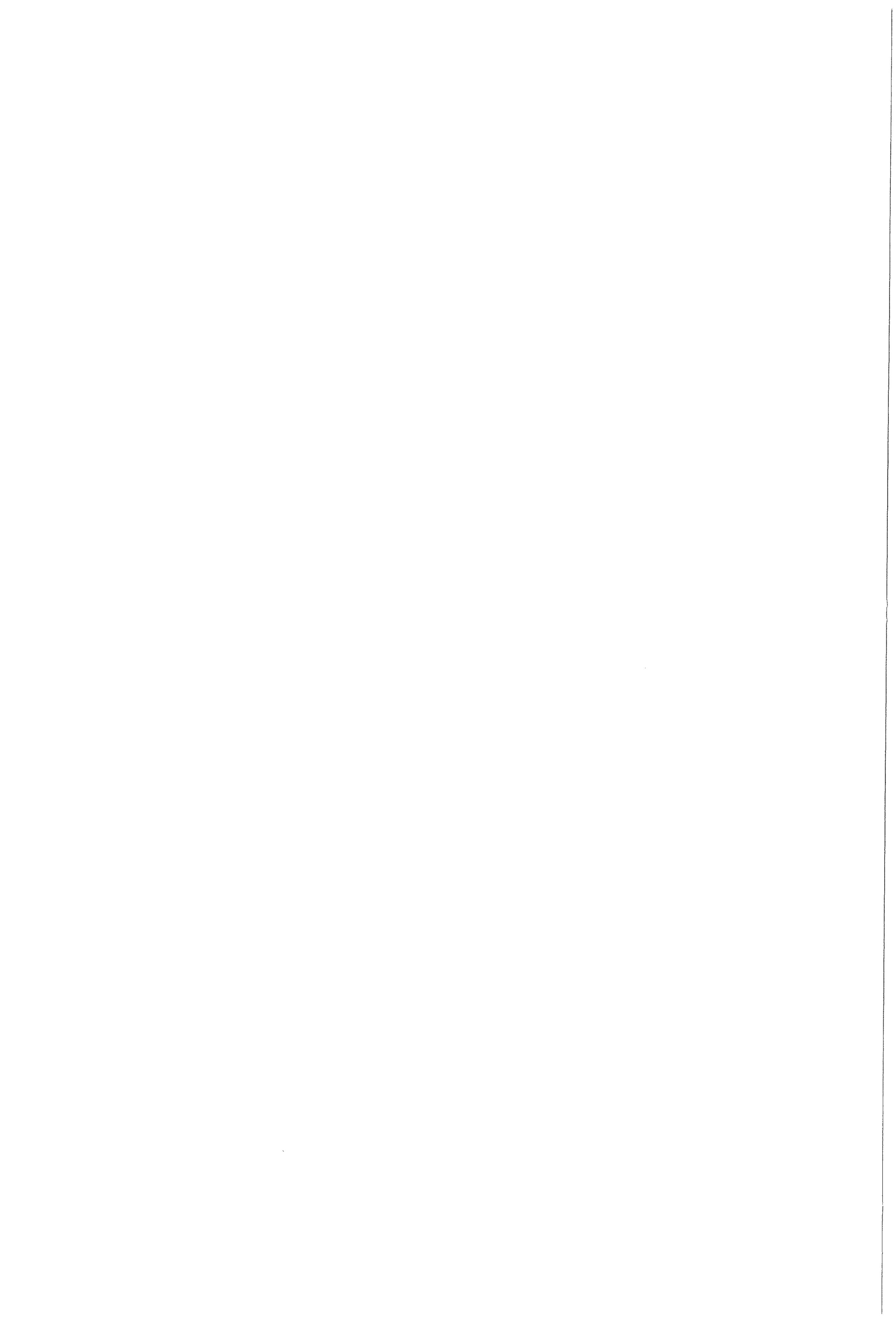

In this report the results of the research project are presented. The report is divided in six chapters, which will be shortly discussed below. Supplementary experimental results and calculations are given in the appendices.
In chapter 2 the *theory* of obtaining soft magnetic properties is summarised. Also the magnetic recording process is described and the role of FeHfO is discussed. Subsequently an important magnetic parameter, the relative magnetic permeability, is defined and a relation between the resistivity and the permeability of soft magnetic films (as a function of frequency) is derived. Next ferromagnetic resonance is added to this description.
Another part of this chapter deals with crystallisation processes in amorphous materials. A relation between the so-called fraction transformed and time is derived under isothermal and isochronal conditions, based on the J(ohnson)-M(ehl)-A(vrami) equation. Also a relation that describes crystallisation during a full heat treatment (isothermal and isochronal) is given.
The *experimental* equipment is described in chapter 3. First the principles of sputter depositing thin films are explained. Next the two different annealing set-ups that are used to induce a uniaxial anisotropy are explained. These are a resistively heated oven (classical thermal processing) and one based on heating by radiation (rapid thermal processing). Next the structural characterisation methods X-ray diffraction and transmission electron microscopy are treated. The composition of the films as a function of depth is measured with Auger electron spectroscopy. The equipment to monitor structural changes upon annealing (by means of electrical resistance) and to measure the resistivity (four-point probe method) are treated as well. At the end of this chapter the principles of the magnetic measurements (permeability, BH-loops and magnetostriction) are summarised.
The experimental *results* are presented in chapter 4. First the sputter conditions are optimised with respect to the magnetic and electrical properties of the films. It is with the films of optimal composition that further investigations are performed. After a second optimisation procedure for the heat treatment, the structure of the optimal films is monitored upon annealing, using both X-ray diffraction (XRD) and transmission electron microscopy (TEM). Resistance changes during annealing are presented under isochronal and combined isochronal/isothermal conditions. For comparison, a resistance measurement on another soft magnetic material is treated as well.
At the end of this chapter the obtained films are scaled up to thicknesses of more than 10 μm, to investigate the frequency dependence of the permeability up to 200 MHz.
The experimental results are *discussed* in chapter 5. First the changes of structural parameters (like mean grain size, lattice spacings and integrated peak area) upon annealing are discussed. The resistance measurements during annealing are translated into a volume fraction as a function of time. An attempt is made to explain these curves in terms of the JMA-equation, using a single activation energy, or in terms of a first order transition, using an activation energy spectrum. At the end of this chapter the frequency dependence of the complex permeability is compared to the models presented in chapter 2.
Finally some *conclusions* are drawn and *recommendations* are given for continuing the research on soft magnetic FeHfO films with a high resistivity.

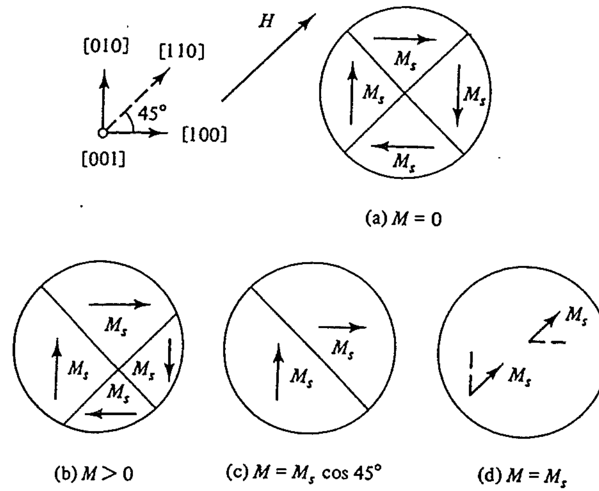

Figure 2.1 Changes in the magnetic domain structure of a single crystal with ⟨100⟩ preferential directions, when a magnetic field **H** is applied in the [110] direction [5].

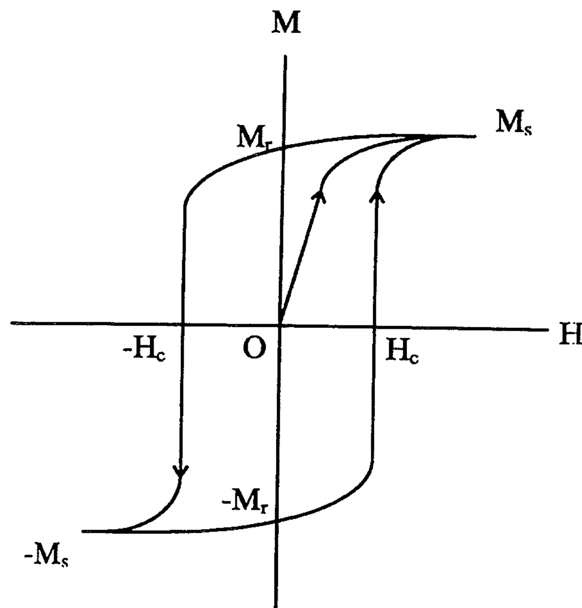

Figure 2.2 Schematic representation of the magnetisation loop of a single crystal with ⟨100⟩ preferential directions starting from the demagnetised state (M = 0, H = 0). The magnetic field is applied along the [110] direction. Coercivity H_c, remanence M_r and saturation magnetisation M_s are indicated.

2. Theory

2.1 Soft magnetic materials

2.1.1 Introduction

Ferromagnetism finds its origin in the motion of electrons around their own axis (*spin*). All electron spins can be considered as a small circular currents, resulting in a magnetic moment that is assigned to the atom (atomic magnetic moment). When the individual magnetic moments are aligned parallel, as they do in ferromagnets, the moments add up to a *magnetisation*. The magnetisation vector **M** [A/m] is equal to the (vector)sum of the individual magnetic moments per unit of volume.
The direction of this magnetisation is not random, but restricted to certain preferential directions with respect to crystal orientation, shape of the specimen, internal stresses and magnetic fields. This phenomenon is called *magnetic anisotropy* and will be discussed in the next section.
Because in general there is more than one preferential direction, the magnetic moments will be arranged in such a way that the magnetostatic energy of the sample is minimal. That is: the material is not fully magnetised but divided into *domains*, each with the same magnetisation but orientated along different preferential directions. The total magnetisation of the specimen, however, is zero. The magnetic domains are separated by *domain walls*. These domain walls have a finite thickness, because the magnetic moments gradually rotate from one preferential direction to the other. Its width is determined by both the magnetic anisotropy and *exchange interaction*. This spin-spin interaction tries to align all magnetic moments (in ferromagnets).

Consider the total magnetisation $M = |\mathbf{M}|$ as a function of the applied magnetic field strength H [A/m], starting from the demagnetised state (see figures 2.1 and 2.2). The first (easiest) process that takes place is *domain wall motion*. Domains with a local magnetisation close to the field direction grow, the other domains shrink. Further magnetisation in the field direction is induced by *rotation* of the local magnetisations towards the field direction. When the total magnetisation and the field are parallel, the material is saturated and the total magnetisation has reached its maximum value: the *saturation magnetisation* M_s. When the field strength is now gradually reduced, the local magnetisations rotate back to the nearest preferential directions. Consequently, there is still a total magnetisation when the applied field is zero. This value of the total magnetisation is called the *remanence* M_r. Now the field is applied in the opposite direction and again increased in magnitude. Mathematically this is expressed as a negative field that decreases (becomes more negative). Domains that have a magnetisation close to the "new" field direction start growing, whereas domains with a local magnetisation direction that is very different from the field direction shrink. There is a situation that the total magnetisation becomes zero. The corresponding magnetic field is called the *coercivity* H_c. Further reducing the (negative) field results in a decrease of the total magnetisation as described above, etc.
So, the magnetisation process is not totally reversible, but shows *hysteresis*: the magnetic behaviour of the material depends on its history. The magnetisation curve (and hysteresis) are characterised by coercivity and remanence. A material with large coercivity and large remanence (large hysteresis) is called a *hard magnetic* material. When both coercivity and remanence are small (small hysteresis) the behaviour is denoted as *soft magnetic*. This material class will be dealt with in this report.

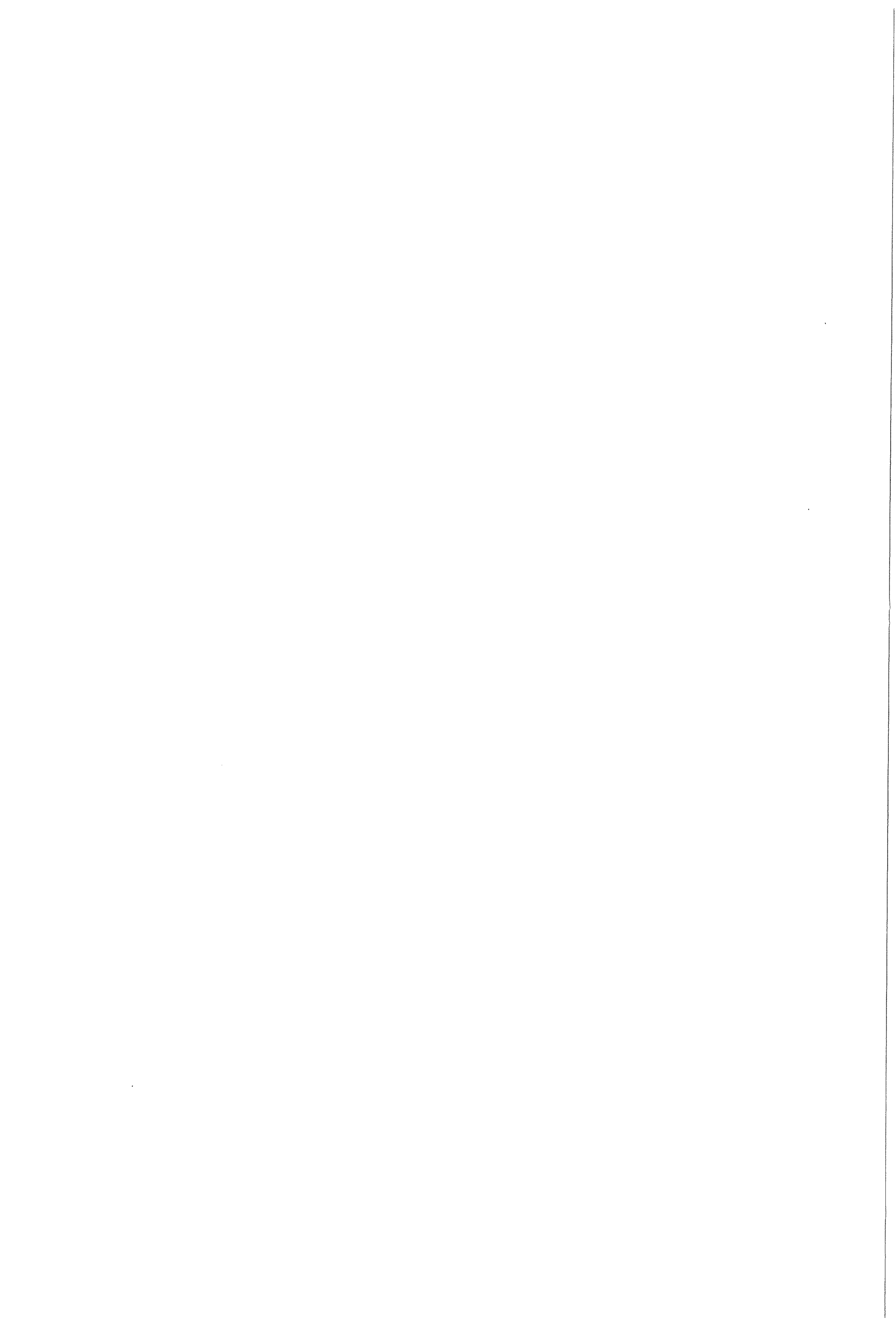

2.1.2 Magnetic anisotropy

Magnetic anisotropy is the phenomenon that the energy of a magnetic material depends on the direction of the magnetisation. In other words: there are certain preferential directions for the magnetisation. Here only *uniaxial* anisotropies are considered. Uniaxial means that there is one preferential axis (two directions) present and, consequently, the domain pattern is characterised by 180° domain walls only.
The energy density ε^{un} [J/m^3] of a single domain particle with uniaxial anisotropy is given by:

$$\varepsilon^{un} = K_u \sin^2 \theta \tag{2.1}$$

with K_u the uniaxial anisotropy constant [J/m^3] and θ the angle between the magnetisation and the preferential direction. As can be seen from equation (2.1) the energy of the particle is minimal if the magnetisation and preferential direction are parallel ($K_u > 0$).
Preferential directions can be defined with respect to several axes, depending on the kind of anisotropy. The most important ones are:

- magnetocrystalline anisotropy,
- shape anisotropy,
- magneto-elastic anisotropy and
- induced anisotropy.

The individual anisotropies are briefly discussed below. For an extensive review of these anisotropies one is referred to textbooks by Cullity [5] and Chikazumi [6].

Magnetocrystalline anisotropy
The most important anisotropy is crystal anisotropy. This anisotropy is a result of spin-orbit coupling. When an external field is applied not only the spin motions of electrons are reoriented, but also their orbital motions (because of the spin-orbit coupling). This orbital motion is strongly related to the crystal lattice and therefore the energy is strongly dependent on crystallographic directions. The energy to rotate a spin away from its preferred crystal direction is the energy required to overcome this spin-orbit coupling.
Crystal anisotropy usually is dominant over other types of anisotropy and the uniaxial anisotropy constant can be as large as 10^5 J/m^3.

Shape anisotropy
When a specimen is magnetised magnetic north and south poles appear at its surface. These poles give rise to an internal field that opposes the magnetisation and the externally applied magnetic field: the *demagnetising field* vector $\mathbf{H}^{dem}$ [A/m]. This field depends on the exact shape of the specimen and the induced magnetisation. It becomes stronger if the induced magnetisation increases and if the magnetic poles are located closer to each other.
Mathematically it can be expressed by:

$$\mathbf{H}^{dem} = -\overline{\overline{N}}\mathbf{M}, \tag{2.2}$$

where $\overline{\overline{N}}$ is the demagnetising tensor that accounts for the shape of the specimen. The tensor elements can only be calculated for simple cases (sphere, ellipsoid, thin plate).

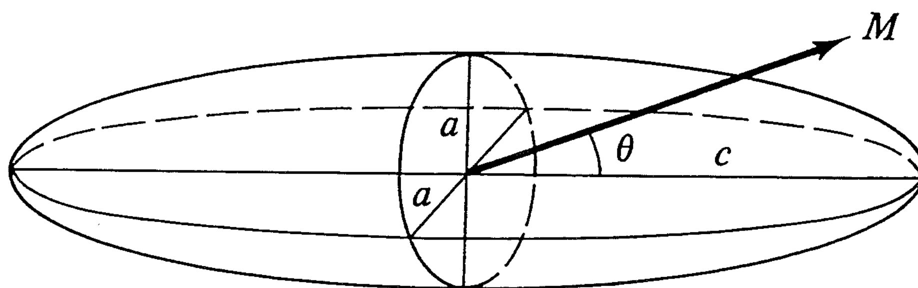

Figure 2.3 Single domain particle in the form of a long, thin ellipsoid of rotation [5].

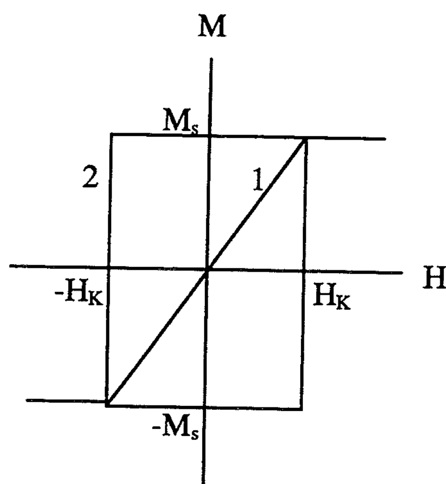

Figure 2.4 Magnetisation loops in the hard axis (1) and easy axis (2) direction, calculated for a single domain particle with uniaxial anisotropy.

A consequence of demagnetising fields is that the magnetisation has certain preferential directions with respect to the shape of the specimen. Consider a single domain particle in the form of a ellopsoid, see figure 2.3. The energy per unit of volume of a specimen is given by:

$$\varepsilon_{shape} = -\tfrac{1}{2}\mathbf{M}_s \cdot \mathbf{B} = -\tfrac{1}{2}\mu_0 \mathbf{M}_s \cdot \mathbf{H}^{dem} = \tfrac{1}{2}\mu_0 \mathbf{M}_s \cdot \overline{\overline{\mathbf{N}}}\mathbf{M}_s . \tag{2.3}$$

In this expression, μ_0 is the permeability of vacuum ($\mu_0 = 4\pi\cdot10^{-7}$ N/A^2). The element of the demagnetising tensor in the long c-axis direction is minimal because the magnetic poles are separated as far as possible. So the shape anisotropy energy is minimal if the magnetisation is orientated along this axis. In this special case shape anisotropy can be written in the form of equation (2.1) with $K_u = ½\mu_0(N_a-N_c)M_s^2$, where $N_{a,c}$ are the tensor elements along the principle axes a en c ($N_a > N_c$).
For a thin film with dimensions l = 34 mm, w = 5 mm and d = 0.7 μm the demagnetising factor is estimated to be $7.07\cdot10^{-6}$ in the length direction (see appendix C). If the thin film material has a saturation polarisation I_s (= $\mu_0 M_s$) of 1.1 T, the shape anisotropy energy density is calculated to be less than 5 J/m^3 (if the magnetisation lies in the length direction). However, this value is much larger if the magnetisation lies in the width and, especially, the thickness direction of the film.

Magneto-elastic anisotropy
When a material is magnetised its dimensions change. The length change of the specimen in the field direction divided by its original length is called the magnetostriction coefficient λ. This value can be positive or negative, depending on the material. Usually one is interested in the magnetostriction at saturation: λ_s.
In single crystals the magnetostriction is a tensor. In polycrystalline materials, however, when no texture is present, the magnetostriction reduces to a scalar. In that case the magneto-elastic energy can be written as an expression of the form (2.1) with $K_u = 3/2\lambda_s\sigma$, where σ is the internal stress. If a tensile stress is applied to the specimen ($\sigma > 0$) and if $\lambda_s > 0$, the energy is minimal for $\theta = 0, \pi$ and the preferential directions are parallel to the stress. This holds true when both stress and magnetostriction are negative. When they are of opposite sign the energy is minimal for $\theta = ½\pi$ and the preferential directions are perpendicular to the stress.
Taking $\lambda_s = 3\cdot10^{-7}$ and $\sigma = 100$ MPa, the uniaxial magneto-elastic anisotropy constant is determined to be 45 J/m^3.

Induced anisotropy
By annealing a magnetic material in a magnetic field it is possible to insert a preferential axis (two directions). The mechanism of inducing magnetic anisotropies is not fully understood. It is believed that in the presence of the magnetic field atoms are rearranged in pairs with their axis parallel to the field direction, breaking up their original random distribution. By cooling down the specimen these pairs are frozen in. The pairs formed now act as preferential direction for the magnetisation. The induced uniaxial anisotropy constant is typically a few hundreds J/m^3.

Magnetic anisotropy has a large effect on the properties of magnetic materials. Consider a single domain particle with uniaxial anisotropy that is magnetised in a direction parallel to the preferential axis (*easy axis*) and in a direction perpendicular to the preferential axis (*hard axis*). In this ideal situation the MH-loops are a square and a straight line, respectively, as shown in figure 2.4 [7,8].

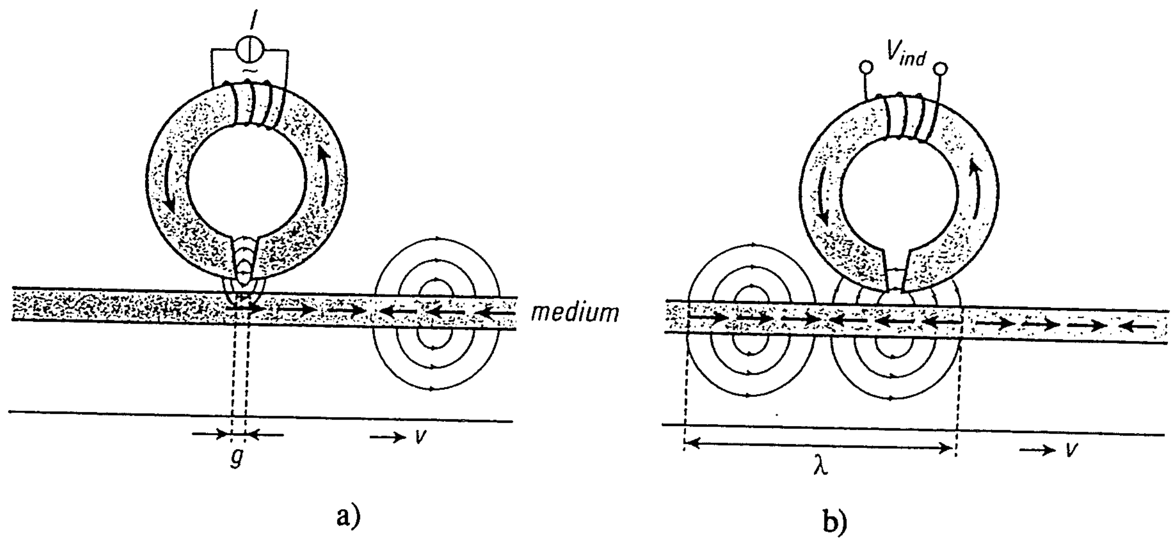

Figure 2.5 Principles of magnetic recording [1]:
a) writing process and
b) reading process.

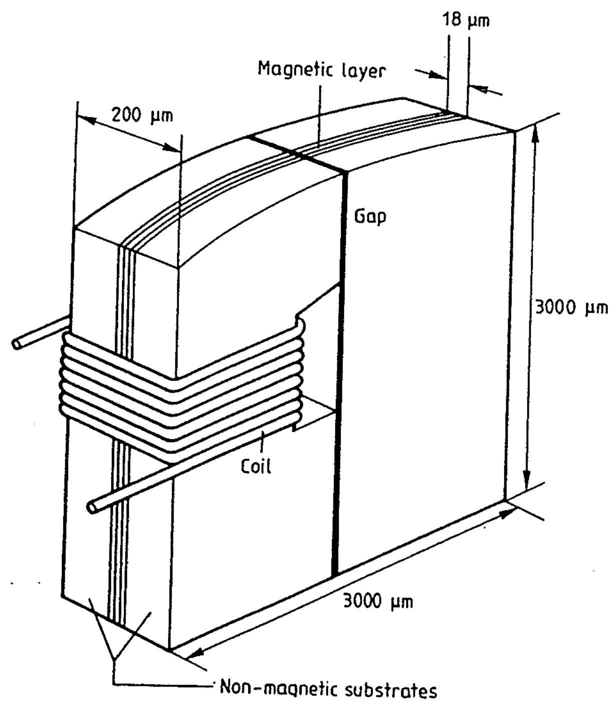

Figure 2.6 Sandwich video head [12].

The field necessary to saturate the particle in the latter case is called the anisotropy field H_K [A/m] and is related to the uniaxial anisotropy constant according to:

$$H_K = \frac{2K_u}{\mu_0 M_s}. \tag{2.4}$$

So by controlling the magnetic anisotropy (magnitude and preferential directions) one is able to obtain MH-loops in-between these two extremes.

2.1.3 Applications

Soft magnetic properties are found when the anisotropy field is small, as follows from figure 2.4. That means that one is interested in materials with a large saturation magnetisation and a small anisotropy. Because of its large magnetic moment, iron based alloys are expected to exhibit soft magnetic behaviour, if all anisotropies can be controlled [8]:

1. Magnetocrystalline anisotropy. This kind of anisotropy can be controlled by making the crystallites smaller than the domain wall width. It can be shown [9,10] that in that case the crystal anisotropy is averaged over many crystals and, therefore, reduced in magnitude. The domain wall width in iron is estimated to be 35 nm [6]. This is the upper limit for the grain size in iron based soft magnetic materials.
2. Shape anisotropy. In thin films the in plane demagnetising factors are very small compared to the one perpendicular to the plane of the film. Consequently, the magnetisation is confined to directions in the plane of the film.
3. Magneto-elastic anisotropy. In the previous section it was argued that there are two quantities that effect the magneto-elastic anisotropy constant in polycrystalline materials. Besides the magnetostriction coefficient, also internal stresses have to be minimised.
4. Induced anisotropy. When all of the preceding anisotropies are small one can introduce a magnetic anisotropy. In this way the domain pattern can be controlled [11,12. This subject is discussed in section 2.3.2.

Real materials consist of an assembly of single domain particles (domains) seperated by domain walls and show hysteresis, as stated in section 2.1.1. Then also the coercivity and remanence must be small. Materials that obey these guidelines are soft magnetic.
An important application of soft magnetic thin films is as a *flux guide* in magnetic recording heads for data storage [1,12]. The principle of magnetic recording is schematically shown in figure 2.5. The recording head essentially consists of a soft magnetic ring-shaped material with a gap. Several windings of a coil are attached to pick up or induce magnetic flux changes in the gap. In the "write" mode a current is sent through the windings, causing a magnetic field across the gap. Part of this field magnetises the tape, that moves along the gap. Reversal of the current results in reversal of the writing signal. Because the tape is hard magnetic, an electrical signal can be stored magnetically in this way.
The "reading" process is essentially the opposite. The magnetic tape moves along the head. The external field of the tape is guided by the soft magnetic material through the windings of the coil. The changes in magnetisation of the tape are now translated in an induction voltage (i.e. an electrical signal).
A more efficient design of a magnetic head is shown in figure 2.6. This so called sandwich head consists of a soft magnetic film (thickness order: ten micrometers) sandwiched between two non-magnetic ceramic substrates. At Philips Research in Eindhoven several soft magnetic

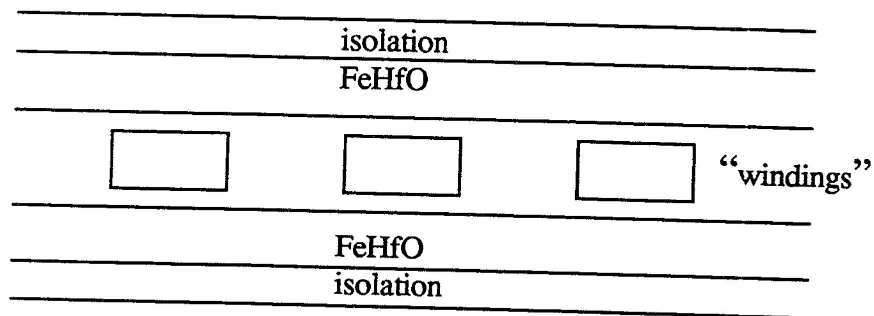

Figure 2.7 Planar coil sandwiched between two soft magnetic layers and coated with an insulator.

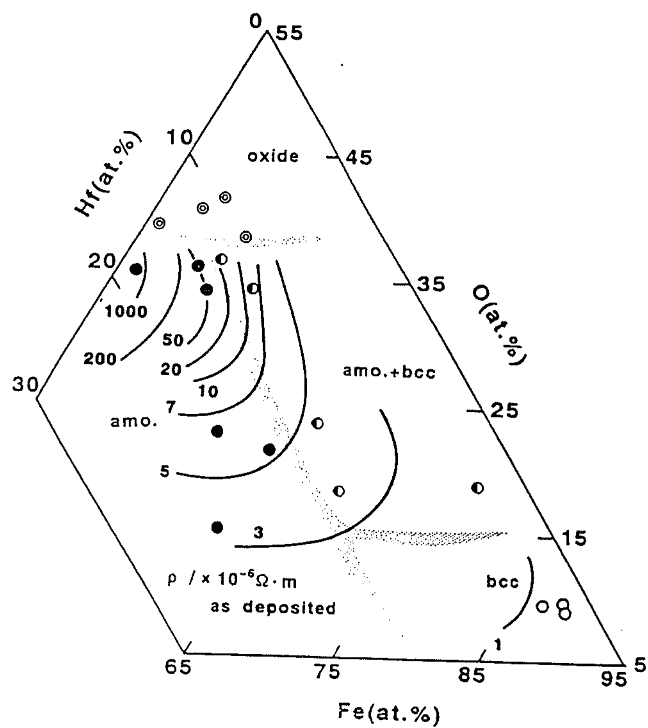

Figure 2.8 Compositional dependence of structure and resistivity ρ (in 100 μΩcm) for as deposited FeHfO films [4].

flux guides have been developed. Currently amorphous CoZrNb is used in video heads [13]. Trends in the recording industry towards higher recording densities and higher operating frequencies have lead to the development of a new class of soft magnetic materials: nanocrystalline materials. All these films are iron based, because of the need for a high saturation magnetisation to saturate the hard magnetic tape material. Examples of materials from this class developed at Philips are FeSiNbN and FeTaN [3]. These materials show excellent soft magnetic properties.
Disadvantages of these materials are:

- low resistivity (< 100 μΩcm): the magnetic properties at higher operating frequencies deteriorate, because of eddy currents (see section 2.3); this effect becomes stronger with increasing film thickness.
- poor wear resistance: because the wear of the soft magnetic material is larger than that of the substrate the distance between tape and flux guide increases with time; consequently the signal to noise ratio deteriorates with time, thereby limiting the life time of magnetic heads.

The first problem is overcome by dividing the soft-magnetic material into 10 to 20 thin layers separated by ultrathin isolating Si_3N_4 layers. Another possibility is to search for materials that combine soft magnetic behaviour and a high specific resistance. At first sight this may seem paradoxical because of the large amount of iron needed in soft magnetic materials. However, in the literature materials are reported that indeed show this combination. One of them is FeHfO. This material was originally developed for use in micromagnetic devices, such as thin film inductors and thin film transformers. A schematic drawing of a planar coil is shown in figure 2.7. The inductance (and quality factor) of the coil can be substantially improved by sandwiching the coil with a material that has good soft magnetic properties up to high frequencies. So the most important application of soft magnetic FeHfO films is as a flux guide either in magnetic recording heads or in planar micromagnetic devices.
In the next section some experimental results reported on FeHfO in the literature will be summarised and discussed.

2.2 Literature survey on FeHfO films

A large amount of research on FeHfO films with good soft magnetic properties and a high electrical resistivity has been done at the Central Research Lab. of Alps Electric Co. Ltd. by Makino et al. [4,14-17]. Their results will be briefly discussed in this section.
All films were sputter deposited in a reactive mixture of Ar and O_2 on glass substrates and are 2 μm thick. The sputter deposition process is described in section 3.1. Using X-ray diffraction (XRD) they examined the compositional dependence of the structure of these films, see figure 2.8. After deposition the structure of the films could be classified into four groups [4]:

1. single b.c.c. Fe,
2. b.c.c. Fe and an amorphous phase,
3. amorphous phase and
4. oxide structures (mixture of FeO, Fe_2O_3 and HfO_2).

As can be seen in figure 2.8, the resistivity strongly depends on the composition. Good soft magnetic properties are only observed on the boundary between the second and third group for films with an O-to-Hf ratio of 3.2 to 4.0, i.e. very fine b.c.c. Fe (grain size < 10 nm) in an amorphous phase. Energy dispersive spectroscopy (EDS) showed that the amorphous phase contains considerably larger amounts of Hf and O than the b.c.c. Fe phase [14,15].

a)

b)

Figure 2.9 Structural changes upon annealing of several FeHfO films [4]:
a) DSC curves (heating rate 0.67 K/s),
b) XRD patterns (CoK_{α} radiation) in the as deposited state, annealed for 1 hour at 673 K and then heated to 783, 893 and 973 K.

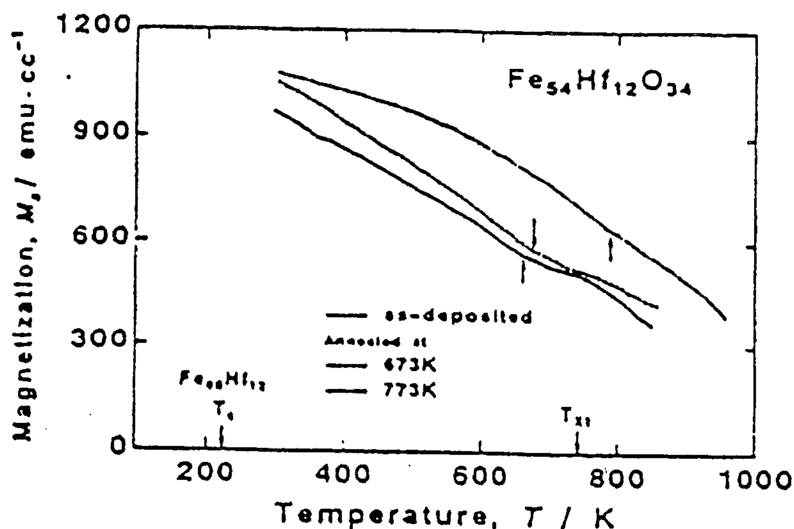

Figure 2.10 Temperature dependence of the saturation magnetisation for $Fe_{54}Hf_{12}O_{34}$ films in an as deposited state and after annealing [14] ($10^4/4\pi$ emu/cc equals 1 T).

Structural changes of two films with compositions $Fe_{55}Hf_{11}O_{34}$ and $Fe_{46}Hf_{18}O_{36}$ (at%) upon annealing are monitored using XRD and differential scanning calorimetry (DSC) [4,15]. The results are shown in figure 2.9. Makino et al. conclude that the structural changes in both films occur in two stages: low temperature crystallisation of b.c.c. Fe and high temperature crystallisation of HfO_2.
The temperature dependence of the saturation magnetisation of $Fe_{55}Hf_{11}O_{34}$ films (annealed and as deposited) shows inflection points between 700 and 800 K, see figure 2.10. These inflection points are regarded as the Curie temperature T_c of the amorphous phase and are much higher than the Curie point of FeHf, which is well below room temperature [14]. It is found that the Curie temperature of the amorphous phase rapidly rises with the amount of oxygen above 25 at%. Therefore the increase of T_c of the amorphous phase upon annealing is attributed to the depletion of oxygen from the b.c.c. phase to the amorphous phase.
Films that have undergone annealing treatments show better soft magnetic properties than as deposited films [16-18]. The optimum annealing conditions are determined to be: 400°C for 3 hours in a static magnetic field and 6 hours at 400°C in a rotating magnetic field. After the annealing treatments slightly larger b.c.c. Fe grain sizes are observed, but still well below the domain wall width of iron. The increase of grain size in combination with the higher T_c of the amorphous phase upon annealing, presumably enhances the exchange interaction between the b.c.c. Fe crystallites. So the anisotropy is more effectively averaged out than in the as deposited structure, which may result in better soft magnetic properties.
Measured properties are typically:

- relative permeability at 10 MHz: $\mu_{10\,MHz} = 1960$,
- specific resistance: $\rho = 0.80$ mΩcm,
- coercivity: $H_c = 45$ A/m,
- saturation polarisation: I_s (= $\mu_0 M_s$) = 1.2 T,
- saturation magnetostriction coefficient: $\lambda_s = +3\cdot10^{-6}$.

Finally a schematic drawing of the structure of (optimal) FeHfO films is given in figure 2.11^a. These films consist of b.c.c. Fe nanocrystals that are randomly dispersed in an amorphous matrix, which contains most of the Hf and O. For comparison, also the structure of soft magnetic FeTaN (and FeSiNbN) is shown in figure 2.11^b: Fe (FeSi) nanocrystals and TaN (NbN) on the triple points. TaN (and NbN) are believed to prohibit the Fe (FeSi) grain growth. No amorphous phase is observed in these materials after annealing.

2.3 The magnetic permeability

2.3.1 Definition of the magnetic permeability

A frequently used property in the characterisation of soft magnetic materials is the relative permeability μ_r, which will be written as μ in the remainder of this report. The permeability is a measure for the magnetic response of a material to an externally applied magnetic field. The total permeability $\mu_0\mu$ connects the magnetic flux density vector **B** [T] and the magnetic field vector **H** [A/m]:

$$\mathbf{B} = \mu_0 \mu \mathbf{H}. \tag{2.5}$$

Generally the permeability is a function of both position within the specimen and magnetic field strength. Usually only the initial permeability is considered, so one can ignore the H-dependence.

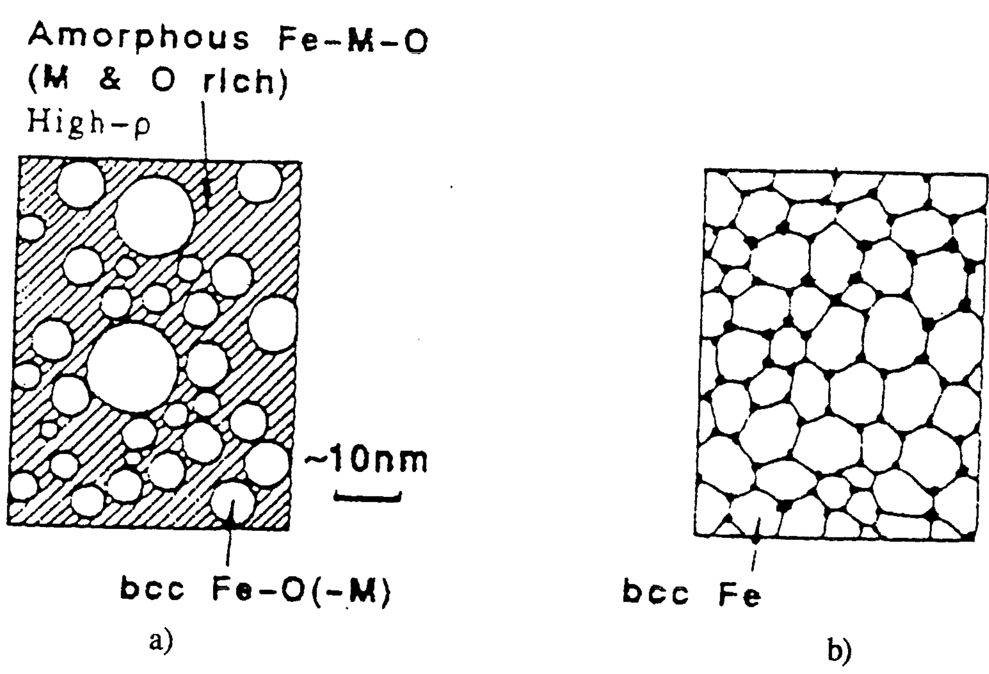

Figure 2.11 Schematic representation of the microstructure of:
a) FeHfO films
b) FeTaN/FeNbSiN films and
annealed at optimal conditions [17].

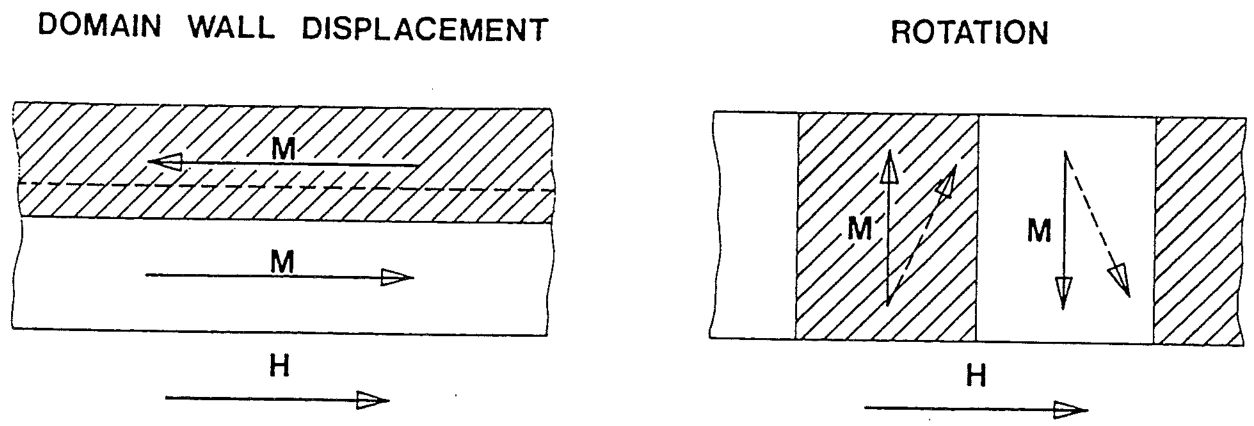

Figure 2.12 Domain wall movement (left) and rotation (right) of the magnetisation [12].

Generally the magnetic permeability depends on the anisotropy directions and should therefore be described with tensor mathematics. It is assumed that the material is homogeneous, so the permeability tensor has constant elements μ_{ij} (i,j =1, 2 or 3).

2.3.2 The complex magnetic permeability

As mentioned in the introduction of this chapter there are two mechanisms that contribute to the magnetic permeability [12,19]:

- domain wall motion and
- rotation of the magnetisation.

Both processes are illustrated in figure 2.12 for a 180° domain wall. If a magnetic field is applied along a preferential direction of the magnetisation (easy axis) only domain wall motions take place. If the field is applied perpendicular to a preferential direction (hard axis) only rotational processes contribute to the magnetisation change.
Domain wall motions are caused by local rotation of the magnetic moments near the domain wall over large angles (180°). When an ac magnetic field is applied along the preferential direction, local electrical currents are induced that oppose the domain wall motion (*eddy currents*). These eddy currents give rise to signal loss (see next section).
Rotation takes place homogeneously in the material and over much smaller angles. The associated eddy currents are smaller and the hindrance of the magnetisation process is less at high frequencies. Therefore, it is expected that both domain wall motion and rotation processes occur at low frequencies, whereas only rotation processes take place at high frequencies of the ac magnetic field [19]. This is illustrated in figure 2.13.
From the viewpoint of the magnetic recording industry the high frequency range is the most interesting part. Therefore one is specifically interested in the *permeability measured in the hard axis direction*, because the high frequency permeability is then solely determined by rotation processes (and has its maximum value). It is this permeability that we are concerned with in this report.

At high frequencies of an oscillating magnetic field, the magnetic induction cannot follow the changes in magnetic field directions and is an angle η behind in phase [20]. If an ac field of the form $H(t) = H_0\cos(\omega t)$ is applied (ω [rad/s] is the angular velocity), the corresponding magnetic induction is given by:

$$\begin{aligned} B(t) &= B_0 \cos(\omega t - \eta) = B_0 \cos\omega t \cos\eta + B_0 \sin\omega t \sin\eta \\ &= \mu_0\mu' H_0 \cos\omega t + \mu_0\mu'' H_0 \sin\omega t \end{aligned} \tag{2.6}$$

with

$$\mu_0\mu' = \frac{B_0}{H_0}\cos\eta \tag{2.7^a}$$

and

$$\mu_0\mu'' = \frac{B_0}{H_0}\sin\eta . \tag{2.7^b}$$

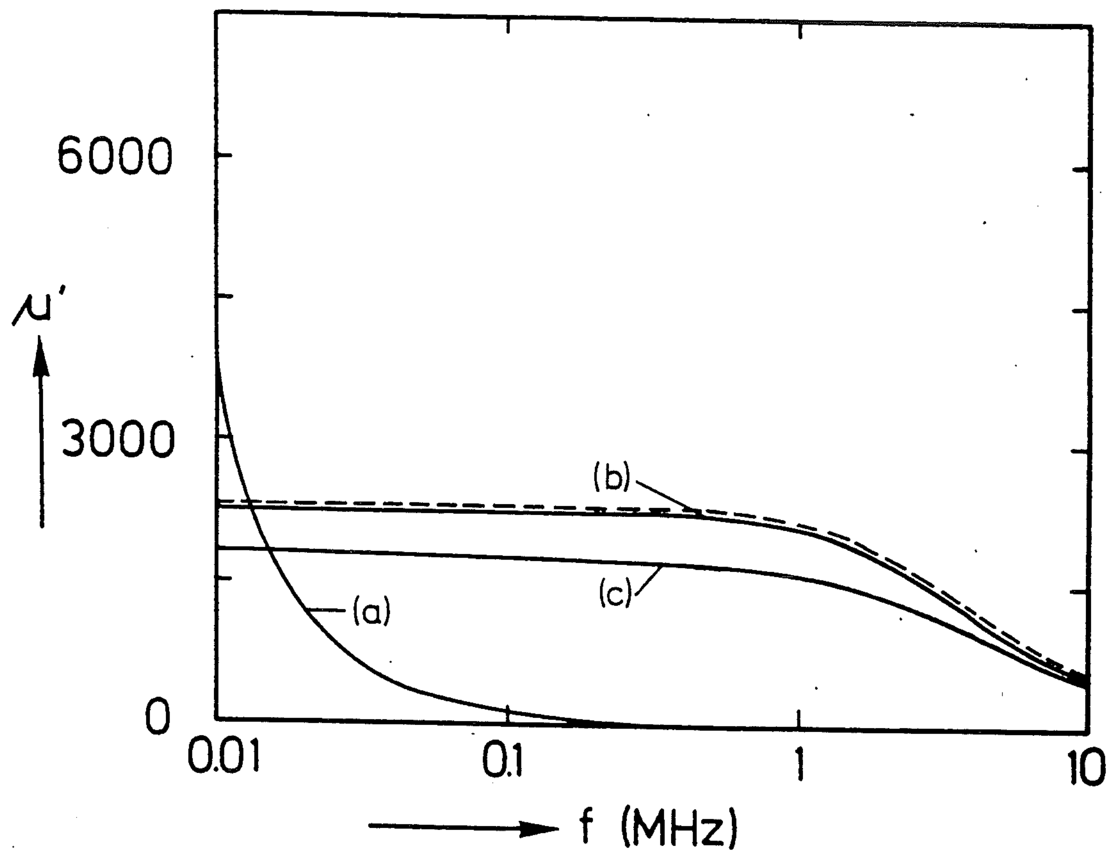

Figure 2.13 Frequency dependence of the permeability of magnetically annealed ribbons measured in:

a) the direction in which the magnetic field was applied during annealing (in the plane of the ribbon),
b) perpendicular to the direction in which the magnetic field was applied during annealing (in the plane of the ribbon) and
c) perpendicular to the direction in which the magnetic field was applied during annealing (and perpendicular to the plane of the ribbon).

The dashed line is calculated assuming rotation processes only [19].

B_0 [T] is the amplitude of the corresponding oscillating magnetic flux density signal. Usually a complex notation is much more convenient. The magnetic field is written as (the real part) of $H(t) = H_0\exp(j\omega t)$ and the *complex permeability* is defined as:

$$\hat{\mu} = \mu' - j\mu''. \tag{2.8}$$

Then the corresponding magnetic induction signal is written as:

$$\begin{aligned} B(t) &= \mu_0 \hat{\mu} H(t) = \mu_0 H_0 (\mu' - j\mu'')(\cos\omega t + j\sin\omega t) \\ &= \mu_0 \mu' H_0 \cos\omega t + \mu_0 \mu'' H_0 \sin\omega t + j(\mu_0 \mu' H_0 \sin\omega t - \mu_0 \mu'' H_0 \cos\omega t) \end{aligned} \tag{2.9}$$

so the real part of B(t) corresponds to equation (2.6).
μ' should be regarded as the component of **B** that is in phase with **H** and corresponds to the "normal" permeability as introduced in the previous section; μ'' expresses the component of **B** that is delayed by a phase angle $\pi/2$ from **H** and characterises the energy loss, as will be explained in the next section.

2.3.3 Loss mechanisms

In the previous section is was argued that an ac magnetic field and the corresponding magnetic induction signal are out of phase at high frequencies of the applied field. Because the energy of a magnetic material is minimal if the magnetic induction and the magnetic field are parallel, it follows that this phenomenon costs energy. So part of the energy supplied by the ac magnetic field is lost. If a dc magnetic field is applied the permeability has a maximal value $\mu = \mu'$, because all the energy is used to magnetise the soft magnetic material in the field direction. Two important loss terms can be distinguished [21]:

1. The first type of loss to be considered is *eddy current loss*. This is a result of electromagnetic induction: an electrical field is induced when a magnetic material is magnetised by an alternating magnetic field. The resulting electrical eddy currents flow in such a manner that magnetic field changes are opposed (Lenz's law). So the effective magnetisation and thus permeability are reduced.

2. The second type of loss is of quantum mechanical nature: *resonance loss*. It is known that electron spins precess around the direction of a magnetic field. However, in real magnetic materials the precession is not free and approaches the field direction (*damping*). When an alternating magnetic field is applied to the material the precession will be induced at the resonance frequency. So the energy supplied by the magnetic field is used to induce the precession, that is energy is absorbed (lost) and the effective permeability decreases. This phenomenon is called ferromagnetic resonance.

Next we will discuss both types of losses and introduce equations that describe the frequency dependence of the complex permeability in soft magnetic thin films. The expressions are combined to describe the effect of both eddy currents and ferromagnetic resonance in soft magnetic thin films.

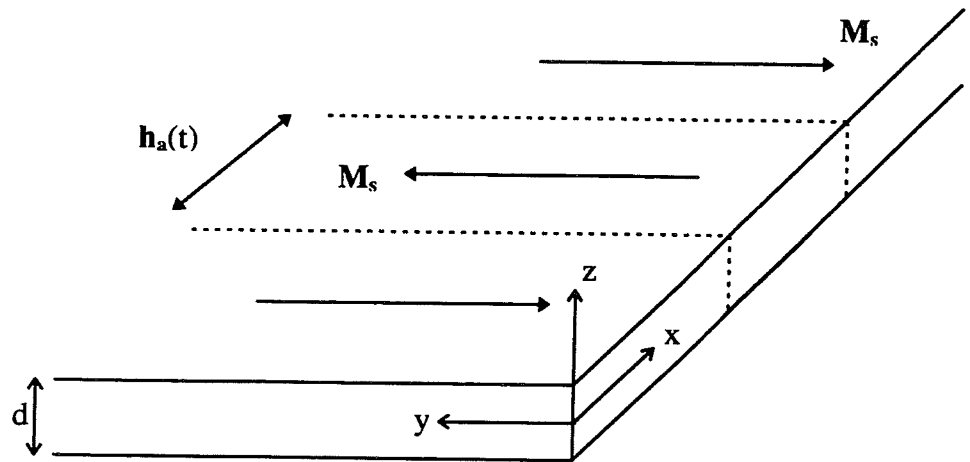

Figure 2.14 Schematic representation of the magnetic structure of the FeHfO films. A small amplitude alternating magnetic field is applied along the x-axis. All domains are parallel to the y-direction.

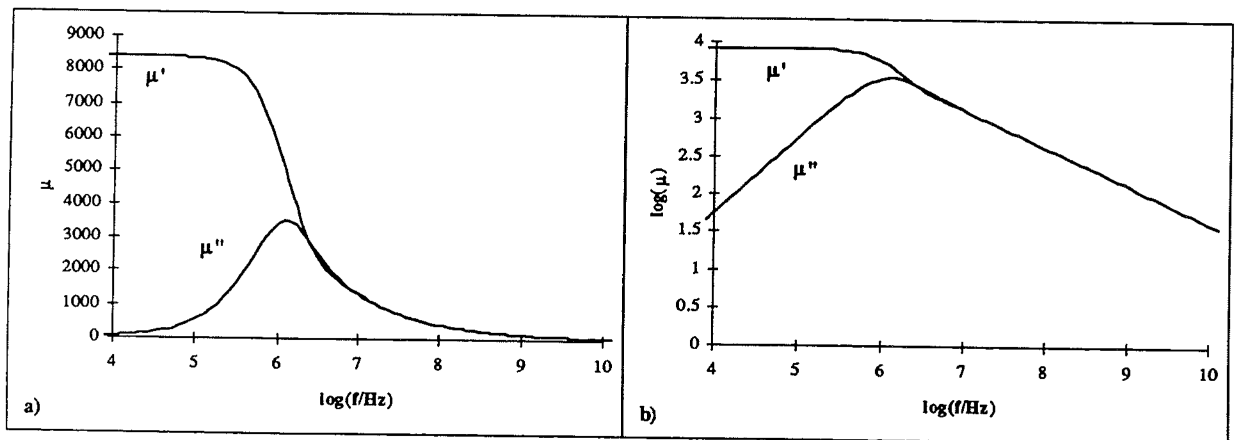

Figure 2.15 The magnetic permeability as a function of the frequency of the applied field, assuming eddy current loss only using properties of FeTaN ($d = 10$ μm, $\rho = 83$ μΩcm and $\mu_i = 8400$ [21]). Two graphs are given:
a) μ vs. log(f) and
b) log(μ) vs. log(f).

Eddy current loss
In soft magnetic iron based films with a small resistivity, the most important loss is the eddy current loss. The situation is as follows: the soft magnetic material is magnetised by a small amplitude alternating magnetic field in the x-direction (see figure 2.14):

$$\mathbf{h}_a(t) = h_0 e^{j\omega t}\mathbf{e}_x. \tag{2.10}$$

In this expression $\mathbf{e}_x$ is the unit vector along the x axis. It is assumed that the film thickness d is much smaller than the length l and width w of the film. Therefore only eddy currents in the y-direction have to be considered.
In appendix A.1 the relevant Maxwell equations are solved and the solution is written as a complex permeability:

$$\hat{\mu}_e = \mu_e' - j\mu_e'' = \frac{\mu_i}{k}\frac{(\sinh k + \sin k) - j(\sinh k - \sin k)}{\cosh k + \cos k}, \tag{2.11}$$

where μ_i is the relative intrinsic permeability of the material (the permeability in absence of eddy current, i.e. at low frequencies). k is defined as the ratio of the film thickness and the so-called *skin depth* δ [m]. The skin depth should be regarded as a measure for the penetration depth of the external magnetic field: the field is opposed by the eddy currents; this effect is strongest at the centre of the sample and reduces towards its surface. More details are given in the appendix. The skin depth is related to the specific resistance ρ [Ωm], the intrinsic permeability of the thin film material and the frequency f (= $\omega/2\pi$) of the applied magnetic field [Hz]:

$$\delta = \sqrt{\frac{2\rho}{\omega\mu_0\mu_i}}. \tag{2.12}$$

A graphical representation of the relation between μ', μ'' and the frequency f is given in figure 2.15^a, using properties of FeTaN films: d = 10 μm, ρ = 83 $\mu\Omega$cm and μ_i = 8400 [21].
At low frequencies k is small and equation (2.11) can be rewritten as:

$$\hat{\mu}_e = \mu_i\left(1 - \tfrac{1}{6}jk^2\right), \tag{2.13^a}$$

whereas at high frequencies (k large):

$$\hat{\mu}_e = \frac{\mu_i}{k}(1 - j). \tag{2.13^b}$$

So at low frequencies $\mu' = \mu_i$ and $\mu'' \propto k^2 \propto f$; whereas at high frequencies μ', $\mu'' \propto 1/k \propto 1/\sqrt{f}$. Plotting log($\mu'$), log($\mu''$) versus log(f) gives straight lines at low and high frequencies with slopes 0; +1 and -½ , see figure 2.15^b.

Resonance loss
Ferromagnetic resonance occurs at high frequencies, typically in the GHz-range. For conventional nanocrystalline soft magnetic materials Fe-(Ta,Nb,Si)-(N,C,B) [3] with low electrical resistivity (several tens of $\mu\Omega$cm) eddy current loss occurs in the MHz region, as was seen in the previous section. So in the frequency range of normal applications (< 10 MHz)

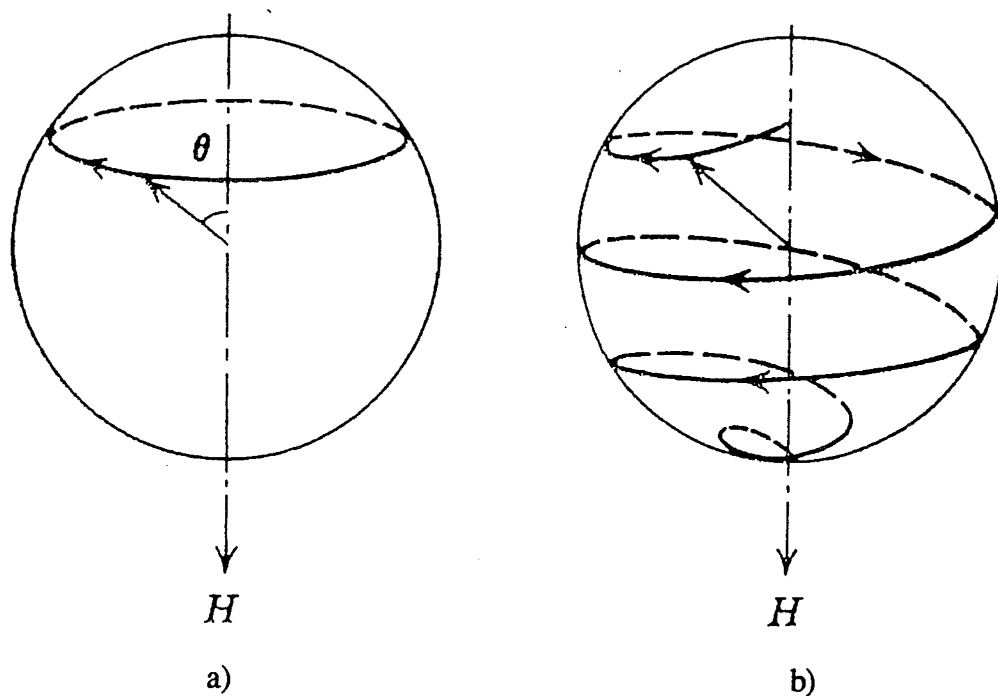

Figure 2.16 Two modes of precession of a magnetic moment (spin) [6]:
a) free precession and
b) damped precession.

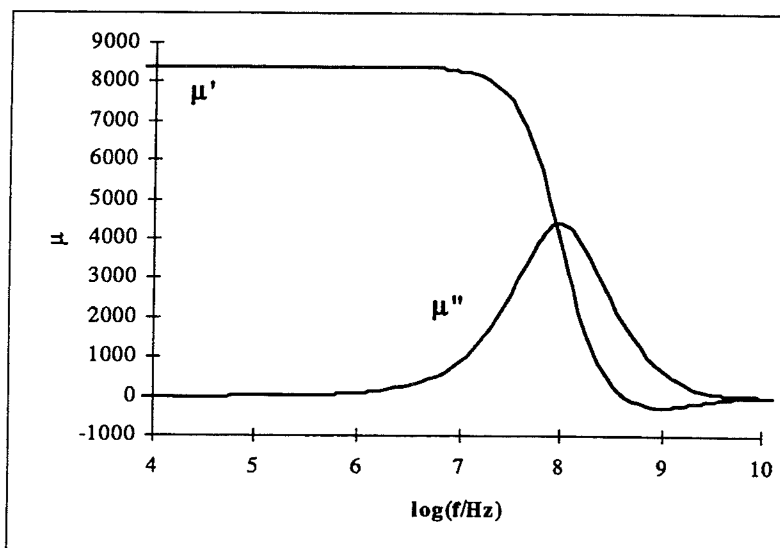

Figure 2.17 The magnetic permeability as a function of the frequency of the applied field, assuming resonance loss only using properties of FeTaN [21] ($\alpha = 0.05$, $\gamma = 176$ GHz/T, d = 10 μm, $\mu_0 M_s = 1.4$ T and $K_u = 93$ J/m^3).

eddy current loss is dominant in these materials. However, soft magnetic FeHfO has an electrical resistivity of several mΩcm instead of μΩcm. In that case it is expected that both eddy current loss and ferromagnetic resonance determine the frequency dependence of the permeability in the MHz-range.
The quantum mechanical phenomenon ferromagnetic resonance may be treated classically, if the magnetic atomic moments (spins) are taken to be coupled to give a macroscopic magnetisation [20] Now the precession of the magnetisation has to be considered. In the ideal situation the magnetisation vector precesses around a certain field direction:

$$\frac{1}{\gamma}\frac{d\mathbf{M}}{dt} = \mu_0 \mathbf{M} \times \mathbf{H}, \tag{2.14}$$

where γ is the gyromagnetic factor; $\gamma \approx 176$ GHz/T in ferromagnetic materials, see appendix A.2. Solving this equation for the simple case that a constant magnetic field is applied in the z-direction gives $M_x=\mu_0 H\sin(\theta)\cos(\omega_0 t)$, $M_y=\mu_0 H\sin(\theta)\sin(\omega_0 t)$ and $M_z=\mu_0 H\cos(\theta)$, with $\omega_0=\gamma\mu_0 H$ being the Larmor frequency [6]. The magnetisation precesses around the z axis at angular velocity ω_0 [rad/s]. See figure 2.16[a].
In real materials the precession of the magnetisation is not free and energy is transferred to the crystal lattice. So damping occurs, causing the magnetisation vector to spiral towards the field direction (see figure 2.16[b]). Such a motion is well described by a phenomenological approach made by Landau and Lifshitz [22]:

$$\frac{1}{\gamma}\frac{d\mathbf{M}}{dt} = \mu_0 \mathbf{M} \times \mathbf{H} - \frac{\alpha}{\gamma M_s}\mathbf{M} \times \frac{d\mathbf{M}}{dt}. \tag{2.15}$$

The first term on the right hand side forces the magnetisation to move on a cone, whereas the second term moves the magnetisation towards the field direction. The result is that the magnetisation spirals towards the field direction. The rate at which this process occurs is determined by α, the damping constant. It will be assumed that $\alpha^2 \ll 1$, which is usually true (see appendix A.2).
Again the small amplitude magnetic field $\mathbf{h}_a(t)$ (equation (2.11)) is applied in the x-direction. A uniaxial anisotropy is induced in the y-direction, so all domains are oriented along this direction (see figure 2.14). Further it is assumed that:

1. the film thickness is very small compared to its length and width,
2. consequently, the demagnetising factor in the z-direction equals 1,
3. the amplitude of the ac magnetic field h_0 is small compared to the anisotropy field H_K and
4. the saturation magnetisation M_s is large compared to the anisotropy field H_K.

In appendix A.2 a solution of eq. (2.15) is found using a harmonic approximation. The result can be written as a complex permeability in the x-direction:

$$\mu_f' = \mu_0^2 M_s^2 \frac{\mu_0^2 M_s H_K - \frac{\omega^2}{\gamma^2}}{\left[\mu_0^2 M_s H_K - \frac{\omega^2}{\gamma^2}\right]^2 + \left[\frac{\omega}{\gamma}\alpha\mu_0 M_s\right]^2} + 1, \tag{2.16a}$$

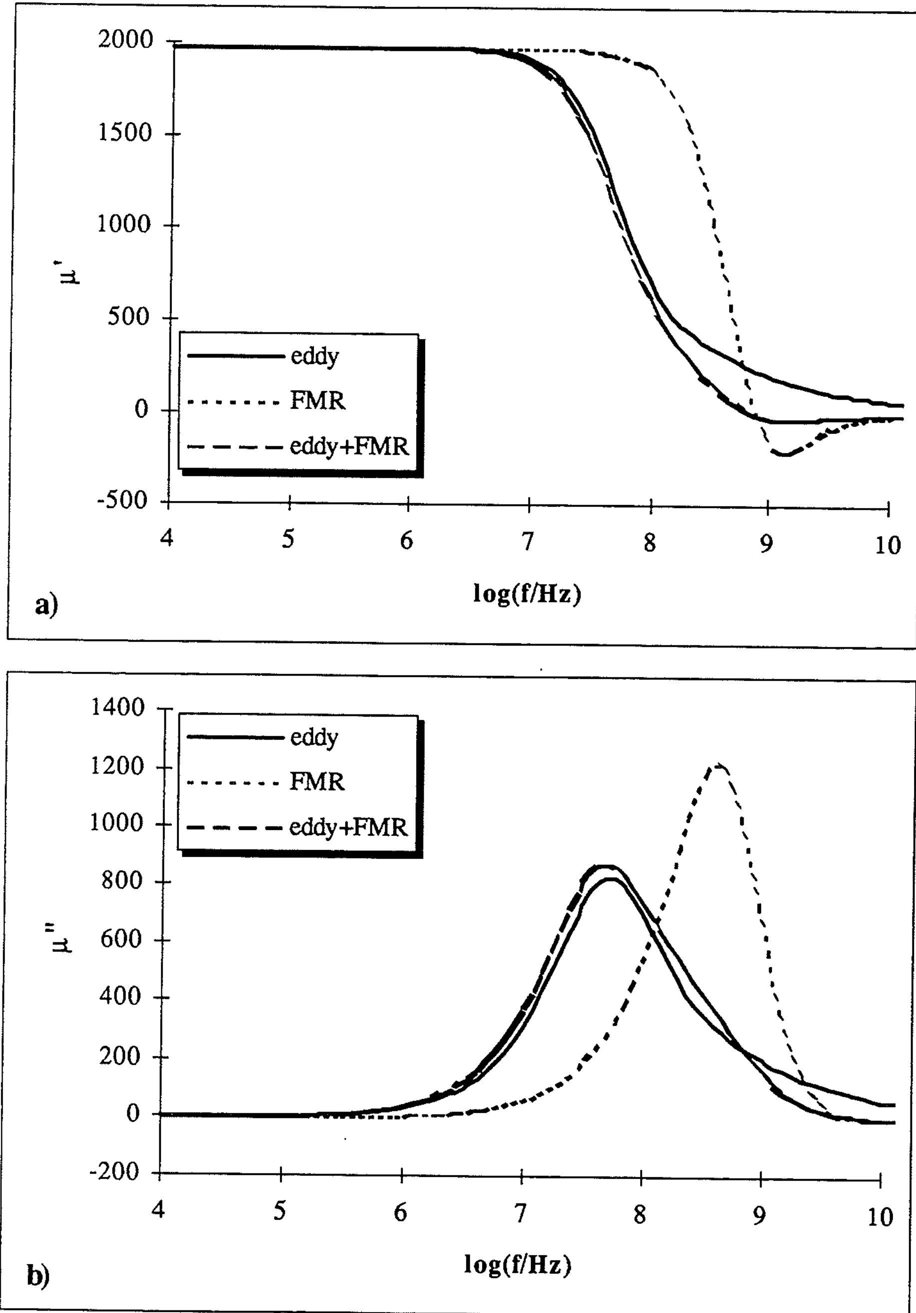

Figure 2.18 The magnetic permeability μ as a function of the frequency f of the applied field, assuming eddy current loss only, resonance loss (FMR) only and both eddy current- and resonance loss:
a) μ' vs. log(f) and
b) μ'' vs. log(f).
The following parameters of FeHfO were used: $d = 10\ \mu m$, $\rho = 0.80\ m\Omega cm$ and $\mu_0 M_s = 1.2$ T [16]. K_u is estimated to be 290 J/m^3; $\alpha = 0.05$, $\gamma = 176$ GHz/T.

$$\mu_r'' = \frac{\omega}{\gamma}\alpha\mu_0 M_s \frac{\mu_0^2 M_s^2 + \frac{\omega^2}{\gamma^2}}{\left[\mu_0^2 M_s H_K - \frac{\omega^2}{\gamma^2}\right]^2 + \left[\frac{\omega}{\gamma}\alpha\mu_0 M_s\right]^2}. \tag{2.16^b}$$

These results are visualised in figure 2.17 for FeTaN ($d = 10$ μm, $\rho = 83$ μΩcm, $\mu_0 M_s = 1.4$ T and $K_u = 93$ J/m^3). Note that μ' changes its sign: the magnetisation opposes the magnetic field. The ferromagnetic resonance frequency is defined as the frequency at which the real part of the permeability is zero. From equation (2.16^a) it follows that:

$$f_{res} = \frac{\mu_0\gamma}{2\pi}\sqrt{M_s H_K} = \frac{\gamma}{2\pi}\sqrt{2\mu_0 K_u}. \tag{2.17}$$

More accurate expressions are given in the appendix.
For $\omega \to 0$ the (complex) permeability becomes real and equal to the slope of the static MH-loop of a single domain particle, measured in the hard axis direction. From equations (2.4), (2.5) and figure 2.4 it follows that this slope is equal to:

$$\mu_0\mu_{rot} = \frac{B_s}{H_K} = \frac{\mu_0(M_s + H_K)}{H_K} \approx \frac{\mu_0 M_s}{H_K} \Rightarrow \mu_{rot} = \frac{\mu_0 M_s^2}{2K_u}. \tag{2.18}$$

This permeability is called the rotational permeability, because no domain wall motions are involved [11].

Eddy current and resonance loss
Now the results given in equations. (2.11) and (2.16) can be combined to describe the effect of eddy currents *and* ferromagnetic resonance. This can be done by substituting the permeability (2.16) because of ferromagnetic resonance for μ_i in equation (2.11). Note that the skin depth becomes a complex quantity as well. It is possible to obtain expressions for the real and imaginary part of the permeability in closed form. However, it is not very useful to mention these expressions here. Therefore they are given in appendix A.3. These expressions contain properties of both eddy current loss and ferromagnetic resonance:

- at low frequencies the permeability becomes real and equal to the rotational permeability (2.18); μ'' increases with slope +1 on log-log scale due to the eddy current loss,
- at very high frequencies the magnetic moments cannot follow the changes in the magnetic field direction at all; therefore the permeability reaches 1 (the permeability of vacuum),
- at intermediate frequencies the permeability becomes negative, because of ferromagnetic resonance.

Because of its low resistivity, the permeability is mainly determined by eddy current loss in FeTaN. Therefore, the combined description is not very illustrative for this material. In figure 2.18 the calculated permeability of FeHfO is given as a function of the frequency of the applied magnetic ac field for all three cases (only eddy currents, only ferromagnetic resonance and both eddy currents and ferromagnetic resonance). The saturation magnetisation, intrinsic permeability and specific resistivity needed in the calculation are obtained from section 2.2; the uniaxial anisotropy constant is estimated to be $K_u = 290$ J/m^3 using equation (2.18).

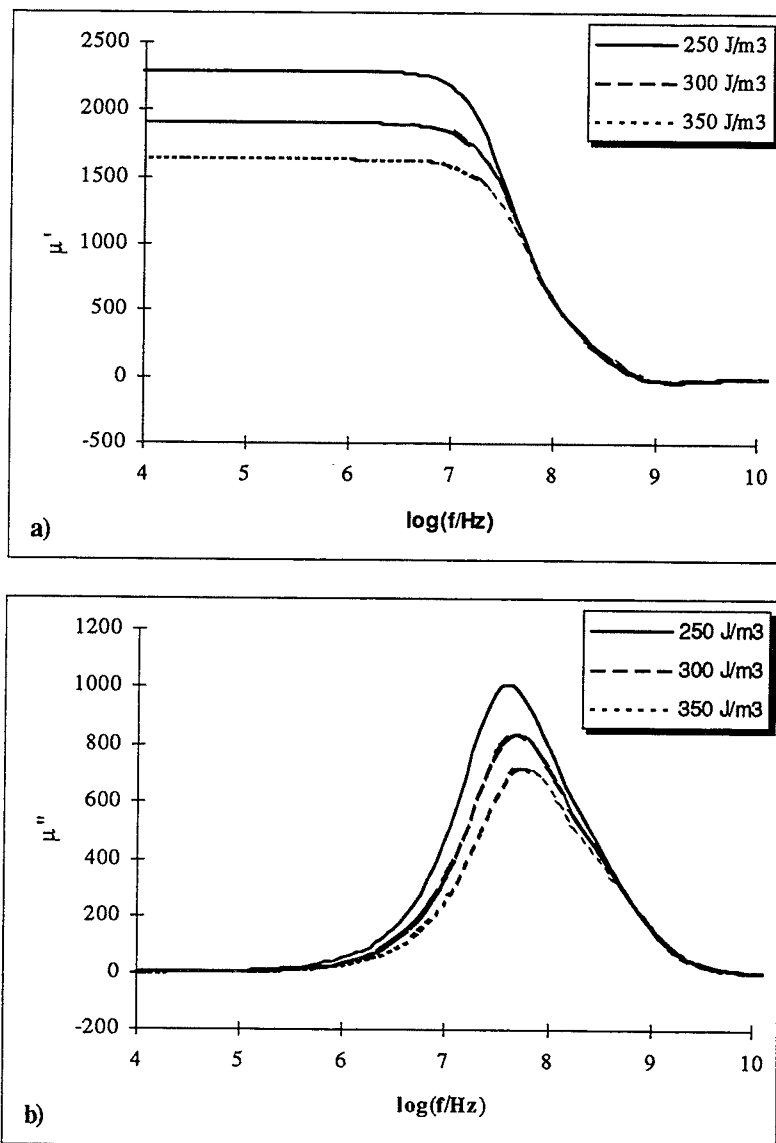

Figure 2.19 Influence of the uniaxial anisotropy constant K_u [J/ m^3] on the μ(f) function, assuming both eddy current- and resonance loss using proprrties of FeHfO (d = 10 μm, ρ = 0.80 mΩcm and $\mu_0 M_s$ = 1.2 T [16]; α = 0.05, γ = 176 GHz/T; K_u is estimated to be 290 J/m^3):
a) μ′ vs. log(f) and
b) μ″ vs. log(f).

The parameters in the model are: the thickness d, the saturation magnetisation M_s, the gyromagnetic factor γ, the damping constant α, the electrical resistivity ρ and the uniaxial anisotropy constant K_u. All of these parameters can be measured or are (approximately) known, except for K_u. The influence of this parameter on the permeability spectra is shown in figure 2.19 for FeHfO.

2.4 Crystallisation kinetics

2.4.1 Introduction

Thermodynamics predicts the stable configuration of a system. The system to be considered in this report is the amorphous/nanocrystalline alloy FeHfO.
Glasses are unstable, because the Gibbs free energy of the crystalline state is less than the free energy of the amorphous state. Crystallisation causes the free energy to change by an amount of:

$$\Delta G^0 = G_A^0 - G_C^0 < 0 \tag{2.19}$$

per unit of volume. $G^0_{A,C}$ are the free energies per unit of volume [J/m^3] of the amorphous and the crystalline state, respectively.
Although thermodynamics is capable of predicting the stable phases, nothing can be said about the kinetics of phase transformations. The rate of transformation can be extremely low, even if the desired configuration is very favourable, i.e. $\Delta G^0 \ll 0$. Therefore, it is possible for amorphous alloys to exist at relatively low temperatures for extended amounts of time.
The crystallisation process is demonstrated in figure 2.20. In order to transform from one atomic configuration (the amorphous state) to another (the crystalline state) transport of atoms has to take place. Experimental observations of crystallisation processes as a function of temperature indicate that the material has to overcome an energy barrier in order to crystallise.

2.4.2 Nucleation and growth

Phase transformations are usually divided into homogeneous and heterogeneous transformations [23]. A homogeneous transformation begins at randomly oriented, indistinguishable sites, whereas heterogeneous transformation takes place on specific sites (surfaces, grain boundaries, dislocations). In a glass there are no distinguishable sites. The crystallisation process is therefore considered to be a homogeneous transformation.
Homogeneous transformations usually occur in two stages: nucleation and growth. Because of thermal fluctuations, many small clusters of ordered atoms exist in the amorphous alloy. Let us calculate the excess free energy $\Delta G(r)$ [J] associated with a spherical cluster of ordered atoms with radius r [m]. There are two contributions of opposite sign: a *volume* ($\propto r^3$) decrease, which is proportional to ΔG^0 of equation (2.19) and a positive contribution, which arises from the creation of *interface* ($\propto r^2$) between the amorphous and crystalline phase. The excess free energy $\Delta G(r)$ [J] is given by:

$$\Delta G(r) = \tfrac{4}{3}\pi r^3 \Delta G^0 + 4\pi r^2 \gamma_{A,C}. \tag{2.20}$$

$\gamma_{A,C}$ is the interfacial energy of the amorphous/crystalline interface [J/m^2]. The excess free energy of the spherical cluster is plotted in figure 2.21 as a function of its radius. Because of the different powers of r, there is a maximum at $r = r_c$, the critical nucleus size. Below this size

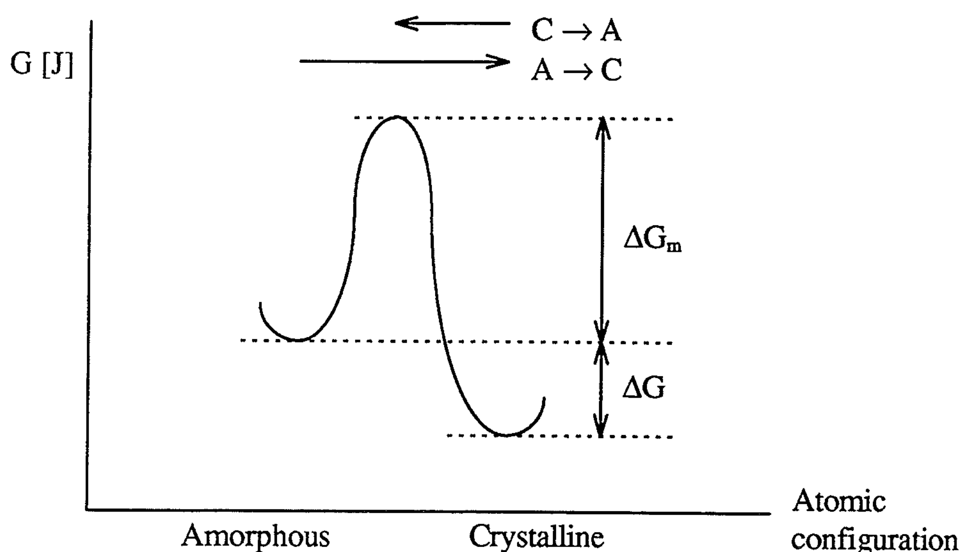

Figure 2.20 Schematic representation of the crystallisation process of a glass. In order to jump from the amorphous (A) to the crystalline (C) atomic configuration) the atoms have to overcome an energy barrier ΔG_m. Atoms jumping in the opposite direction face an energy that is ΔG higher, corresponding to the free energy difference between crystalline and amorphous atomic configuration. There is a net particle flux from the amorphous to the crystalline atomic configuration.

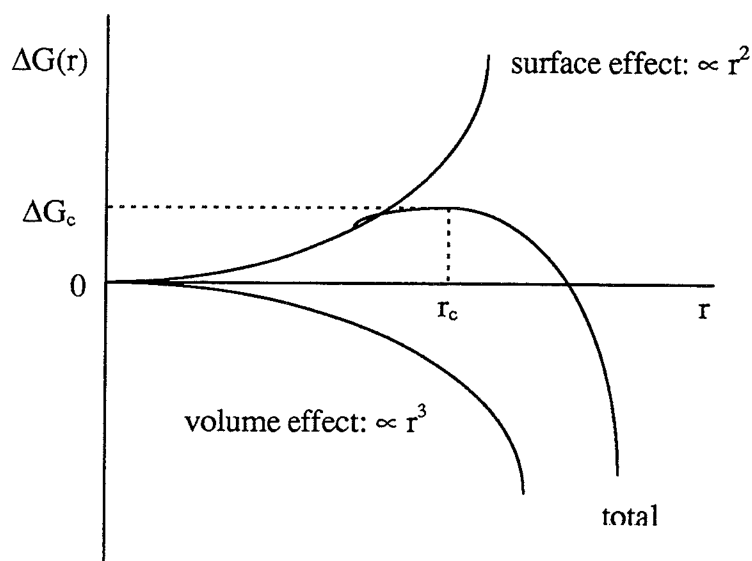

Figure 2.21 Excess free energy $\Delta G(r)$ of a spherical cluster of ordered atoms as a function of the radius r. There is a negative volume effect ($\propto r^3$) and a positive surface effect ($\propto r^2$). A maximum ΔG_c is observed at $r = r_c$, the critical nucleus size.

the free energy increases with r. These particles are called *embryos*. Particles with $r > r_c$ are referred to as *nuclei*. The maximum excess free energy at $r = r_c$ is ΔG_c [J].
The process of forming clusters with radius r_c (critical nuclei) is called nucleation. The probability to find a critical nucleus at a certain time is proportional to $\exp(-\Delta G_c/k_BT)$, with k_B Boltzmann's constant en T the absolute temperature [K]. The nucleation rate n [nuclei m^{-3} s^{-1}] is proportional to this exponent [23,24]:

$$n = n_0 \exp\left(-\frac{\Delta G_c}{k_B T}\right). \tag{2.21}$$

In this expression n_0 [nuclei m^{-3} s^{-1}] is a constant, which contains the atomic jump frequency and the overall atom concentration. The *activation energy for nucleation* is written as: $Q_n = N_A \Delta G_c$ in J/mole; N_A is Avogradro's number.
After reaching their critical size, the nuclei start growing. The growth rate can be obtained by considering the sum of two atomic fluxes of opposite sign, as indicated in figure 2.20. Atoms jumping from the amorphous to the crystalline phase have to overcome an energy ΔG_m [J] each; atoms jumping from the crystalline to the amorphous phase have to overcome a larger energy $\Delta G_m + \Delta G$ [J]. ΔG_m is the energy of an atom needed for transfer from one phase to the other phase; ΔG is the absolute energy difference between the amorphous and the crystalline phase (per atom). Therefore the flux to the crystalline phase is larger. The growth rate of nuclei v [m/s] is proportional to the effective atomic flux and is given by [23,24]:

$$v = v_0 \exp\left(-\frac{\Delta G_m}{k_B T}\right)\left\{1 - \exp\left(-\frac{\Delta G}{k_B T}\right)\right\}. \tag{2.22}$$

v_0 [m/s] is a constant that contains the atomic diameter and the atomic jump frequency. In the case of growth in glasses the temperature is relatively low, $\Delta G \gg k_BT$. In that case the growth rate can be described by $v = v_0\exp(-Q_g/RT)$ with $Q_g = N_A \Delta G_m$ [J/mole], *the activation energy for growth*. The pre-exponential constant v_0 is assumed to be constant, because the temperature dependence of v_0 can be ignored compared to the exponential dependence.

2.4.3 Overall crystallisation kinetics

This section concerns a description of the kinetics of crystallisation. In the first part a relation is obtained between the volume fraction of crystallised material and the time under isothermal conditions. In the next sections these equations are made suitable for describing non-isothermal crystallisation.

Isothermal crystallisation kinetics
First the problem is simplified. Besides isothermal conditions, we employ some other assumptions:

1. The crystallisation process is homogeneous and follows the nucleation and growth mechanism as described in the section 2.4.2.
2. The number of nuclei per unit of volume as a function of time is given by $N(t) = N_0 + nt$, where n is the nucleation rate: $n = n_0\exp(-Q_n/RT)$; the number of nuclei present at t=0 is N_0 (per m^3). The volume of the nuclei is very small with respect to the total volume V_0.
3. The growth rate can be described by: $v = v_0\exp(-Q_g/RT)$.

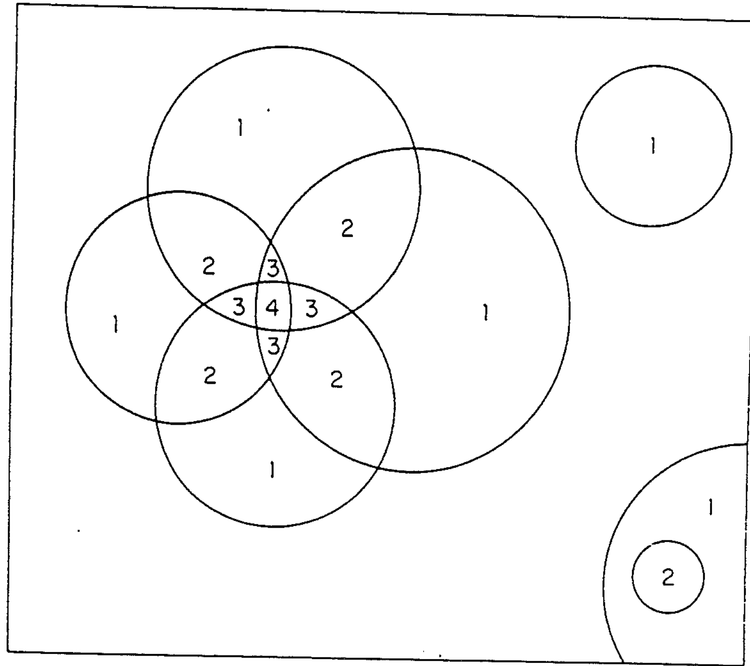

Figure 2.22 Schematic picture of a material transforming by the growth of spheres [28]. The total volume of the individual spheres is called the extended volume. The real volume is significantly smaller because of overlapping. Orders of overlap are indicated.

Grain growth is governed by either the rate of transfer of atoms across the advancing interface (interface control) or the rate of diffusion of atoms towards or away from the growing crystal (diffusion control). In the former case, the grain size is proportional to time t. In the latter case it is proportional to the square root of t. Generally the volume V of a particle, starting to grow at t = 0, is given by:

$$V(t) = \sigma(vt)^{pb}. \tag{2.23}$$

The exponent depends on the rate determining step (p = ½ for diffusion control and p = 1 for interface control) and the dimension of the crystalline particles (b = 1, 2 or 3 for needle, plate or spherical particles); σ [m^{3-pb}] is a geometric factor (for instance: $\sigma = 4\pi/3$ m^{3-3p} for a spherical particle).

In the model presented a problem arises at the moment that particles begin to overlap. Since the total volume of the crystalline phase is the sum of the individual particle sizes (2.23), the predicted volume becomes greater than the real volume. From this point on, we will call the volume calculated by equation (2.23) the *extended volume*, which has to be corrected for overlapping particles. Avrami [25-27] demonstrated that there exists a proportionality between a small increase in extended volume dV^{ex} and a small increase in real volume dV:

$$dV = \left(1 - \frac{V}{V_0}\right) dV^{ex}. \tag{2.24}$$

Dividing equation (2.24) by the total volume V_0 makes it dimensionless. The dimensionless quantities V/V_0 and V^{ex}/V_0 are called *volume fractions* (f and f^{ex} resp.). Integration in terms of these volume fractions, using $f^{ex}(t=0) = 0$, gives: $f = 1-\exp(-f^{ex})$. Greer [28] demonstrated this relation to be a good approximation by expanding the expression in a series: $f = f^{ex} - f^{ex}/2! + f^{ex}/3! - \ldots$. It can be seen that these terms correct for the various order of overlap, as illustrated in figure 2.22.
The increase of extended volume dV^{ex} in a time interval dt at time t is the sum of two contributions:

1. growth of the N_0V_0 nuclei present at t = 0, that have grown for t seconds and now grow during the interval dt;
2. growth of the nuclei formed at between $t = \tau$ and $\tau + d\tau$, that have grown for $t-\tau$ seconds and now grow during the interval dt.

First the volume increase of the N_0V_0 nuclei present at time t = 0, because of growth in the interval dt, is calculated. Differentiating equation (2.23) with respect to time gives the volume increase of one nuclei in a time interval dt at time t. Multiplying the result by N_0V_0 gives the first contribution: $\sigma N_0 V_0 pbv^{pb} t^{pb-1} dt$.
Secondly, the amount of nuclei that are formed in a time interval between $t = \tau$ and $\tau + d\tau$ is calculated by differentiating the number of nuclei with respect to time: $nV_0 d\tau$. These nuclei are smaller than the nuclei formed at t = 0, because they have grown during a shorter period $t-\tau$. Therefore, the volume increase because of growth of these nuclei during the interval dt is equal to $\sigma pbv^{pb}(t-\tau)^{pb-1}dt$. The second volume increase is found by integrating of the product of these two, $nV_0 d\tau \cdot \sigma pbv^{pb}(t-\tau)^{pb-1}dt$, for all times τ (< t).

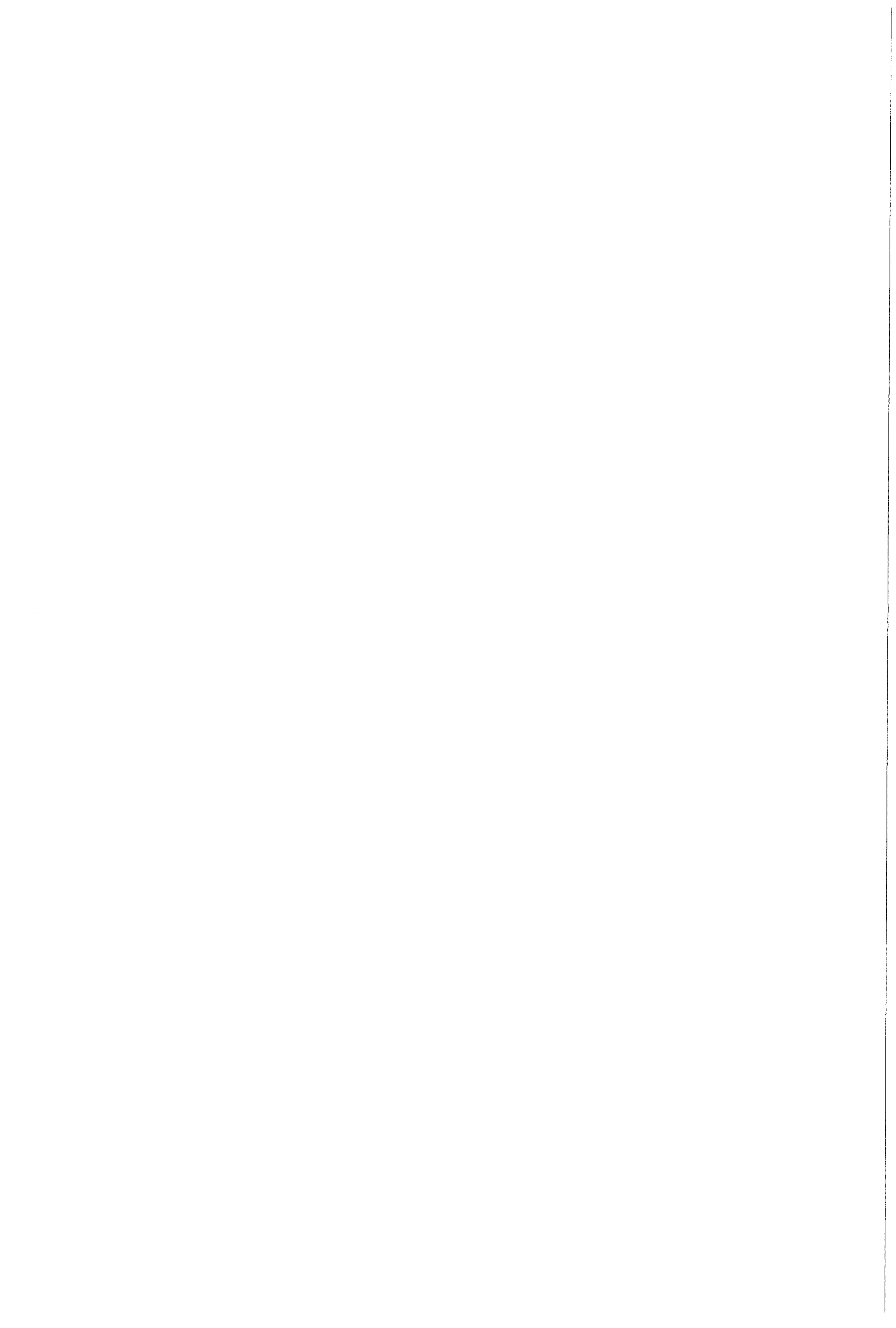

So the total increase of extended volume in the interval dt is given by:

$$dV^{ex}(t) = \sigma V_0 \left\{ N_0 pbv^{pb} t^{pb-1} + pbnv^{pb} \int_{\tau=0}^{t} (t-\tau)^{pb-1} d\tau \right\} dt. \qquad (2.25)$$

The integral is equal to t^{pb}/pb. Recognising $f_{ex}(t) = V_{ex}(t)/V_0$, the following expression for the (real) fraction transformed is found:

$$f_{p,b}(t) = 1 - \exp\left\{-\sigma(vt)^{pb}\left[N_0 + nt\right]\right\}. \qquad (2.26)$$

Equation (2.26) can be reduced to the well-known J(ohnson)-M(ehl)-A(vrami) equation [30,31]:

$$f(t) = 1 - \exp\left[-\left(\frac{t}{\tau}\right)^m\right], \qquad (2.27)$$

with:

$$\tau = \tau_0 \exp\left(\frac{Q_x}{RT}\right). \qquad (2.28)$$

In these expressions m is called the Avrami-parameter and τ [s] is a time constant that contains a pre-exponential time constant τ_0 (approximately 1/Debye-frequency) and Q_x [J/mole], the activation energy for the *whole* crystallisation process being a combination of the activation energy for nucleation and for growth.
Many crystallisation processes are well described [28,32] by the JMA-equation. Usually only this empirical justification of the JMA-equation is emphasised. However, the JMA-equation follows from equation (2.26) if:

1. $N_0 \gg nt$. Nucleation of new particles can be ignored compared to the number of nuclei present at $t = 0$ (per unit of volume). Growth only takes place at these nuclei. In this case the Avrami-parameter is equal to bp and the activation energy for the whole crystallisation process is equal to the activation energy for growth Q_g,

2. $nt \gg N_0$. Growth takes place on newly nucleated particles only. The Avrami parameter is now 1 + pb. The activation energy for the whole crystallisation is given by [31,32]:

$$Q_x = \frac{Q_n + pbQ_g}{1 + pb}. \qquad (2.29)$$

Non-isothermal crystallisation kinetics
The treatise of the kinetics of non-isothermal crystallisation has already been given in 1957 by Kissinger [33]. He divided the non-isothermal process in numerous isothermal processes, obeying the JMA-equation. The following derivation of the non-isothermal fraction transformed is slightly different.

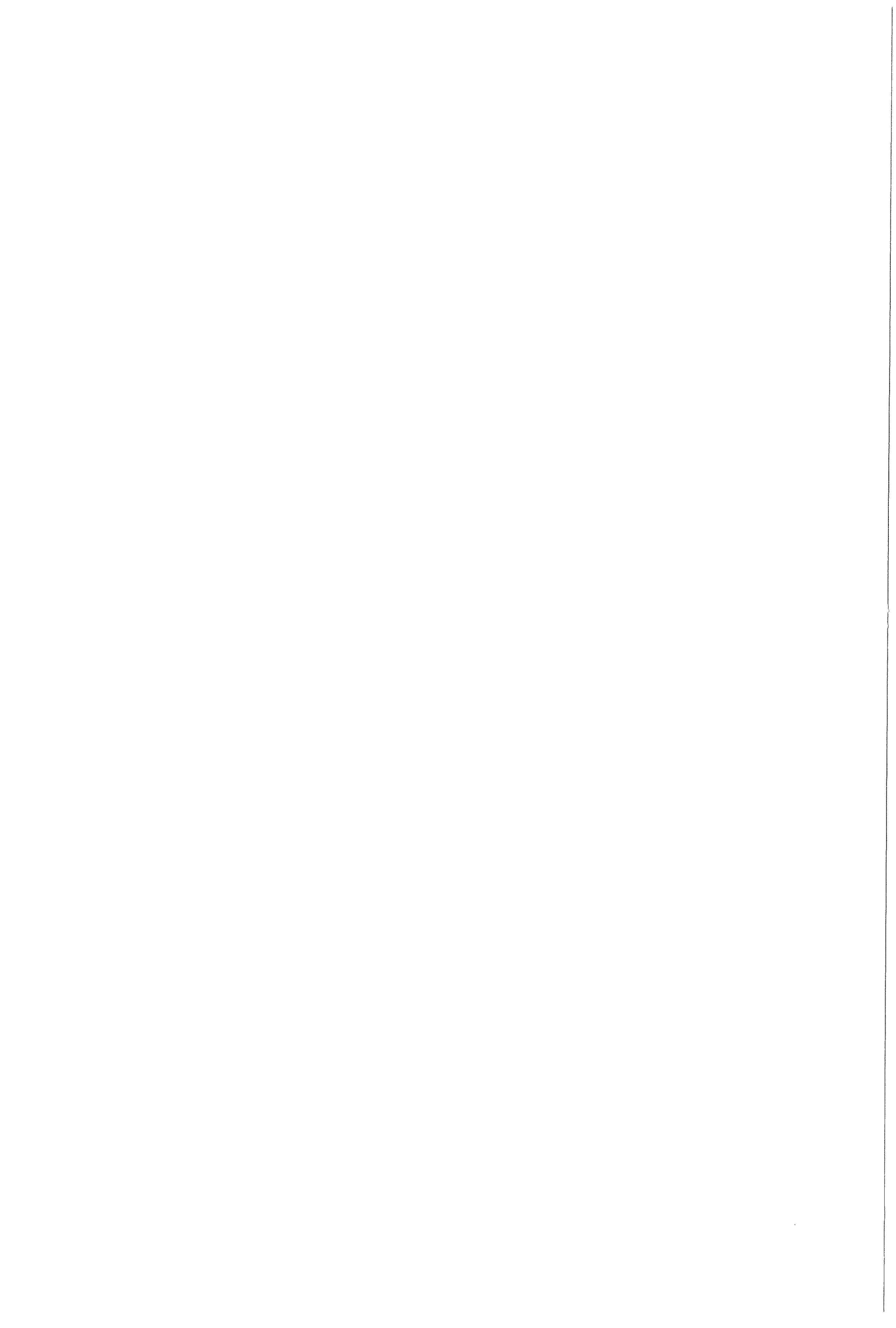

Differentiating the JMA-equation (2.27) with respect to time gives the isothermal transformation rate:

$$\frac{df}{dt} = m\tau^{-m}t^{m-1}\exp\left[-\left(\frac{t}{\tau}\right)^m\right]. \qquad (2.30)$$

Since f is an explicit function of t, an alternative form of (2.30) is:

$$\frac{df}{dt} = m\tau^{-1}(1-f)\left[-\ln(1-f)\right]^{\frac{m-1}{m}}. \qquad (2.31)$$

This expression reduces to the rate equation for a first order transition for m = 1 [34].
So far the temperature profile has not been discussed. Usually a constant heating rate is assumed, that is $T(t) = T_0 + \phi t$. T_0 [K] is the starting temperature and ϕ [K/s] is the heating rate. The temperature dependence, and thus time dependence, is inserted in equation (2.31) by means of τ (equation (2.28)). It is assumed that τ_0 is independent of temperature. While this may not be true [29], the temperature dependence of τ_0 can be ignored compared to the exponential dependence.
Integration of equation (2.31), using the substitution:

$$x = \frac{Q_x}{R(T_0 + \phi t)}, \qquad (2.32)$$

gives the following expression for the non-isothermal fraction transformed:

$$f(t, x(t)) = 1 - \exp\left\{-\left[\frac{(T_0 + \phi t)g(x(t))}{\phi\tau_0}\right]^m\right\}, \qquad (2.33)$$

where g(x) is defined as:

$$g(x) \equiv e^{-x}\sum_{n=1}^{\infty}(-1)^{n+1}\frac{n!}{x^n} = e^{-x}\left\{\frac{1!}{x} - \frac{2!}{x^2} + \frac{3!}{x^3} - \ldots\right\}. \qquad (2.34)$$

The integration procedure is given in appendix B.
The activation energy for the whole crystallisation process is of the order 10^5 J/mole, while the maximum temperature is of the order 10^3 K. Therefore, the minimal value of x is approximately 10. Using this value in equation (2.34) it can be seen that the first three terms of the series expansion are a good approximation of the entire summation.

Combined non-isothermal and isothermal crystallisation kinetics
In the experiments to be described the time t_1, necessary for heating up to a fixed temperature T_1, cannot be ignored. Therefore both non-isothermal and isothermal crystallisation occur. The temperature profile to be described is illustrated in figure 2.23. From t = 0 until $t = t_1$ the material is heated from $T = T_0$ to $T = T_1$ with a constant heating rate. For $t > t_1$ the temperature is kept constant at temperature T_1 (= $T_0 + \phi t_1$). It is assumed that the fraction transformed can be described with the isothermal JMA equation (2.27) from $t = t_1$, using the substitutions: $f \rightarrow [f(t)-f(t_1)]/[1-f(t_1)]$ and $t \rightarrow t-t_1$.

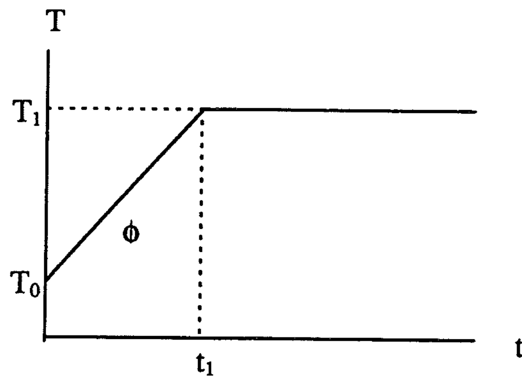

Figure 2.23 Temperature profile of a typical heat treatment:

- $T = T_0 + \phi t$ for $0 \leq t \leq t_1$ and
- $T = T_1 (= T_0 + \phi t_1)$ for $t > t_1$.

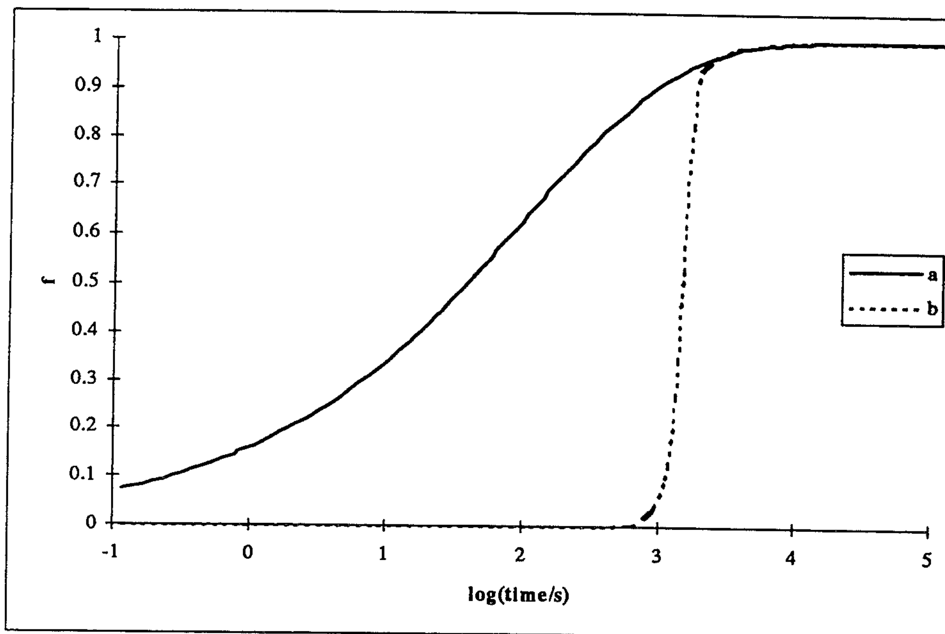

Figure 2.24 Volume fraction crystallised material f as a function of time during crystallisation at temperature $T_1 = 550$ K, which is reached

a) instantly and

b) in a finite time $t_1 = 1.6$ ks required to heat the specimen (heating rate $\phi = 10$ K/min).

The following parameters are used in the calculation: $Q_g = 158$ kJ/mole, $m = 0.38$ and $\tau_0 = 10^{-13}$ s.

The combined non-isothermal and isothermal fraction transformed is given by:

$$f(t) = \begin{cases} 1 - \exp\left\{ -\left[\frac{(T_0 + \phi t) g(x(t))}{\phi \tau_0} \right]^m \right\} & 0 \le t \le t_1 \\ f(t_1) + (1 - f(t_1)) \left\{ 1 - \exp\left[-\left(\frac{t - t_1}{\tau} \right)^m \right] \right\} & t > t_1 \end{cases} \quad . \tag{2.35}$$

The difference between isothermal crystallisation and crystallisation including the heating process is shown in figure 2.24. As expected, the heating effect shifts the f-log(t) curve to longer times.

2.4.4 Activation Energy Spectra

In this section a slightly different model is presented to describe the crystallisation process (non-isothermal and isothermal). The rate equation for a first order transition is considered (m = 1 in the JMA equation). Instead of a single activation energy, it is assumed that there is a spectrum of activation energies.
Each activation energy spectrum (AES) is characterised by a distribution function. Let the distribution function for the activation energies Q be g(Q) and be defined between Q_{min} and Q_{max}. The most important properties of this function are [35,36]:

1. The probability to find an activation energy between Q and Q + dQ is equal to g(Q)dQ.
2. Consequently:

$$\int_{Q_{min}}^{Q_{max}} g(Q)dQ = 1. \tag{2.36^a}$$

3. The probability to find an activation energy between Q_1 and Q_2 ($Q_{min} < Q_1 < Q_2 < Q_{max}$) is:

$$\Pr\{Q_1 < \underline{Q} < Q_2\} = \int_{Q_1}^{Q_2} g(Q)dQ. \tag{2.36^b}$$

4. The expectation of a function f(Q) of the variable Q is given by:

$$E\{f(\underline{Q})\} = \int_{Q_{min}}^{Q_{max}} f(Q)g(Q)dQ. \tag{2.36^c}$$

Two special expectations are the average $E\{\underline{Q}\} = Q_0$ [J/mole] of the distribution and the variance $E\{(Q-Q_0)^2\} = \sigma_Q^2$ (σ_Q [J/mole] is the standard deviation). Both parameters are characteristic for the distribution function.

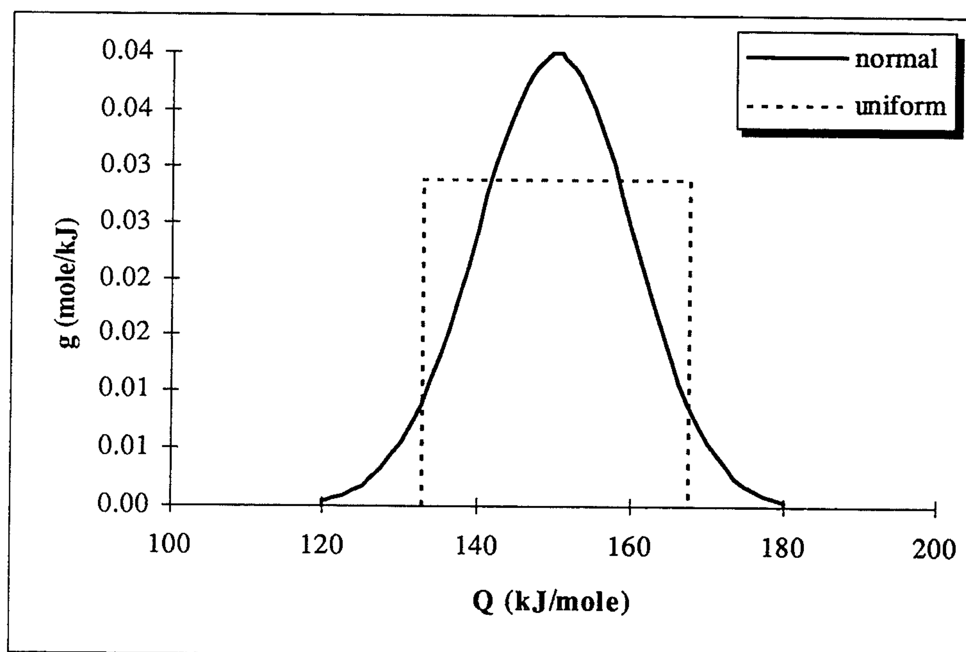

Figure 2.25 Activation energy spectra g(Q) calculated taking the average $Q_0 = 150$ kJ/mole and the standard deviation $\sigma_Q = 10$ kJ/mole deviation for two situations:
a) the uniform distribution and
b) the normal distribution.

Two distributions are used in this report. For simplicity reasons we start with the *uniform* distribution (see figure 2.25). A uniform activation energy spectrum is described by the distribution function:

$$g_1(Q) = \begin{cases} \dfrac{1}{Q_{max} - Q_{min}} & Q_{min} \le Q \le Q_{max} \\ 0 & \text{elsewhere} \end{cases} . \tag{2.37}$$

The parameters are: $Q_0 = (Q_{min}+Q_{max})/2$ and $\sigma_Q = (Q_{max}-Q_{min})/2\sqrt{3}$.
The most probable distribution function, however, is the *normal* distribution (see figure 2.26). A normal activation energy spectrum is described by the distribution function:

$$g_2(Q) = \frac{1}{\sigma_Q\sqrt{2\pi}} \exp\left[-\tfrac{1}{2}\left(\frac{Q-Q_0}{\sigma_Q}\right)^2\right]. \tag{2.38}$$

This distribution extends from $Q = -\infty$ to $+\infty$, so we are forced to limit the activation energy interval. This can be done quite easily if one realises that almost all energies (99.74%) are found in the interval $Q_0-3\sigma_Q < Q < Q_0+3\sigma_Q$. In that case renormalising (2.38) is done by dividing by 0.9974.
Using these distributions, the expectation of the fraction transformed $E\{f(Q)\}$ can be calculated (numerically). The procedure is described in the chapter 5.

2.4.5 Observation of the crystallisation process by means of electrical resistivity

Any physical property that changes monotonically as a result of crystallisation can be used to monitor crystallisation processes. It is important that the particular physical property can be measured instantly. Electrical resistivity is one of those physical properties.
Usually it is assumed that the measured resistivity is a linear function of the fraction transformed [37,38]:

$$\rho_{eff} = \rho_C f + \rho_A (1-f), \tag{2.39^a}$$

with ρ_{eff} [Ωm] the effective resistivity of a the material that consists of crystalline particles with resistivity ρ_C [Ωm] in an amorphous medium of resistivity ρ_A [Ωm]. In theory this means that the material crystallises in planes normal to the current or measuring direction.
Kelton and Spaepen [39] argue that the linear assumption is a good one, unless the resistivities of the amorphous and crystalline phase are different by less than a factor of 5. The analysis of resistivity that Kelton and Spaepen follow, is based on Maxwell's [40] treatment of an analogous problem. He calculated the effective resistivity ρ_{eff} for a number of randomly located spheres with resistivity ρ_C in a medium with resistivity ρ_A as a function of the (small) volume fraction f of the spheres.
The result is:

$$\rho_{eff} = \frac{2\beta+1-(1-\beta)f}{2\beta+1+2(1-\beta)f}\rho_A . \tag{2.39^b}$$

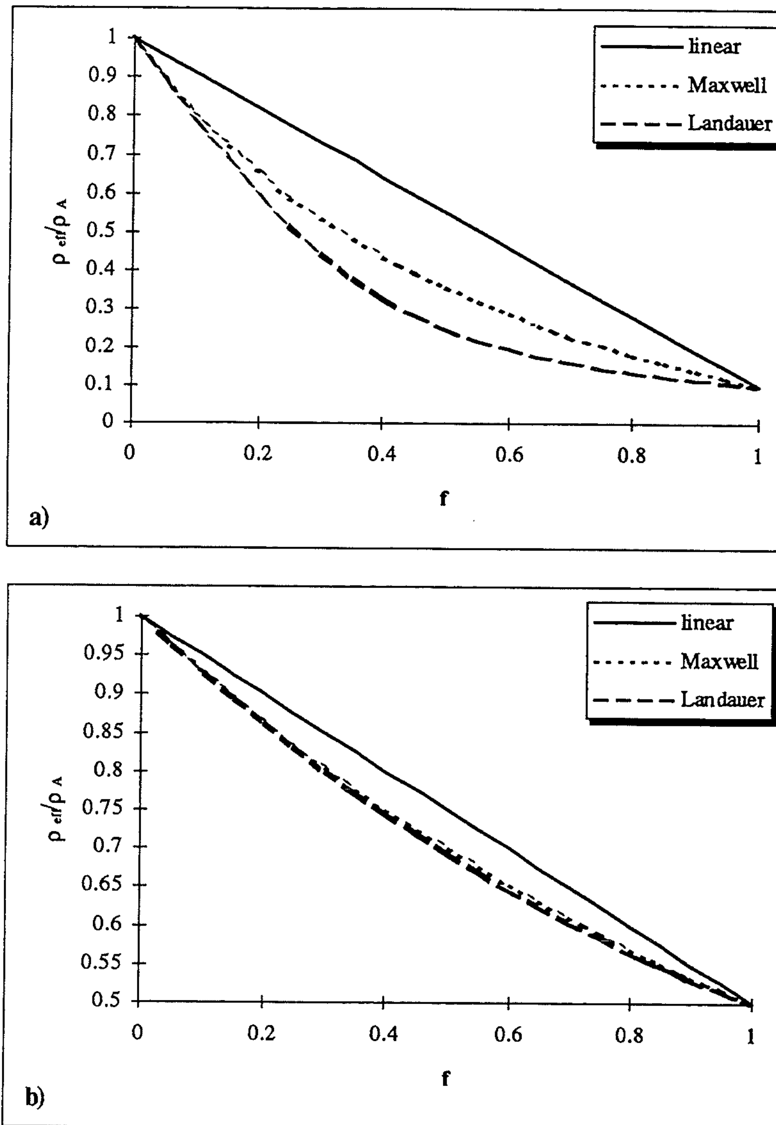

Figure 2.26 Three relations (linear, Maxwell, Landauer) between the (normalised) effective resistivity ρ_{eff}/ρ_A and the volume fraction crystalline material f, using:
a) $\rho_A = 1000$ μΩcm and $\rho_C = 100$ μΩcm ($\beta = 0.1$),
b) $\rho_A = 1000$ μΩcm and $\rho_C = 500$ μΩcm ($\beta = 0.5$).

β is a dimensionless quantity, defined as ρ_C/ρ_A.
Another relation for a random two-phase mixture is given by Landauer [41]. The Landauer approximation can be written as [42]:

$$\rho_{eff} = \tfrac{1}{2}\left\{(1-3f)\rho_A - (2-3f)\rho_C + \sqrt{\left[(1-3f)\rho_A - (2-3f)\rho_C\right]^2 + 8\rho_A\rho_C}\right\} \quad (2.39^c)$$

These three relations between the effective resistivity and the volume fraction are plotted in figure 2.26 for several values of β and ρ_C. There is a significant deviation from linear behaviour for the latter two models. This deviation becomes less if β approaches 1. In first approximation we will adopt the linear assumption.

One final remark should to be made. The relations (2.41) are invalid in the case of well-conducting crystallites in an almost insulating amorphous matrix. That problem is attacked by percolation theory [43]. Without going into detail, the most important result of this theory will be given. The percolation theory predicts a critical volume fraction at which the resistivity drops effectively to zero. That means that relations (2.41) can not be used if resistivity shows such a drop.

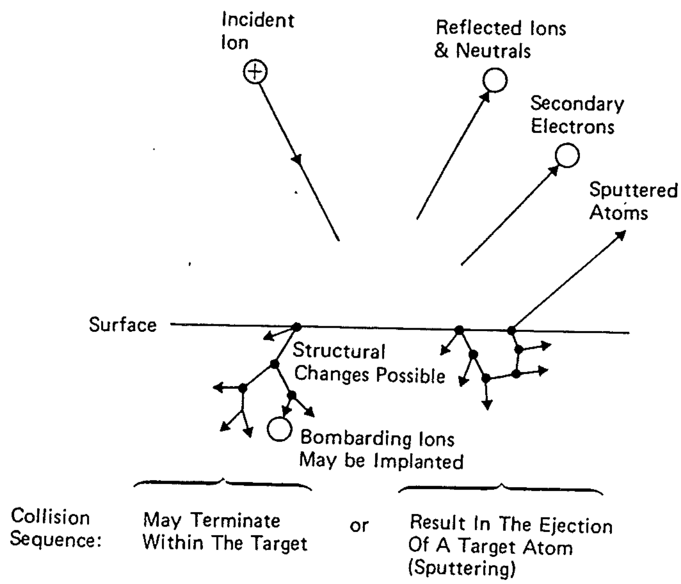

Figure 3.1 Possible interactions of an ion with a solid surface (target) [44].

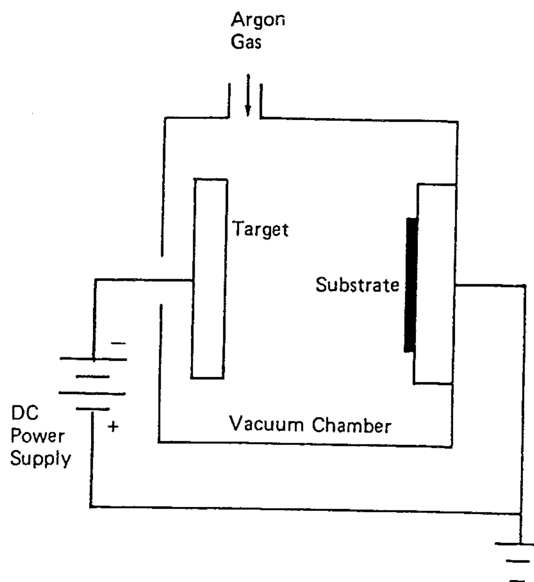

Figure 3.2 A DC diode sputtering system [44].

3. Experimental methods

3.1 Sputter deposition

3.1.1 Introduction

Consider a single ion that approaches the surface of a solid. The solid is called a *target*. Several phenomena may occur [44,45], see figure 3.1:

- reflection of the ion,
- release of a (secondary) electron from the target,
- ion implantation,
- structural rearrangements at the target surface,
- emission of radiation,
- release of an atom from the target.

The last process is known as *sputtering* and is used in several thin film deposition techniques (DC diode-, RF diode- and DC magnetron sputtering for example). Clearly the particles arriving at the target need to have sufficient energy to overcome the binding energy of the target atoms. Usually ions are used because they are easy to accelerate.
The simplest way to sputter-deposit a material from a target is by applying a constant voltage difference between target and *substrate* (DC diode sputtering). However, the most commonly used sputtering method employs a high frequency voltage (RF diode sputtering). The details and differences of these sputtering methods are explained in the next section.

3.1.2 The sputtering process

DC diode sputtering
A conventional DC diode sputtering system is shown in figure 3.2. It essentially consists of a vacuum chamber, an electrical circuit and a gas inlet. The target is the cathode of the electrical circuit, the substrate is the anode.
After the vacuum chamber is evacuated, a continuous flow of sputtering gas is injected. This sputtering gas usually is an inert gas (Ar). However, if a reaction with the target material is desired, also reactive gases (like O_2) are attributed, causing *reactive* sputtering. The substrate is grounded and a highly negative voltage (several kV) is applied to the target. Electrons are inserted by means of a glowing spiral until the glow discharge becomes self-sustaining (*plasma*). The electrons are accelerated to the substrate. On their way to the substrate they collide with sputtering gas atoms, breaking them up into ions and electrons. The positive ions are accelerated to the target, the electrons (and negative ions from the reactive gas) to the substrate. These ions and electrons may cause additional ionisation by collisions with sputtering atoms. The positive ions that reach the target may sputter some atoms and (secondary) electrons off, as mentioned in the previous section. In this way the discharge becomes self-sustaining and the sputtered atoms fly off in random direction.
When one of the sputtered atoms arrives at the substrate surface, it may be adsorbed (see figure 3.3). Adsorbed atoms diffuse across the surface until they evaporate or join another atom to form a pair. In time also clusters of 3, 4, etc. atoms are formed. This *nucleation* stage leads to the formation of metastable islands that start *growing*. Eventually conglomerates are

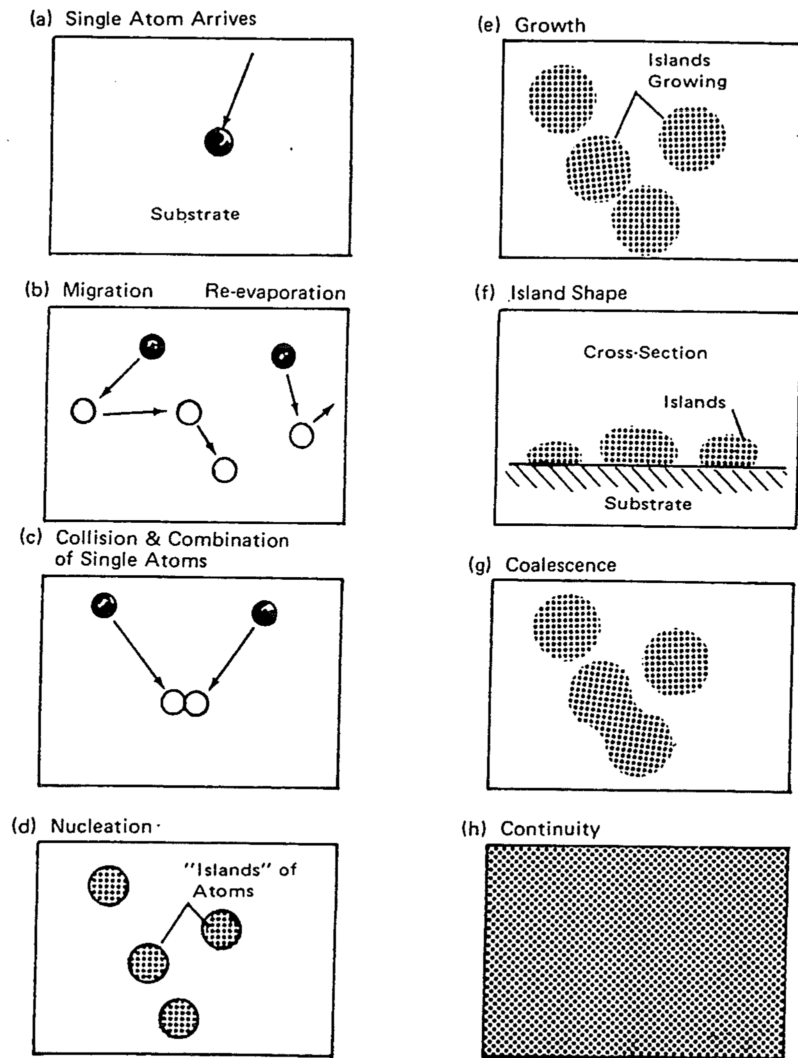

Figure 3.3 Formation of a thin film [44].

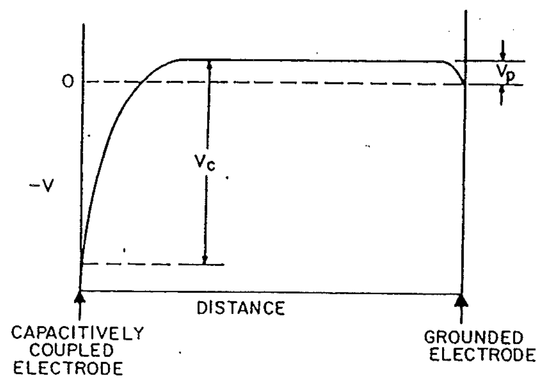

Figure 3.4 Distribution of the average voltage in a RF glow discharge from a small, capacitively coupled electrode (target) to a large, directly coupled electrode (substrate) [45].

formed, resulting in a continuous film. The film structure depends strongly on the sputter conditions and the apparatus geometry [46].
The most important variables during sputter deposition are:

1. The pressure of the sputtering gas. There are two extremes of the pressure. At low pressures, the number of ionising collisions between electrons and atoms is too low to make the discharge self-sustaining. At high pressures the mean free path of the sputtered atoms is small and a lot of backscattering to the target (and no deposition) takes place.
2. In reactive sputtering, the incorporation of the reactive component of the sputtering gas is determined by its partial pressure. This partial pressure is very low and can usually be ignored with respect to the pressure of (inert) sputtering gas.
3. The applied voltage. At low voltages the kinetic energy of the ions is too small to sputter atoms off, whereas at high voltages the process becomes very inefficient.

RF diode sputtering
Although DC diode sputtering is the simplest way to deposit a continuous film on a substrate, it is not applied very much. The main reasons are its relatively high operating pressure, low deposition rate and high inefficiency (a lot of energy is dissipated at the target surface) [47]. By superimposing a high frequency voltage (MHz region) on the DC voltage, electrons have to travel a much longer way to the target. Consequently, the ionisation efficiency is higher and the pressure can be lower. Another advantage of this sputtering method is that also insulators can be deposited.
In principle both target *and* substrate are sputtered during RF diode sputtering. To obtain sputtering from only one electrode (target), the target must be capacitively coupled to the RF generator and its area must be small compared to that of the directly coupled electrode (substrate) [44,45]. In practice these conditions can easily be fulfilled, because the directly coupled electrode is the system ground (substrate, substrate holder, chamber walls, etc.). The average potential varies between target electrode and ground electrode as shown in figure 3.4. An additional parameter in RF sputtering is, except for partial pressures and the average potential, the power supply of the RF generator. This parameter determines the deposition rate.

It should be noted that the given description of the sputtering process is a simplification of the actual plasma processes occurring. One should consider all possible elastic and inelastic collisions between the particles (neutrals, ions, electrons, photons) present in the vacuum chamber. This situation becomes even more complex if one realises that also excited particles, chemical reactions and contaminants play a role in the sputtering process. Fortunately, not all phenomena are equally important and only a small degree of ionisation is reached ($< 10^{-4}$), so the plasma gas mostly consists of neutrals.

3.1.3 The experimental RF reactive sputtering set-up

The experimental RF reactive sputtering set-up (Perkin Elmer sputtering model 2400) is schematically shown in figure 3.5. First, the vacuum chamber configuration is considered. This chamber is evacuated by means of a sequence of a pre-vacuum pump and a turbo molecular pump. Also a liquid nitrogen (LN_2) pump is used to trap water vapour by condensation on a cold surface. In this way base pressures below $5 \cdot 10^{-7}$ mbar are reached.
Because the pumping speed is large, the reactive gas flows also have to be large to reach the operating pressure (mbar range). However, at high gas flow, the flow in the vacuum system becomes (too) turbulent. Another way to increase the operating pressure is by throttling: a

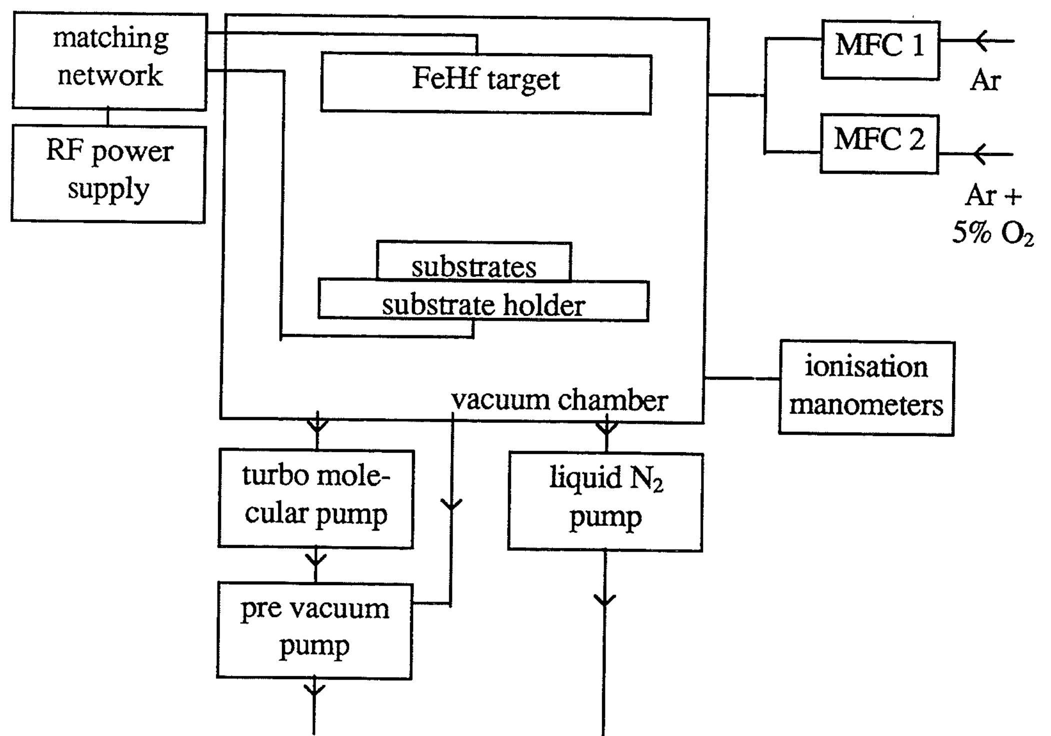

Figure 3.5 Schematic representation of the experimental RF reactive sputtering set-up (Perkin Elmer sputtering model 2400).

valve is used to reduce the pumping speed for obtaining higher pressures. Note that not only the pumping speed for the inserted gases is reduced, but also the pumping speed for contaminants.
Two gas inlets are used: one for pure Ar and one for a mixture of 95% Ar with 5% O_2 (< 10 ppm contamination). Each gas line is connected to a mass flow controller (MFC). These controllers are calibrated for the relevant gases. The maximum flow of the MFC for pure Ar is 100 sccm and that for the mixed gas is 20 sccm. The sccm stands for standard (273 K, 1 atm) cubic centimetre per minute. These flows can be varied accurately (within 1%) between 5 and 95% of its maximum flow with a system designed by Bronckhorst Hi-Tec. Both flows are mixed before entering the vacuum chamber.
The target is produced by hot isostatically pressing (HIP) and has the composition $Fe_{83}Hf_{17}$ (purity 99.8 at%), according to the specifications of the supplier. The diameter of the target is 15 cm and is bonded to a water cooled, isolating backing plate, which is surrounded by a dark shield (to restrict ion bombardment and sputtering to the target material only).
Prior to every sputter deposition, the target is presputtered to remove surface contaminants (oxides, absorbed gases) and to equilibrate the target surface. Because the sputtering yield is different for each atom species, the target surface is initially enriched with the most difficultly sputtered atoms. The presputtering time is chosen to be 30 minutes, which is sufficient to reach steady state conditions.

The substrate holder is an stainless steal plate with a diameter of 20 cm. The following substrates were used [48]:

- D263 glass (K, B, Al, Sb, Na, Zn, Si, Ti, O),
- single crystalline (111) GGG-garnet ($Gd_3Ga_5O_{12}$),
- single crystalline (100) Si,
- HTCS-II (majority of $ZrTiO_2$ with $CaTiO_3$-TiO_2),
- HCH ($CaTiO_3$).

The last three substrates were used in two modifications: with and without a 0.5-1 μm SiO_2 buffer layer (low pressure chemical vapour deposition) to prevent interface mixing. The dimensions of all substrates are 5 x 34 mm^2 (except for GGG: 5 x 32 mm^2); thicknesses varying between 0.3 and 3 mm. These dimensions are chosen to minimise demagnetising effects during magnetic measurements; thin substrates are used in the magnetostriction measurement (see section 3.6).
The substrates are all chemically cleaned in acetone/soap, water and iso-propanol to remove gross surface contaminants. Prior to deposition the substrates are sputter etched in argon, which means that the substrates are used as target for a short period of time. The other electrode sputter etching is a special electrode (not the target material). In this way the substrates are cleaned from smaller surface contaminants.
A Randex matching network and a power stabiliser are used between the RF generator and the glow discharge to optimise the power dissipation in the plasma. This matching network consists of variable resistances, inductor coils and capacitors and performs automatically. The operating frequency of the RF generator is 13.56 MHz (frequency allotted by international agreement for unlimited radiation).
The power supply, gas flows and pumping speed (throttling) can be varied. The average target potential (*bias*), is coupled to the power supply and can not be varied independently. Also the target composition has not been changed.
Pressures are measured with ionisation manometers. In the low pressure range(< 10^{-3} mbar) a Balzers IMG 060B ion gauge controller and at higher pressures an MKS controller is used.

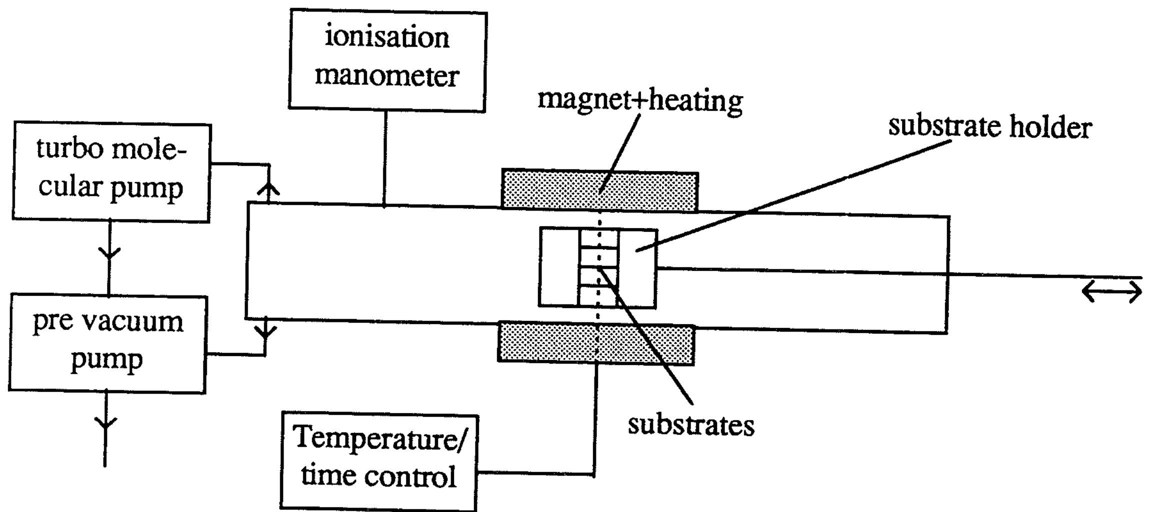

Figure 3.6 Schematic representation of the conventional thermal processing (CTP) set-up for annealing soft-magnetic films in a magnetic field.

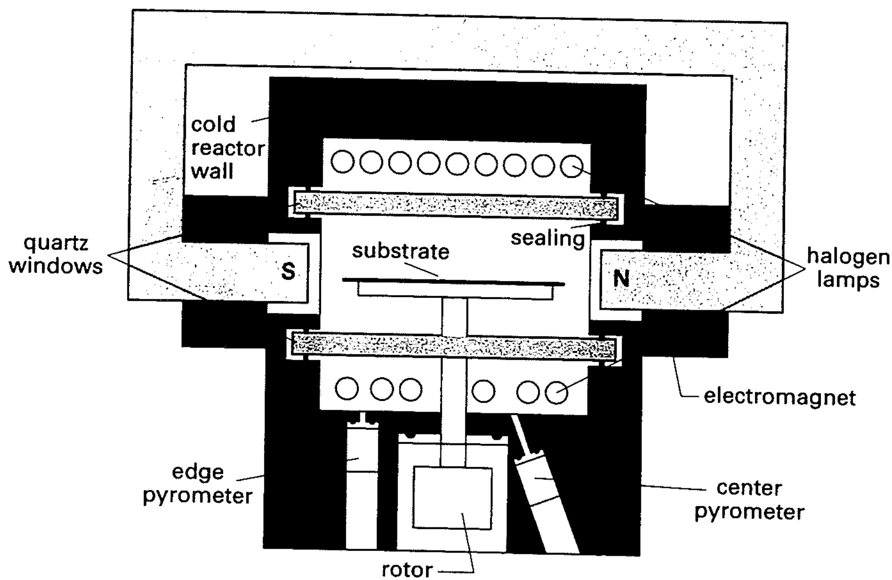

Figure 3.7 Schematic representation of the AST Elektronik SHS1000 MA prototype RTP reactor for annealing soft-magnetic films in a magnetic field [1].

3.2 Annealing

All films are annealed under the influence of a magnetic field to induce a uniaxial anisotropy, for reasons described in the previous chapter. This field must be large enough to saturate the films in all the film plane directions and is applied in the *width direction* of the films. In the next sections two different annealing processes are described: classical and rapid thermal processing.

3.2.1 Classical thermal processing

The conventional annealing set-up (CTP), based on resistive heating, is shown in figure 3.6. A permanent magnet with a magnetic field strength of 8 kA/m is placed around the oven. The samples are inserted and the oven is evacuated to prevent chemical reactions. Two pumps are used: a pre-vacuum pump and a turbo molecular pump. At a pressure below 10^{-6} mbar the samples are heated to a programmed annealing temperature T_a and kept at that temperature for several hours. The annealing time t_a is defined as the time during which the samples are at the peak temperature T_a. Because of the isolation around the oven the total annealing cycle time (evacuation, heating, isotherm trajectory and cooling) is one day. The magnetic field is applied during all stages of the annealing treatment.
The temperature is measured with a chromel-alumel (K-)thermocouple, calibrated in the range from -50 to +1250 °C, and registered as a function of time. The pressure is measured with a Granville-Phillips gauge controller 271 (low pressure ionisation manometer).

3.2.2 Rapid thermal processing (RTP)

Rapid Thermal Processing (RTP) is based on radiant heating (lasers, electrons, lamps, ion beams) instead of resistive heating. Consequently, the energy is transferred mostly to the specimen and the surrounding walls stay relatively cold: they are *not* in thermal equilibrium. Therefore, the effective thermal mass in RTP is much smaller than in CTP. This is the main reason why Rapid Thermal Processing has been replacing the conventional batch furnace processes more and more in submicron semiconductor industry [49,50]. The main obstacle for full acceptance of RTP is the pyrometric temperature control.
A new application of RTP might be in the area of thin film recording heads [1,51-53], when an electromagnet is added to the system. A prototype reactor is present at Philips Research in Eindhoven. The 150 mm diameter prototype RTP reactor SHS1000 MA is schematically shown in figure 3.7. It is co-designed by AST Elektronik and Philips Research [1] and consists of a quartz tube process chamber surrounded by two series of tungsten halogen lamps. Each lamp can be adjusted individually. The metal housing is reflective, so it enhances the efficiency of the RTP reactor. The quartz tube is transparent for the largest part of the wavelength spectrum of the lamps, but it is an absorber for radiation between 2.7 and 2.8 μm. This wavelength range is used to measure the specimen temperature by means of phonon detectors (pyrometers). Photons with wavelengths (energies) between 2.7-2.8 μm, coming from the heated specimen, generate free current carriers in this semi-conducting device. The electrical current increases with higher specimen temperatures. It should be noticed that these pyrometers are calibrated assuming a constant emissivity of the specimen. However, the emissivity of the samples is not known and it changes upon annealing. For this reason the samples are placed on a graphite susceptor with a well-known, constant emissivity (0.95, i.e. almost a blackbody) and the temperature of this susceptor is measured instead. It is assumed that the small, thin samples have the same temperature as the large, thick susceptor.
Two pyrometers are used to measure the radiation from the susceptor.

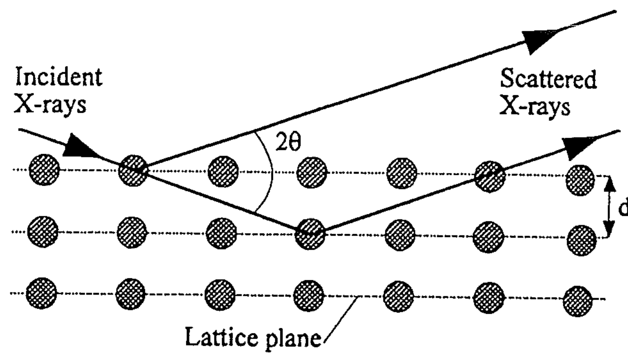

Figure 3.8 X-ray diffraction at a two dimensional lattice.

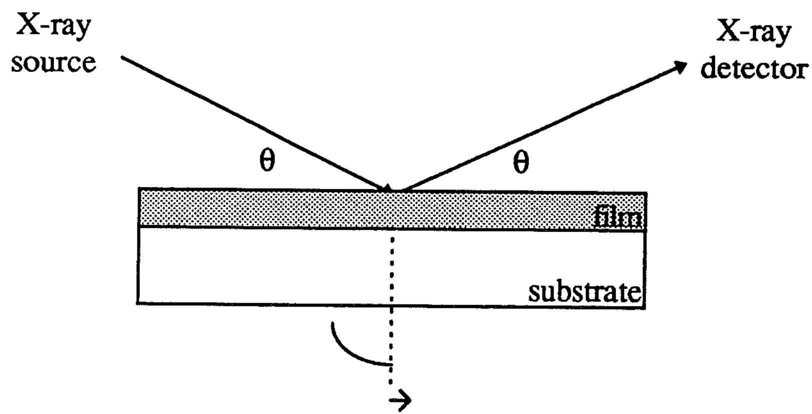

Figure 3.9 Schematic drawing of a thin film X-ray diffractometer. The sample is rotated in its plane; the X-ray source and detector motions are coupled.

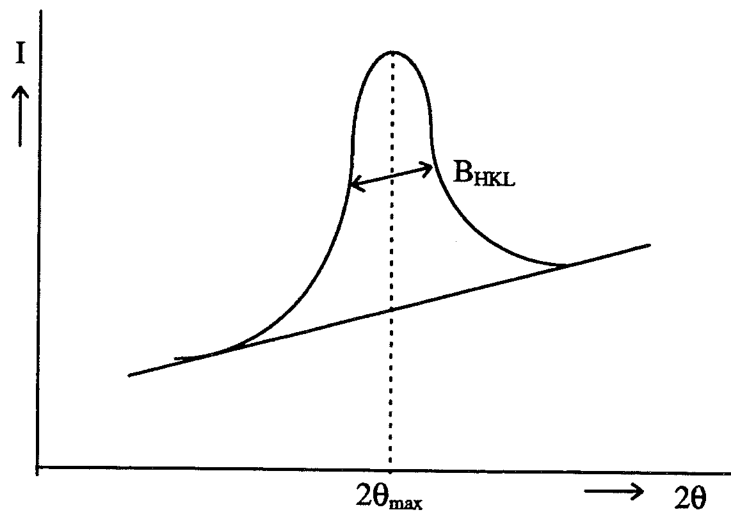

Figure 3.10 Peak broadening, characterised by the full width at half maximum (FWHM). The peak is located at θ_{max}. A linear background is included in the drawing.

The temperature uniformity is estimated by measuring the magnetostriction coefficient (see section 3.6.3) of thin magnetic films positioned across the susceptor. It is known that this property strongly depends on the annealing temperature for particular soft magnetic films [51]. In this way the temperature uniformity is estimated to be within 5°C [1].
The RTP reactor can not be evacuated. However several gases can be induced, either reactive (H_2, N_2) or inert (Ar). To create an inert atmosphere Ar is used. The Ar flow is regulated by a mass flow controller (MFC) with a maximum flow of 10 l/min. The MFC is fully controllable (within 1%) from 0 to 9.5 l/min.
The electromagnet is controllable up to 52.8 kA/m. The field uniformity across a 150 mm wafer is better than 99% [1]. The magnetic field is applied during the whole annealing cycle. An annealing cycle is characterised by the peak temperature T_a at which the samples are kept during the annealing time t_a (typically several seconds).
The temperature profile, gas flows and magnetic field can be programmed. Because heat transfer is based on radiation, heating rates can be as high as +100 °C/s. However heating- and initial cooling down rates are kept relatively low (±10 °C/s), thereby limiting temperature non-uniformities.

3.3 Structural characterisation

3.3.1 X-ray diffraction

The wavelength of X-radiation is of the same order as the atomic distances in crystals (several Å). Therefore, X-ray diffraction (XRD) is a powerful technique in investigating crystal structures.
X- radiation is produced in an X-ray tube by bombarding an anode with highly energetic electrons. The radiation spectrum depends on the anode material. From this X-ray spectrum the strongest characteristic wavelength is isolated.
A periodic structure with plane distances d_{HKL} [m] diffracts X-rays of wavelength λ [m] in a direction, determined by the Bragg condition [54,55]:

$$2d_{HKL}\sin\theta = \lambda\,. \qquad (3.1)$$

In this expression 2θ is the angle between the incident and diffracted beam. A schematic representation of the basic diffraction principle is given in figure 3.8 for a two dimensional structure. It seems that the X-rays are "reflected" at those crystal planes.
In figure 3.9 the principle of a thin film diffractometer is shown: the position of the X-ray source and the detector are changed, while making both the same angle $\theta(t)$ with the film surface . In this way an intensity (I) scan can be made as a function of 2θ, because the angle at which a crystal contributes to the diffraction pattern depends on the distance d_{HKL} of the (HKL) planes that are *parallel* to the surface of the film. The reflections in the diffraction pattern are related to the crystal lattice, so they can be used to identify crystal structures. During this XRD scan the specimen is rotated in its film plane, consequently no texture in the film plane can be detected.

Ideally, diffraction peaks should be δ-functions. In practice however, the peaks are always broadened. A reason for this phenomenon is, apart from geometric (apparatus) broadening, that the material is not single-crystalline. If all peak broadening is attributed to the presence of small grains, it can be shown [56] that the peak width is related to the mean grain size perpendicular to the (HKL) planes D_{HKL} [m].

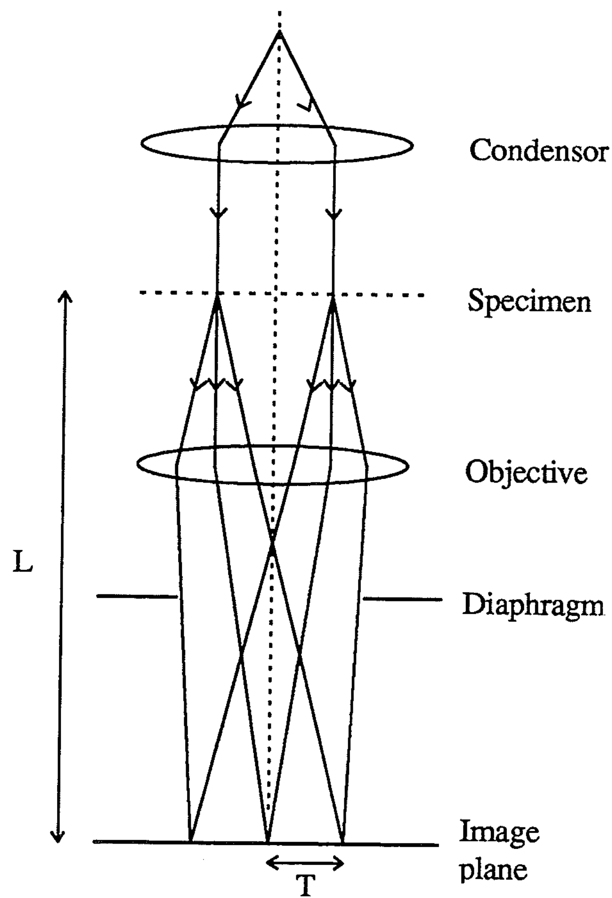

Figure 3.11 Schematic representation of a transmission electron microscope [55]; L -camera length and T = distance between (000) and (HKL) diffraction spots.

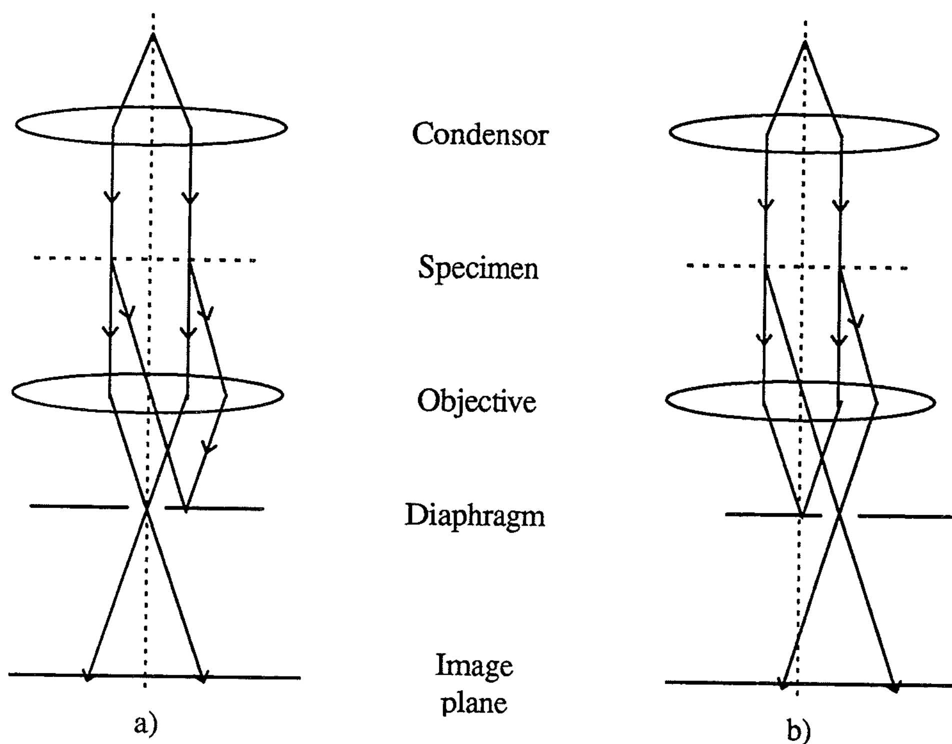

Figure 3.12 Diffraction contrast imaging in a TEM [55]:
a) bright field image and
b) dark field image.

This expression is called the Scherrer equation and is written as:

$$D_{HKL} = \frac{0.94\lambda}{B_{HKL}\cos\theta_{max}}, \quad (3.2)$$

where B_{HKL} [rad] is the full width of the HKL-diffraction peak in the I-2θ scan at half its maximum after background correction and θ_{max} is the angle where the peak is located. Note that in this way the grain sizes in the direction normal to the film are measured.
The procedure for obtaining B_{110} from a diffraction peak is shown in figure 3.10. In the neighbourhood of a diffraction peak the background signal is removed. This is done by fitting a linear background signal at both sides of the peak. Now this linear background signal is subtracted from the total (measured) signal and only the diffraction peak remains. This peak is approximated by a Gaussian profile of the form:

$$I_{cor}(2\theta) = p_1 \exp\left[-p_2(2\theta - p_3)^2\right], \quad (3.3)$$

where p_i (i = 1, 2 or 3) are constants that must be determined by least square fitting the equation to the corrected intensity signal; p_1 [intensity] is related to the peak height, p_2 $[1/(°2\theta)^2]$ to its width and p_3 [°2θ] to its position on the 2θ axis.
The full width at half maximum of the fitted Gaussian profile, B_{110} [°2θ], is equal to $2\sqrt{(\ln 2/p_2)}$; the area under the Gaussian profile is equal to $p_1\sqrt{(\pi/p_2)}$, as follows from equation (3.3).

All X-ray measurements have been performed on a Philips PW 1800 diffractometer, using $CuK\alpha_1$ radiation ($\lambda_{CuK\alpha1}$ = 1.5405 Å).

3.3.2 Transmission electron microscopy

X-ray diffraction and electron diffraction are closely related. Electron diffraction can be described by equation (3.1) as well, with λ the de Broglie wavelength. However, the penetration depth of electrons in solids is rather small (100 nm) compared to the penetration depth of X-rays (10 μm). Therefore only very thin films can be investigated by means of electron diffraction, in particular because only transmission geometries are possible in electron diffraction.
Transmission electron microscopy (TEM) makes use of the interaction between electrons and atoms by looking at the transmitted electrons. In TEM two kinds of images can be made: images of the diffraction pattern of the object and images of the object itself. In both cases the electrons travel through the film and are counted by a detector that is, contrary to XRD, situated on the other side of the sample.
A TEM essentially consist of a condensor system, a specimen, an objective and a diaphragm, all in evacuated atmosphere (see figure 3.11). The condensor system contains a set of magnetic lenses and projects the diverging electron beam in the form of a parallel beam on the specimen. The specimen is made by sputter depositing a 50 nm thin film on a TEM window (this window is made by sputter-depositing a thin Si_3N_4 film on single-crystalline Si; little holes are etched in the silicon and an electron transparent Si_3N_4 membrane remains [57]). The objective converges all electrons that coming from the film at a certain angle with the incident beam to points, forming a diffraction pattern. This diffraction pattern can be projected on an image plane.

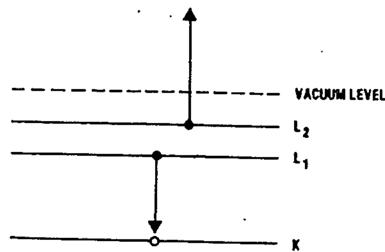

Figure 3.13 Basic principle of Auger electron spectroscopy (AES): two electron de-excitation processes [58]. In the energy level diagram relaxation of an L_1 electron takes place by dropping into the K level and emitting an L_2 electron as an Auger electron.

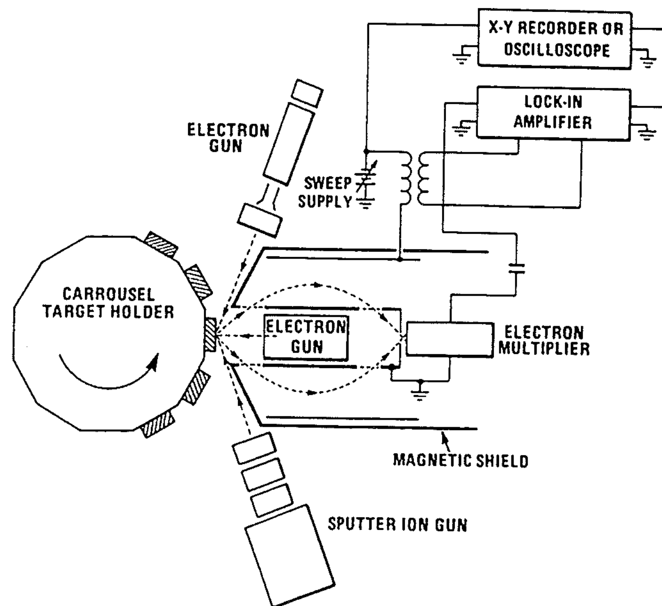

Figure 3.14 A cylindrical mirror analyser in an Auger spectrometer [58]

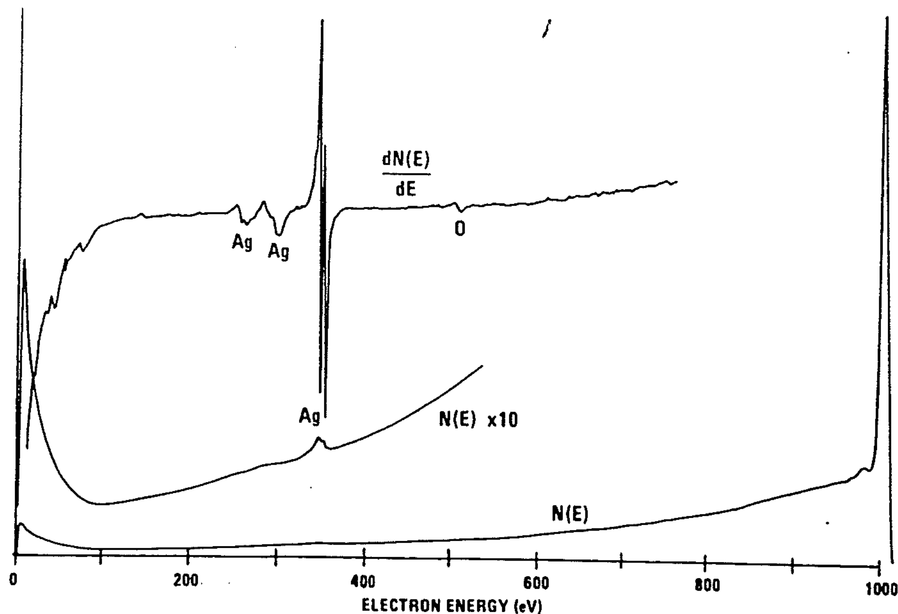

Figure 3.15 Energy distribution N(E) and dN/dE for a silver target with primary beam of electrons at 1000 eV [58]. The peak-to-peak distance in the dN/dE signal can be used for quantitative analysis of the composition of the target material.

Measuring the distances T [m] between the (000) spot (incident beam) and the (HKL) diffraction spots, the lattice spacing d_{HKL} can be calculated, since $\lambda \ll d_{HKL}$ equation (3.1) becomes, with $2\theta \approx D/L$ [55]:

$$Td_{HKL} = L\lambda . \tag{3.4}$$

In this expression L is the camera length (an apparatus constant) and λ is the (de Broglie) wavelength of the electrons, see figure 3.11. Comparison of the obtained lattice spacings with literature gives information about the crystal structure of the particle.
It is also possible to obtain a diffraction pattern from a single particle in the film by adjusting the selected area diaphragm (*microdiffraction*).
Another "image" can be obtained by looking at the incident (primary) beam only. Using the diaphragm, the reflected beams can be filtered out. See figure 3.12. Projecting this beam on a fluorescent screen gives an idea of the film structure (*diffraction contrast imaging*). This is called a *bright field* image. It is also possible to look at a diffracted (secondary) beam only: *dark field* imaging.
In a TEM X-rays are generated from the specimen in the same way as the are generated in an X-ray tube. In the previous section it was argued that the emitted radiation depends on the (anode) material used. This principle can be used for element analysis in a TEM. By looking at the energy (wavelength) of the emitted X-rays elements can be recognised and an element-specific map of the sample can be made. This technique is called energy dispersive X-ray detection (EDX).

A Philips EM 400 (120 kV) transmission electron microscope, equipped with a LaB_6 electron gun, is used. The microdiffraction is done on a Philips CM 30 (300 kV), also with a LaB_6 gun.

3.4 Auger electron spectroscopy

If a solid is irradiated by energetic electrons, the excited atoms can release their energy by emission of X-rays, as seen in the previous section. Another way of releasing their energy is by transition with the emission of electrons. The latter process is used in Auger electron spectroscopy (AES) [58,59].
The principle of AES is illustrated in figure 3.13 for a free atom. An incident electron with primary energy E_p ionises a core level (K). The vacancy is immediately filled by an outer electron (L_1). The energy difference may be transferred to another electron in this shell (L_2), which is ejected as an Auger electron, leaving the atom in a doubly ionised state. The energy of these transitions (and electrons) is characteristic for the atomic species and can be used for qualitative and quantitative analysis by measuring the energy distribution N(E): number of electrons N with kinetic energy E.
An AES system consists of an ultrahigh vacuum system, an electron gun and an energy analyser. Usually a so-called cylindrical mirror analyser (CMA) is used, because of its superior signal to noise ratio (see figure 3.14). The ejected electrons are bowed by applying a negative potential V to the outer electrode of the two cylindrical electrodes. Only electrons with a certain energy (proportional to V) are counted by the detector.
Because the energy distribution of Auger electrons is superimposed on a rather large background, it is more convenient to look at the differentiated (total) energy distribution function dN(E)/dE. This is shown in figure 3.15 for the spectrum measured at a silver target. Experimentally this is accomplished by adding a small ac voltage and measuring the in-phase signal with a lock-in amplifier.

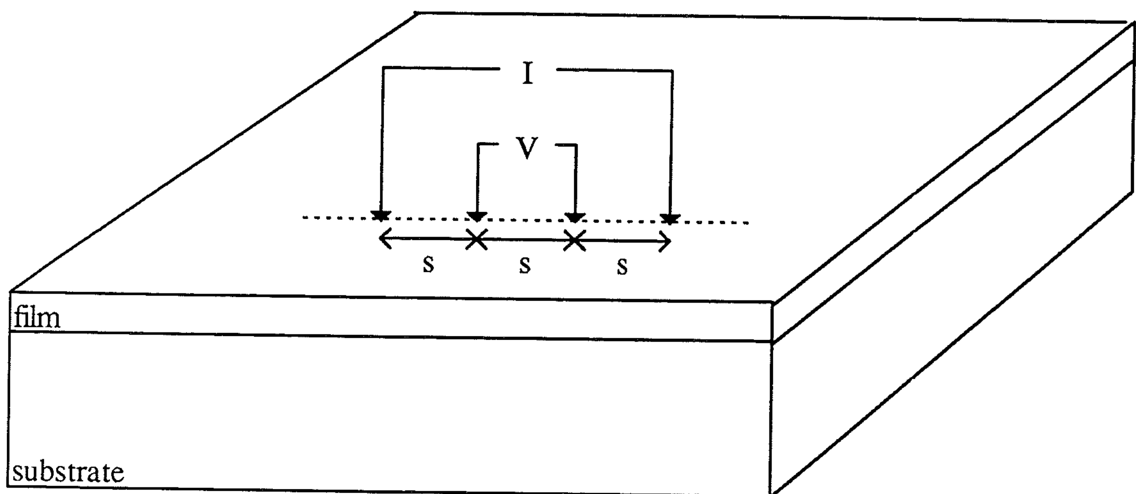

Figure 3.16 Schematic representation of the four-point probe set-up for measuring sheet resistance.

Because of the limited mean free paths of Auger electrons (5-20 Å) AES is a surface sensitive method. This means that if sputter etch equipment is added, also depth profiles of the composition can be measured with reasonable depth resolution.
Quantitative analysis is based on the method of elemental sensitivity factors [60]. The atomic concentration of element X in a compound can be estimated by:

$$[X]=\frac{\frac{I_X}{S_X}}{\sum_\alpha \frac{I_\alpha}{S_\alpha}}, \tag{3.5}$$

where I_α is the Auger peak to peak amplitude (see figure 3.15) of the dN(E)/dE signal for element α and S_α is the relative sensitivity between any element α and a reference element. Usually the strongest Auger transition is used.
In this report the following sensitivity factors with respect to the reference element silver are used: $S_{Fe} = 0.20$, $S_O = 0.50$; $S_N = 0.32$ and $S_C = 0.20$ [60]. For hafnium the Auger transition at 185 eV was used; the relative sensitivity factor of this transition is determined to be $S_{Hf} = 0.35$ (by verifying the composition of a film with RBS).

A Physical Electronics Auger electron spectroscope (single pass) is used. The energy of the primary electrons is 3 kV. The electron beam has a cross section of 0.1 mm^2. The energy of the sputter ions (Ar^+) is 2 kV; the incident angle is 15°.

3.5 Electrical resistivity measurements

Two types of resistivity measurements are performed. The resistivity of various films is determined by means of the four-point probe method. Also structural changes upon annealing are monitored measuring resistance changes.

Specific resistivity (four-point probe method)
The electrical resistance R [Ω] of a thin film (length l, width w and thickness d) is related to the specific resistivity ρ [Ωm] according to:

$$R=\frac{\rho l}{wd} \tag{3.6}$$

The sheet resistance of a film is defined as the resistance of a square film (w = l) by

$$R_s=\frac{\rho}{d}. \tag{3.7}$$

Note, that this resistance is independent of w (= l). For a semi-infinite film the resistance and sheet resistance are equal ($R = R_s$).
The sheet resistance can be measured by means of the four-point probe method [61-63]. A VEECO Instruments Inc. EPP 5000 four-point probe meter was used. The experimental set-up is shown in figure 3.16. Four probes are placed on the film in a line at a constant spacing. A current I is sent through the outer probes and the voltage V is measured between the inner two probes.

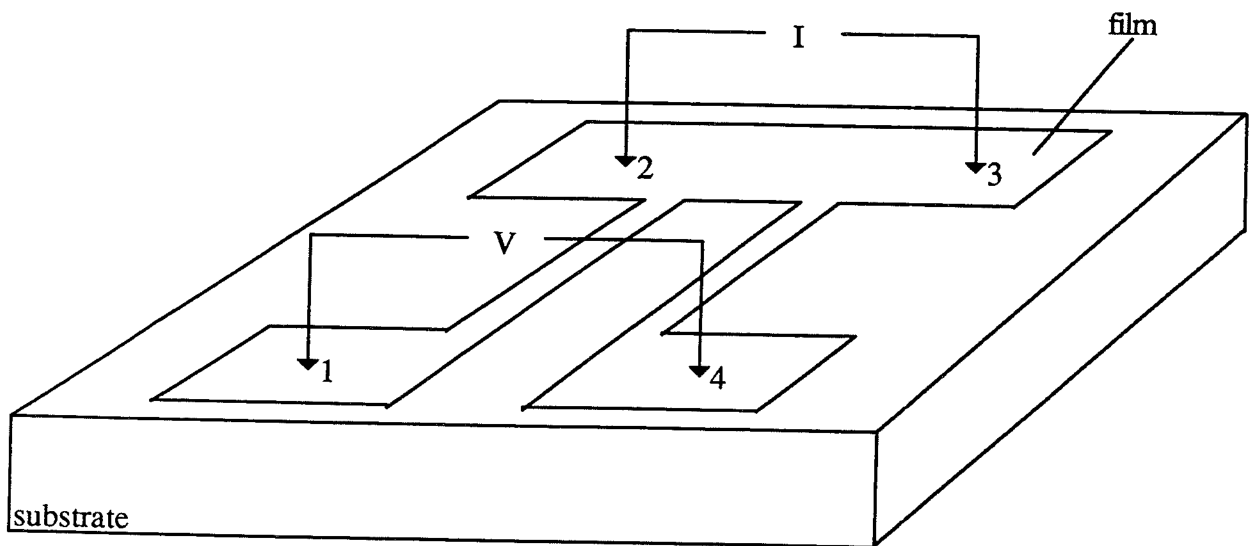

Figure 3.17 Film pattern used in the temperature/time dependent resistance measurement.

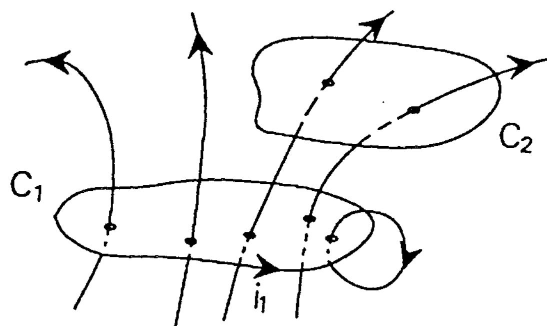

Figure 3.18. Principle of mutual induction. An electrical current i_1 in circuit 1 causes an magnetic flux. Part of the flux lines go through another electrical circuit (2), causing an electrical induction voltage in this circuit.

The sheet resistance of a film is given by [62,63]

$$R_s = C_R \frac{\pi}{\ln 2} \frac{V}{I}, \tag{3.8}$$

if the electrode spacing is much larger than the film thickness. C_R is a geometric factor ($0 < C_R < 1$) that corrects for the overestimation because of the existence of edges in finite, non-square films. C_R equals 0.616 for films with a width of 5 mm and length of 34 mm. The specific resistivity can be calculated from equation (3.7) if the film thickness d is known.

Measurement of resistance upon annealing
The temperature/time dependent resistivity is measured in a different way. Films are deposited on 2x2 cm^2 non-conducting substrates using a mask to obtain film patterns as in figure 3.17. Now four probes are pressed on the film and a current is sent through the film between probes 2 and 3. The voltage is measured between probes 1 and 4. Dividing voltage and current yields a resistance. It is possible to translate this measured resistance into a specific resistivity. However, if one is only interested in relative changes of the resistivity this resistance is sufficient.
All measurements are performed at pressures below 10^{-6} mbar. This pressure is reached using a pre-vacuum and a turbo molecular pump. The pressure is measured with a P270 gauge controller from Granville-Phillips (low pressure ionisation manometer). The temperature profile can be programmed and is controlled using a chromel-alumel (K-) thermocouple. The specimen is resistively heated. Resistance, temperature and time are measured with equipment from Keithley: a digital multimeter 195 and a programmable current source 224, a system scanning thermometer 740 and a scanner 705.
Before starting the measurement, the specific resistivity is estimated (four-point probe measurement) and the current is set at approximately 1 mA. In this way the Joule heating in the film is kept within limits. Resistance is measured every 30 seconds. The obtained value is an average of two measurements (opposite current directions).

3.6 Magnetic characterisation

3.6.1 Measuring the complex magnetic permeability

Consider two electrical circuits 1 and 2 (see figure 3.18). An electrical current $i_1(t)$ flows through circuit 1 for $t \geq 0$; no current flows through circuit 2 at $t = 0$. The current in circuit 1 causes a magnetic induction in the neighbourhood of the circuit for $t > 0$. Part of this magnetic induction goes through circuit 2. The magnetic flux, as a result of the current i_1 in circuit 1, that goes through circuit 2 is denoted as Φ_{21} [Wb]. This flux is related to $i_1(t)$ by

$$\Phi_{21}(t) = L i_1(t). \tag{3.9}$$

The proportionality constant L is known as the *mutual inductance* [H].
Consider an ac current of the form $i_1(t) = i_0 \exp(j\omega t)$, causing an induction voltage in circuit 2 of:

$$u_{21}(t) = \frac{d\Phi_{21}}{dt} = j\omega L i_1(t) \tag{3.10}$$

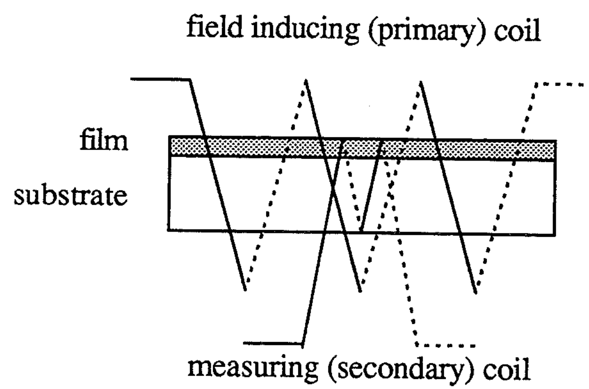

Figure 3.19 Experimental set-up for measuring the complex permeability. The magnetic film is magnetised by the primary (field inducing) coil; the magnetic induction signal is picked up by the secondary (measuring) coil.

So, when a (known) current $i_1(t)$ is sent through circuit 1 the mutual inductance L can be obtained by measuring the induction voltage $u_{21}(t)$ in circuit 2. The proportionality constant Z = jωL is the impedance of the circuits.

The magnetic permeability measurement is based on this principle. The experimental set-up is illustrated in figure 3.19. A primary (field inducing) coil magnetises the soft magnetic material. This causes a flux $\Phi_{21}(t)$ in the secondary (measuring). This flux depends on the magnetic induction of the soft magnetic material and hence on its relative permeability. By determining the mutual inductance of the secondary (measuring) coil the measured permeability can be obtained.
The magnetic field produced by the primary coil (n_1 windings and length l_1 [m]) is in the ideal situation equal to:

$$H_1^{id}(t) = \frac{n_1 i_1(t)}{l_1}, \tag{3.11}$$

where $i_1(t)$ is the electrical ac current [A] that flows through the windings of the coil. Now the magnetic flux Φ_{21} [Wb] measured by the secondary (measuring) coil is given by

$$\Phi_{21}(t) = n_2 Bs = n_2 \mu_0 \mu H_1^{id}(t)\, s, \tag{3.12}$$

with n_2 the number of windings of the secondary coil and s the cross-sectional area [m^2] of the sample.
Combination of equations (3.9), (3.11) and (3.12) yields:

$$\mu_{meas} = L \frac{l_1}{n_1 n_2 s \mu_0}. \tag{3.13}$$

Measuring the mutual inductance L yields, using equation (3.13), the measured relative permeability μ_{meas}. Note that all given equation are also true if one integrated field inducing/measuring coil is used. In that situation L is called the *self inductance* of the coil and all all suffices can be omitted ($n_1 = n_2 = n$ for instance).

Bernards et al [64] point out that this "raw" permeability strongly depends on the shape of the samples and on the precise experimental geometry (one or two coils). The following corrections have to be made:

1. The field produced by the primary coil is not uniform as stated by equation (3.11), but becomes weaker at the ends of the coil. Therefore the applied field H is overestimated. A correction factor C_H is introduced to correct for this effect.
2. The field experienced by the soft magnetic material is lower than the external field H, because of (internal) demagnetising fields. To correct for this effect the demagnetising factor N in the field direction is estimated.
3. Although the measuring coil is wound as closely as possible around the sample, some magnetic flux is not detected because part of the fluxlines close inside the measuring coil. A second correction factor C_f is introduced to take this effect into account.

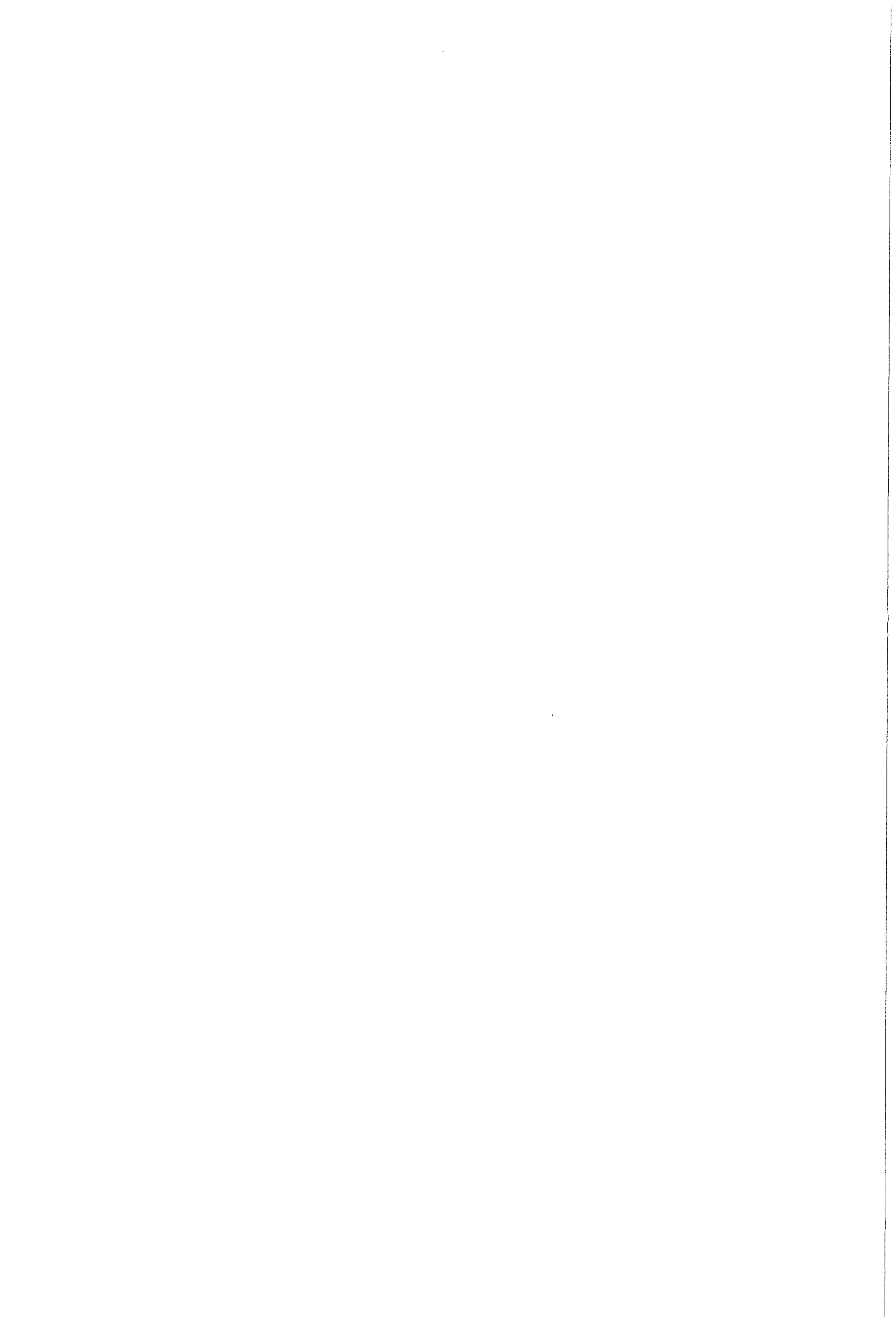

The procedure of these correction is explained in appendix C. The resulting relative permeability is given by

$$\mu = \frac{1}{C_H C_f / \mu_{meas} - N}. \qquad (3.14)$$

The demagnetising factor N and the correction factors C_i ($0 < C_i < 1$) are defined in appendix C.

If the inductance of the air filled measuring coil is equal to L_0, the inductance of the measuring coil with the soft magnetic material as a core is $L = \mu L_0$. Because the permeability is complex, the inductance of the coil is complex as well. Then the impedance in (3.10) becomes: [20]:

$$Z = j\omega\hat{L} = j\omega(L' - jL'') = \omega L'' + j\omega L' \equiv R + j\omega L. \qquad (3.15)$$

Thus the impedance of the coils consists of a real part (resistance R) and an imaginary part (ωL). The imaginary part determines the "normal" permeability μ'; the resistance is a measure for μ''.
The measured complex permeability is now equal to [65]:

$$\hat{\mu}_{meas} = \hat{L}\frac{l_1}{n_1 n_2 s \mu_0} \qquad (3.16)$$

or:

$$\mu'_{meas} = L\frac{l_1}{n_1 n_2 s \mu_0} \qquad (3.17^a)$$

and

$$\mu''_{meas} = \frac{R}{2\pi f}\frac{l_1}{n_1 n_2 s \mu_0}, \qquad (3.17^b)$$

where f ($= \omega/2\pi$) is the frequency of the alternating magnetic field [Hz]. Substituting the complex measured permeability (3.17) into the expression for the relative permeability (3.14) results in the following equations:

$$\mu' = \frac{C_H C_f \mu'_{meas} - N\left[(\mu'_{meas})^2 + (\mu''_{meas})^2\right]}{\left[C_H C_f - N\mu'_{meas}\right]^2 + \left[N\mu''_{meas}\right]^2} \qquad (3.18^a)$$

and

$$\mu'' = \frac{\mu''_{meas} C_H C_f}{\left[C_H C_f - N\mu'_{meas}\right]^2 + \left[N\mu''_{meas}\right]^2}. \qquad (3.18^b)$$

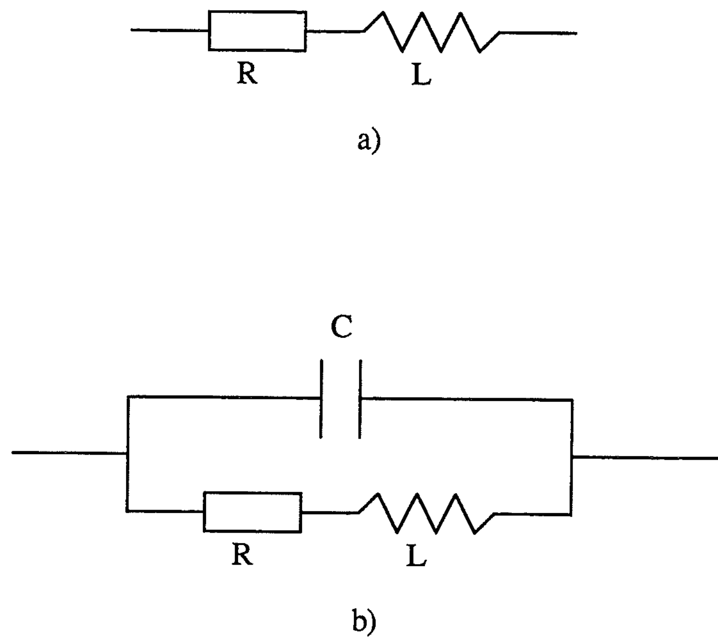

Figure 3.20 Equivalent circuits used to simulate the magnetic permeability measurement at:
a) low frequencies (10 kHz - 13 MHz) and
b) high frequencies (0.1 - 200 MHz).

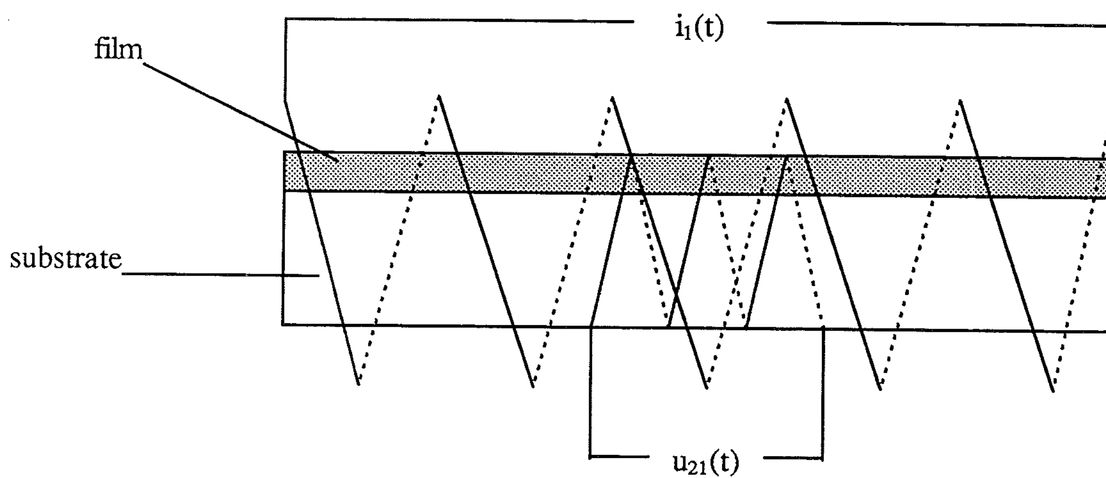

Figure 3.21 Principle of the BH-loop measurement.

The complex permeability can therefore be determined by measuring the impedance of the coils with the ferromagnetic sample as a core.

In our investigations we use two different set-ups: a low frequency (LF) set-up for permeability measurements from 10 kHz to 13 MHz and a high frequency (HF) set-up for permeability measurements from 0.1 to 200 MHz.
The LF set-up consists of two coils: a primary (field inducing) coil and a secondary (measuring) coil, whereas the HF set-up consists of one integrated field inducing/measuring coil, as described in appendix C.
In the LF set-up an empty measurement (*without* sample) is done before measuring the permeability. The equivalent circuit is given in figure 3.20^a. This results in resistances R_0 and inductances L_0 as a function of the measuring frequency. These values are stored and subtracted from the measured resistances R and inductances L (at the corresponding frequencies). The impedance in the LF-set-up is measured with an HP 4192A Impedance Analyser.
In the HF set-up an additional capacitance C between the coil and the soft magnetic film is added to the equivalent circuit [66], see figure 3.20^b. Now an empty measurement *with* the sample in *saturation* is done. The (empty) measured impedance is simulated as a function of the frequency using appropriate values for R_0, L_0 and C. The measured impedance is corrected for the capacitance according to:

$$\frac{1}{Z} = \frac{1}{Z_{meas}} - j\omega C = \frac{1}{R + j\omega L}, \tag{3.19}$$

and R and L are determined as a function of the frequency. The impedance in the HF set-up is measured with an HP 4195 Spectrum Analyser and an HP41951-60001 Impedance Test Adapter.

Finally the corrected resistances R-R_0 and inductances L-L_0 are used to calculate the complex permeability by means of the equations (3.14) and (3.18).

3.6.2 Measuring BH-loops

The magnetic induction B is measured as a function of the applied field H (BH-loop), by means of the induction method [13,67,68]. The experimental set-up is illustrated in figure 3.21: a primary (field inducing) and a secondary (measuring) coil are wound around the sample.
A low frequency (160 Hz) ac current $i_1(t)$ is sent trough the primary coil, causing an alternating magnetic field of the form (3.11). This alternating field causes an induction voltage $u_{21}(t)$ [V] in the secondary coil:

$$u_{21}(t) = -\frac{d\Phi_{21}(t)}{dt}, \tag{3.20}$$

where Φ_{21} is the magnetic flux [Wb] in the secondary coil because of the current in the primary coil.
Now two measurements are done: with and without sample. If the cross-sectional area of the film is equal to s (= wd) and that of the measuring coil s_2 [m^2], the induction voltages can be

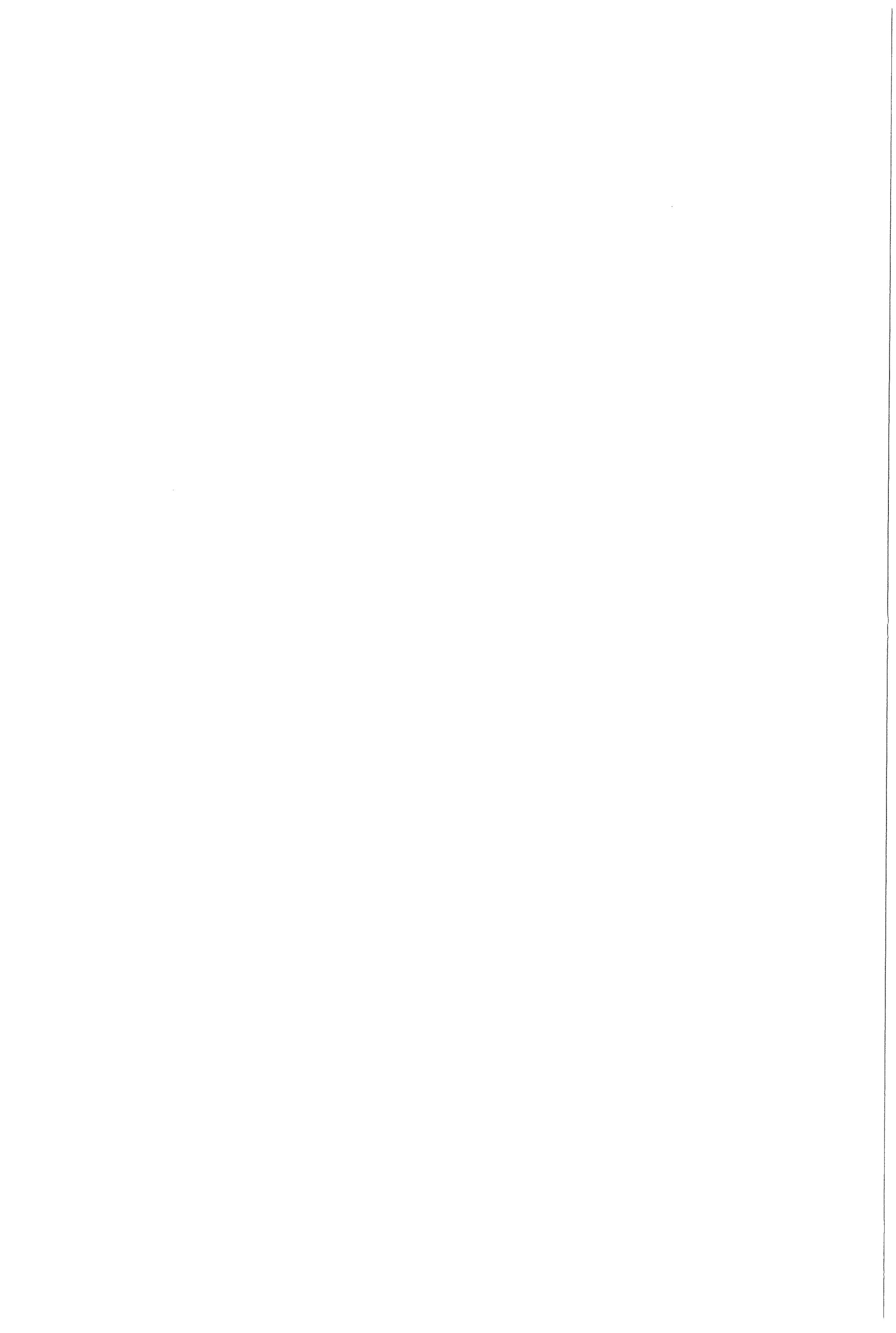

written as:

$$u_{21}^{with}(t) = -n_2 \frac{d}{dt}\left\{Bs + B_{air}(s_2 - s)\right\}, \qquad (3.21^a)$$

and

$$u_{21}^{empty}(t) = -n_2 \frac{d}{dt}\left\{B_{air} s_2\right\}, \qquad (3.21^b)$$

where B is the magnetic induction in the soft magnetic film material, B_{air} the magnetic flux density in air and n_2 is the number of windings of the secondary coil. Strictly speaking also the substrate flux density should be considered. However, only non-magnetic substrates are used, so the magnetic flux density of the substrate and air are nearly the same. Both inductions are a function of time as a consequence of the ac field.
Combination of the above equations gives:

$$d\left\{B(t) - B_{air}(t)\right\} = -\frac{1}{n_2 s}\left\{u_{21}^{with}(t) - u_{21}^{empty}(t)\right\}dt. \qquad (3.22)$$

Because $B_{air}(t) \ll B(t)$, the magnetic induction of the soft magnetic material is found by integrating (3.22) with respect to time. The result yields, in combination with the applied field H(t), the BH-loop of the soft magnetic thin film.

The sinusoidal current i(t) is generated with an HP 8116A pulse/function generator and amplified by a Kepco operational power supply/amplifier. The input signal (i) and the induction signals (u^{with} and u^{empty}) are stored in a Tektronix 7854 oscilloscope in the form of 3 x 1028 points as a function of time, each as an average of 20 cycles. The integration procedure is performed by the oscilloscope and the remanence and coercivity are estimated by linear extrapolation. The saturation magnetic induction is calculated as the (absolute) average of the two saturation magnetic inductions measured in opposite directions. The area between the BH-loop and the B-axis is calculated for all four parts of the BH-loops and averaged to obtain the uniaxial anisotropy constant K_u [J/m^3]. The results are transferred to a HP computer and stored.
No field corrections, missing flux corrections and demagnetising field corrections are made. Moreover the magnetic induction $B = \mu_0(M + H)$ is measured instead of the magnetisation M. The magnetic field is equal to the sum of the applied field and the demagnetising field. This field, however, is small because the demagnetising factor in the length direction of the film is at most 10^{-4}, see appendix C. Usually the applied fields are much larger than this demagnetising field. The induced magnetisation in soft magnetic films is also very large compared to the applied field. So the measured BH-loop can essentially be considered as the polarisation ($I = \mu_0 M$) vs. applied field curve.

3.6.3 Measuring the saturation magnetostriction coefficient

The saturation magnetostriction coefficient λ_s is measured using the cantilever method by Klokholm [69]. The experimental set-up was designed by Brouha et al. [70] and adjusted by Van de Riet [3].

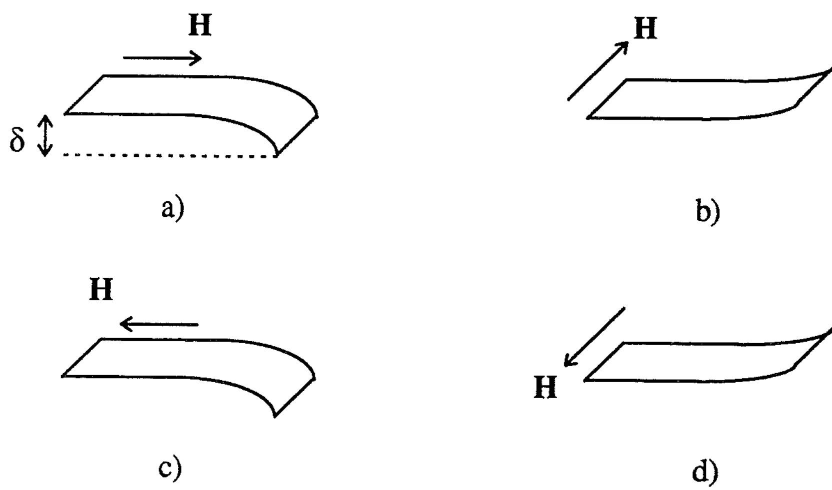

Figure 3.22 Princple of the magnetostriction measurement: a rotating magnetic field causes the specimen (= substrate + film) to bow at doubled frequency; δ is called the deflection [m].

Two sinusoidal waves, shifted in phase over 90° and with a frequency of 20 Hz, are generated by an Eureko 604 tone generator. These waves are amplified by a Philips FA 951 amplifier and connected to a pair of Helmholtz coils, causing a rotating magnetic field. The maximum field strength is approximately 1.4 kA/m [3], which is in most soft-magnetic thin films deposited on strips (measuring 5 x 34 mm^2) large enough to saturate the film in all in plane directions.
The sample (= substrate + film) is fixed at one end, while the other end is free. The rotating field is applied in the plane of the film. Because of its magnetostriction, the film periodically changes its length and, consequently, the specimen bends in two directions, depending on the field direction (see figure 3.22). Note that this bending takes places at doubled frequency (40 Hz). The deflection δ [m] of the specimen is defined as the distance between the original position and the position at maximal bend at a distance l' from the fixed end. δ is "translated" into a voltage by the optical sensor KD 100 (sensitivity 3.9 nm/mV). This voltage is measured as a function of the angle of the rotating field, using a two phase lock in analyser from EG&G Brookdael. The difference between the maximum and minimum voltage is read out on a Philips PM 2518 multimeter and is proportional to the deflection of the specimen (proportionality constant: $2\sqrt{2}\cdot 3.9\cdot$nm/mV).
Because the film (μm range) is so much thinner than the substrate (mm range), deflection and saturation magnetostriction coefficient are proportional. It can be shown that the following relation exists between the deflection and the saturation magnetostriction coefficient [71]:

$$\lambda_s = \delta \frac{E_s t_s^2}{E_f t_f} \frac{2}{9l'^2} \frac{1+\nu_f}{1+\nu_s}, \tag{3.23}$$

where $E_{s,f}$ are the Young's moduli [N/m^2], $t_{s,f}$ are the thicknesses and $\nu_{s,f}$ are the Poisson ratios of the substrate and film, respectively. Relevant Young's muduli are: E_{D263} = 72.9 GPa, E_{Si} = 208 GPa and E_{GGG} = 225 GPa, according to the specifications of the suppliers . It is often assumed that the Poisson ratios of substrate and film material are the same. The distance between the fixing point and the measuring position for the optical sensor is l' [m]; its value is fixed at 28 mm.
The sensitivity of the magnetostriction measurement is at best 10^{-7} [72].

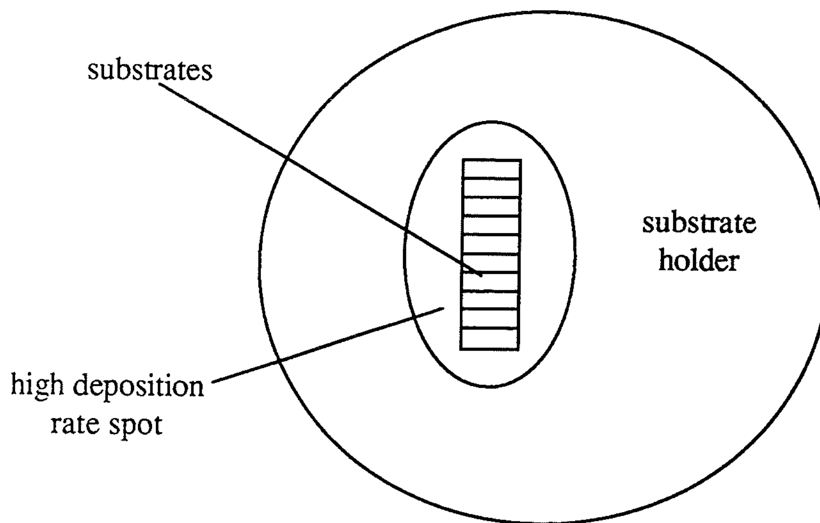

Figure 4.1 Location of the substrates on the substrate holder. Most of the deposition takes place in an ellipsoidal spot near the centre of the substrate holder.

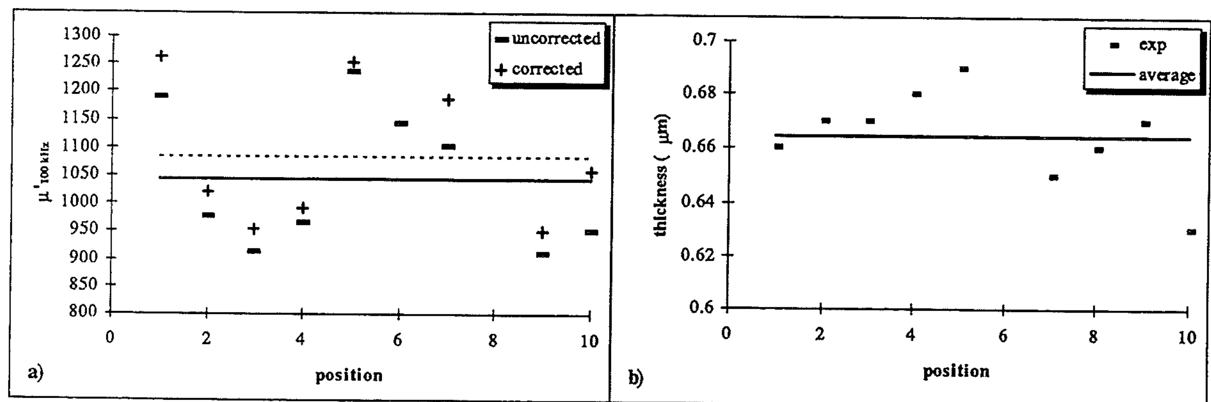

Figure 4.2 Checking the sputter uniformity of films deposited on D263 glass in an oxygen flow of 0.45 sccm (all films are rapid thermal processed for 5 seconds at 350°C): (a) the permeability at 100 kHz $\mu'_{100\,kHz}$ as a function of the position number, assuming a film thickness of 0.70 μm and corrected for thickness effects. Film thicknesses are given in (b). Averages are indicated.

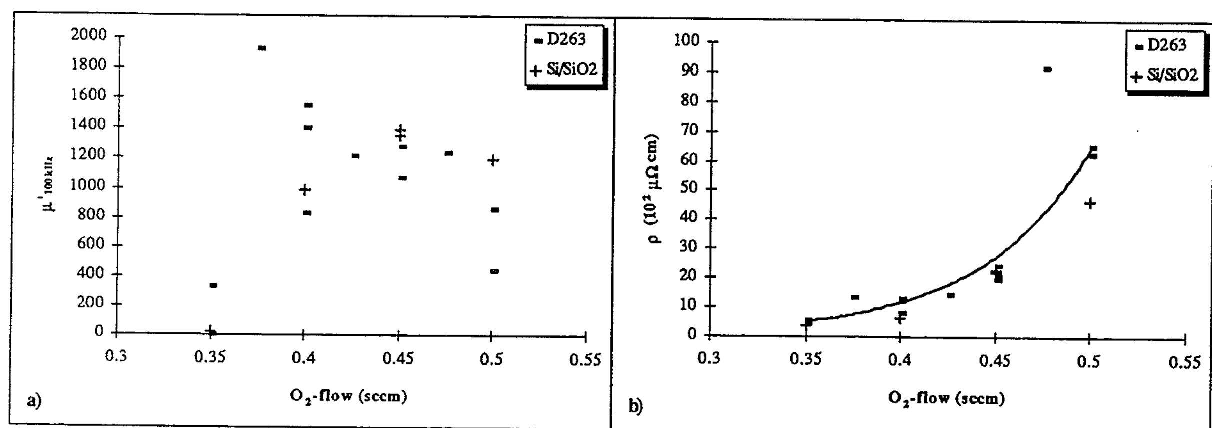

Figure 4.3 Some properties of 0.70 μm FeHfO films deposited on D263 glass and single crystalline (100) Si with a 0.5 μm SiO_2 buffer layer after RTP for 5 seconds at 350°C:

a) permeability at 100 kHz $\mu'_{100\,kHz}$ and

b) resistivity ρ [mΩcm] as a function of the oxygen flow.

4. Results

4.1 Optimisation procedure

4.1.1 Sputter conditions and uniformity

The sputter system is evacuated to pressures below $5 \cdot 10^{-7}$ mbar before the sputtering procedure is started. The procedure consists of three steps:

1. presputtering,
2. sputter etching and
3. sputtering.

The conditions during these three stages are given in table 4.1. All times are sufficient to reach steady state conditions, as confirmed with mass spectroscopy.

Table 4.1. Conditions during presputtering, sputter etching and sputter deposition of FeHfO films.

	pre sputtering	*sputter etching*	*sputter deposition*
target bias (kV)	-2.0	-	-2.0
substrate bias (V)	-	-30	-
RF power (W)	500	300	500
Ar flow (sccm)	30	30	30
O_2 flow (sccm)	0.35-0.50	-	035-0.50
total pressure (mTorr)	3.0	2.1	3.0
time (min/hours)	30 min	2 min	15 min-16 hours

After a few deposition runs it appeared that most of the deposition is restricted to an ellipsoidal spot near the centre of the substrate holder, as illustrated in figure 4.1. To examine the sputter uniformity 10 D263 glass substrates are placed in the spot and covered with a FeHfO film. The sputter conditions are chosen as in table 4.1 with an O_2 flow of 0.45 sccm. After deposition the films are rapid thermal processed for 5 seconds at 350°C in a constant magnetic field. Next the permeability at 100 kHz is measured as a function of the position number of the substrates, assuming that they all have the *same* film thickness of 0.70 μm (see figure 4.2[a]). The permeability is an average of 40 measurements; therefore the experimental error is expected to be small. To exclude thickness effects, the film thicknesses are determined by a wet chemical method and are all equal within the experimental error of the method (about 5%) as shown in figure 4.2[b].
Note that deviations in the permeability as large as 15% are not uncommon. However, no clear change in the permeability is observed near the edges of the deposition spot. Therefore it is concluded that differences in the permeability are not a consequence of systematic inhomogeneties in the plasma above the substrates.

In all deposition runs 10 substrates, centred in the deposition spot in the same way as described above, are covered by FeHfO films. In the next section the oxygen flow and annealing treatment are optimised with respect to the magnetic and electrical properties of the films.

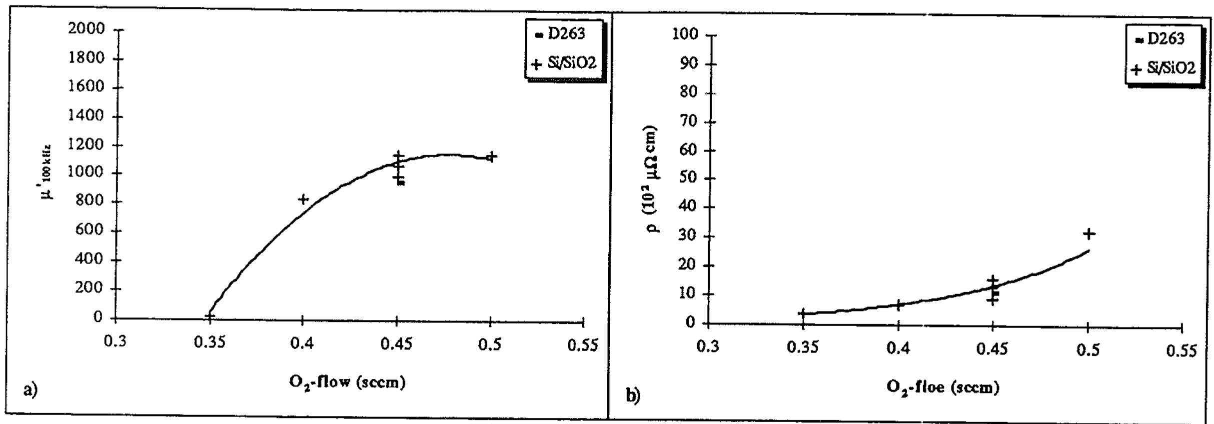

Figure 4.4 Some properties of 0.70 μm FeHfO films deposited on D263 glass and single crystalline (100) Si with a 0.5 μm SiO_2 buffer layer after CTP for 2 hours at 325°C:
a) permeability at 100 kHz $\mu'_{100\,kHz}$ and
b) resistivity ρ [mΩcm] as a function of the oxygen flow.

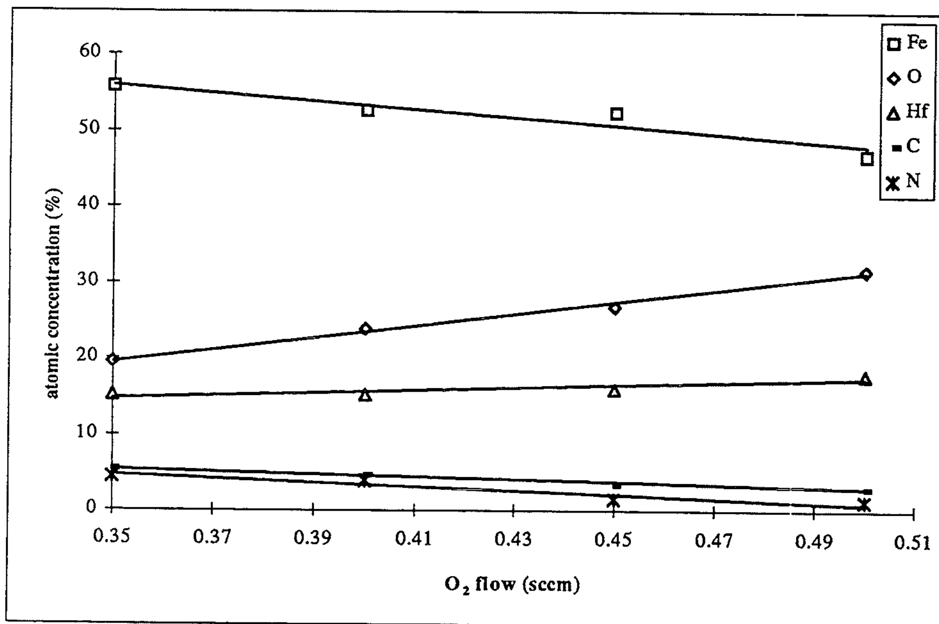

Figure 4.5 Composition [at%] of as deposited FeHfO films as a function of the oxygen flow during deposition measured with Auger electron spectroscopy.

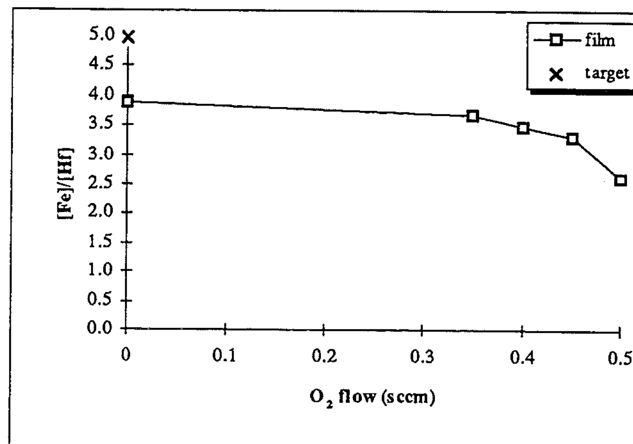

Figure 4.6 Change of the [Fe]/[Hf] ratio in as deposited FeHfO films as a function of the oxygen flow during deposition. The [Fe]/[Hf] ratio in the target is also indicated.

4.1.2 Optimising the oxygen content

Several deposition runs are performed as a function of the oxygen flow on D263 glass and/or single crystalline (100) Si with a 0.5 μm thick SiO_2 buffer layer (short: Si/SiO_2). Oxygen flows between 0.35 and 0.50 sccm are used. The sputter time is one hour for all series. Film thicknesses are all equal to 0.70 μm within the experimental error of the method.
After deposition all films are annealed in a constant magnetic field in the width direction of the films, using the two different annealing set-ups described in chapter 3: RTP and CTP. The annealing times are 5 seconds and 2 hours, respectively; the annealing temperatures 350 and 325°C. After annealing both the permeability at 100 kHz and the resistivity are measured. The permeability is measured in the length direction of the films (hard axis) and is averaged 20 times. The results are shown in the figures 4.3 (RTP) and 4.4 (CTP). It can be seen that the resistivity steeply increases with the oxygen flow (content). The value of the resistivity is higher for RTP (short annealing times) than it is for CTP (long annealing times).
Although there is a lot of scatter in the D263 data, it is possible to recognise an optimum in the permeability as a function of oxygen flow at approximately 0.45 sccm. Generally, the permeability of the films after RTP is higher than after CTP.
More experimental results on this optimisation procedure are given in appendix D.

The composition of *as deposited* films is measured by means of Auger electron spectroscopy (AES) as a function of the oxygen flow (see figure 4.5). Almost no depth profiles were observed, but significant carbon and nitrogen contaminations were found in all films. The nitrogen contamination is not that surprising, because it is the main source of contamination in this vacuum configuration. Carbon, however, is not expected at all. After a rigorous check of the sputter configuration, it appeared that the *target contained 2.9 ± 0.1 at% C*, as determined by wet chemical coulometric analysis. Therefore the target composition is $Fe_{80.8}Hf_{16.3}C_{2.9}$ instead of $Fe_{83}Hf_{17}$. It will be shown that the addition of carbon in FeHfO films is not insignificant.
Note that the [Fe]/[Hf] ratio decreases with increasing oxygen flow (i.e. relatively more Hf is introduced in the films). This effect is shown in figure 4.6.
It is found that a permeability of 10^3 (at 100 kHz) and a resistivity of several mΩcm can be obtained at 0.45 sccm O_2. From figure 4.5 it follows that this flow corresponds to $Fe_{55}Hf_{17}O_{28}$ (+ C, N contamination). It is with these films that further investigations are done.

4.1.3 Optimising the annealing procedure

The second step in the optimisation procedure is the optimisation of the annealing treatment. Films of optimal composition are deposited on D263 glass, Si/SiO_2 and GGG substrates (film thickness: 0.70 μm). The permeability at 100 kHz and the resistivity are measured as a function of annealing temperature. The annealing times were 5 seconds (RTP) and 2 hours (CTP). The results are displayed in figure 4.7 (RTP) and 4.8 (CTP). It can be seen that RTP results in better properties. The optimal annealing treatment is determined to be a rapid thermal process for 5 seconds at 400°C, resulting in:

- a permeability at 100 kHz of 1200-1400 and
- a resistivity of 1-2 mΩcm.

In figure 4.9 two BH-loops are shown for the "optimal" films: one film is annealed along its short axis (width direction of the film) and the other one is annealed along its long axis (length direction of the film). Both BH-loops are measured in the long axis direction, corresponding to

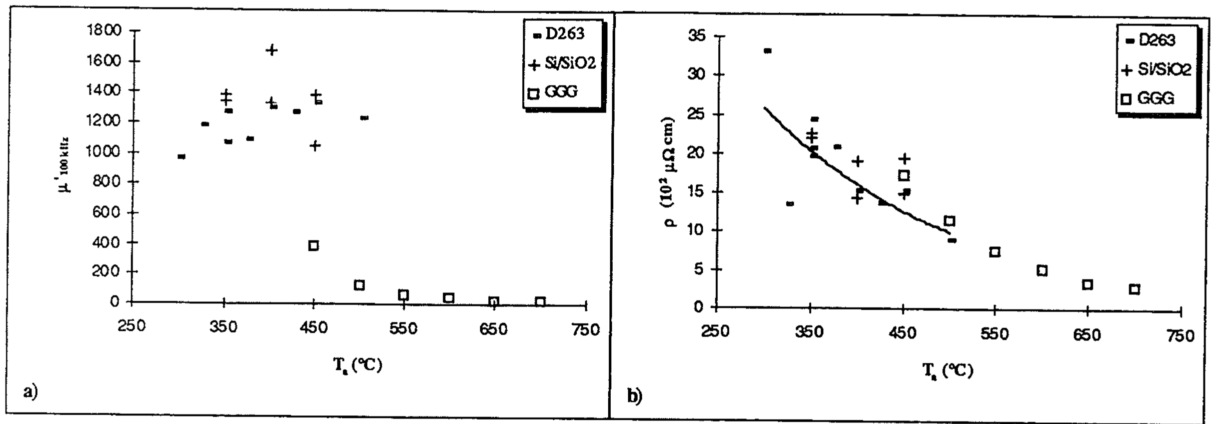

Figure 4.7 Change upon annealing (RTP: 5 seconds) 0.70 μm $Fe_{55}Hf_{17}O_{28}$ films deposited on D263 glass and single crystalline (100) Si with a 0.5 μm SiO_2 buffer layer of:
a) the permeability at 100 kHz $\mu'_{100\,kHz}$ and
b) the resistivity ρ [mΩcm] as a function of the annealing temperature T_a.

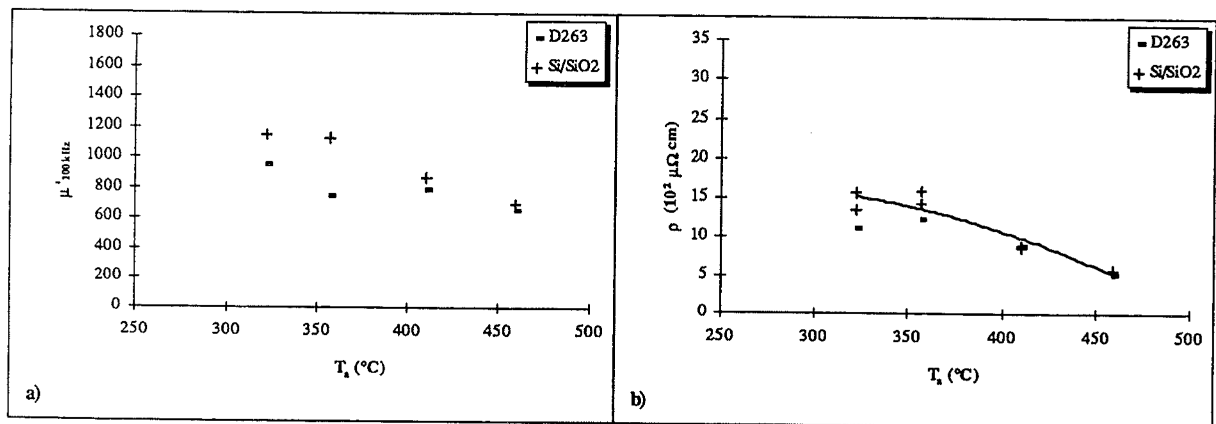

Figure 4.8 Change upon annealing (CTP: 2 hours) 0.70 μm $Fe_{55}Hf_{17}O_{28}$ films deposited on D263 glass and single crystalline (100) Si with a 0.5 μm SiO_2 buffer layer of:
a) the permeability at 100 kHz $\mu'_{100\,kHz}$ and
b) the resistivity ρ [mΩcm] as a function of the annealing temperature T_a.

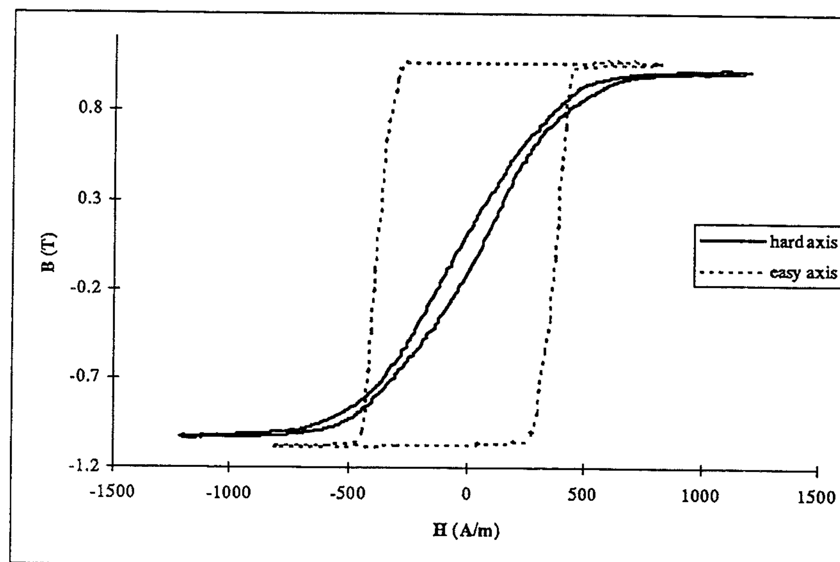

Figure 4.9 BH-loops, measured in the length direction, of two 0.70 μm $Fe_{55}Hf_{17}O_{28}$ films deposited on single crystalline (100) Si with a 0.5 μm SiO_2 buffer layer annealed for 5 seconds at 400°C (RTP) in: (1) the width direction (hard axis loop) and (2) the length direction (easy axis loop) of the film.

the hard and easy axis loop, respectively. As can be seen in the figure, the difference is enormous. Typical BH-loops parameters for the hard axis loop are a saturation induction of 1.1 T, a coercivity below 50 A/m and a uniaxial anisotropy constant of $3 \cdot 10^2$ J/m^3; whereas a coercivity of several hundreds A/m is observed in the easy axis direction.

The last parameter to be discussed is the saturation magnetostriction coefficient λ_s. As mentioned in section 2.2, it is desirable to minimise the magneto-elastic anisotropy. Therefore a value for λ_s of the order 10^{-7} is necessary (in combination with small internal stresses). In figure 4.10 the measured magnetostriction is given as a function of the annealing temperature during RTP and CTP. The Young's modulus of the films is unknown, so the modulus of other nanocrystalline iron based alloys is used (100 GPa). Further it is assumed that the Poisson constants of film and substrate are equal (see section 3.6.3)). All saturation magnetostriction coefficients are positive. It can be seen that the smallest magnetostriction coefficient is obtained using CTP at high temperatures. This value is still about 10 times larger than desirable.
In table 4.2 the conditions and properties of films deposited and annealed under optimal conditions are summarised.

Table 4.2 Magnetic and electrical properties of $Fe_{55}Hf_{17}O_{28}$ after rapid thermal processing for 5 seconds at 400°C.

property	value
$\mu'_{100\,kHz}$ ($\cdot 10^3$)	1.2-1.4
H_c (A/m)	< 50
B_s (T)	1.1
K_u ($\cdot 10^2$ J/m^3)	3
λ_s ($\cdot 10^{-6}$)	4-8
ρ (mΩcm)	1-2

More experimental details on this optimisation procedure are given in appendix D.

4.1.4 Reproducibility

As can be seen in the presented results the scatter in the experimental results is rather large. This scatter may be a result of small differences in substrate surface morphology.
During the research project it became clear that films with optimal composition could be made reproducibly: within about 10% (permeability) and within 25% (resistivity) after the optimal annealing treatment. Films that did not fulfill these requirements were not used in the following investigations. The reproducibility on Si/SiO_2 and GGG is generally better than that on D263. Therefore most investigations were carried out with films deposited on these substrates.

4.2 Structure of the films

Both X-ray diffraction (XRD) and transmission electron microscopy (TEM) are used to elucidate the structure of the films under optimal deposition conditions. The results are presented in the next two sections.

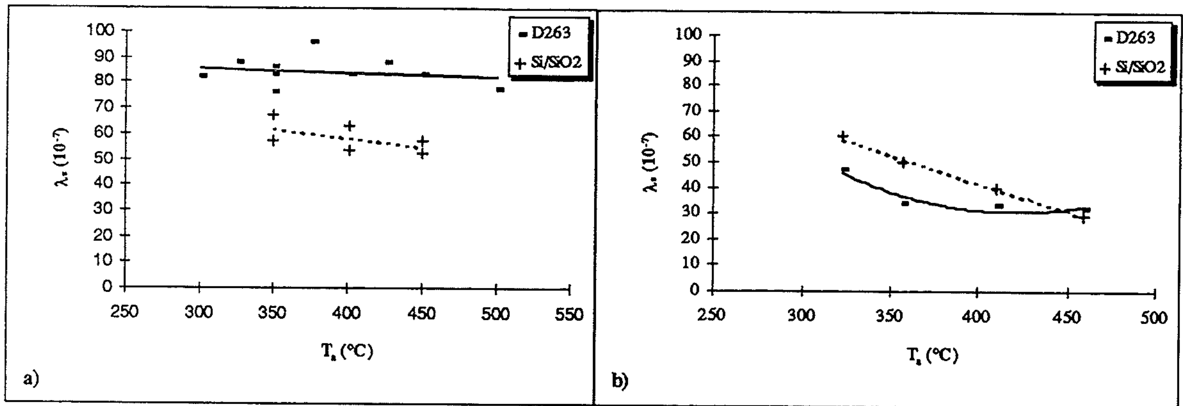

Figure 4.10 The saturation magnetostriction coefficient λ_s of 0.70 μm $Fe_{55}Hf_{17}O_{28}$ films deposited on D263 glass and single crystalline (100) Si with a 0.5 μm SiO_2 buffer layer, using:
a) RTP for 5 seconds and
b) CTP for 2 hours
as a function of temperatures T_a.

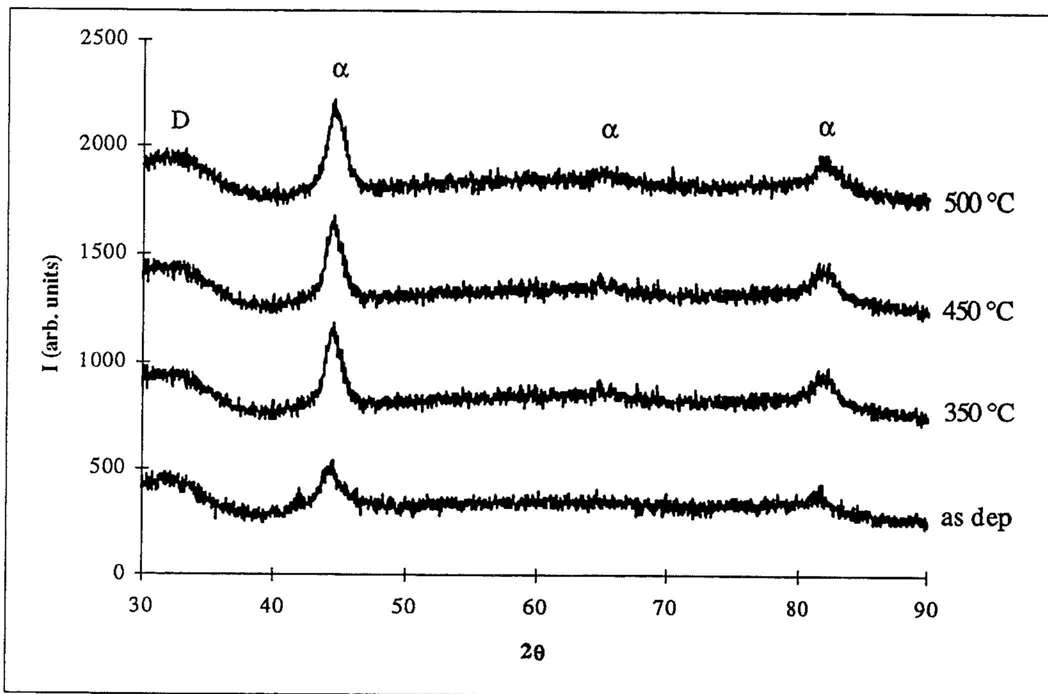

Figure 4.11 XRD scans (intensity I vs. diffraction angle 2θ) of some 0.70 μm $Fe_{55}Hf_{17}O_{28}$ films deposited on D263 glass substrates: as deposited and rapid thermal processed for 5 seconds at 350, 450 and 500°C. Counting time: 2 seconds per 0.04°2θ interval. The following reflections are observed: α = b.c.c. Fe and D = D263 glass.

4.2.1 X-ray diffraction results

In this section some X-ray diffraction results on $Fe_{55}Hf_{17}O_{28}$ films will be presented. The results are divided into classical thermal processed and rapid thermal processed films. The annealing times were chosen to be 2 hours and 5 seconds, respectively. The film thickness of the examined films is 0.70 μm. The results are presented in XRD scans: intensity I vs. scattering angle 2θ. The intensity scales are given in arbitrary units; each scan in one figure is shifted by a fixed intensity amount with respect to the previous curve.

Figure 4.11 shows XRD scans of an as deposited film and of several rapid thermal processed films (at 350, 450 and 500°C). The counting time was set on 2 seconds for every 0.04°2θ. The substrates material is D263 glass. In this figure only one phase is recognised: body centred cubic iron (α-Fe). The peaks visible are the (110) reflection and the (211) reflection. In between these two another peak becomes visible at higher annealing temperature: the (200) α-Fe reflection. The very broad peak in the XRD scans at $2\theta \approx 32°$ is an amorphous D263 reflection.
Figure 4.12[a] shows some XRD results of classical thermal processed films, also deposited onto D263 glass; the counting time is 2 seconds for every 0.04°2θ. These spectra are very much similar to those presented in figure 4.11 (RTP). However, at the highest annealing temperature of 460°C some additional peaks are observed, notably at $2\theta \approx 38$ and 49°2θ. In figure 4.12[b] a more accurate scan is presented: the counting time is increased to 16 seconds for every 0.04°2θ. The additional peaks are caused by diffraction at face centred orthorhombic Fe_3C (*cementite*), whose appearance is a direct consequence of the carbon contamination.
Figure 4.13 shows X-ray scans of rapid thermal processed films deposited on GGG and annealed at higher temperatures. The counting time is 15 seconds (every 0.04°2θ). The very sharp peaks at 25, 50 an 80°2θ are reflections of the single crystalline substrate. Now, apart from the α-Fe diffraction peaks, several other peaks are found. These peaks are caused by diffraction at two different crystal structures of *hafnium oxide* (HfO_2):

1. face centred cubic hafnium oxide (γ-HfO_2) and
2. monoclinic hafnium oxide (m-HfO_2).

The fraction of the γ-HfO_2 phase is found to increase with increasing temperatures up to 700 °C. Also very small peaks of m-HfO_2 peaks become visible. At higher temperatures the fraction m-HfO_2 increases, while almost no γ-HfO_2 phase is found.
Cementite is not observed at all in these films.

4.2.2 TEM results

In this section some transmission electron microscope results on $Fe_{55}Hf_{17}O_{28}$ films are presented. All films are deposited on TEM windows (see section 2.4); their thickness is about 50 nm. Because the thickness of the films treated in this report is much larger, it should be noticed that the very thin films used for TEM investigations may not be representative for the structure of the thicker films.

Figure 4.14 shows the results of an in situ annealing experiment. An as deposited film is heated to 550°C in the TEM and kept at that temperature until a stable picture could be obtained. Both bright field images and electron diffraction patterns of the film before (as deposited) and during annealing are given. From the bright field image it can be seen that the as deposited structure consists of very small crystalline particles (dark spots) in a rather large amorphous matrix (bright regions). The broad rings in the electron diffraction pattern are believed to be caused by the small crystalline particles. It is found that these rings and the small dark spots in

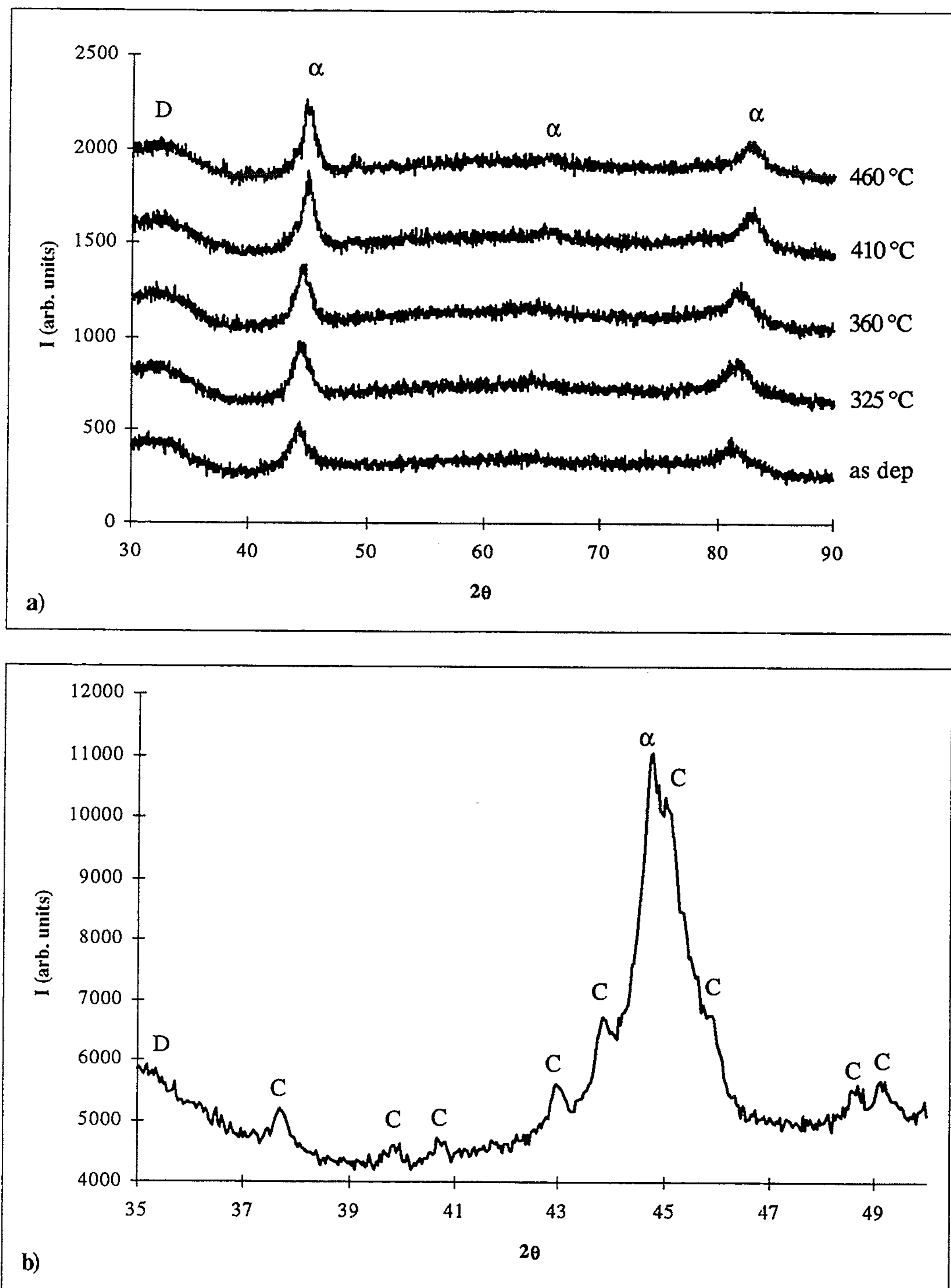

Figure 4.12 XRD scans (intensity I vs. diffraction angle 2θ) of some 0.70 μm $Fe_{55}Hf_{17}O_{28}$ films deposited on D263 glass substrates:

a) as deposited and classical thermal processed for 2 hours at 325, 360, 410 and 460°C. Counting time: 2 seconds per 0.04°2θ interval,
b) classical thermal processed for 2 hours at 460°C. Counting time: 16 seconds per 0.04°2θ interval.

The following reflections are observed: α = b.c.c. Fe, C = face centred orthorhombic Fe_3C and D = D263 glass.

the bright field image are caused by body centred cubic iron (α-Fe) nanocrystals. During annealing a few very large particles appear (bright field image) and some corresponding diffraction spots. Because the diffraction spots are discrete, it is concluded that these particles are single crystals (or contain a few crystals at most). Performing micro diffraction on one particle sustained this conclusion and it was found that the large particles are face centred orthorhombic single crystalline cementite with lattice constants $a_0 = 5.08$ Å, $b_0 = 6.73$ Å and $c_0 = 4.51$ Å. This is in agreement with EDX: the large particles are enriched in iron and depleted in hafnium with respect to the surrounding.
Because the in situ annealing treatment can not be defined accurately, some films are rapid thermal processed and classical thermal processed before their structure is investigated in the TEM. The results are shown in figures 4.15 (RTP) and 4.16 (CTP). These figures contain three bright field images and one diffraction pattern, corresponding to the highest annealing temperature, each. The annealing treatments are:

- figure 4.15: 5 seconds at 350, 400 and 450°C,
- figure 4.16: 2 hours at 325, 360 and 410°C.

In both figures α-Fe nanocrystals and orthorhombic cementite are observed. The surface fraction of cementite, however, is much larger in the classical thermal processed films than in the rapid thermal processed films. Note that α-Fe nanocrystals remain visible through the cementite, so the cementite crystals are believed to be very thick.
The high temperature structure of the films is investigated by rapid thermal processing a series of films at temperatures up to 900°C. Some resulting TEM images are presented in figures 4.17 and 4.18.
Figure 4.17 contains two bright field images and two electron diffraction patterns of films that are annealed for 5 seconds at 600 and 650°C. At the lowest temperature only α-Fe and cementite are observed. At 650°C however, also face centred cubic HfO_2 (γ-HfO_2) is found. This can best be seen in the changes in the diffraction patterns.
Figure 4.18 shows bright field images and diffraction patterns of films annealed for 5 and 30 seconds at 700°C. In the shortest annealed film α-Fe, cementite and γ-HfO_2 are found. In the other film also monoclinic HfO_2 (m-HfO_2) is found.
Annealing at even higher temperatures causes further (re)crystallisation of m-HfO_2, while cementite and γ-HfO_2 disappear.

4.3 Electrical resistivity measurements

Structural changes upon annealing can be followed by measuring the electrical resistivity during the annealing treatment. The two most frequently used kinds of experiments are isothermal (constant temperature) and isochronal (constant heating rate) measurements. The last type of experiments is frequently used to investigate in what temperature range different processes occur. Therefore the first experiments to be described are isochronal ones. Next some isothermal experiments are performed. However, because of the limited heating rate of the experimental equipment, all these measurements contain an isochronical part as well.
Patterned films (thickness 0.70 μm) of optimal composition $Fe_{55}Hf_{17}O_{28}$ are deposited on single crystalline (100) Si substrates, as described in section 2.5. To make sure that only the resistivity of the film material is measured, a 0.5 μm thick isolating SiO_2 buffer layer is used between the silicon and the film. All measurements are performed at pressures below 10^{-6} mbar.

In figure 4.19 the result of an isochronal experiment is shown. The resistivity ρ is measured as a function of temperature at a heating rate of 0.48°C/min. The resistivity is normalised at its initial value $\rho_0 = \rho(t = 0)$. The resistivity decreases continuously to less then 10% of its initial

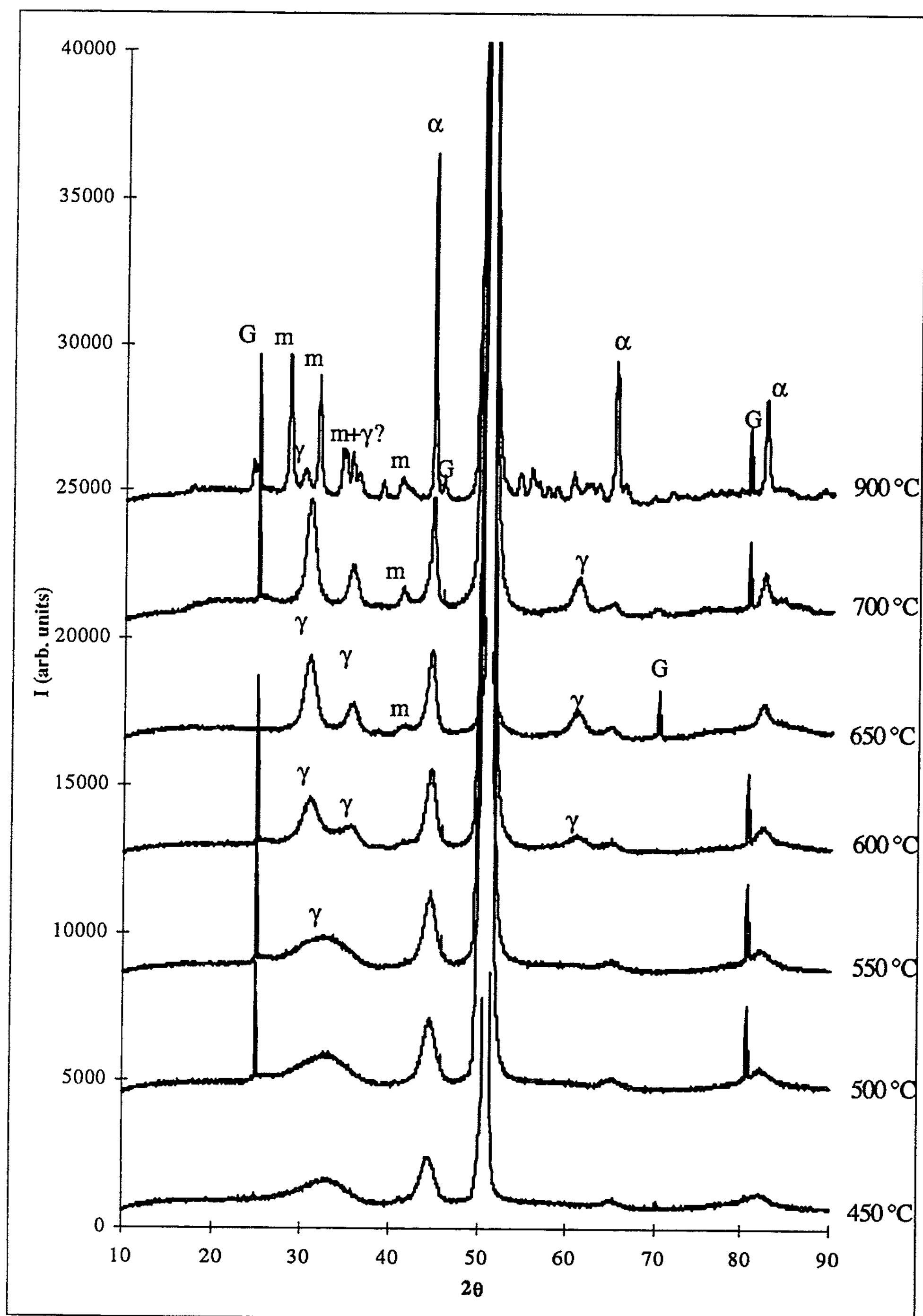

Figure 4.13 XRD scans (intensity I vs. diffraction angle 2θ) of some 0.70 μm $Fe_{55}Hf_{17}O_{28}$ films, deposited on GGG substrates and rapid thermal processed for 5 seconds, as a function annealing temperature. The counting time is set on 15 seconds per 0.04°2θ interval. The following reflections are observed: α = b.c.c. Fe, γ = f.c.c. HfO_2, m = monoclinic HfO_2 and G = GGG. The peaks observed at the highest temperature that are not assigned, are all m-HfO_2 reflections.

value above 450°C. Changes of slope at 160, 360 and 430°C are observed, which may indicate the beginning of atomic ordering processes (crystallisation).
For comparison an isochronal experiment is performed on an amorphous $Fe_{77}Nb_{10}Si_2N_{11}$ film, sputtered under optimal conditions [3] on GGG (insulator). The resistivity change of this film with temperature upon annealing at a heating rate of 2.0°C/min is shown at figure 4.20. The resistivity drops very quickly at about 350°C. Otherwise no changes of slope are observed. This behaviour is characteristic for a single crystallisation process.
Now some isothermal resistivity measurements will be treated. In first approximation the temperatures at which changes of slope are observed in figure 4.19 are used in a step annealing experiment: an $Fe_{55}Hf_{17}O_{28}$ film is subsequently heated as fast as possible to the annealing temperatures 140, 325, 375 and 425°C. The sample is annealed isothermally at every temperature for 12 hours (before heating to the next temperature). The resistivity is measured during the whole step annealing process (see figure 4.21^a). The result is shown in figure 4.21^b. Time is measured from the moment that heating from the former to the new (higher) annealing temperature is started. The resistivity is normalised with respect to the resistivity measured at the end of every previous isothermal period. Note that each curve contains a heating stage as well (with different heating rates). The slight increase that is observed during the heating stage is a consequence of the temperature dependence of resistivity. It is necessary to correct for this effect, as will be shown in the next chapter. A very small decrease in resistivity is observed at the lowest annealing temperature. When the specimen is heated from 140 to 325°C the resistivity decreases by about 25% and keeps decreasing with time during the isothermal part. In the next two steps further decreases are observed. This experiment suggests that there may occur several processes in $Fe_{55}Hf_{17}O_{28}$. Therefore only the low temperature region (corresponding to the first crystallisation process) is investigated.
Three films from the same deposition run are used in the following isothermal experiments. The films are heated to 225, 275 and 300°C, respectively, at the same heating rate of approximately 10°C/min (see figure 4.22^a). The resistivity change as a function of time is shown in figure 4.22^b. After a drop during the heating stage, the resistivity continuously decreases with time. The total decrease at the end of the experiment depends on the annealing temperature: the largest decrease is observed at the highest temperature.
To identify the structural changes in the three films, XRD is performed. The results are shown in figure 4.23, using a counting time of 15 seconds for every 0.04°2θ. The sharp (not assigned) peaks are caused by diffraction at the single crystalline silicon substrates. Two α-Fe reflections are observed: the (110) and the (211) reflection. Annealing at different temperatures does not cause a significant change in these peaks, as illustrated in figure 4.24 for the (110) diffraction peak. However, a significant shift in peak position is observed after annealing at 300°C.

4.4 High frequency permeability measurements

So far only results on 0.70 μm thick film have been presented. In magnetic recording heads, however, films with thicknesses of more than 10 μm are used. Scaling up film thickness usually is accompanied by a deterioration of the properties of these films. Therefore the thickness dependence of the permeability at 100 kHz and the resistivity of $Fe_{55}Hf_{17}O_{28}$ films (RTP: 5 seconds at 400°C) is determined (see figure 4.25). The thicknesses are measured in a scanning electron microscope (SEM); the deposition rate is determined to be 12.1 ± 0.2 nm/min. It can be seen that both properties do not manifest strong thickness dependence. Several series of thick films (10.9 μm) are deposited onto D263 glass, Si/SiO_2 and GGG. After deposition all films are rapid thermal processed for 5 seconds at 400°C.

The complex permeability of the films as a function of the frequency of the applied magnetic field is measured with the HF (one coil) and LF set-up (two coils), as described in the previous chapter. The results of these measurements on the film deposited on GGG is shown in figure 4.26. In this figure both the real and (negative) imaginary part of the complex permeability measured with the HF set-up and only the real part of the permeability measured with the LF set-up are given. The HF measurement is an average of 10 measurements, the LF measurement is averaged twice (empty and sample measurement). Note that there is a significant difference between the permeability measurements using the HF set-up and the LF set-up. Permeability measurements on films deposited on D263 glass, Si/SiO_2 are very similar and are therefore given in appendix E, together with some measurements on films deposited on commercially available substrates (HCH and HTCS-II, see section 3.1.3).
Magnetic parameters like saturation magnetisation, coercivity and uniaxial anisotropy constant are obtained from BH-loop measurements. A typical hard axis BH-loop measured on the film deposited onto GGG is shown in figure 4.27. Magnetic properties and resistivity of the films dealt with in this section and of films deposited onto the commercially available substrates are given in table 4.3. All BH-loops are given in appendix E as well.

Table 4.3 Saturation magnetic induction B_s, resistivity ρ and uniaxial anisotropy constant K_u of 10.9 μm thick $Fe_{55}Hf_{17}O_{28}$ films deposited onto various substrates, after rapid thermal processing for 5 seconds at 400°C.

substrate	**B_s (T)**	**ρ (mΩcm)**	**K_u (J/m^3)**
HCH	1.03	1.67	437
HCH/SiO_2	1.06	1.44	406
HTCS	1.06	1.33	332
$HTCS/SiO_2$	1.06	1.43	340
D263	1.06	1.25	319
Si/SiO_2	1.04	1.20	315
GGG	1.03	1.11	320

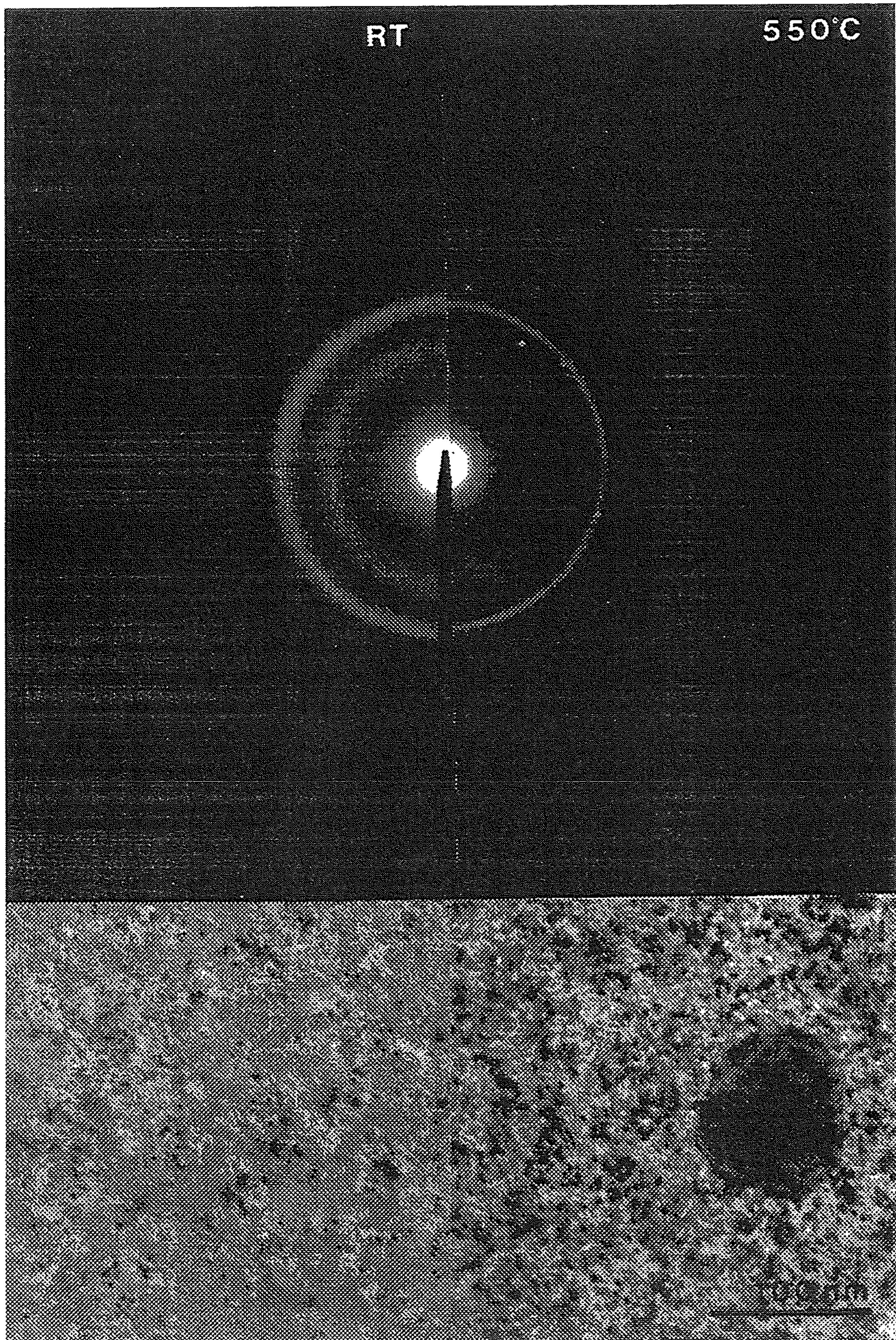

Figure 4.14 TEM bright field images and diffraction patterns of a 50 nm $Fe_{55}Hf_{17}O_{28}$ film:

- left: as deposited and
- right: in situ annealed (heated up to 550°C).

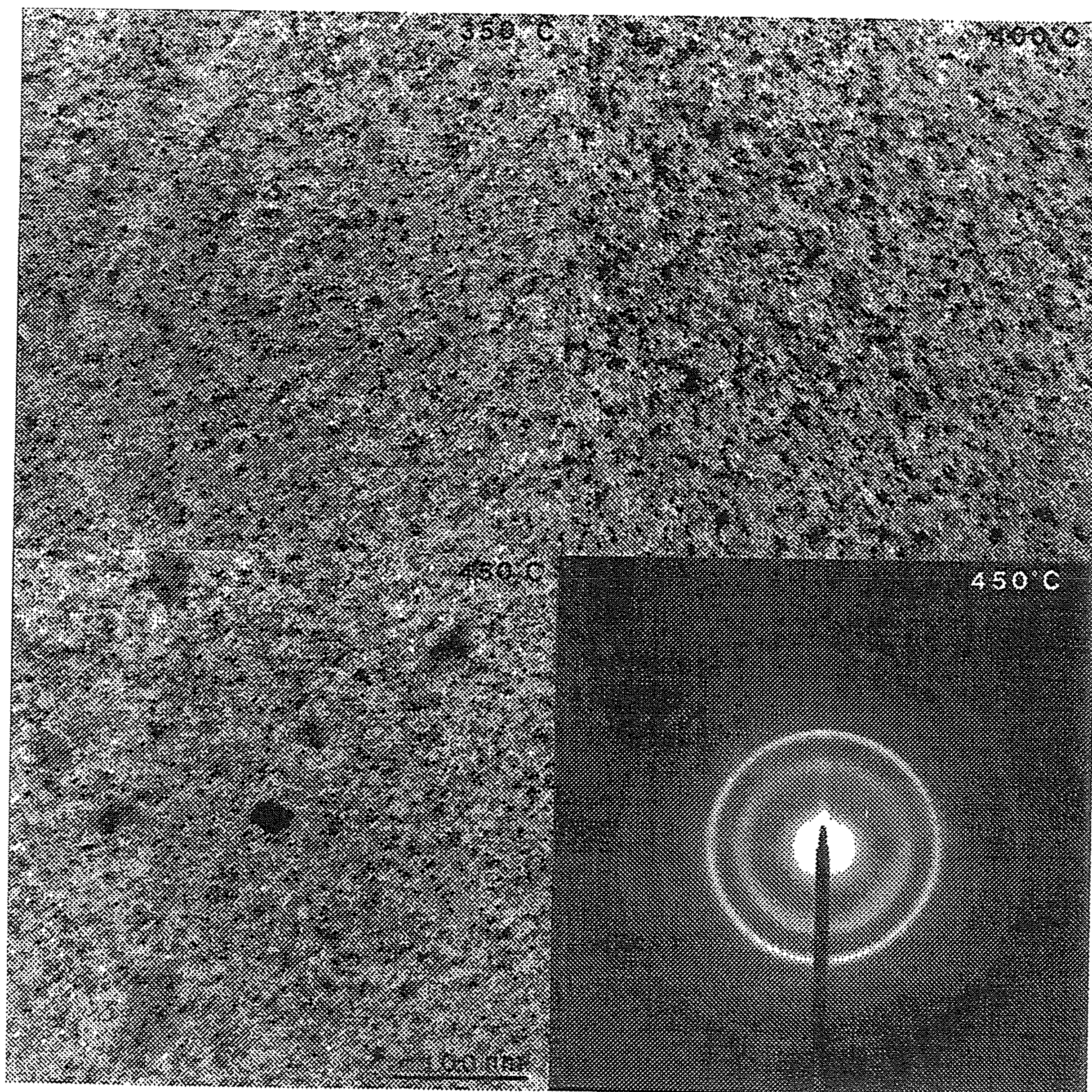

Figure 4.15 TEM bright field images and a diffraction pattern of 50 nm $Fe_{55}Hf_{17}O_{28}$ films, rapid thermal processed for 5 seconds at 350, 400 and 450°C. The diffraction pattern belongs to the film annealed at 450°C.

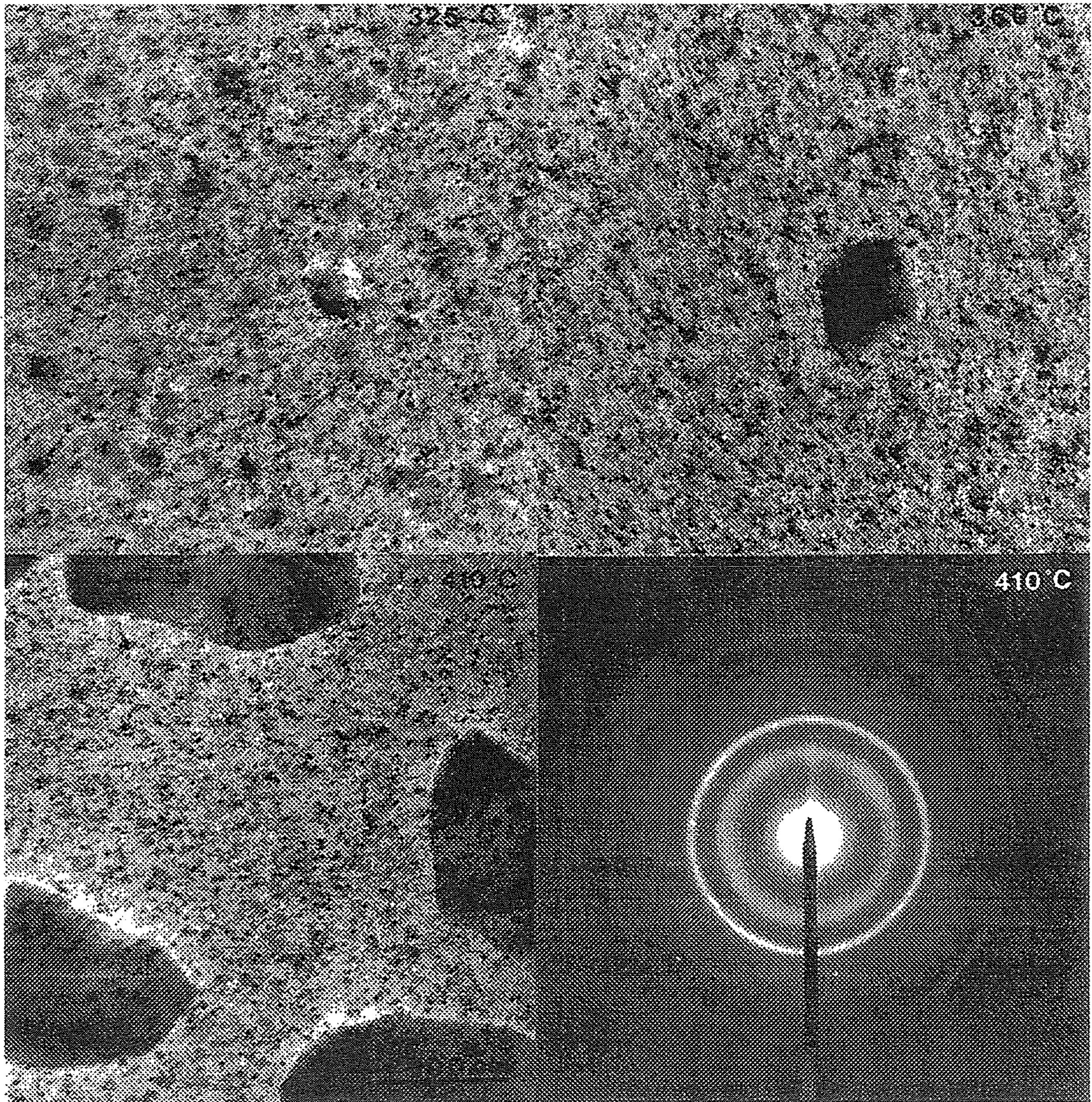

Figure 4.16 TEM bright field images and a diffraction pattern of 50 nm $Fe_{55}Hf_{17}O_{28}$ films, classical thermal processed for 2 hours at 325, 360 and 410°C. The diffraction pattern belongs to the film annealed at 410°C.

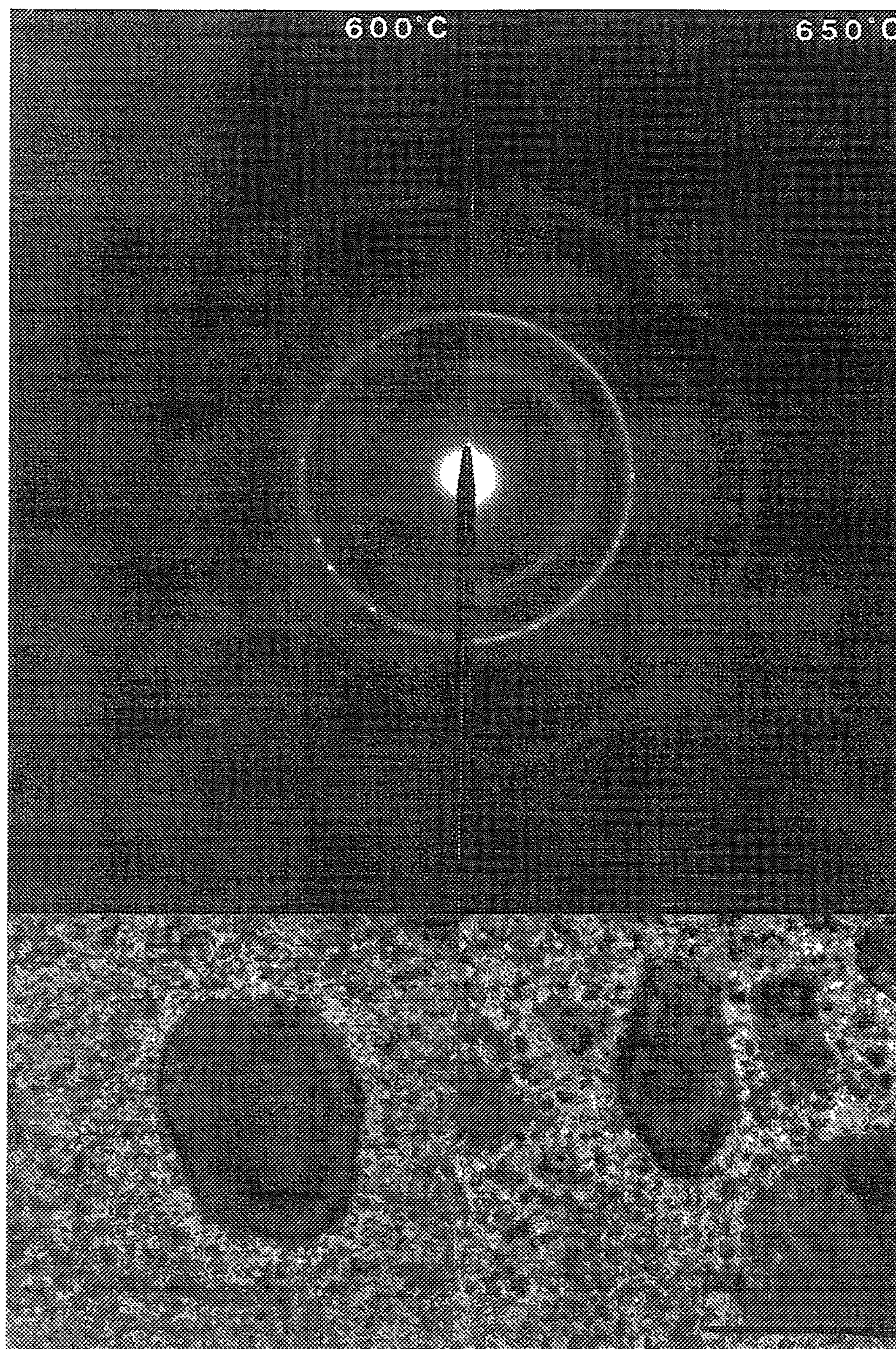

Figure 4.17 TEM diffraction patterns and bright field images of 50 nm $Fe_{55}Hf_{17}O_{28}$ films:

- left: rapid thermal processed for 5 seconds at 600°C
- right: rapid thermal processed for 5 seconds at 650°C.

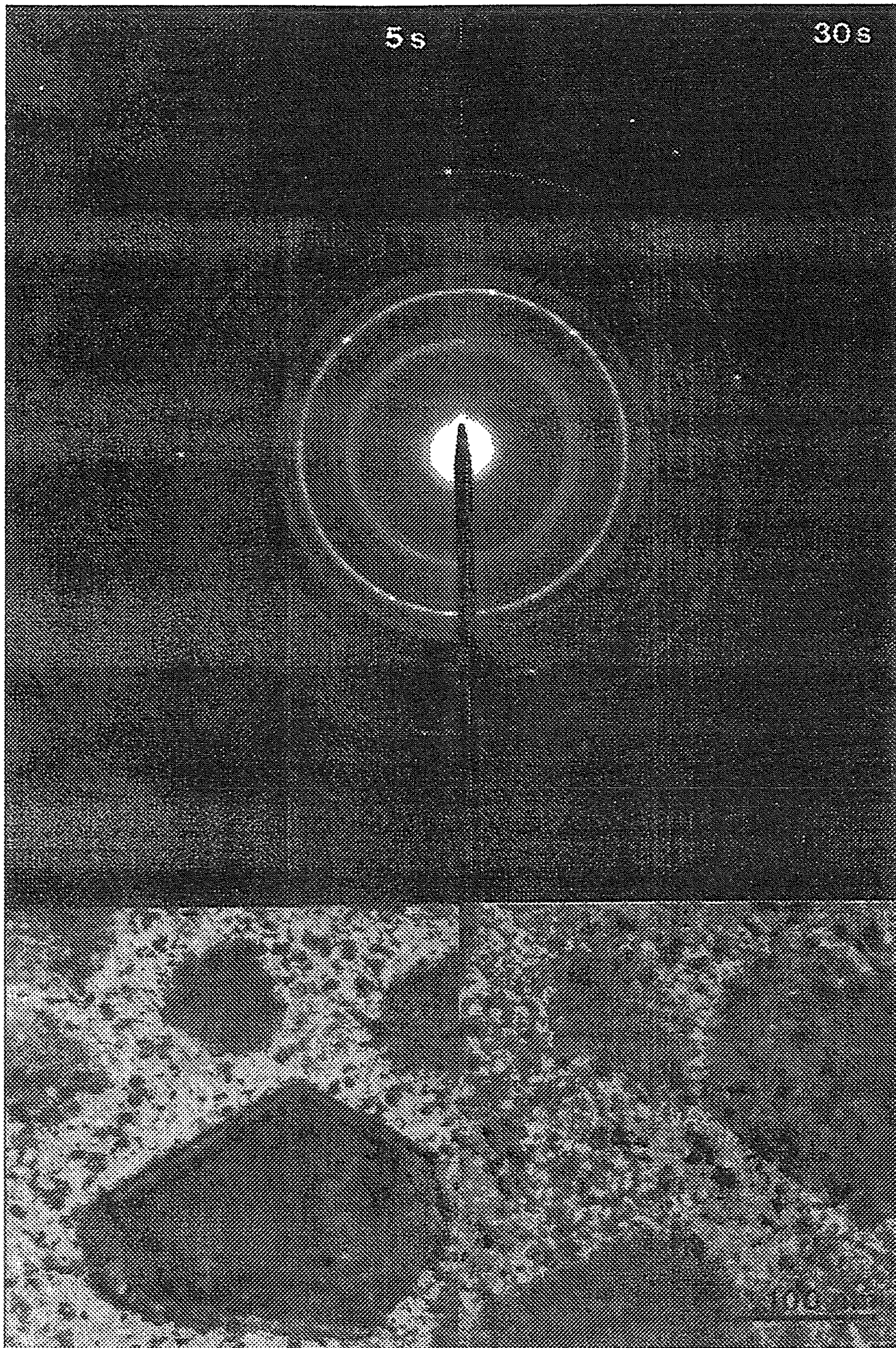

Figure 4.18 TEM diffraction patterns and bright field images of 50 nm $Fe_{55}Hf_{17}O_{28}$ films:

- left: rapid thermal processed for 5 seconds at 700°C
- right: rapid thermal processed for 30 seconds at 700°C.

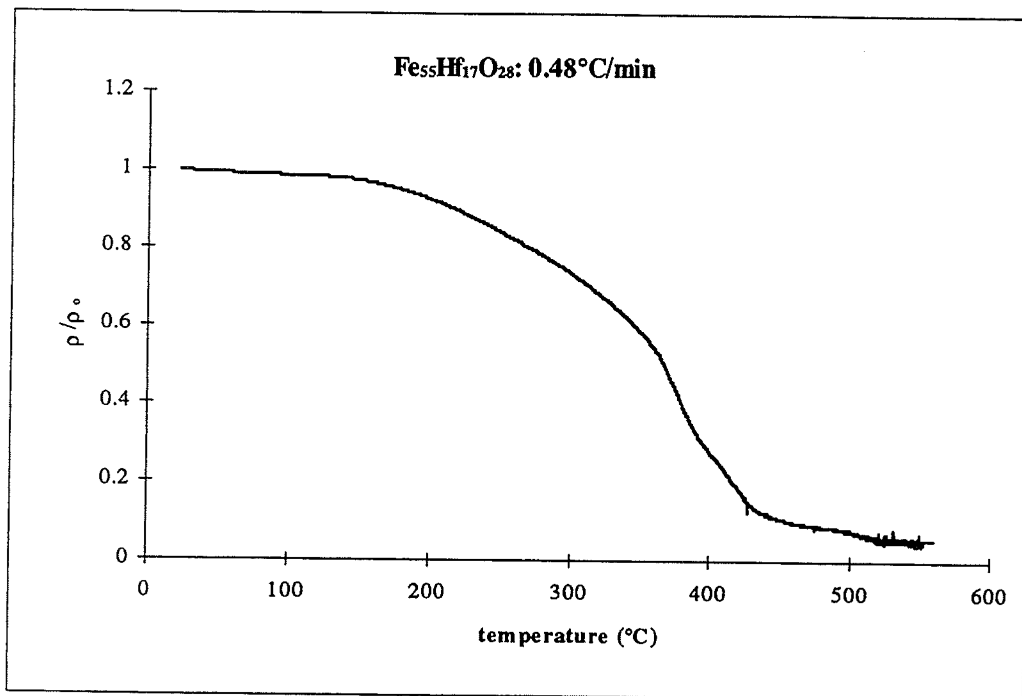

Figure 4.19 Normalised resistivity of a 0.70 μm $Fe_{55}Hf_{17}O_{28}$ film deposited on single crystalline (100) Si with a 0.5 μm SiO_2 buffer layer as a function of temperature during heating at a rate of 0.48°C/s.

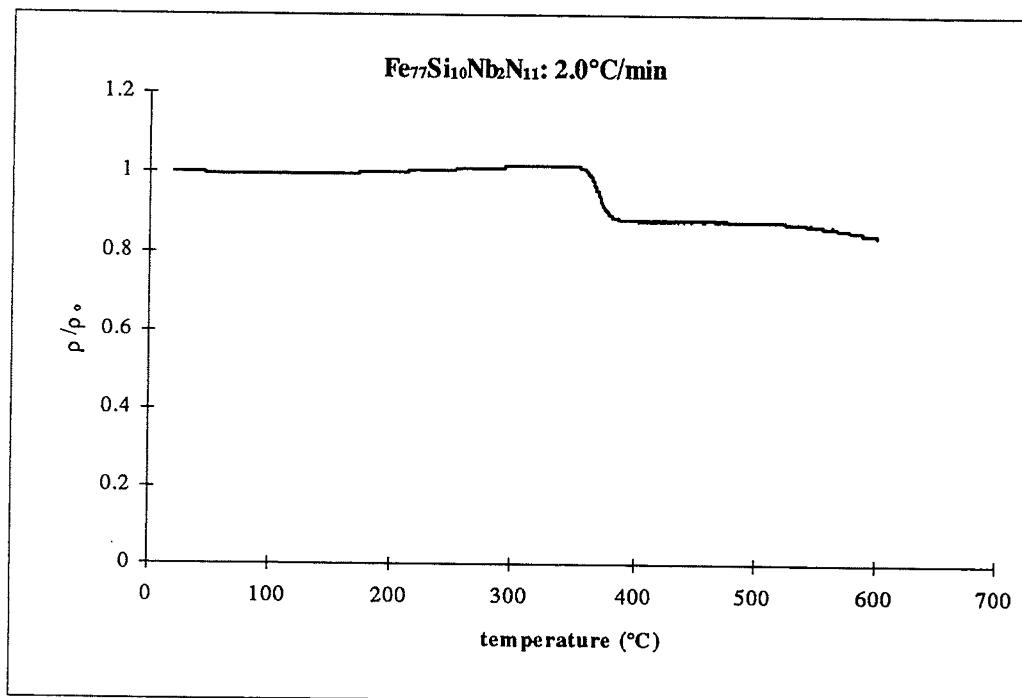

Figure 4.20 Normalised resistivity of a 1 μm $Fe_{77}Nb_{10}Si_2N_{11}$ film deposited on GGG as a function of temperature during heating at a rate of 2.0°C/s.

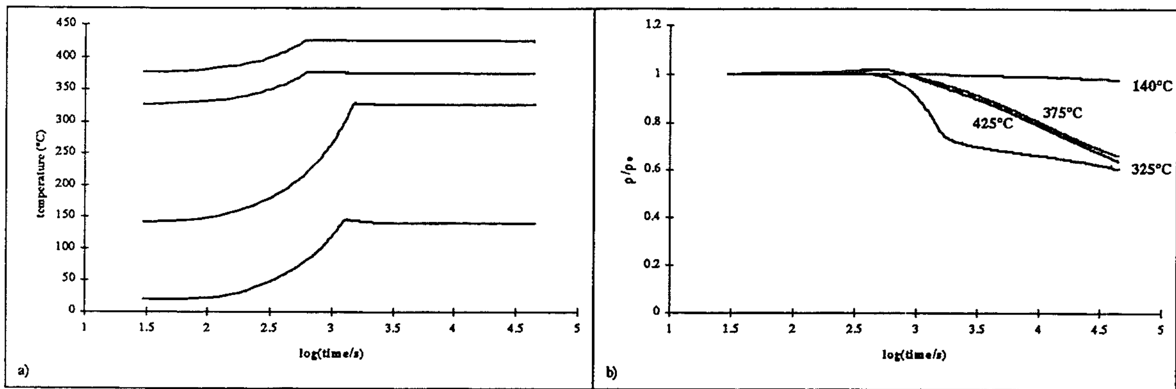

Figure 4.21 Step annealing treatment at 140, 325, 375 and 425°C of a 0.70 μm $Fe_{55}Hf_{17}O_{28}$ film deposited on single crystalline (100) Si with a 0.5 μm SiO_2 buffer layer:
a) temperature and
b) normalised resistivity
as a function of time. Each isothermal period takes 12 hours.

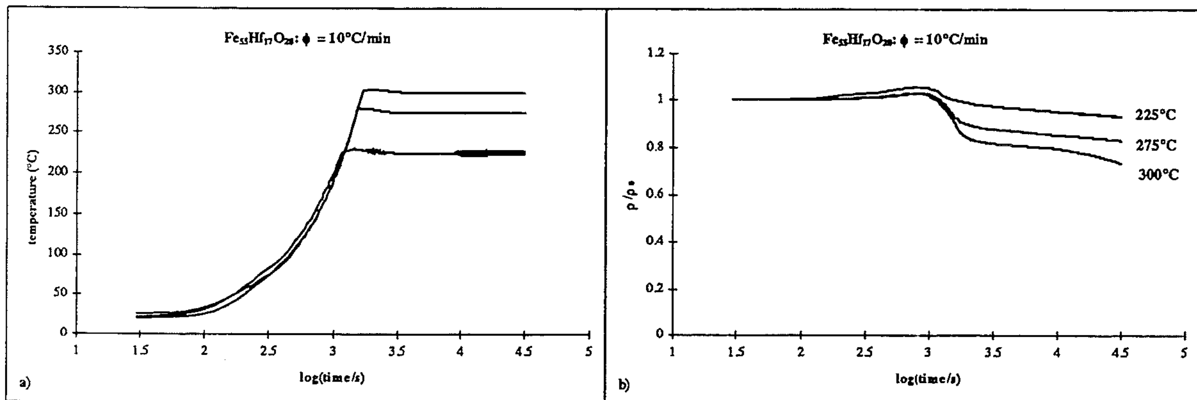

Figure 4.22 Isothermal resistivity measurements on 0.70 μm $Fe_{55}Hf_{17}O_{28}$ films deposited on single crystalline (100) Si with a 0.5 μm SiO_2 buffer layer:
a) temperature profile and
b) normalised resistivity as a function of time during isothermal annealing at 225, 275 and 300°C.
The heating rate is 10°C/min and is included in the measured time.

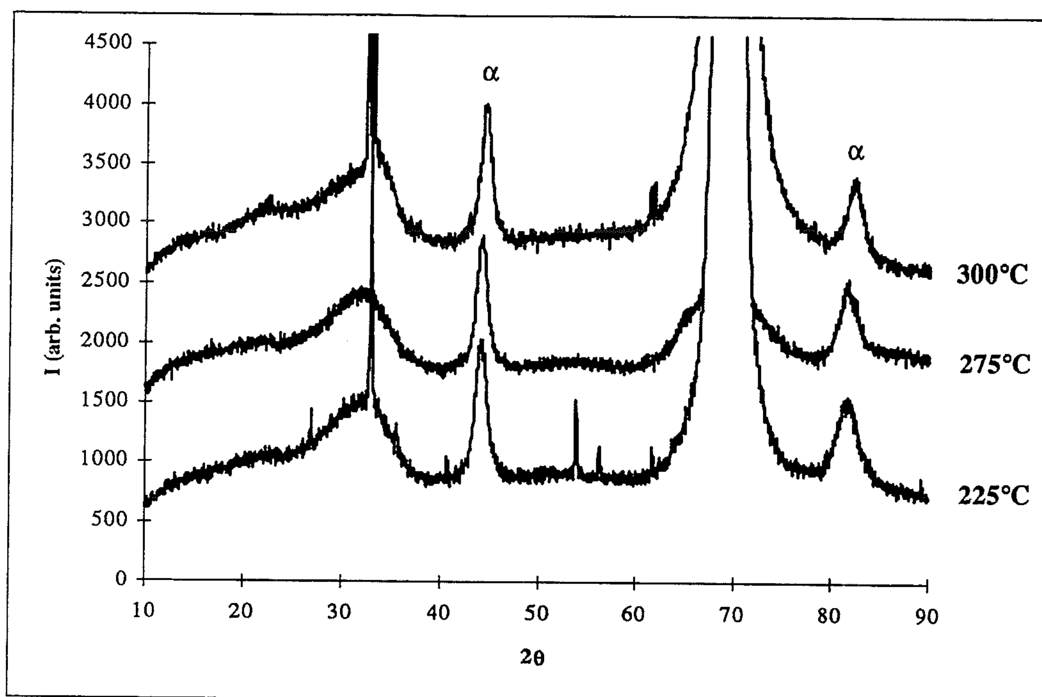

Figure 4.23 XRD scans (intensity I vs. diffraction angle 2θ) of 0.70 μm $Fe_{55}Hf_{17}O_{28}$ deposited on single crystalline (100) Si with a 0.5 μm SiO_2 buffer layer, after isothermal annealing at 225, 275 and 300°C in the resistivity measurement furnace. The counting time is 15 seconds per 0.04°2θ interval.

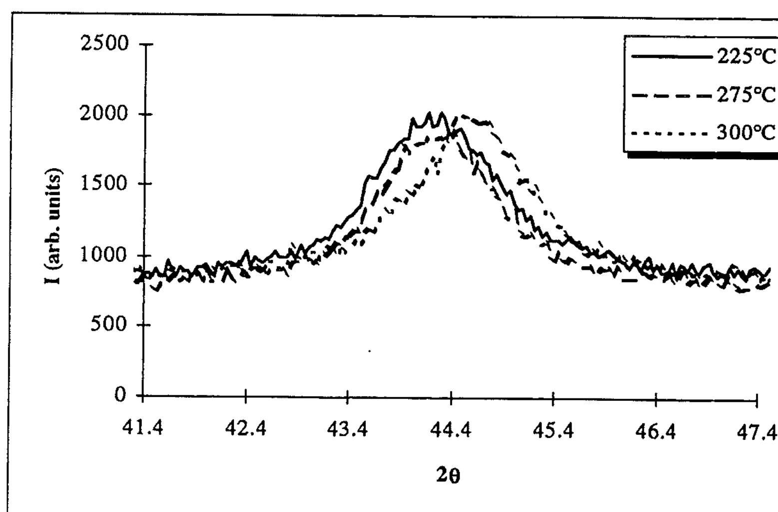

Figure 4.24 The α-Fe (110) diffraction peaks of figure 4.24.

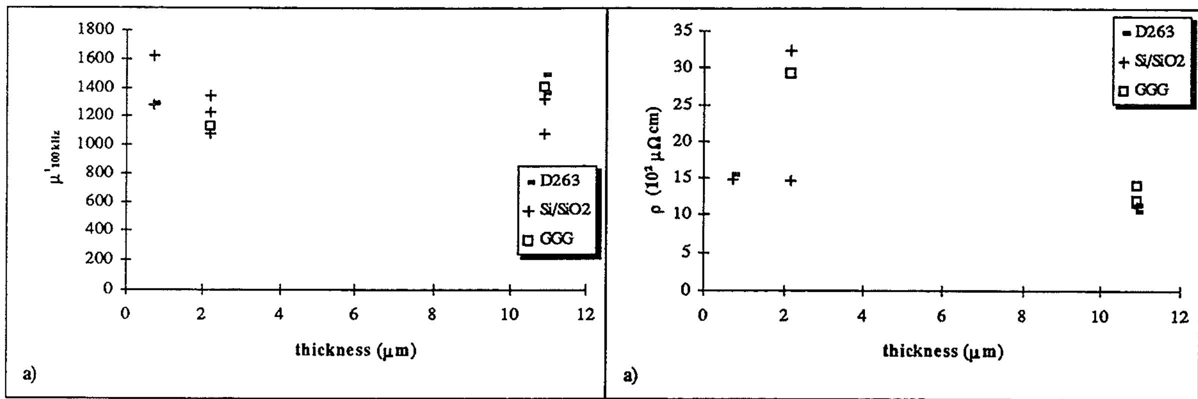

Figure 4.25 Thickness dependence of:
a) the permeability at 100 kHz $\mu'_{100\,kHz}$ and
b) the resistivity ρ [mΩcm]
of $Fe_{55}Hf_{17}O_{28}$ films deposited on D263 glass, single crystalline (100) Si with a 0.5 μm SiO_2 buffer layer and GGG after rapid thermal processing for 5 seconds at 400°C.

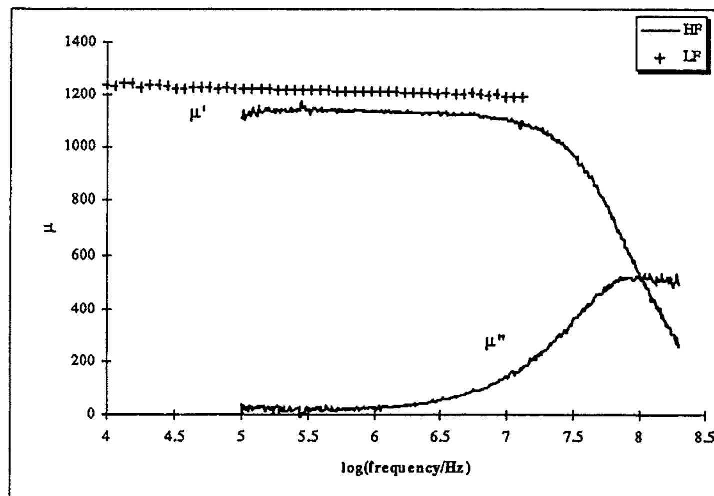

Figure 4.26 High frequency complex permeability as a function of frequency of a 10.9 μm $Fe_{55}Hf_{17}O_{28}$ films deposited GGG. The low frequency permeability measurement is also displayed. The film is rapid thermal processed for 5 seconds at 400°C.

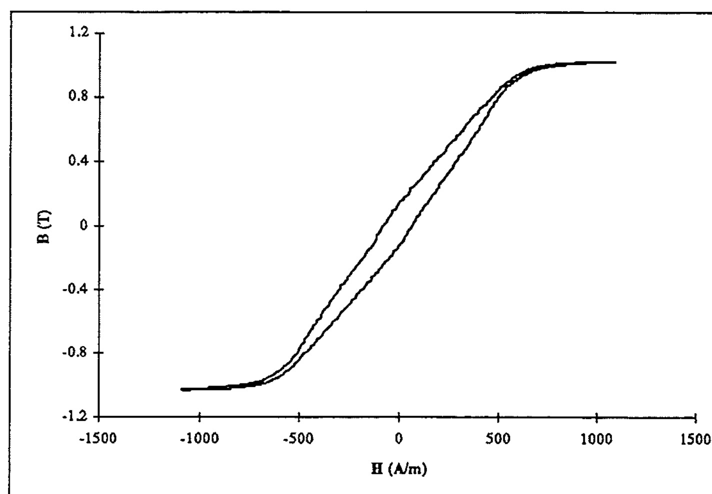

Figure 4.27 Typical hard axis BH-loop measured on a 10.9 μm $Fe_{55}Hf_{17}O_{28}$ film deposited on GGG. The film is rapid thermal processed for 5 seconds at 400°C.

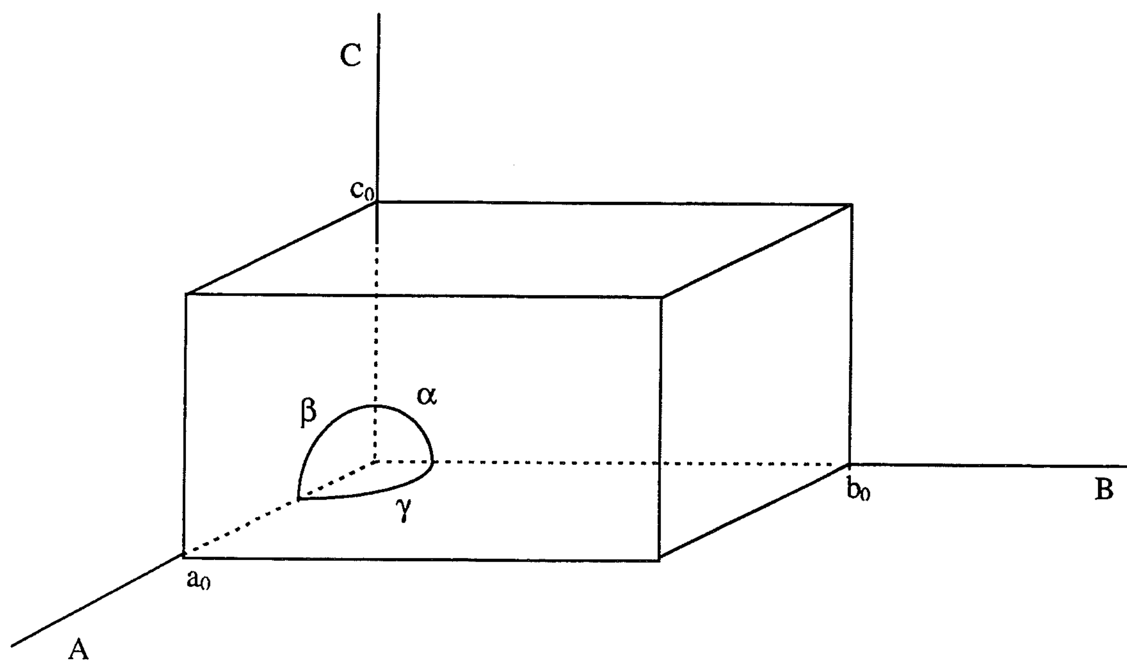

Figure 5.1 Schematic representation of a crystal lattice. The lattice constants along the A, B and C axes are a_0, b_0 and c_0, respectively. The angle between the A and B axis is γ, the angle between the B and C axis is α and the angle between the A and C axis is β.

5. Discussion

5.1 Structure and structural changes upon annealing

In this section the results of the structural characterisation methods XRD and TEM, as presented in section 4.2, will be discussed. First the as deposited structure of $Fe_{55}Hf_{17}O_{28}$ films is treated. Subsequently structural changes upon low temperature annealing (RTP and CTP, below 500°C) and upon high temperature annealing (RTP above 500°C) are discussed.

As deposited structure

The structure of $Fe_{55}Hf_{17}O_{28}$ films after deposition seems to consist of body centred cubic iron (α-Fe), dispersed in an amorphous matrix. According to the literature this phase has a lattice constant of $a_0 = 2.866$ Å [73]. This structure has already schematically been shown in figure 2.11[a]. From the (110) α-Fe peak in the XRD scan of figure 4.11 the mean grain size in the direction perpendicular to the (110) lattice planes D_{110} is estimated to be 3 nm. At the end of this section it will be shown how this value can be obtained form an XRD scan. The α-Fe nanocrystals are believed to be randomly orientated in the thickness direction of the film, because the (110) and (211) peak heights in the XRD scans appear in the same ratio as found in an α-Fe powder (i.e. a random distribution of orientations).
Because electron diffraction is performed in the transmission mode, only electrons diffracted at planes that are *perpendicular* to the film surface are measured. Therefore it is concluded from the appearance of the broad *rings* in the as deposited diffraction pattern of figure 4.14 that the α-Fe nanocrystals are randomly orientated in the film plane as well.
The lattice parameter that follows from the (110) α-Fe reflection in the XRD scan is equal to: a = 2.885 Å, slightly larger than expected from the lattice constant of α-Fe (2.866 Å). This increased lattice parameter may be related to dissolution of large (Hf) atoms in the b.c.c. iron lattice. From Vegards Law it follows that this increase in lattice parameter is can be explained by substitutional dissolution of 2.5 at% Hf in the b.c.c. iron lattice. However, the *equilibrium* solvability of Hf in Fe is much smaller (0.51 at%).

Low temperature annealing structural changes

Upon annealing at temperatures up to 500°C the α-Fe integrated peak areas (= area between the X-ray diffraction peak and the background signal) becomes slightly larger and the peaks become sharper, as can be seen in figures 4.11 and 4.12. This means that both the fraction nanocrystalline α-Fe and the mean grain size increase. Numerical values are given in tables 5.1 and 5.2. In other words: further α-Fe crystallisation is induced by annealing treatments. This can also be seen in the TEM electron diffraction patterns of figure 4.14, where the electron diffraction rings become sharper upon annealing.
The α-Fe lattice parameter a calculated from the XRD scans are, generally, larger than the reported values. Upon annealing this differences becomes smaller (see table 5.1 and 5.2). These are indications that dissolved atoms leave the α-Fe nanocrystals upon annealing.
A new phase is formed upon annealing at low temperatures: face centred orthorhombic cementite (see figure 4.12[b]). An orthorhombic structure is characterised by three different lattice constants, while all three crystal axes make angles of 90° with each other (see figure 5.1). The lattice parameters of cementite are estimated by performing microdiffraction at one particle in the TEM: $a_0 = 5.08$ Å, $b_0 = 6.73$ Å and $c_0 = 4.51$ Å. These values agree reasonably

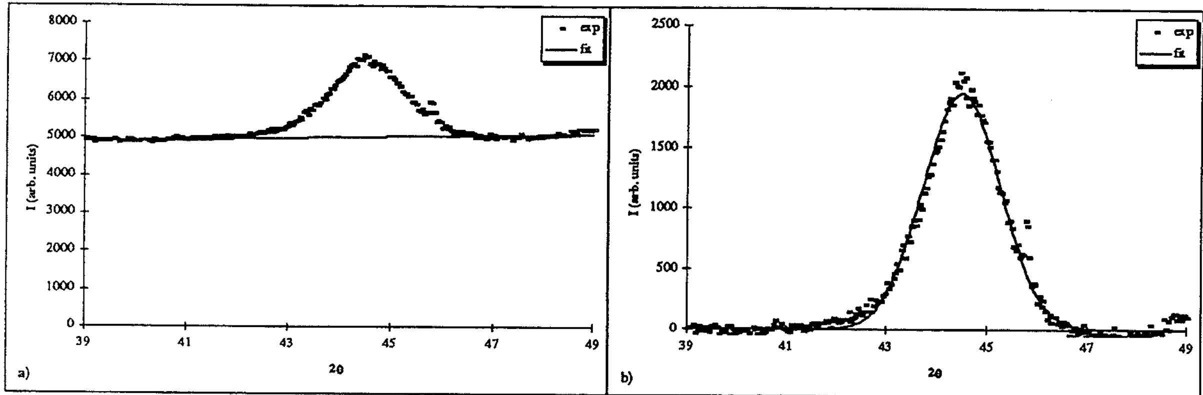

Figure 5.2 The (110) α-Fe diffraction peak of a 0.7 μm $Fe_{55}Hf_{17}O_{28}$ film deposited on GGG and rapid thermal processed for 5 seconds at 500°C (isolated from figure 4.13):
a) the background signal is assumed to be linear and
b) after subtracting this background the peak is fitted with a Gaussian profile.

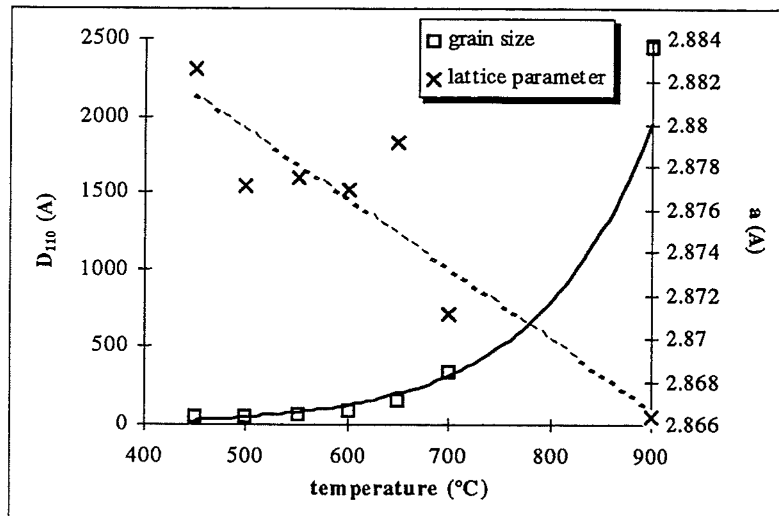

Figure 5.3 Estimated grain sizes D_{110} and lattice spacings a of α-Fe in 0.7 μm $Fe_{55}Hf_{17}O_{28}$ films deposited on GGG and rapid thermal processed for 5 seconds as a function of the annealing temperature T_a (from figure 4.13).

well with the reported values: $a_0 = 5.092$ Å, $b_0 = 6.744$ Å and $c_0 = 4.527$ Å [74]. From the TEM observations (see figure 4.16) it seems that the large cementite particles are single crystalline and very small in the thickness direction of the films.
Once again, it should be noted that the very thin films used for TEM investigations may not be representative for the thicker films described in this report.

High temperature annealing structural changes

Annealing films deposited on GGG at temperatures above 500°C results in more reflections (crystallisation) in the XRD scans (see figure 4.13). Even at the lowest annealing temperature a very broad peak is observed around 33°2θ. This broad peak probably is present in the XRD scans measured at films deposited onto D263 glass as well. Unfortunately, this peak position coincidences with the glass reflection of the substrate, therefore it was not observed before for the films deposited on D263 glass. Reconsidering the TEM electron diffraction patterns, very broad rings are observed that can not be attributed to b.c.c. iron reflections. These broad diffraction peak and ring are thought to be caused by the amorphous phase.
Above 550°C it separates into two sharper peaks, which are believed to be caused by face centred cubic HfO_2 (γ-HfO_2). The lattice parameter of γ-HfO_2 is determined to be 5.04 Å, slightly less than the reported value of 5.115 Å [75]. Further growth of γ-HfO_2 is observed up to 700°C. A monoclinic HfO_2 structure (m-HfO_2) becomes visible as well. At the highest annealing temperature (900°C) hafnium oxide is found in majority as m-HfO_2, apart from a small γ-HfO_2 reflection. A monoclinic structure is characterised by three different lattice constants and one angle between the crystal axes that is not equal to 90°; usually β is used for this angle (see figure 5.1). The numerous reflections coincide well with the lattice parameters $a_0 = 5.29$ Å, $b_0 = 5.18$ Å, $c_0 = 5.11$ Å and $\beta = 99.3°$ [76].
In figure 4.13 no cementite reflections are found at all. However, these reflection were present in the films investigated in the TEM (except at 900°C) and several films used in other XRD experiments. Therefore it is concluded that the appearance of cementite is not reproducing very well.
The (200) α-Fe reflection at the highest temperature is relatively strong compared to the (110) reflection. Because there are no other reflections expected at this position, it is concluded that the α-Fe crystals show texture in the film thickness direction: the crystals are preferentially orientated with their (200) planes parallel to the film surface.
In the electron diffraction patterns in figure 4.18 it can be seen that the α-Fe rings are more intense at certain positions; this effect is attributed to grain growth (crystal density decreases, causing less but more pronounced reflections in certain directions). To illustrate the α-Fe grain growth, the increase of the mean α-Fe grain size in the direction perpendicular to the (110) lattice planes D_{110} is estimated.
The procedure described in section 3.3.1 is illustrated in figure 5.2 for a $Fe_{55}Hf_{17}O_{28}$ film deposited on GGG and rapid thermal processed for 5 seconds at 500°C. The background signal from the (110) α-Fe reflection in the measured XRD scan is removed by subtracting the fitted linear background. The remaining diffraction peak is approximated by a Gaussian profile with parameters p_1, p_2 and p_3 (equation (3.3)). Using the obtained values for p_1, p_2 and p_3 the mean grain size perpendicular to the (110) planes D_{110} [Å], the lattice parameter a [Å] and the integrated peak area can be estimated. The results of the calculations are given in tables 5.1 to 5.3.

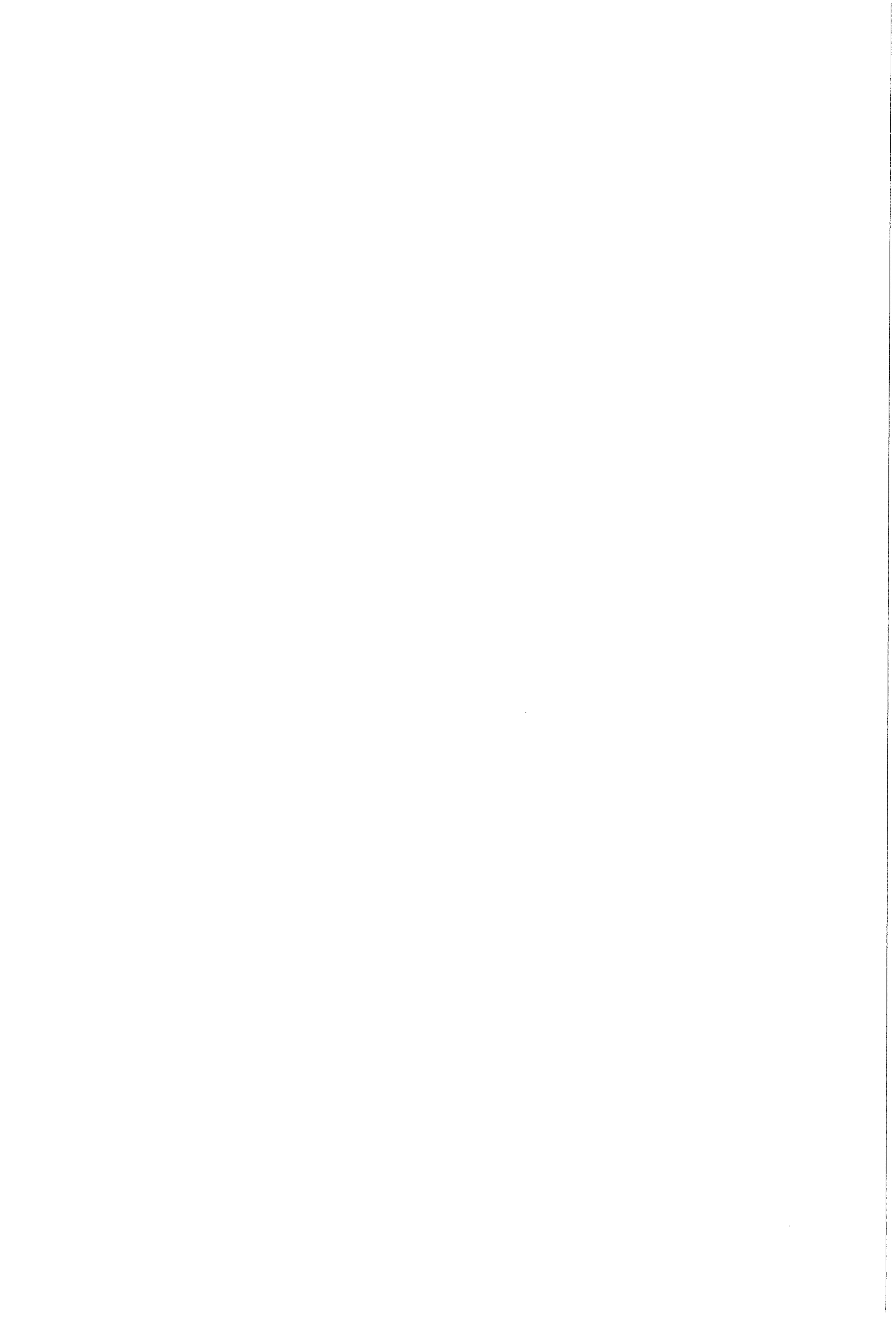

Table 5.1 Some structural parameters of 0.70 μm thick $Fe_{55}Hf_{17}O_{28}$ films deposited on D263 glass, as a function of the annealing temperature (RTP: 5 seconds): mean grain size in the thickness direction of the α-Fe nanocrystals (D_{110}), lattice parameter (a) and integrated peak area, as calculated from the (110) α-Fe reflection in figure 4.11.

T_a (°C)	a (Å)	D_{110} (Å)	peak area (I·°2θ)
as dep	2.885	32	404
350	2.876	69	579
450	2.876	69	579
500	2.850	59	669

Table 5.2 Some structural parameters of 0.70 μm thick $Fe_{55}Hf_{17}O_{28}$ films deposited on D263 glass, as a function of the annealing temperature (CTP: 2 hours): mean grain size in the thickness direction of the α-Fe nanocrystals (D_{110}), lattice parameter (a) and integrated peak area, as calculated from the (110) α-Fe reflection in figure 4.12[a].

T_a (°C)	a (Å)	D_{110} (Å)	peak area (I·°2θ)
as dep	2.893	51	377
325	2.883	62	477
360	2.876	74	450
410	2.853	75	479
460	2.852	84	480

Table 5.3 Some structural parameters of 0.70 μm thick $Fe_{55}Hf_{17}O_{28}$ films deposited on GGG, as a function of the annealing temperature (RTP: 5 seconds): mean grain size in the thickness direction of the α-Fe nanocrystals (D_{110}), lattice parameter (a) and integrated peak, as calculated from the (110) α-Fe reflection in figure 4.13.

T_a (°C)	d_{110} (Å)	D_{110} (Å)	peak area (I·°2θ)
450	2.883	51	2862
500	2.877	54	3786
550	2.877	51	3814
600	2.877	96	3535
650	2.879	154	2965
700	2.871	340	2486
900	2.866	2248	3250

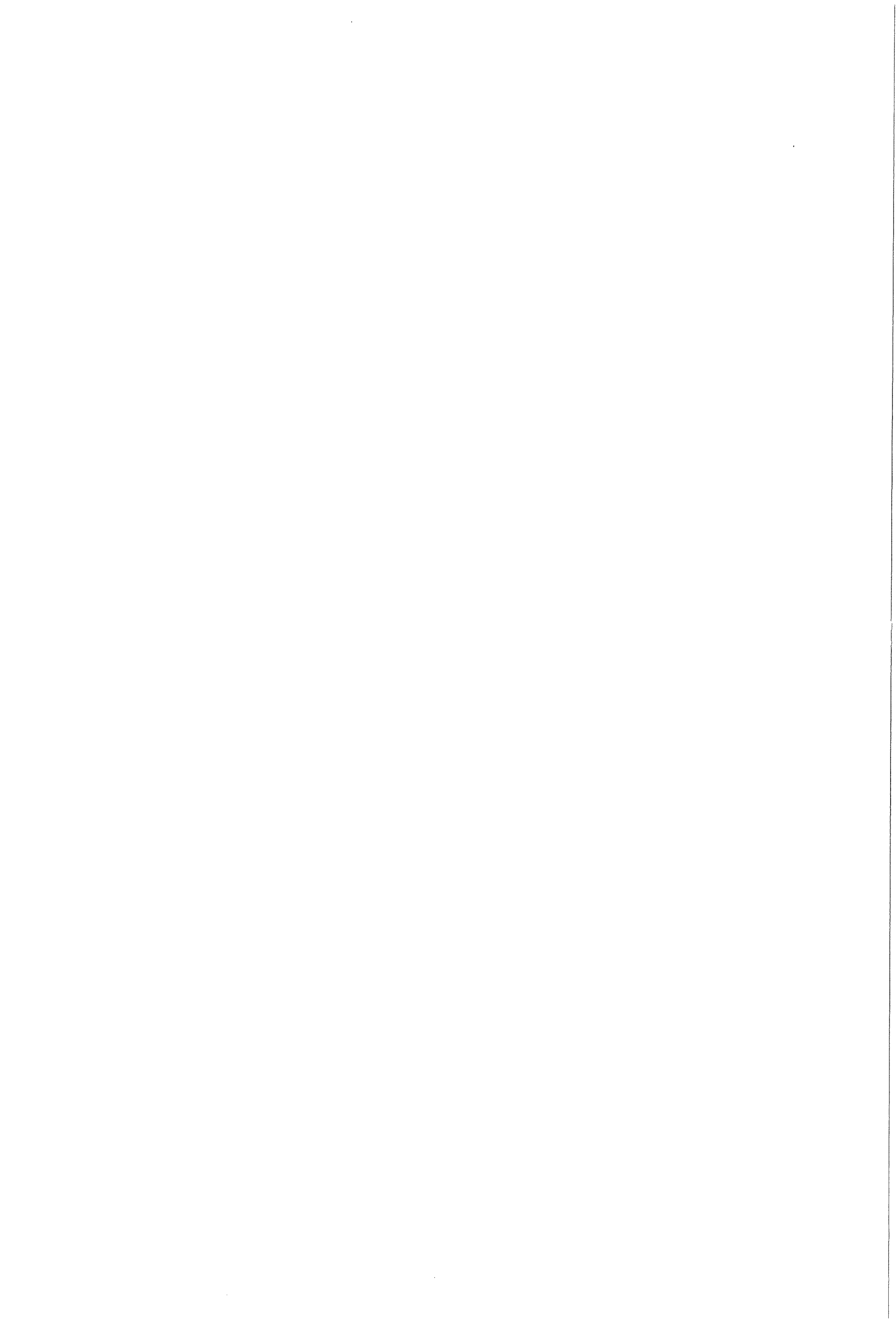

From these tables it can be seen that:

- In almost all situations the lattice parameter a is larger than the value for pure α-Fe (2.866 Å). Upon annealing this difference becomes smaller. The only peaks that have smaller lattice parameters are those annealed at high temperatures (CTP). These peaks contain a significant contribution from Fe_3C (see figure 4.12[b]); which shifts them to larger scattering angles (smaller lattice spacings).
- The mean grain size D_{110} strongly increases, especially at annealing above 500°C.
- An increase of the integrated peak area (fraction crystallised α-Fe) is observed upon low temperature annealing; at higher temperatures no further increase is found.

It should be noted that this is not an exact method: it is semi-quantitatively at best. The calculated grain sizes are all minimum values and are only indications of the grain size (as long as the crystallites are sufficiently small). Because the counting time was 15 seconds per 0.04°2θ interval for the high temperature annealed films, table 5.3 is expected to be the most accurate. In figure 5.3 the mean grain size and lattice parameter from this table are plotted as a function of the annealing temperature. It can be seen that D_{110} increases exponentially, whereas the lattice parameter decreases approximately linear with the annealing temperature.

5.2 Interpretation of the resistivity measurements

In this section an attempt is made to treat one of the atomic ordering processes in 0.70 μm thin $Fe_{55}Hf_{17}O_{28}$ films during annealing (semi-)quantitatively. The isothermal and isochronal resistivity experiments presented in the section 4.3 are used for this purpose. In this section it will be shown how a fraction transformed can be calculated from the resistivity measurements. Subsequently the obtained fraction transformed vs. time curves will be fitted using the well-known JMA equation. Finally the curves are interpreted in terms of the rate equation for a first order transition, assuming an activation energy.

5.2.1 Calculation of the fraction transformed

It is assumed that all measured in resistance changes can be attributed to changes in resistivity. In other words: it is assumed that no changes in film dimensions take place during the annealing treatment.

In order to calculate a fraction transformed from the measured resistance curves, the measurements must be corrected for the temperature dependence of resistivity first. The temperature dependence of the resistivity may be approximated by

$$\frac{\rho(T)}{\rho_0} = 1 + \kappa(T - \Theta), \tag{5.1}$$

where $\rho(T)$ is the (measured) resistivity at temperature T and ρ_0 is the resistivity at the beginning of the experiment; the parameters κ [1/K] and Θ [K] are determined by least squares fitting the equation to the measured resistivity change in the beginning of the heating stage. The temperature dependent contribution is subtracted from the measured resistivity $\rho(t,T)$:

$$\frac{\rho_{cor}(t)}{\rho_0} = \frac{\rho(t,T)}{\rho_0} - \kappa[T - \Theta]. \tag{5.2}$$

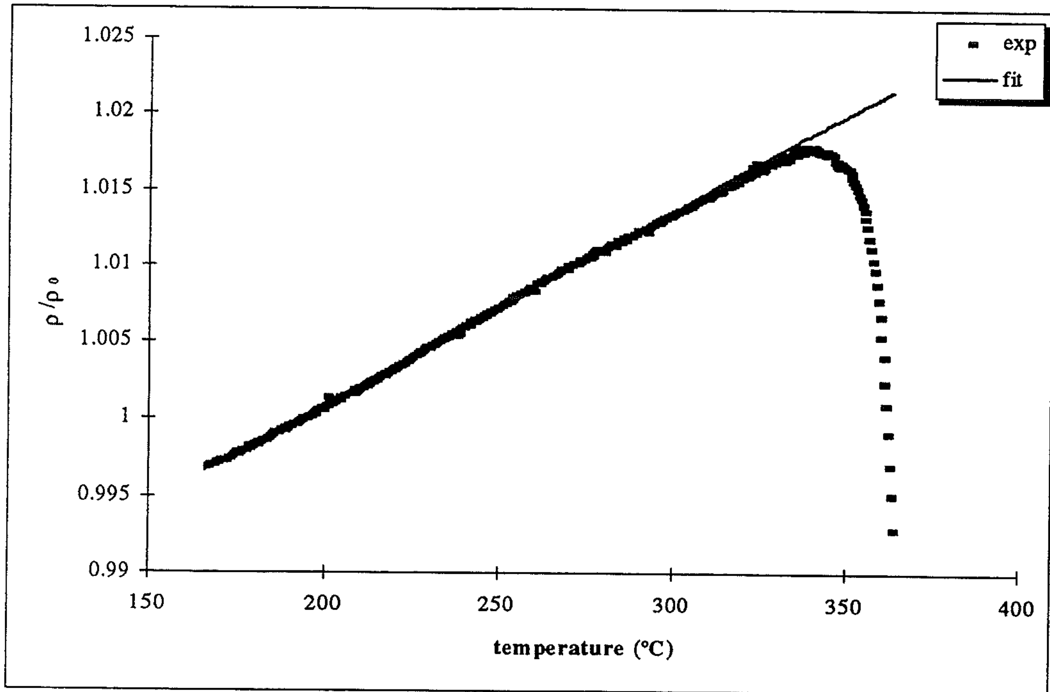

Figure 5.4 Low temperature part of the normalised resistivity of a 1 μm $Fe_{77}Nb_{10}Si_2N_{11}$ film deposited on GGG as a function of temperature during heating at a rate of 2.0°C/min (from figure 4.20). The temperature coefficient of the resistivity is estimated from the linear part.

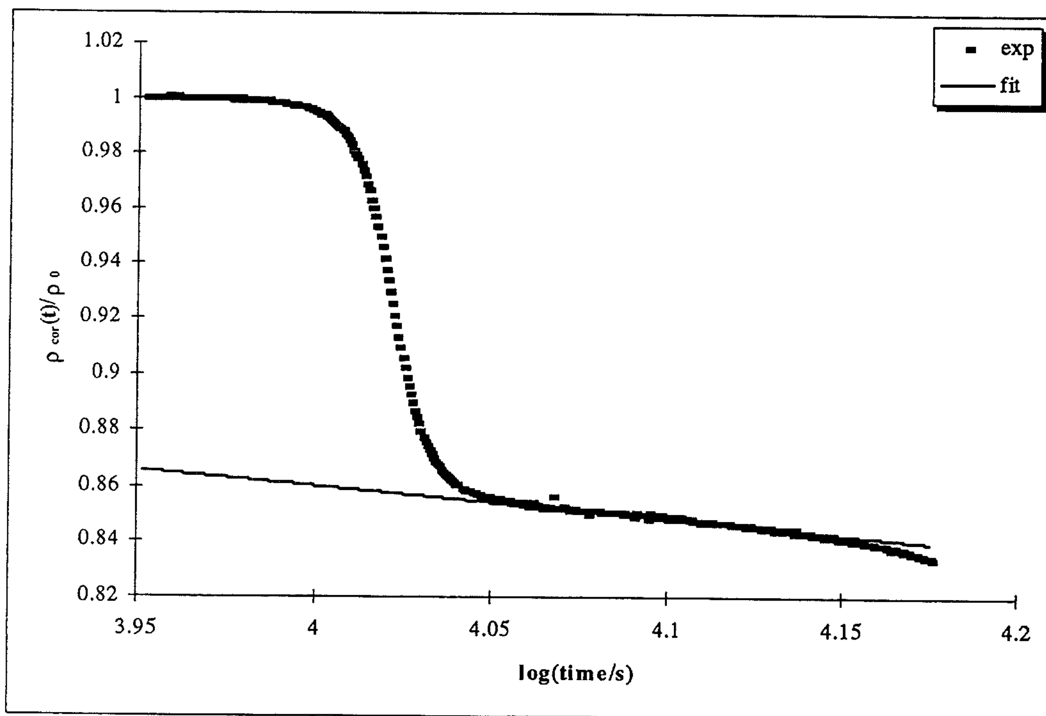

Figure 5.5 Normalised resistivity, corrected for the temperature dependence of the resistivity, of a 1 μm $Fe_{77}Nb_{10}Si_2N_{11}$ film deposited on GGG as a function of log(time) during heating at a rate of 2.0°C/min (from figure 4.20). It is assumed that the crystallisation process ends at the straight line. In comparison with figure 5.4 the ordinate is taken as a time scale through: : $T(t) = 19.3°C + 0.033°C/s \cdot t$.

Another complication is found at the end of the process: the resistivity keeps decreasing with time, as can be seen in figure 4.22. It is assumed that the transformation ends at the line [77]:

$$\frac{\rho_{cor,e}(t)}{\rho_0} = a + b \cdot \log(t/\sec). \tag{5.3}$$

The parameters a and b are determined by least squares fitting this expression to the corrected resistivity as a function of log(time). Now the parameters a and b are known, the (corrected) resistivity can be "translated" into a volume fraction transformed f. In section 2.5 three expressions for the resistivity of a two phase mixture are given. In first approximation, the linear relationship is usually good enough. The experimental fraction transformed is estimated by (according to equation (2.39^a)):

$$f_{linear}(t) = \frac{1 - \frac{\rho_{eff}(t)}{\rho_a}}{1-\beta} \approx \frac{1 - \frac{\rho_{cor}(t)}{\rho_0}}{1 - \frac{\rho_{cor,e}(t)}{\rho_0}} \tag{5.4^a}$$

In this expression β is defined as the ration of the resistivity of the crystalline and the amorphous phase (ρ_C/ρ_A). Because none of these resistivities are known accurately, ρ_C is approximated by $\rho_{cor,e}(t)$ and ρ_A by ρ_0; the effective resistivity ρ_{eff} is equal to the corrected resistivity $\rho_{cor}(t)$.
When the resistivities of the two phases are very different, significant deviations from linear behaviour are observed, as shown in figure 2.26. In that case the expressions obtained by Maxwell [40] and Landauer [41] are more useful in the calculation of the experimental fraction transformed f. Rewriting equations (2.39^b) and (2.39^c), while using the same substitutions $\rho_C \rightarrow \rho_{cor,e}(t)$, $\rho_A \rightarrow \rho_0$ and $\rho_{eff} \rightarrow \rho_{cor}(t)$, gives:

$$f_{Maxwell}(t) \approx \frac{\left(1 - \frac{\rho_{cor}(t)}{\rho_0}\right)\left(2\frac{\rho_{cor,e}(t)}{\rho_0} + 1\right)}{\left(1 - \frac{\rho_{cor,e}(t)}{\rho_0}\right)\left(2\frac{\rho_{cor}(t)}{\rho_0} + 1\right)} \tag{5.4^b}$$

and

$$f_{Landauer}(t) = \frac{1}{3}\frac{\left(\frac{\rho_{cor}(t)}{\rho_0} + 2\frac{\rho_{cor}(t)}{\rho_0}\right)\left(1 - \frac{\rho_{cor}(t)}{\rho_0}\right)}{\left(1 - \frac{\rho_{cor,e}(t)}{\rho_0}\right)\frac{\rho_{cor}(t)}{\rho_0}}. \tag{5.4^c}$$

The isochronal resistivity measurement on $Fe_{77}Nb_{10}Si_2N_{11}$, shown in figure 4.20, is used to illustrate the described procedure; the heating rate is 2.0°C/min. It is known that α-Fe(Si) (b.c.c. iron with significant amounts of dissolved silicon) crystallises at about 350°C in this amorphous material. Crystallisation of the grain growth inhibitor NbN occurs in a much higher temperature range [3], finally resulting in a structure as shown in figure 2.11^b. Therefore the observed decrease in resistivity is attributed to the crystallisation of α-Fe(Si).

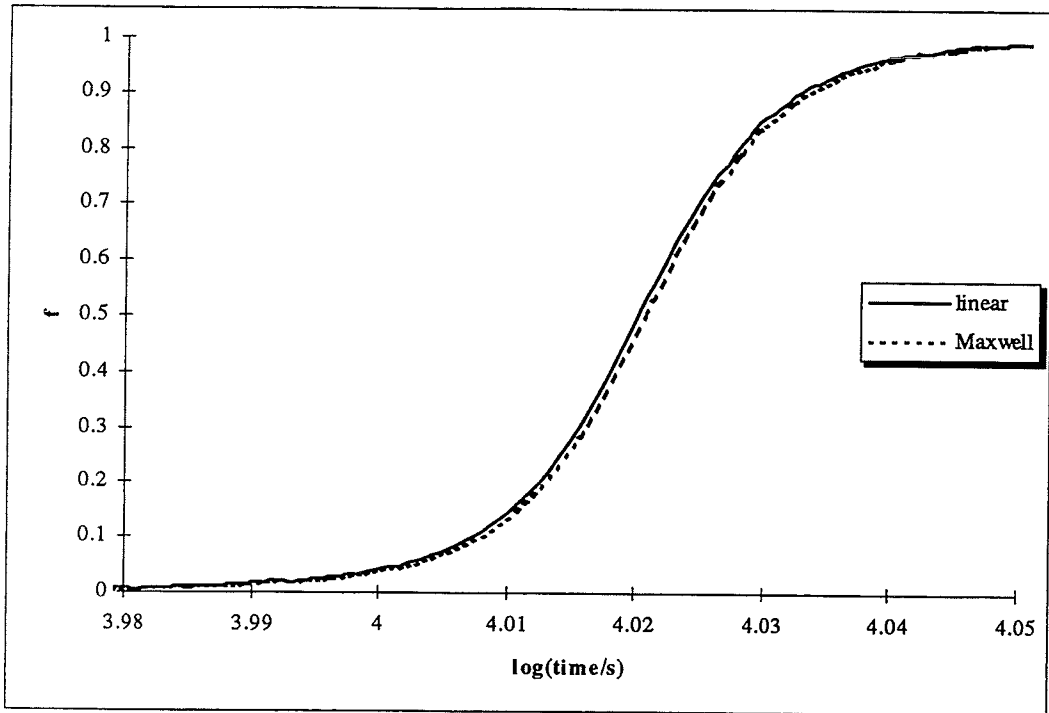

Figure 5.6 Fraction transformed f as a function of log(time) of a 1 μm $Fe_{77}Nb_{10}Si_2N_{11}$ film deposited on GGG, calculated from the isochronal resistivity measurement of figure 4.20. Two expressions were used to calculate f: the linear relation (5.5^a) and the Maxwell relation (5.5^b).

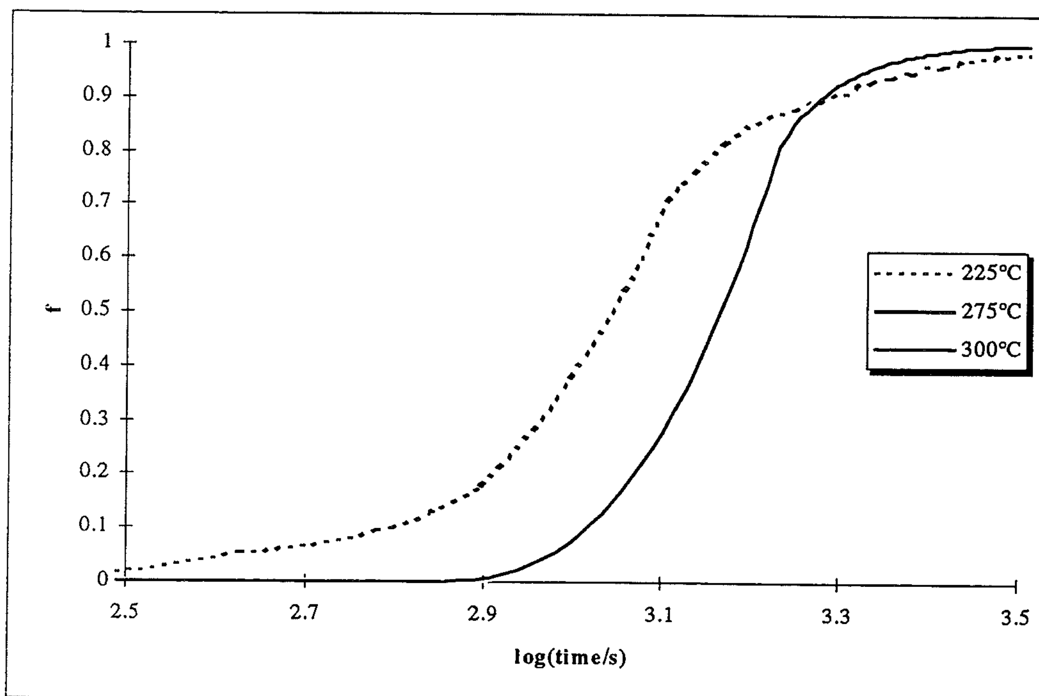

Figure 5.7 Fractions transformed f as a function of log(time) of 0.7 μm $Fe_{55}Hf_{17}O_{28}$ films deposited on single crystalline (100) Si with a 0.5 μm SiO_2 buffer layer, calculated from the resistivity measurements at 225, 275 and 300°C in figure 4.22. The Maxwell relation (5.5^b) was used to calculate f.

The temperature coefficient of resistivity is calculated by fitting equation (5.1) to the linear part (for $T < 300$ °C) of the measured ρ/ρ_0 curve in figure 4.20. A close up is shown in figure 5.4. In this figure both measurement and fitting results are displayed. κ and Θ are determined to be 127 ppm/K and 193°C, respectively. The measured resistivity is corrected using these values in equation (5.2). The corrected, normalised resistivity $\rho_{cor}(t)/\rho_0$ is shown in figure 5.5 as a function of log(time). Note that both time and temperature can be used on the x-axis, because the are linearly related by: $T(t) = T_0 + \phi t$ ($\phi = 2.0$°C/min). It can be seen in this figure that the resistivity keeps decreasing slightly with time after the drop at 10^4 seconds (≈ 350°C). Fitting equation (5.3) at this linear part gives the parameters: $a = 1.33$ and $b = -0.117$. Finally the fraction transformed is calculated, using the linear expression (equation (5.4^a)) and the Maxwell equation (5.4^b). The maximal difference between these two calculations is less than 10% (see figure 5.6), while the maximum difference between the Landauer and Maxwell expression is well below 1%. Therefore only the Maxwell equation will be used in further investigations.

In the same way as described for $Fe_{77}Nb_{10}Si_2N_{11}$, volume fraction transformed vs. time curves can be obtained from the resistivity measurements on $Fe_{55}Hf_{17}O_{28}$ films at 225, 275 and 300°C in figure 4.22. However, it is not yet clear what processes exactly occur during these annealing treatments. Several processes can be distinguished a priori, as argued in section 5.1:

1. crystallisation of α-Fe,
2. crystallisation of cementite and
3. crystallisation of hafnium oxide.

The last two crystallisation processes are not very likely, because they occur at higher temperatures and no cementite or hafnium oxide reflections are found in the XRD scans on the films used in the resistivity measurements (see figure 4.23). Unfortunately, no XRD scans were performed on an the as deposited samples, before the resistivity measurements. Therefore the mean grain sizes for the annealed specimens are calculated from the (110) α-Fe peak in this figure and compared to that calculated from the (110) peak in the XRD scan on an as deposited film (maximum $D_{110} = 51$ Å, see section 5.1); D_{110} is found to be 76 Å (225°C), 84 Å (275°C) and 87 Å (300°C). So an increase in the mean grain size perpendicular to the (110) planes of α-Fe is observed. Also, a peak shift is observed in the α-Fe peak upon annealing (see figure 4.24).
Therefore, the resistivity drop is most probably determined by further *crystallisation of* α*-Fe.* The total decrease depends on the isothermal annealing temperature and may also be related to the amount of *transfer of dissolved atoms* from the α-Fe crystals to the amorphous surroundings.
The fraction transformed vs. log(time) curves calculated from the resistivity measurements of figure 4.22 according to the described procedure are shown in figure 5.7.
It should be noted that the measurement at 225°C could not be translated into a volume fraction very well. Because the resistivity is measured every 30 seconds the number of fitting points for the determination of the temperature dependence of resistivity is the smallest of all three measurements. This in combination with non-linear behaviour during heating causes a strong dependence on the fitting range. For example, by choosing a slightly different range a curve is obtained that differs by 30% from the curve presented in figure 5.7.

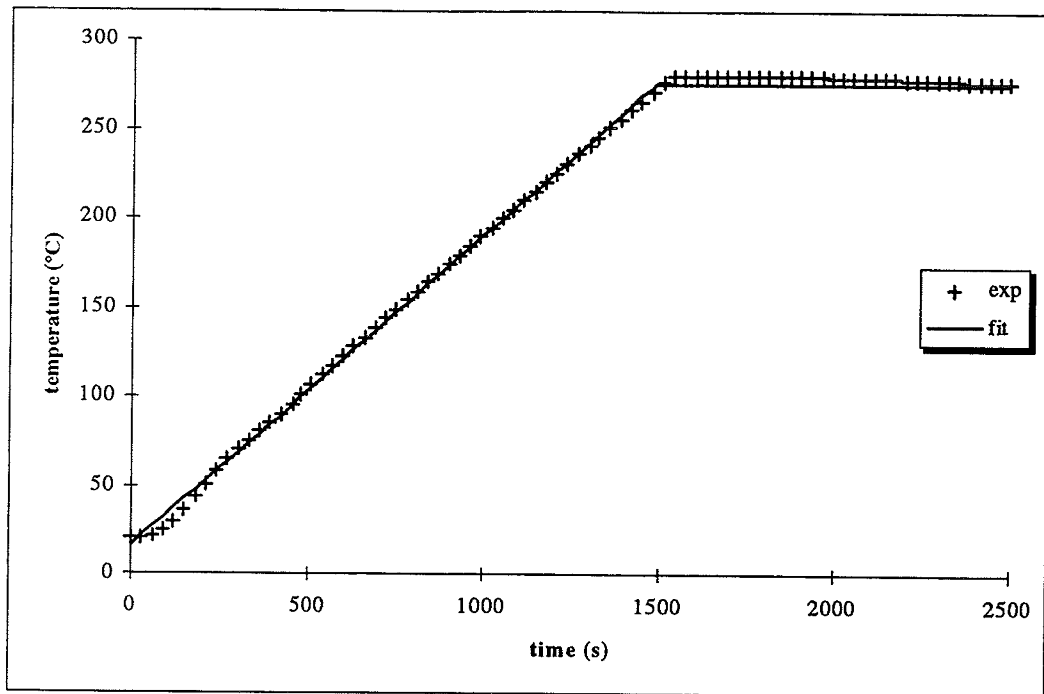

Figure 5.8 Measured and approximated temperature profile during the resistivity measurement at 275°C on a 0.7 μm $Fe_{55}Hf_{17}O_{28}$ films deposited on single crystalline (100) Si with a 0.5 μm SiO_2 buffer layer. The approximated temperature profile during annealing is drawn using the parameters: T_0 = 16.1°C, ϕ = 10.5°C/min and t_1 = 1485 s.

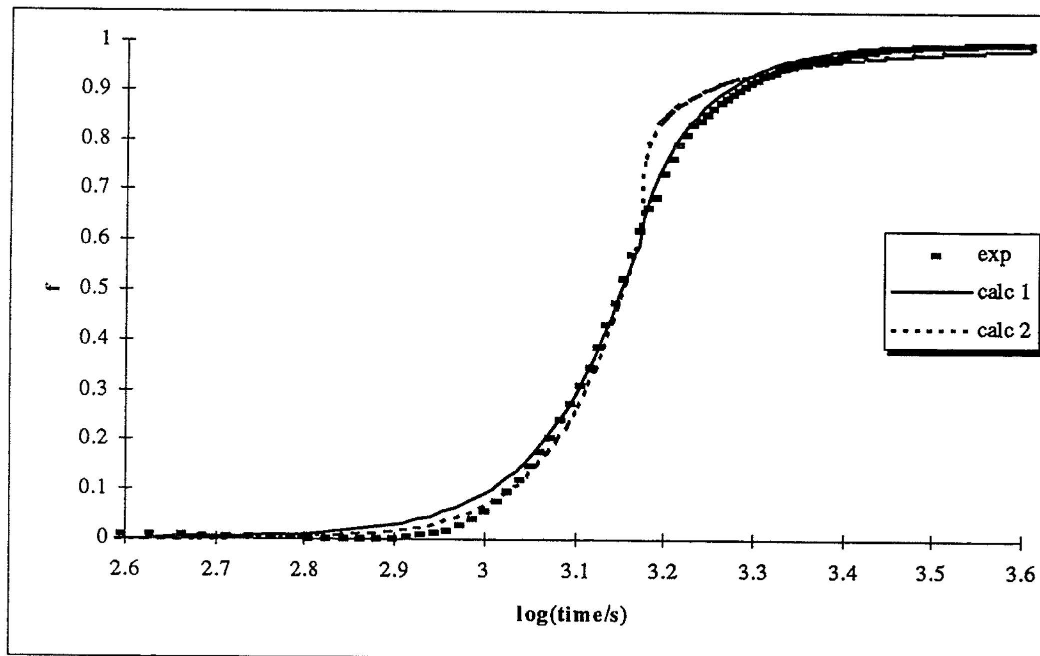

Figure 5.9 The results of fitting the fraction transformed f vs. log(time) curve of figure 5.7 for the experiment on $Fe_{55}Hf_{17}O_{28}$ at 275°C with the combined non-isothermal and isothermal JMA equation (2.35). Two different fitting results are displayed:

- calculation 1: Q_g = 63.9 kJ/mole; m = 0.77; $\tau_0 = 1.90 \cdot 10^{-4}$ s and
- calculation 2: Q_g = 158 kJ/mole; m = 0.38 (taking $\tau_0 = 10^{-13}$ s).

5.2.2 Interpretation of the fraction transformed curves in terms of the JMA equation

In a first attempt to interpret the fraction transformed vs. time curves of figure 5.7, the experimental results are compared with equation (2.26), describing crystallisation proceeding by the mechanism of nucleation and growth. Because the as deposited films already contain a significant amount of crystallised α-Fe, it is assumed that the predominant process is *growth* of α-Fe (i.e. *nucleation* is ignored). In that case equation (2.26) reduces to the well known JMA equation (2.27), as shown in section 2.4.3. The important parameters in this equation are:

1. the activation energy Q_x [J/mole] for the whole crystallisation process,
2. the Avrami parameter m and
3. the pre-exponential time constant τ_0 [s].

When no nucleation is taken into account, Q_x reduces to the activation energy for growth Q_g [J/mole] and the Avrami parameter reduces to bp (b = dimension of crystallites; p = rate determining step factor).
Equation (2.27) can only be used if isothermal conditions are fulfilled. As already mentioned in chapter 4, significant resistivity changes take place during the heating stage. Therefore a non-isothermal part with a constant heating rate is added, as described by equation (2.35). Additional parameters in this expression are the temperature at the beginning of the experiment T_0 [K], the heating rate ϕ [K/s] and the time t_1 [s] necessary to reach the isothermal annealing stage. These parameters can be obtained easily from the measured temperature profile. In figure 5.8 an example of a temperature profile for the film is heated to T_1 = 275°C is given. The heating rate is determined to be 10.5 K/min and the temperature T_0 is found to be 16.1°C, while t_1 is 1485 seconds.
These values are substituted in equation (2.35) and the calculated fraction transformed is compared to the experimental fraction transformed as a function of time. The remaining three parameters (Q_g, m and τ_0) are varied to obtain the best least squares fit. The results of this fitting procedure for the three measurements at 225, 275 and 300°C are given in table 5.4. In the last column of the table the sum of the least squares, divided by the number of fitting points minus the degrees of freedom in the fitting procedure is given as well. This quantity, denoted as χ^2, is a measure for the agreement between the fit and the experiment (and should be small). The fraction transformed curve for the resistivity experiment at 275°C, calculated using the best fit values from this table, is shown in figure 5.9.

Table 5.4 Fitting procedure for the JMA equation (2.35), including a heating stage, with respect to the experimental fraction transformed vs. log(time) curves of figure 5.7. The parameters Q_g, m and τ_0 are determined by means of a least squares fitting procedure; χ^2 is given as well.

T_1 (°C)	Q_g (kJ/mole)	m	τ_0 (s)	χ^2 (10^{-5})
225	43.1	0.70	$1.15 \cdot 10^{-2}$	3.5
275	63.9	0.77	$1.90 \cdot 10^{-4}$	7.2
300	43.1	1.0	$2.82 \cdot 10^{-2}$	4.1

The agreement between experiment and theory is very good. However, the obtained values are not very realistic, especially the time constant. These values should be of the order of the

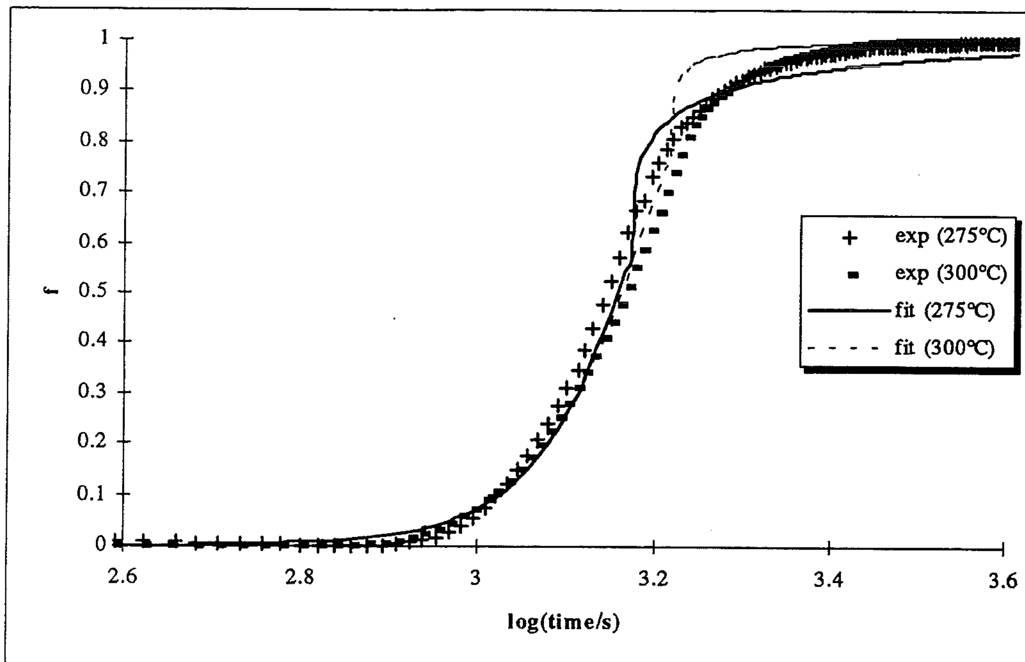

Figure 5.10 The results of fitting the fractions transformed f vs. log(time) curves of figure 5.7 for the experiments on $Fe_{55}Hf_{17}O_{28}$ at 275°C and 300°C simultaneously with the combined non-isothermal and isothermal JMA equation (2.35). The fitting results are also displayed, using: Q_g = 159 kJ/mole and m = 0.36 (taking $\tau_0 = 10^{-13}$ s).

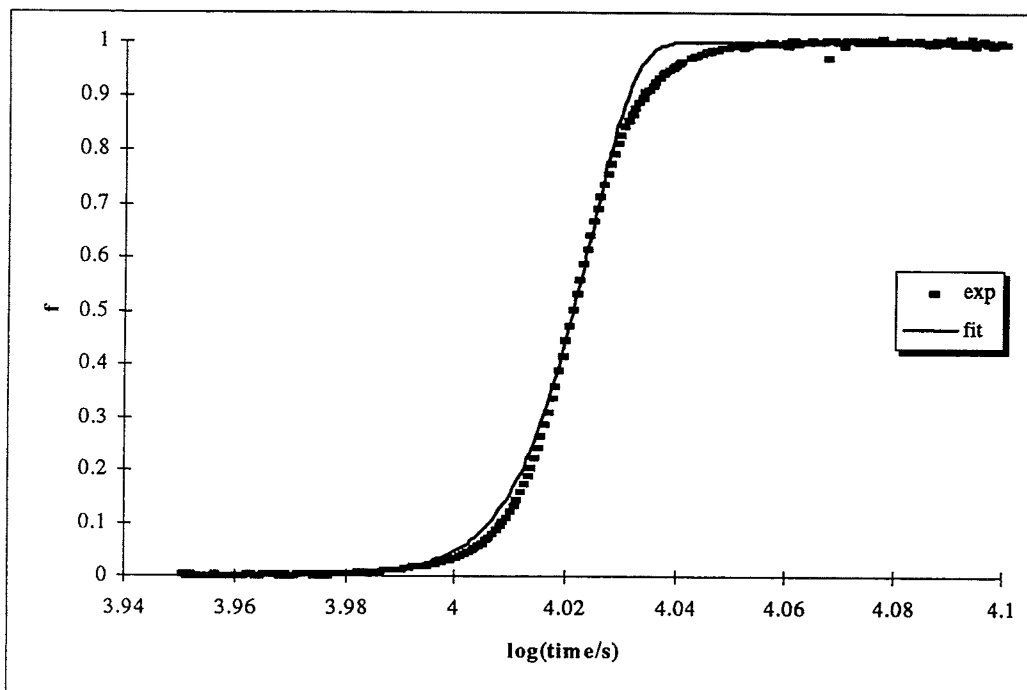

Figure 5.11 The results of fitting the fraction transformed f vs. log(time) curve of figure 5.6 for the isochronal experiment on $Fe_{77}Nb_{10}Si_2N_{11}$ with the non-isothermal JMA equation (2.33). The fitting result is also displayed, using: Q_g = 194 kJ/mole, m = 2.9 and $\tau_0 = 9.0 \cdot 10^{-14}$ s.

Debye frequency ($\approx 1/10^{13}$ Hz), but the obtained values are all about 10 orders of magnitude too large. Therefore a second calculation is performed, in which the time constant τ_0 is chosen to be 10^{-13} s and only Q_g and m are varied. The results of this calculation are given in table 5.5; the result at 275°C is shown in figure 5.9.

Table 5.5 Fitting procedure for the modified JMA equation (2.35), including a heating stage, with respect to the experimental fraction transformed vs. log(time) curves of figure 5.7. The parameters Q_g and m are determined by means of a least squares fitting procedure, while τ_0 is taken to be 10^{-13} s; χ^2 is given as well.

T_1 (°C)	Q_g (kJ/mole)	m	χ^2 (10^{-4})
225	145	0.37	9.4
275	158	0.38	3.5
300	161	0.31	2.4

The agreement between theory and experiment is not so good as in the former calculation, especially at the point where the isothermal stage begins.
The obtained parameters seem to depend less on the annealing temperature than those presented in table 5.4. Therefore both the fraction transformed curves at 275 and 300°C are fitted with respect to the *same* Q_g, and m (again choosing $\tau_0 = 10^{-13}$ s). The measurement at 225°C is omitted, because it could not be translated into a volume fraction very well.
The results are shown in figure 5.10; the obtained values are:

- activation energy for growth: Q_g = 159 kJ/mole and
- Avrami parameter: m = 0.36,

while $\chi^2 = 4.7 \cdot 10^{-4}$. Again the calculated isothermal parts differ significantly from the experimental values.

For comparison the result of the isochronal resistivity measurement on $Fe_{77}Nb_{10}Si_2N_{11}$, displayed in figure 5.6, is interpreted in terms of the JMA equation (2.33). The fitting procedure is performed with respect to Q_g, m and τ_0. The result of this calculation is shown in figure 5.11 using the obtained values:

- activation energy for growth: Q_g = 194 kJ/mole,
- Avrami parameter: m = 2.9 and
- time constant: $\tau_0 = 9.0 \cdot 10^{-14}$ s

giving $\chi^2 = 2.8 \cdot 10^{-4}$. Good agreement between theory and experiment is observed. The Avrami parameter m = 2.9, is often found in crystallisation processes of metallic glasses and can be understood by assuming interface controlled growth (p = 1) of three dimensional (b = 3) iron crystals.
Comparing the two different materials, it is seen that $Fe_{77}Nb_{10}Si_2N_{11}$ has a higher activation energy for crystallisation. This might explain the amorphous as deposited structure, whereas FeHfO already shows crystallisation during deposition. Both values of the activation energies for crystallisation are relatively small. Therefore it seems a good approximation that only the growth process was considered, because the activation energies including a nucleation stage usually are much larger than activation energies for growth only.
All in all, not very satisfactory, since in addition to the poor fits the value of the Avrami parameter in $Fe_{55}Hf_{17}O_{28}$ m = 0.36 cannot be obtained by assuming realistic values for p and b.

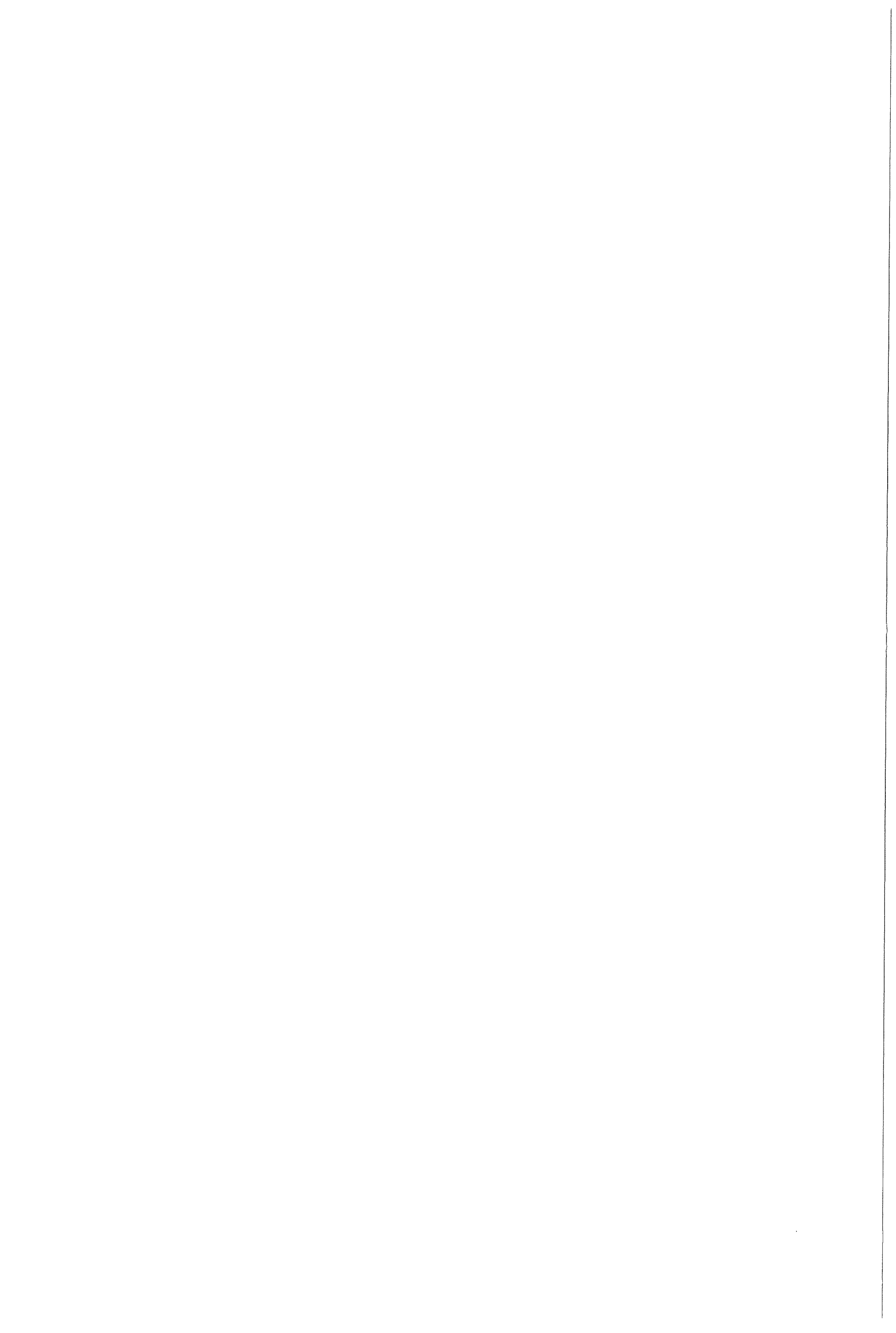

Therefore another approach is used to interpreted the fraction transformed vs. time curves in the next section.

5.2.3 Interpretation of the fraction transformed curves in terms of activation energy spectra

In this section an alternative interpretation of the fraction transformed vs. time curves of figure 5.7 is presented: a first-order transition process is assumed and an activation energy spectrum (AES) is inserted. Then the expectation of the fraction transformed $E\{f(t;\underline{Q})\}$ can be calculated (see section 2.4.4). The numerical procedure to calculate $E\{f(t;\underline{Q})\}$ does not depend on the specific choice of the AES; therefore this will be discussed first. Subsequently the numerical procedure is applied, using a uniform and a normal distribution of activation energies.

Consider the activation energy spectrum g(Q), which is defined between Q_{min} and Q_{max}. Apart from it shape, an AES is characterised by two parameters: the average Q_0 and standard deviation σ_Q. Both parameters can be expressed in terms of Q_{min} and Q_{max} for each specific distribution.

For the calculation, the entire Q interval is divided in n+1 smaller intervals of width:

$$h = \frac{Q_{max} - Q_{min}}{n+1}. \tag{5.5}$$

For interval i the activation energy is given by $Q_i = Q_{min} + (i+½)h$ ($i = 0, 1, 2, \ldots, n$). The expectation of the volume fraction, see equation (2.36^c), can be approximated by:

$$E\{f(t;\underline{Q})\} = h\sum_{i=0}^{i=n} f(t;Q_i)g(Q_i), \tag{5.6}$$

where the function $f(t,Q_i)$ is given by equation (2.35) with m = 1. This summation is performed at every time t of interest. In the calculation of Q_0, σ_Q and τ_0 are the degrees of freedom for adjusting the expression to the measured fractions transformed.

The number of intervals must be sufficiently large to obtain accurate fractions transformed. For n > 100, $E\{f(t,\underline{Q})\}$ does not change with a further increase of n. Therefore n = 100 is used in the following calculations.

Uniform distribution

In first approximation a uniform activation energy spectrum $g_1(Q)$ is used (see section 3.4.4). If all three parameters Q_0, σ_Q and τ_0 may be varied freely, unrealistically large time constants τ_0 are obtained. Therefore, its value is fixed at 10^{-13} s, like in the previous section. Now the experimental fraction transformed vs. log(time) curves are least squares fitted, using the equations (5.6), (2.37) and (2.35). The obtained values for Q_0 and σ_Q are given in table 5.6. In figure 5.12 both fitting and experimental results are compared for the measurement at 275°C.

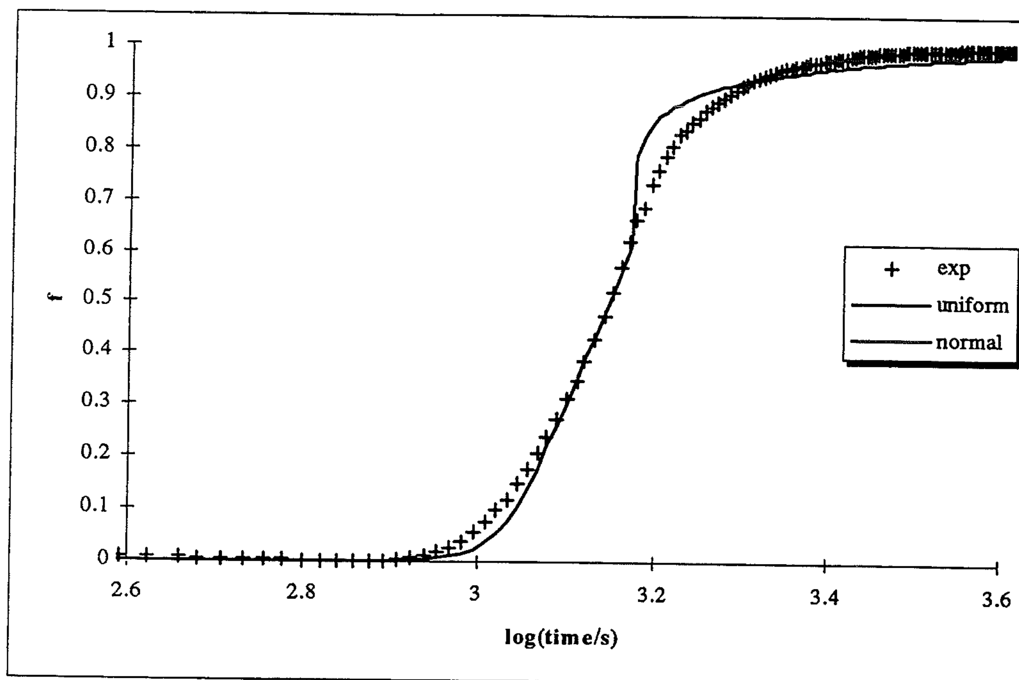

Figure 5.12 The results of fitting the fraction transformed f vs. log(time) curve of figure 5.7 for the experiment on $Fe_{55}Hf_{17}O_{28}$ at 275°C with the AES equation (5.7), assuming a uniform and a normal activation energy spectrum. The fitting results are:

- *uniform* activation enery spectrum: Q_0 = 155 kJ/mole; σ_Q = 10.7 kJ/mole and
- *normal* activation enery spectrum: Q_0 = 155 kJ/mole and σ_Q = 11.2 kJ/mole.

The time constant τ_0 is taken to be 10^{-13} s.

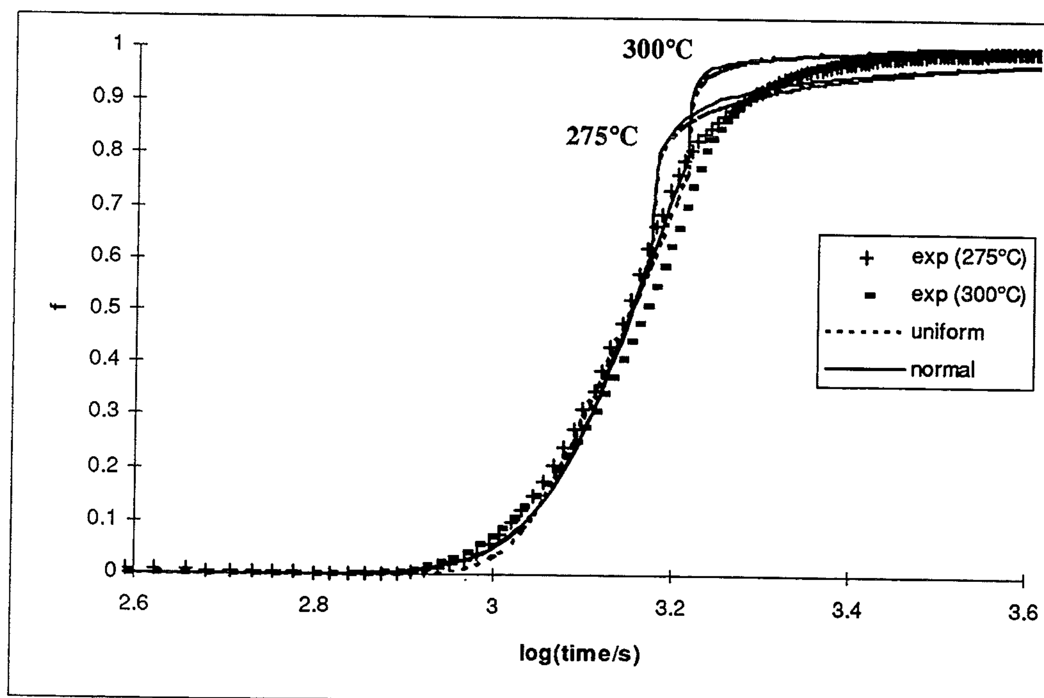

Figure 5.13 The results of fitting the fractions transformed f vs. log(time) curves of figure 5.7 for the experiments on $Fe_{55}Hf_{17}O_{28}$ at 275°C and 300°C simultaneously with theAES equation (5.7), assuming a uniform and a normal activation energy spectrum. The fitting results are:

- *uniform* activation enery spectrum: Q_0 = 156 kJ/mole; σ_Q = 11.4 kJ/mole and
- *normal* activation enery spectrum: Q_0 = 156 kJ/mole and σ_Q = 12.1 kJ/mole.

The time constant τ_0 is taken to be 10^{-13} s.

Table 5.6 Fitting results for a *uniform* activation energy spectrum, with respect to the experimental fraction transformed vs. log(time) curves of figure 5.7. The parameters Q_0 and σ_Q are determined by means of a least squares fitting procedure, while τ_0 is taken to be 10^{-13} s; χ^2 is given as well.

T_1 (°C)	Q_0 (kJ/mole)	σ_Q (kJ/mole)	χ^2 (10^{-3})
225	142	10	1.3
275	155	11	3.9
300	157	14	2.5

Finally the measurements at 275°C and 300°C are fitted simultaneously. The least squares fitting results are (see figure 5.13):

- average of the uniform AES: Q_0 = 156 kJ/mole and
- standard deviation of the uniform AES: σ_Q = 11 kJ/mole

resulting in $\chi^2 = 5.2 \cdot 10^{-4}$.

Normal distribution

Secondly, a normal activation energy spectrum $g_2(Q)$ that extends from $Q_0 - 3\sigma_Q$ to $Q_0 + 3\sigma_Q$ is used (see section 3.4.4). On similar grounds as discussed before, τ_0 is fixed at 10^{-13} s. Again the experimental fraction transformed vs. log(time) curves are least squares fitted, using the equations (5.6), (2.38) and (2.35). The obtained Q_0 and σ_Q are given in table 5.7. In figure 5.12 the fitting and experimental results are shown for the measurement at 275°C.

Table 5.7 Fitting results for a *normal* activation energy spectrum, with respect to the experimental fraction transformed vs. log(time) curves of figure 5.7. The parameters Q_0 and σ_Q are determined by means of a least squares fitting procedure, while τ_0 is taken to be 10^{-13} s; χ^2 is given as well.

T_1 (°C)	Q_0 (kJ/mole)	σ_Q (kJ/mole)	χ^2 (10^{-3})
225	143	11	1.5
275	155	11	5.3
300	157	14	3.8

Simultaneously fitting the measurements at 275°C and 300°C gives (see figure 5.13):

- average of the normal AES: Q_0 = 156 kJ/mole and
- standard deviation of the normal AES: σ_Q = 12 kJ/mole.

resulting in $\chi^2 = 6.3 \cdot 10^{-4}$.

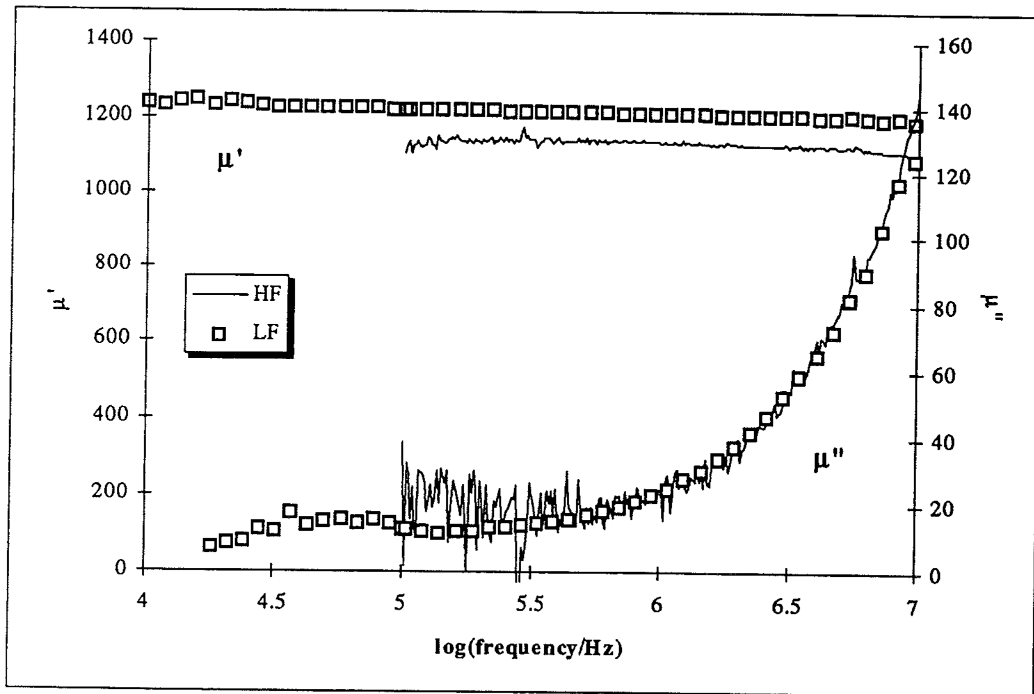

Figure 5.14 Frequency dependence of the complex permeability of a 10.9 μm $Fe_{55}Hf_{17}O_{28}$ film deposited on GGG after rapid thermal processing for 5 seconds at 400°C, measured with the LF and the HF set-up.

Comparing all fitting results presented in the sections 5.2.2 and 5.2.3 for the realistic situation ($\tau_0 = 10^{-13}$ s), it can be seen that:

1. The activation energy for growth using an Avrami exponent and the average activation energy using an AES are approximately the same. However, because of the extremely small Avrami exponents a description with an AES might be more plausible.
2. The description with a normal AES is not significantly better that the description with a uniform AES. Also approximately the same standard deviations are found.
3. The fitted fractions transformed differ from the experimental values from the moment that the isothermal stage is reached. This discrepancy may be caused by the choice of the pre-exponential factor τ_0. It appears that the calculated fractions transformed depend heavily on this parameter. Therefore a small increase in τ_0 may cause better agreement.
4. It can be seen that the non isothermal parts agree reasonably well. Therefore another explanation for the discrepancy in the isothermal part might be that the combined non-isothermal (constant heating rate) and isothermal equation (2.35) does not supply an appropriate description for the isothermal part.

5.3 Comparing the measured and calculated high frequency permeability

In section 4.4 the experimentally determined frequency dependence of a number of 10.9 μm $Fe_{55}Hf_{17}O_{28}$ films deposited onto various commercial substrates were presented. All these films were annealed under the optimal conditions found in section 4.1: rapid thermal processing for 5 seconds at 400°C.
In this section the experimental complex permeability as a function of frequency will be compared to the theoretical expressions mentioned in appendix A. In the next section the parameters in the different models and the fitting procedure are discussed. Subsequently an example of this procedure is shown and all results are given.

5.3.1 Model parameters

The theoretical model that describes the frequency dependence of the complex permeability can be separated in three parts, each based on one of the three assumptions:

1. only eddy current loss,
2. only ferromagnetic resonance loss and
3. both eddy current and ferromagnetic resonance loss.

The experimental parameters used in the model for the first situation are the resistivity ρ, the film thickness d and the intrinsic permeability μ_i of the thin film material. The intrinsic permeability is estimated for this situation by the rotational permeability, as given by equation (2.18). Additional model parameters are therefore the saturation magnetisation M_s and the uniaxial anisotropy constant K_u. When only ferromagnetic resonance loss is assumed, again the saturation magnetisation and the uniaxial anisotropy constant are needed. Besides these parameters, the damping constant α and, strictly speaking, the gyromagnetic factor γ need to be known. Fortunately, γ can be taken to be 176 GHz/T, as discussed in appendix A.2. Common values for the damping constant are $0.03 < \alpha < 0.07$ [21]. In the third case, all parameters mentioned above are involved.
Both the thickness and the resistivity can be measured directly. The saturation magnetisation follows from the hard axis BH-loop. The uniaxial anisotropy constant, however, can only be obtained from a BH-loop with a large inaccuracy. Therefore, K_u and α are the degrees of

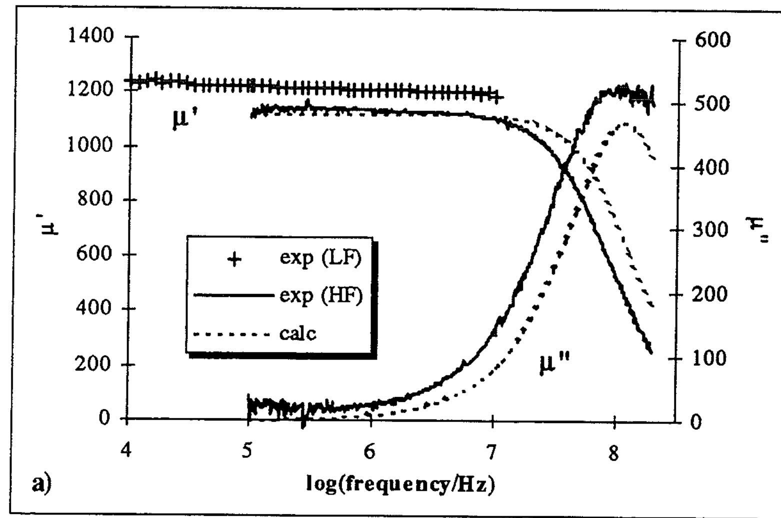

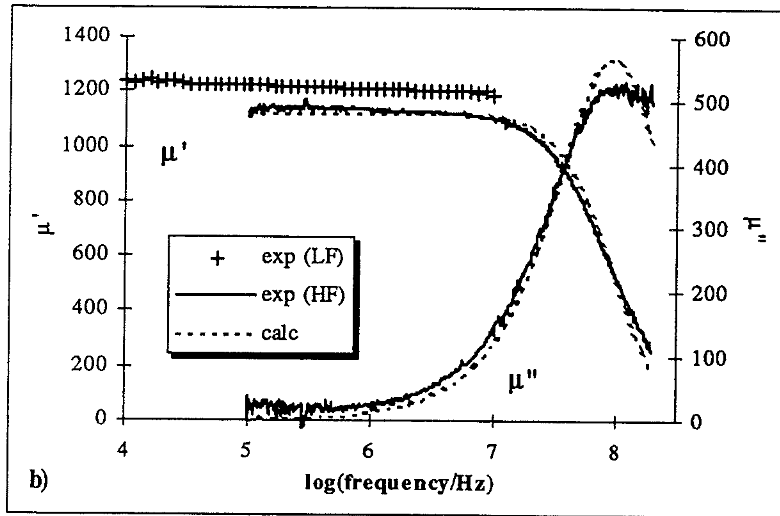

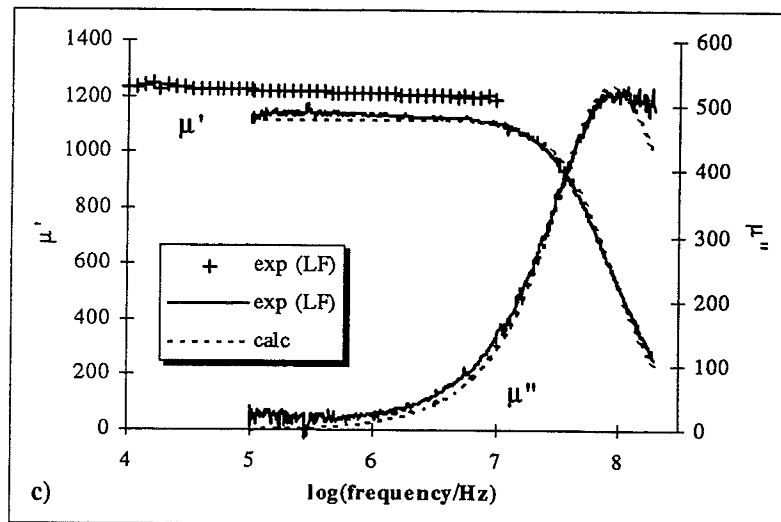

Figure 5.15 Calculated and experimental frequency dependence of the complex permeability of a 10.9 μm thick $Fe_{55}Hf_{17}O_{28}$ film deposited on GGG (RTP: 5 seconds at 400°C; γ = 176 GHz/T, B_s = 1.03 T and ρ = 1.2 mΩcm), assuming:
a) only eddy current loss (K_u = 377 J/m^3),
b) only ferromagnetic resonance loss (α = 0.280 and K_u = 377 J/m^3) and
c) both eddy current and resonance loss (α = 0.101 and K_u = 377 J/m^3).
The parameters α and K_u are obtained by least squares fitting the equations (A.10), (A.19) and (A.30) to the *real and imaginary* part (procedure A) of the complex permeability, measured with the HF set-up.

freedom in the fitting procedure for the experimental frequency spectra of the permeability. The obtained K_u should be of the same order of the anisotropy constant obtained from the BH-loop, while α should be in the range $0.03 < \alpha < 0.07$.

A problem is the significant difference in the results obtained with the experimental LF and HF set-ups (see figure 4.26). There seems to be a systematic instrumental error, because the LF permeability is always larger than the HF permeability. Part of this discrepancy may be caused by the difference in coil set-up [64,65]. Another cause might be in the empty measurement correction procedure, as described in section 3.6.1.
The discrepancy in the imaginary part of the permeability, however, is much smaller than in the real part. This is illustrated in figure 5.14 for a film deposited on GGG. Therefore, two fitting procedures are performed in the next section:
A) both the real part μ' and the (negative of the) imaginary part μ'' of the complex permeability are fitted with respect to α and K_u and
B) only the (negative of the) imaginary part μ'' is fitted with respect to α and K_u.
Experimental permeabilities determined by means of the HF set-up are used.

5.3.2 Fitting results

In figure 5.15 and 5.16 an example of both fitting procedures (A and B) is given for the film deposited on GGG, with $B_s = 1.03$ T, $K_u = 3.2 \cdot 10^2$ J/m^3 (from the BH-loop) and $\rho = 1.2$ mΩcm (see table 4.3). The drawn (noisy) lines are experimental results (HF set-up); the plusses are experimental LF results and the dashed lines are calculations (using the "best fit" parameters).

A. Simultaneously fitting μ' and μ''

In figure 5.15 the results of fitting procedure A (both the real and imaginary part of the complex permeability) are given. In the upper plot only eddy current loss is assumed in the calculation. Therefore the only variable is K_u, which is determined to be 377 J/m^3 by a least squares fit. The middle plot is based on the model that only resonance loss occurs. The parameters used in this calculation are: $\alpha = 0.280$ and $K_u = 377$ J/m^3. The lower plot is drawn assuming the combination of both types of losses. The fit parameters are now determined to be: $\alpha = 0.101$ and $K_u = 377$ J/m^3. Note that all uniaxial anisotropies are equal to 377 J/m^3, which is not that surprising because all expressions contain the rotational permeability (which strongly determines μ', see figure 2.19). It is of the right order of magnitude, comparing with the value $3.2 \cdot 10^2$ J/m^3 from the BH-loop.
From this figure it follows that eddy current loss only cannot explain the frequency dependence of the complex permeability. Assuming resonance loss only gives much better results. The damping constant, however, is large compared to the reported values. Assuming both eddy current and resonance loss gives a smaller and therefore more probable value of the damping constant.

B. Fitting μ'' only

Figure 5.16 contains the results of fitting procedure B (only the imaginary part of the complex permeability). Again the fitting procedure is performed for the three different models. The "best fit" parameters are determined to be: $K_u = 313$ J/m^3 (eddy current loss only); $\alpha = 0.293$ and $K_u = 385$ J/m^3 (resonance loss only) and $\alpha = 0.0449$ and $K_u = 342$ J/m^3 (both eddy current and resonance loss).

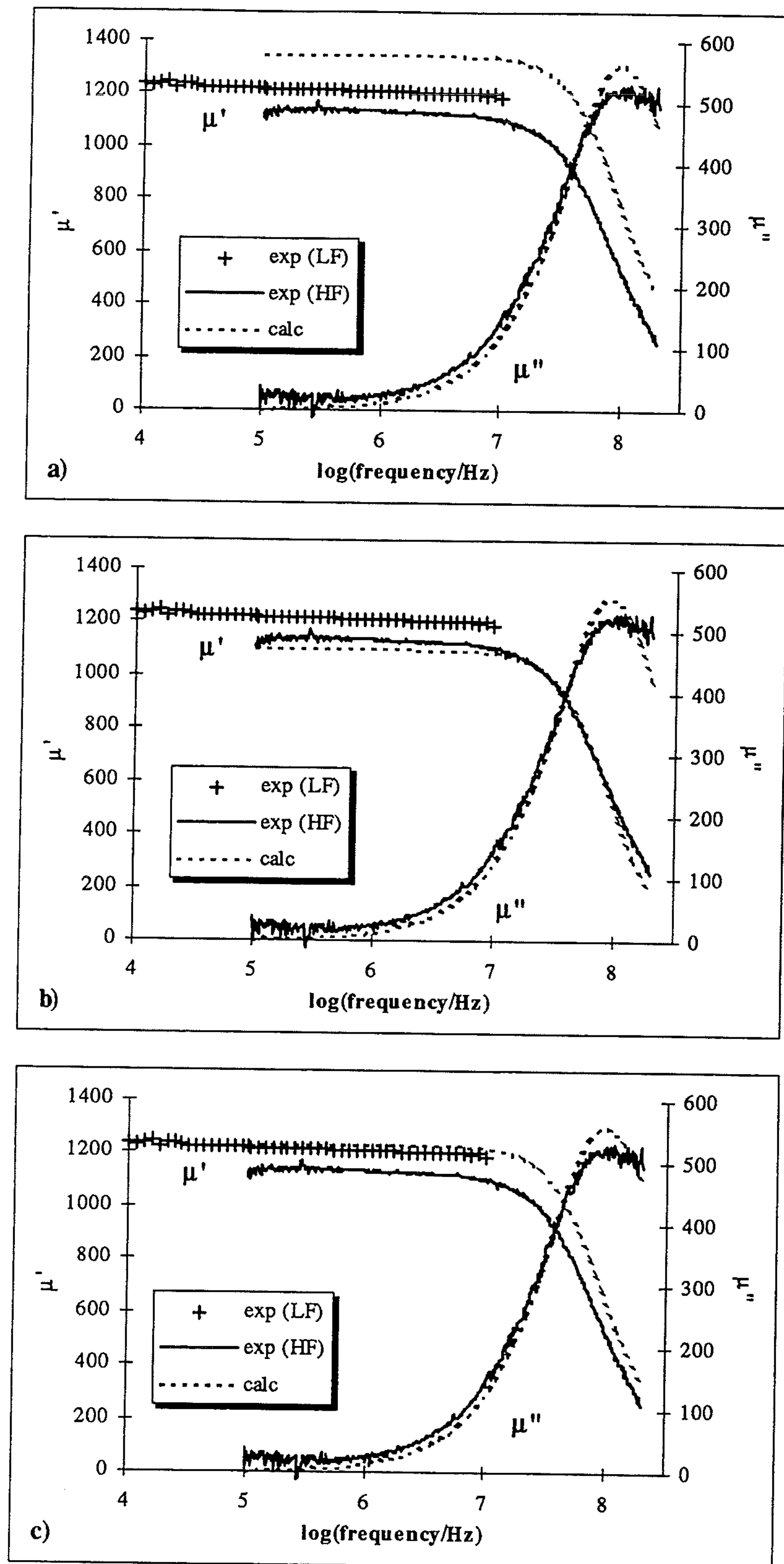

Figure 5.16 Calculated and experimental frequency dependence of the complex permeability of a 10.9 μm $Fe_{55}Hf_{17}O_{28}$ film deposited on GGG (RTP: 5 seconds at 400°C; γ = 176 GHz/T, B_s = 1.03 T and ρ = 1.2 mΩcm), assuming:
a) only eddy current loss (K_u = 313 J/m^3),
b) only ferromagnetic resonance loss (α = 0.293 and K_u = 385 J/m^3) and
c) both eddy current and resonance loss (α = 0.0449 and K_u = 342 J/m^3).
The parameters α and K_u are obtained by least squares fitting the equations (A.10), (A.19) and (A.30) to the *imaginary* part (procedure B) of the complex permeability, measured with the HF set-up.

Adjusting the calculated curves to the imaginary part of the complex permeability only, gives significant deviation between the measured and calculated real part of the permeability (as might be expected). However, in the case that only resonance loss is assumed the deviation is small. But again, the damping constant is unrealistically large. In the lower plot it can be seen that the calculated permeability assuming both eddy current and resonance loss coincides with the permeability measured with the LF set-up.
This may be explained by (re)considering the empty measurement in the HF set-up. In the empty measurement the impedance of the coil as a function of frequency is fitted by taking appropriate values for the inductance, resistance and capacitor (as described in section 3.6.3). However, the simulated impedance is not perfectly in agreement with the measured impedance. Therefore the obtained value for C may be incorrect, giving wrong permeabilities according to equation (3.19). It should be noted that the effect of C on both real and imaginary part of the permeability is different. Therefore, it is possible that the imaginary part of the permeability is (approximately) right, whereas the real part differs significantly. It is believed that the low frequency permeability measurement is the good permeability, because at low frequencies the capacitative behaviour is of minor importance.

Summarising, it was seen that the occurrence of resonance loss only is not realistic. Also eddy currents loss alone could not explain the frequency dependence of the permeability. The combined description gave the best results and will be used from this point on. The two fitting procedures A and B are used. The results of these fitting procedures are given in tables 5.8 and 5.9 for films deposited on several substrates. The values of the model parameters M_s and ρ used in the fitting procedure as well as the experimental K_u are given in table 4.3. More details are given in appendix E.

Table 5.8 Results of the fitting procedure A for the experimental μ' and μ'' frequency dependence, measured on 10.9 μm thick $Fe_{55}Hf_{17}O_{28}$ films deposited onto various substrates after rapid thermal processing for 5 seconds at 400°C, with respect to α and K_u. Experimental data from table 4.3 were used.

substrate	α	K_u (J/m^3)
HCH	0.185	670
HCH/SiO_2	0.135	457
HTCS	0.105	392
HTCS/SiO_2	0.111	392
D263	0.0885	405
Si/SiO_2	0.107	410
GGG	0.101	377

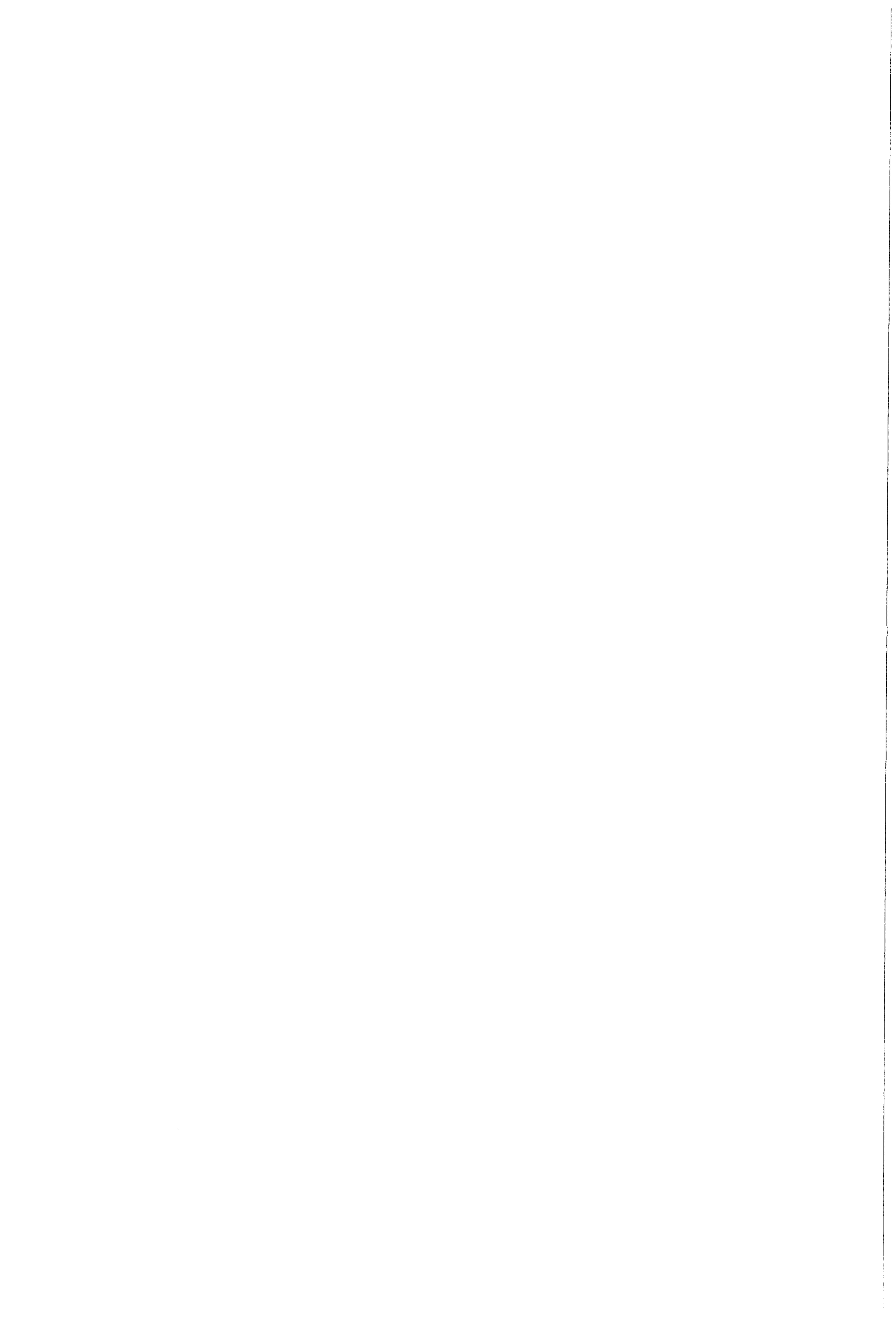

Table 5.9 Results of the fitting procedure B for the experimental μ″ frequency dependence, measured on 10.9 μm thick $Fe_{55}Hf_{17}O_{28}$ films deposited onto various substrates after rapid thermal processing for 5 seconds at 400°C, with respect to α and K_u. Experimental data from table 4.3 were used.

substrate	α	K_u (J/m^3)
HCH	0.0646	554
HCH/SiO_2	0.0554	404
HTCS	0.0488	357
$HTCS/SiO_2$	0.0586	360
D263	0.0537	382
Si/SiO_2	0.0745	389
GGG	0.0449	342

Consider the results obtained by fitting the experimental μ′ and μ″ simultaneously (fitting procedure A). From table 5.8 it can be seen that the values obtained for the damping constant are rather large. Also the uniaxial anisotropy constant is significantly larger than that obtained from the BH-loops (comparing the experimental values in table 4.3).
The second fitting procedure (B, only μ″) gives smaller values for both the damping constant and the uniaxial anisotropy constant. This results in larger calculated values for μ′, closer to the experimental values obtained with the LF set-up.

It is concluded that the frequency dependence of the complex permeability cannot be explained by assuming eddy current loss only. The combination of eddy currents and ferromagnetic resonance, however, gives a much better agreement. For a model in which the structural parameters (like the α-Fe grain size) are not (directly) taken into account, the agreement between theory and experiment is surprisingly good. However, further investigations are necessary to find the cause of the difference between experimental results obtained with the HF and LF set-up.

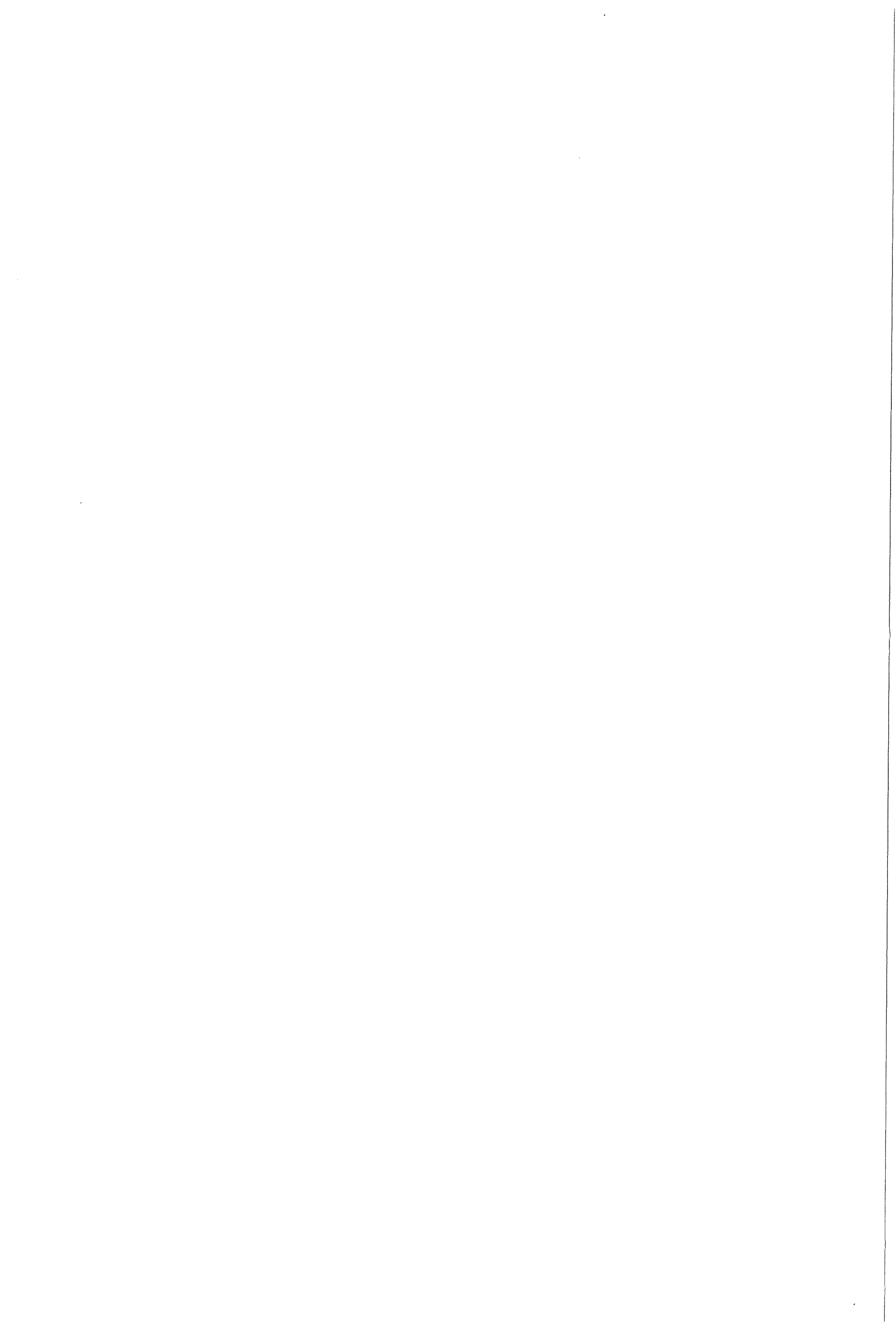

6. Conclusions and recommendations

6.1 Conclusions

$Fe_{55}Hf_{17}O_{28}$ films made by RF reactive sputter deposition in a mixture of Ar and O_2 show good soft magnetic properties ($\mu_r > 1000$ at 10 MHz, $H_c < 50$ A/m) and a saturation magnetic induction of 1.1 T in combination with a high resistivity of 1-2 mΩcm after annealing them for 5 seconds in a constant magnetic field, using rapid thermal processing. However, the saturation magnetostriction coefficient is large; values of +5 10^{-6} are not uncommon.

The structure of the $Fe_{55}Hf_{17}O_{28}$ films after deposition consists of body centred cubic iron nanocrystals (that most probably contain some dissolved atoms), randomly dispersed in an amorphous matrix. It is believed that the matrix contains most of the oxygen and hafnium and it is kept responsible for the high resistivity.
Upon annealing several atomic ordering processes occur:

1. The b.c.c. iron nanocrystals grow, the fraction crystalline iron increases and transfer of dissolved atoms from the iron to the surrounding matrix is observed.
2. Crystallisation of hafnium oxide in two crystal structures is found: face centred cubic and monoclinic hafnium oxide. Low temperature annealing (below 700°C) induces crystallisation of f.c.c. HfO_2, whereas mainly monoclinic HfO_2 is found at 900°C.
3. In some films face centred orthorhombic cementite is formed; presumably as a consequence of carbon contamination.

The crystallisation process of b.c.c. iron is monitored by means of resistance measurements. An attempt was made to interpret these measurements in terms of the JMA equation that describes the combination of isochronal and isothermal crystallisation. Assuming a time constant $\tau_0 = 10^{-13}$ s (as follows from the Debye frequency) an activation energy for growth of approximately 159 kJ/mole and an Avrami parameter of 0.36 are obtained. Because this Avrami exponent could not be understood assuming realistic values for the rate determining step of the process and the dimension of the crystallites, the measurements were interpreted in terms of a first order transition, using an activation energy spectra. Assuming either a uniform or a normal distribution gave approximately the same results: an average activation energy of 156 kJ/mole and a standard deviation of 12 kJ/mole. It should be noted that these parameters strongly depend on the choice of the time constant.
Significant deviations from the calculations are observed from the moment that the isothermal stage is reached. However, the isochronal part coincidences well with the experiment, as verified for $Fe_{77}Nb_{10}Si_2N_{11}$, because realistic Avrami parameters ($\tau_0 = 9.0\ 10^{-14}$ s, $Q_g = 194$ kJ/mole and $m = 2.9$) were found in an isochronal experiment.
It is concluded that the description might be an oversimplification of the atomic processes occurring. It is also possible that several atomic ordering processes take place at the same time.

The frequency dependence of the complex permeability can be explained by assuming a combination of eddy current loss and ferromagnetic resonance. The uniaxial anisotropy constant and the damping constant are the only degrees of freedom in this macroscopic model. The values of these parameters are only of the right order of magnitude if the fitting procedure is restricted to the imaginary part of the complex permeability. However, the complex

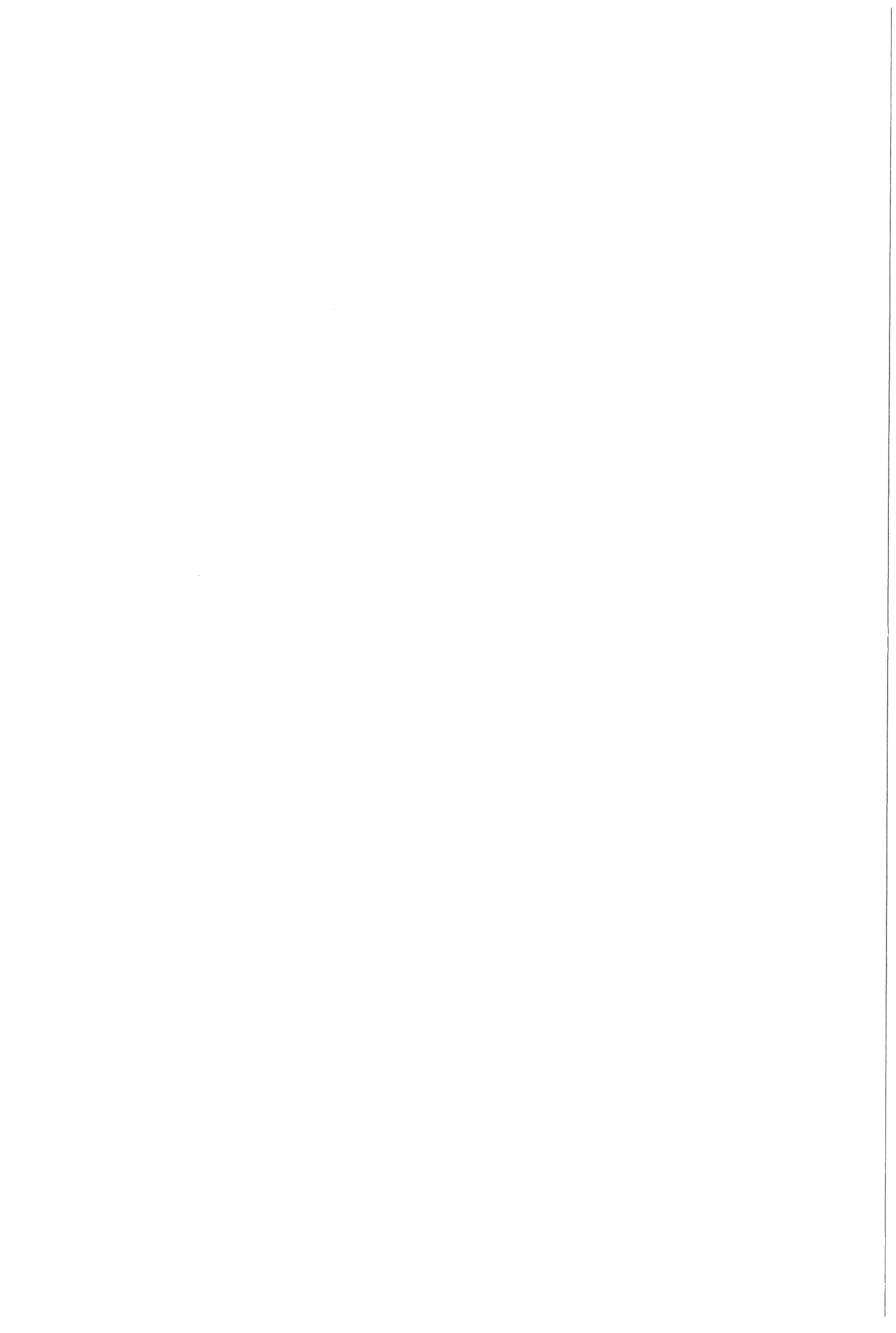

permeability calculated with these values coincides well with the permeability determined experimentally by the LF set-up.

6.2 Recommendations

During the research project several questions arose to which no answers could be obtained, because of the limited amount of time. Therefore, in this part some recommendations for continuing the investigations on soft magnetic FeHfO films with a high resistivity are given:

- It is possible that the optimum found in both oxygen content and annealing treatment is not the absolute optimum. It might be interesting to look at the properties of the films when they are annealed in a rotating magnetic field (RTP and CTP) or annealed twice with diffent directions of the magnetic field [78,79].
- It is important to realise that the magnetostriction coefficient is much too high for application in a magnetic recording head and, even after classical thermal processing. Therefore, it might be interesting to investigate the influence of Si additions, which are known to reduce the magnetostriction [80].
- Some questions remain about the experimental permeability set-ups. It seems that there is a fundamental difference between these two. It is worth while to (re)consider both set-ups.
- The HF set-up can be used to measure the complex permeability on films of the same composition (annealed under identical circumstances), but of different thicknesses. It is expected that ferromagnetic resonance dominates over eddy current loss in thin films, whereas eddy current loss dominates over resonance loss at larger thicknesses. In this way it can be verified whether the loss mechanism that is expected at intermediate film thicknesses (10 μm), is indeed a combination of eddy currents and ferromagnetic resonance.
- Finally, it might be interesting to look at the impedance of the films as a function of the frequency of the electrical signal (current/voltage). It was argued that the structure of the optimal films consists of randomly dispersed b.c.c. iron in an amorphous matrix (that contains most of the O an Hf). However, it might be possible that some oxides are formed at the interface between b.c.c. iron and the "oxide like" matrix, resulting in very thin oxide films around the iron nanocrystallites. By measuring the impedance as a function of frequency one is able to see capacitive behaviour (as already verified). It might even be possible to gain some information about the thickness of the oxide films and the distribution of the iron nanocrystallites.

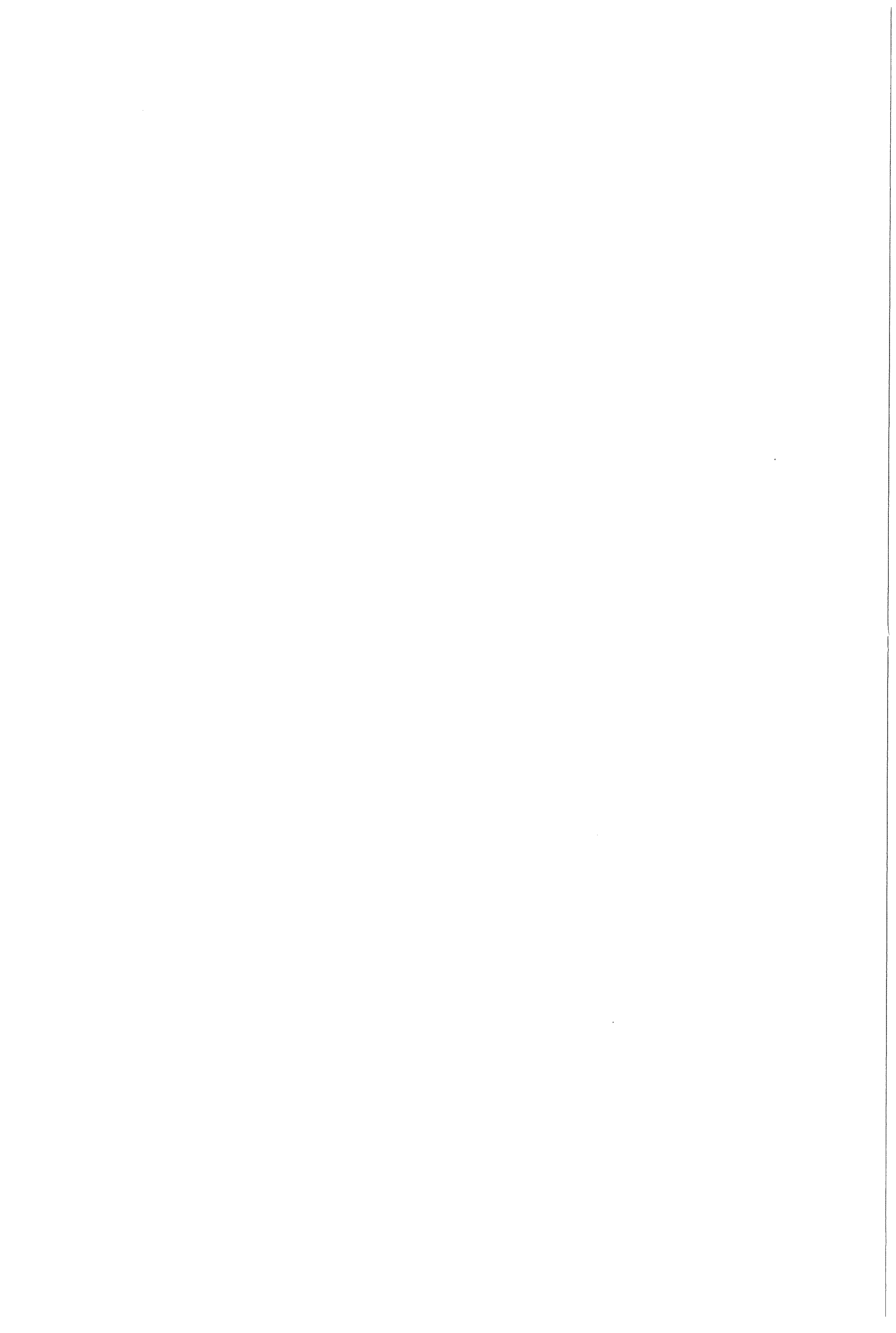

References

1. F. Roozeboom, J.J.M. Ruigrok, W. Klaassens, H. Kegel, M. Falter and H. Walk, Mat.Res.Soc.Symp.Proc. **429** (1996) in press

2. O. Kohmoto, IEEE Trans.Magn. **27** (1991) 3640

3. E. van de Riet, Nat.Lab. Report 6834 (1995)

4. A. Makino and Y. Hayakawa, Mat.Sci.Eng. **A181/A182** (1994) 1020

5. B.D. Cullity, "Introduction to magnetic materials", Addison-Wesley Publishing Co., Massachusetts (1972)

6. S. Chikazumi, "Physics of magnetism", Robert E. Krieger Publishing Co., Malabar (1964)

7. E.C. Stoner and E.P. Wohlfarth, Phil.Trans.Roy.Soc. **A-240** (1948) 599

8. J.M. Huijbregtse, "Magnetische anisotropie in zachtmagnetische materialen", literatuurscriptie TU Delft (1995)

9. G. Herzer, IEEE Trans.Magn. **26** (1990) 1397

10. G. Herzer, Mat.Sci.Eng. **A133** (1991) 1

11. H.J. de Wit, C.H.M. Witmer and F.W.A. Dirne, IEEE Trans.Magn. **23** (1987) 2123

12. H.J. de Wit, Rep.Prog.Phys. **69** (1992) 113

13. H.J. de Wit, C. Witmer, F. Dirne, K. Jager and P. Lasinski, Nat.Lab. Report 6135 (1986)

14. Y. Hayakawa and A. Makino, Nanostructured Materials **6** (1995) 989

15. A. Makino and Y. Hayakawa, J.Magn.Soc.Jap. **18** (1994) 411

16. Y. Hayakawa, K. Hirokawa and A. Makino, J.Magn.Soc.Jap. **18** (1994) 415

17. N. Hasegawa, M. Saito and A. Makino, J.Magn.Soc.Jap. **18** (1994) 750

18. S. Ohnuma and S. Mitani, J.Magn.Soc.Jap. **19** (1995) 19

19. H.J. de Wit and M. Brouha, J.Appl.Phys. **57** (1985) 3560

20. D. Craik, "Magnetism, principles and applications", John Wiley and Sons, Chichester (1996)

21. E. van de Riet, Nat.Lab. Technical Note 240 (1995)

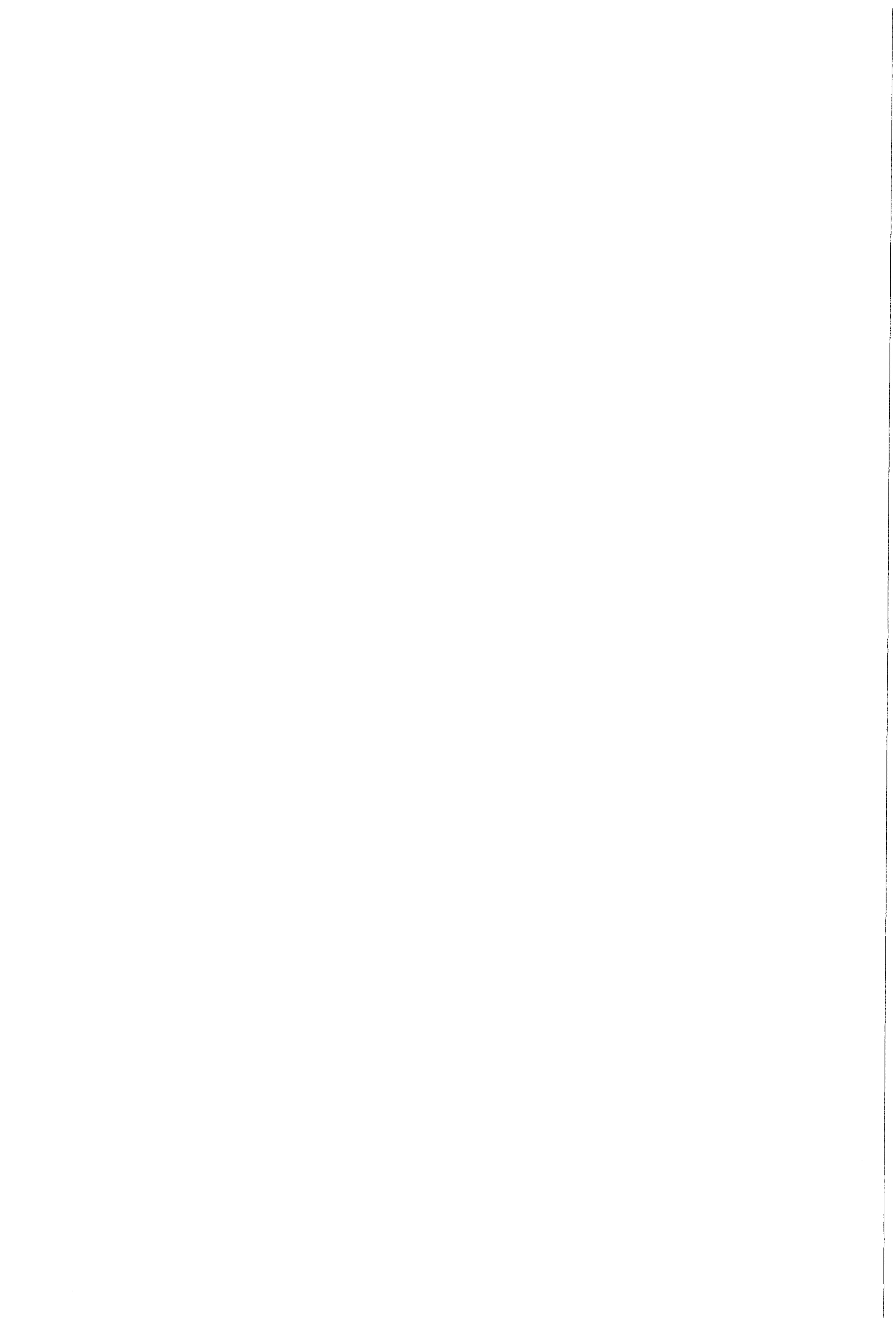

22. L. Landau and E. Lifshitz, Phys.Z.Sowjetunion **8** (1935) 153

23. D.A. Porter en K.E. Easterling, "Phase transformations in metals and alloys", Chapman and Hall, London, 1981

24. M.G. Scott, "Amorphous metallic alloys" ed. F.E. Luborsky, Butterworth, London, 1983

25. M. Avrami, J.Chem.Phys. **7** (1939) 1103

26. M. Avrami, J.Chem.Phys. **8** (1940) 212

27. M. Avrami, J.Chem.Phys. **9** (1941) 177

28. A.L.Greer, Acta Metall. **30** (1982) 171

29. W. Henderson, J.Non-Cryst.Sol. **30** (1979) 301

30. J.W. Christian, "The theory of transformations in metals and alloys", Pergamon, Oxford, (1965)

31. S. Ranganathan and M. Von Heimendahl, J.Mat.Sci. **16** (1981) 2401

32. M. Von Heimendahl and G. Kuglstatter, J.Mat.Sci. **16** (1981) 2405

33. H. Kissenger, Anal.Chem. **29** (1957) 1702

34. E.A. Marseglia, J.Non-Cryst.Sol. **41** (1980) 31

35. J. van Soest, "Elementaire Statistiek", Delftse Uitgevers Maatschappij, Delft (1992)

36. A.J. Meelen, J. van Soest and J.M.G. Vermeulen, "Aanvulling op Elementaire Statistiek", Delftse Uitgevers Maatschappij, Delft (1992)

37. K.Pekala, P. Jaskiewicz, D. Oleszak and R. Trykozko, Appl.Phys. **A55** (1992) 148

38. A. Mitra, V. Rao, S. Pramanik and O.N. Mohanty, J.Mat.Sci. **27** (1992) 5863

39. K.F. Kelton and F. Spaepen, Acta Metall. **33** (1985) 455

40. J.C. Maxwell, "A treatise on electricity and magnetism", Vol I, New York (1954)

41. R. Landauer, J.Appl.Phys. **23** (1952) 779

42. M. Heijting, J. Sietsma and A. van den Beukel, Scr.Metall. **23** (1989) 1401

43. V.K.S. Shante and S. Kirkpatrick, Adv.Phys. **20** (1971) 325

44. B. Chapman, "Glow Discharge Processes, sputtering and plasma etching", John Wiley & Sons, New York, 1980

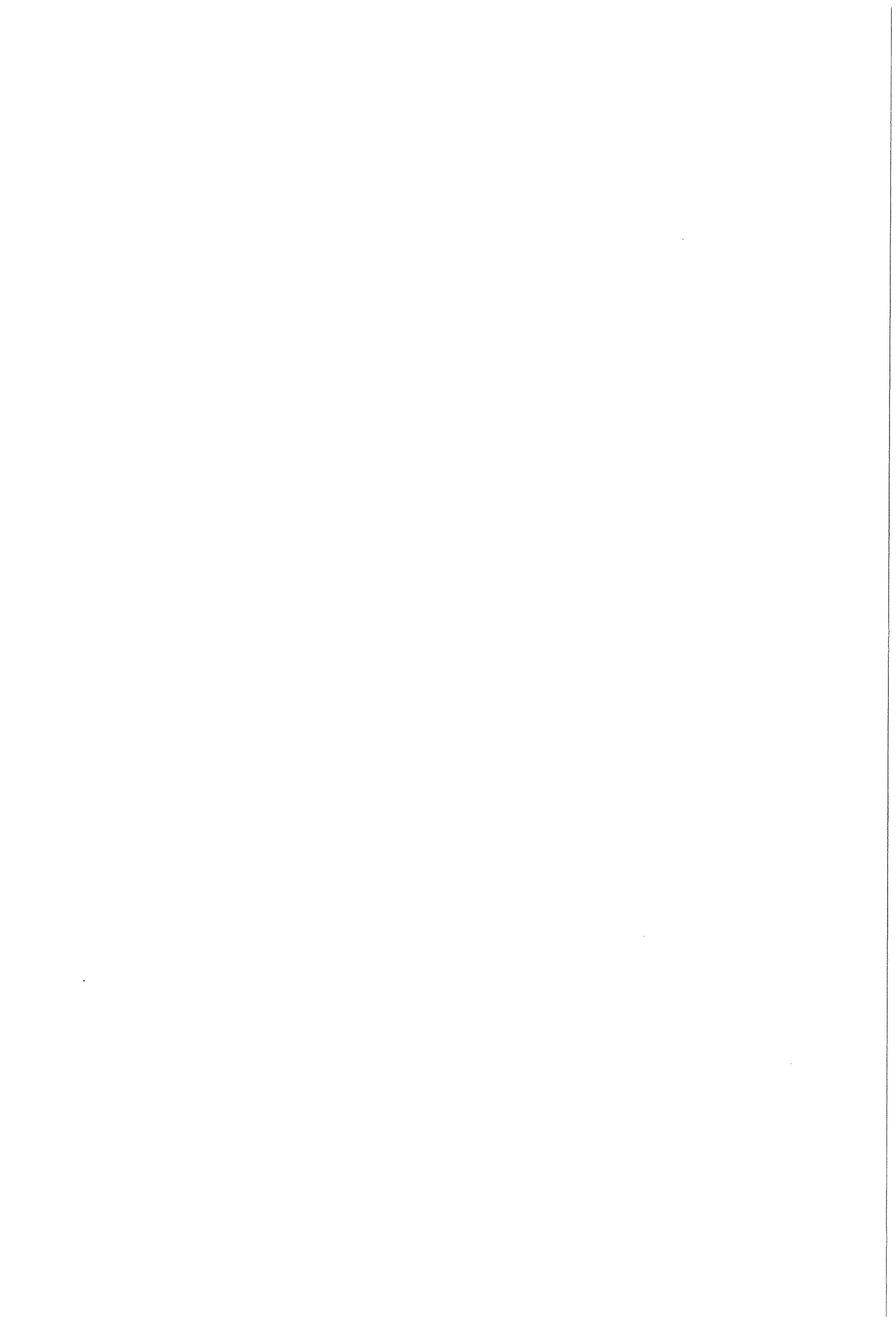

45. J.L. Vossen and J.J. Cuomo in "Thin film processes" ed. J.L. Vossen and W. Kern, Academic Press, Inc., Orlando, 1978

46. J.A. Thornton, J.Vac.Sci.Technol. **11** (1974) 686

47. J.B.A.D. van Zon, NEVAC-blad **33** 2 (1995) 43

48. G.S.A. Theusnissen, Nat.Lab. Technical Note 279/95

49. F. Roozeboom, Mat.Res.Soc.Symp.Prec. **224** (1991) 9

50. F. Roozeboom, Mat.Res.Soc.Symp.Prec. **303** (1993) 149

51. F. Roozeboom and F.W.A. Dirne, J.Appl.Phys. **77** (1995) 5293

52. F. Roozeboom, I. Gideonse, J.P.B. Duchateau, D.G. Neerink and H.T. Munsters, Mat.Res.Soc.Symp.Prec. **342** (1994)

53. F. Roozeboom in "Advances in Rapid Thermal and Integrated Processing" ed. F. Roozeboom, Kluwer Academic Publishers, Dordrecht, 1996

54. R. van Rooijen, H.C.F. Rozendaal, W. Smid and B.J. Thijsse, "Röntgendiffraktie 1", 3^e editie, collegedictaat TU Delft (1988)

55. W. van Hattum, E. Huizer, F. Mertens, H. Rijpkema, W. Smid and B. Thijsse, "Diffraktietechnieken 2", 2^e editie, collegedictaat TU Delft (1984)

56. B.D. Cullity, "Elements of X-ray diffraction", Addison-Wesley Publishing Co., Massachusetts (1967)

57. J.W.M. Jacobs and J.F.C.M Verhoeven, J.Microscopy **143** (1986) 103

58. A. Joshi, L.E. Davis and P.W. Palmberg in " Methods of surface analysis" ed. A.W. Czanderna, Elsevier Scientific Publ. Co., Amsterdam, 1975, Ch. 5

59. L.C. Feldman and J.W. Mayer, "Fundamentals of surface and thin film analysis", 1986, Ch. 11

60. L.E. Davis, N.C. MacDonald, P.W. Palmberg, G.E. Riach and R.E. Weber, "Handbook of electron spectroscopy", Physical Electronics Division, Eden Prairie, 1978.

61. L.B. Valdes, Proc. IRE **40** (1952) 1429

62. L.B. Valdes, Proc. IRE **42** (1954) 420

63. P.J. Severin, Philips Res.Repts **26** (1971) 279

64. J.P.C. Bernards, A.E.T. Kuiper, H.J. de Wit and E. van de Riet, IEEE Trans.Magn. **30** (1994) 4587

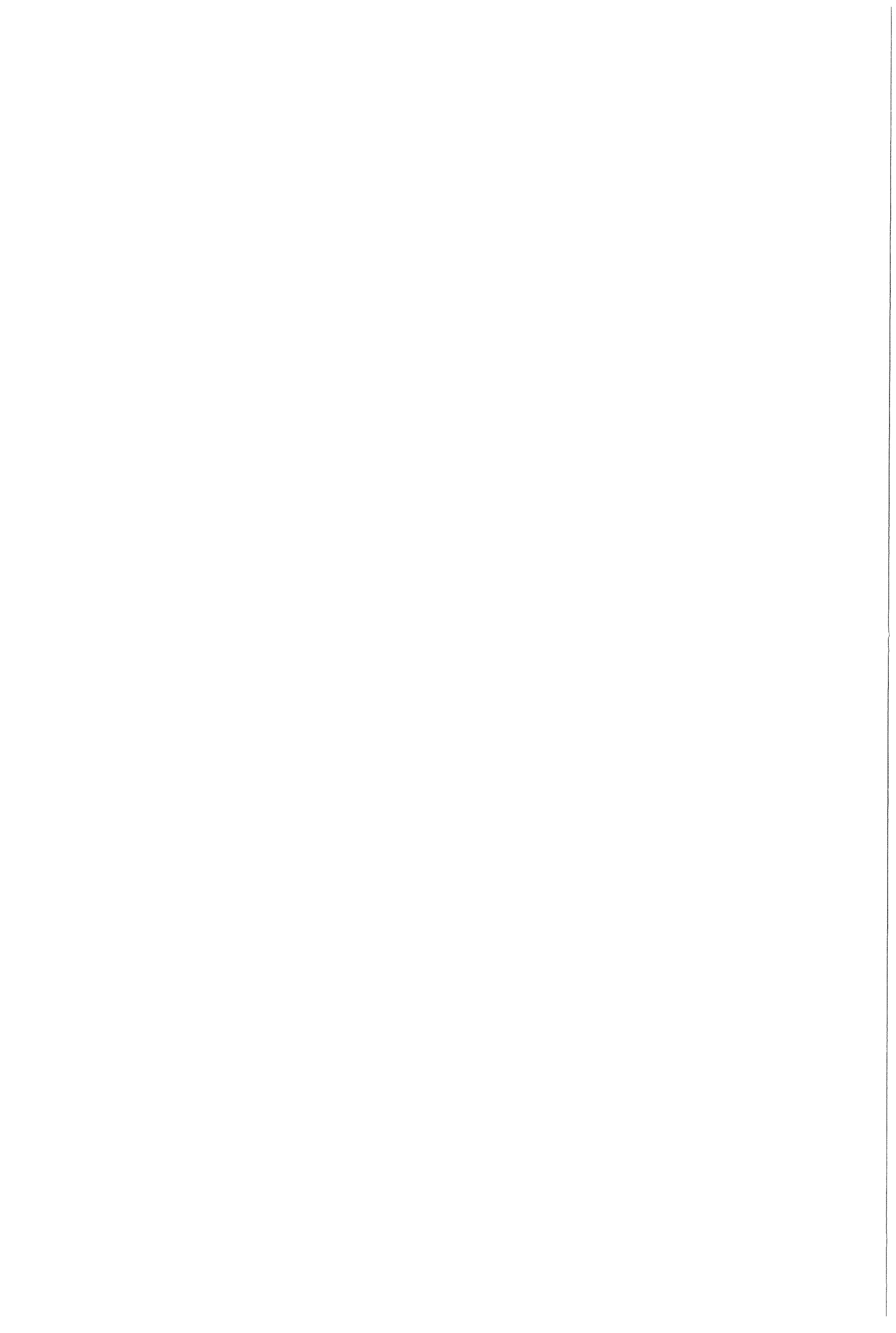

65. J.P.C. Bernards, A.E.T. Kuiper, H.J. de Wit and E. van de Riet, Nat.Lab. Technical Note 307/93

66. E. van de Riet, Nat.Lab. Technical Note 238/95

67. F. Roozeboom and N. Parekh, J.Vac.Sci.Technol. **B8** (1990) 1249

68. E. van de Riet and W. Klaassens, Nat.Lab. Technical Note 239 (1995)

69. E. Klokholm, IEEE Trans.Magn. MAG-**12** (1976) 819

70. M. Brouha, A.J.C. van der Borst and G.W. Turk, ICMFS-11 Conference, Asolimar, 1985, abstract AA-06

71. E. van de Riet, J.Appl.Phys. **76** (1994) 584

72. F.W.A. Dirne and C.J.M. Denissen, J.Magn.Magn.Mat. **78** (1989) 122

73. Powder Diffraction File reference card 6-969

74. Powder Diffraction File reference card 34-1

75. P. Villars and L.D. Cakvert, "Pearons's Handbook of crystallographic data for intermetallic phases, volume 3", ASM (1991), 3897

76. Powder Diffraction File reference card 34-104

77. H.B. van Veldhuizen, "Kristallisatie van amorf $Fe_{40}Ni_{40}B_{20}$", afstudeerverslag TU Delft, 1989

78. E. Van de Riet and W. Klaassens, Nat.Lab. Technical Note 239/95

79. E. Van de Riet, W. Klaassens and F. Roozeboom, J.Magn.Magn.Mat, to be published

80. A. Hosono and Y. Shimada, J.Appl.Phys. **67** (990) 6981

81. Buijze, "Inleiding elektriciteit", Delftse Uitgevers Maatschappij, Delft (1989)

82. J.J.M. Ruigrok, Thesis (1986)

83. D. Spenato, A. Fessanti, J.Gieraltowski, J. Loaec and H. le Gall, J.Phys.D: Appl.Phys. **26** (1993) 1736

84. I.S. Gradshteyn and I.M. Ryzhik, "Table of integrals series and products", Academic Press, London, 1965

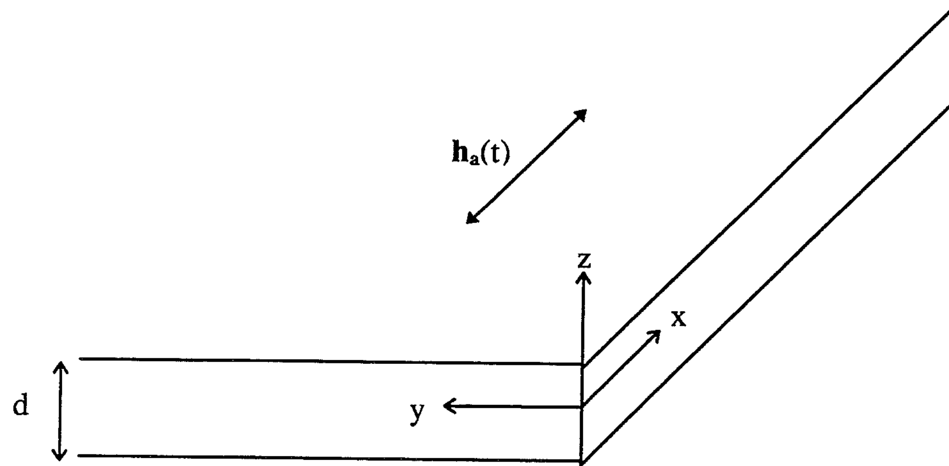

Figure A.1 The thin film is approximate by a semi infinite plate. An oscillating magnetic field is applied along the x-axis.

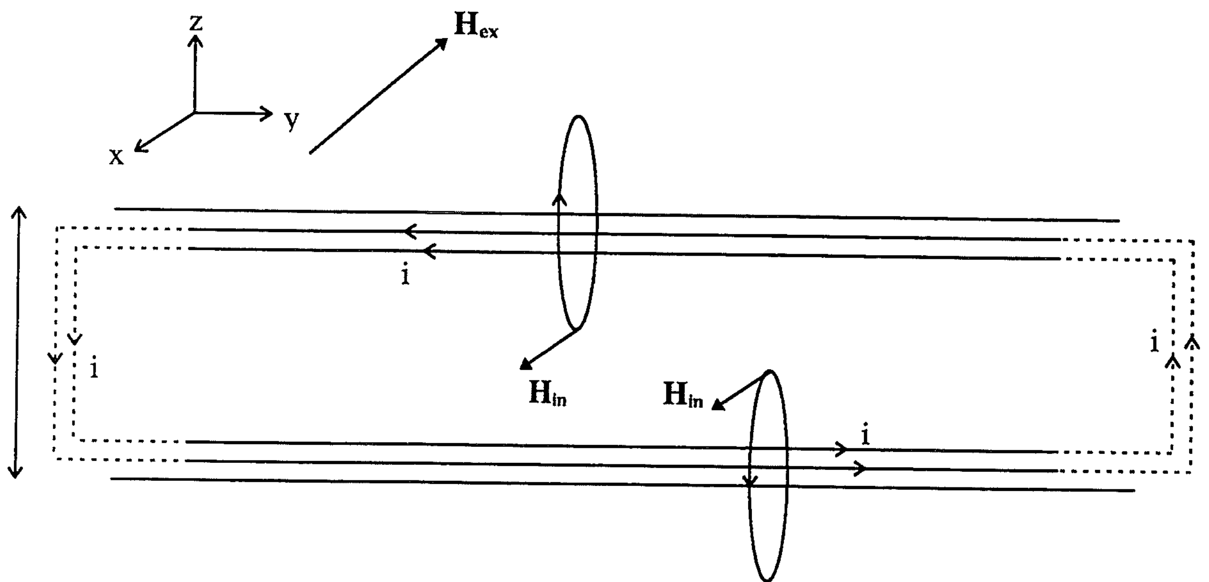

Figure A.2 Generation of eddy currents along the y-axis, when an increasing field H_{ex} is applied along the x-axis. The eddy currents cause an internal field H_{in} that opposes H_{ex}. The total internal field in strongest in the middle of the film.

Appendix A. Equations for eddy current and resonance loss

A.1 Eddy current loss in ferromagnetic thin films

The effect of eddy currents on the complex magnetic permeability is described by the Maxwell equations [81]. Because the soft magnetic film is very thin with respect to the other dimensions (l,w >> d) one can approximate the film by an infinite plate in the x and y-direction (see figure A.1). A small amplitude harmonic magnetic field $\mathbf{h}_a(t)$ is applied in the x-direction (equation (2.10)):

$$\mathbf{h}_a(t) = h_0 e^{j\omega t}\mathbf{e}_x, \tag{A.1}$$

with h_0 the amplitude [A/m] of the ac magnetic field, ω the angular frequency [rad/s] and $\mathbf{e}_x$ the unit vector along the x-axis..
Because of electromagnetic induction an electrical field **E** [V/m] is induced. The resulting eddy currents flow in the y-direction and oppose the applied field. This effect is stronger in the middle of the film than just below the surface, because of the cumulative effect of the currents. (see figure A.2). In other words: the eddy currents screen the H-field inside the film. So the component of the (effective) magnetic field in the x-direction H_x depends only on z.
The relevant Maxwell equations are:

$$\nabla \times \mathbf{E} = -\frac{\partial \mathbf{B}}{\partial t}, \tag{A.2}$$

$$\nabla \cdot \mathbf{B} = 0, \tag{A.3}$$

and

$$\nabla \times \mathbf{H} = \mathbf{J}. \tag{A.4}$$

In these expressions **H** is the effective magnetic field vector [A/m], **B** the magnetic induction vector [T] and **J** the eddy current density vector [A/m^2]. **B** and **H** are related by $\mathbf{B}=\mu_0\mu_i\mathbf{H}$ (μ_i is the relative permeability at low frequencies, when no eddy current loss occurs). Using Ohm's law is $\mathbf{J}=\mathbf{E}/\rho$ (ρ is the electrical resistivity [Ωm]) and the relation:

$$\nabla \times (\nabla \times \mathbf{H}) = \nabla(\nabla \cdot \mathbf{H}) - \nabla^2\mathbf{H} \tag{A.5}$$

in combination with equations (A.2)-(A.4), gives:

$$\nabla^2\mathbf{H} = \frac{\mu_i}{\rho}\frac{\partial \mathbf{H}}{\partial t}. \tag{A.6}$$

It was argued that **H** has only a component in the x-direction that is a function of z. Assuming the usual separation $H=H_z(z)\exp(j\omega t)$ [20] results in the differential equation:

$$\frac{\partial^2 H_x(z)}{\partial z^2} = j\frac{\omega\mu_i}{\rho}H_x(z). \tag{A.7}$$

Because the tangential component of **H** is continuous at the surface of the film, the boundary conditions are $H_x(z = \pm d/2) = h_0$. Solving (A.7) under these boundary conditions gives [21]:

$$H_x(z) = h_0 \tanh\left[(1+j)\frac{z}{\delta}\right]. \tag{A.8}$$

In this expression δ is called the *skin depth* [m]. It is equal to the depth, measured from the surface of a cylindrical specimen, at which the amplitude of the magnetic field is reduced to h_0/e because of eddy currents [6]:

$$\delta = \sqrt{\frac{2\rho}{\omega\mu_0\mu_i}}. \tag{A.9}$$

The effective (complex) permeability can be found by averaging equation (A.8) with respect to the film thickness and dividing by h_0. The result can be written as [82]:

$$\hat{\mu}_e = \mu_e' - j\mu_e'' = \frac{\mu_i}{k}\frac{(\sinh k + \sin k) - j(\sinh k - \sin k)}{\cosh k + \cos k}, \tag{A.10}$$

where the abbreviation $k = d/\delta$ was introduced.

A.2 Resonance in ferromagnetic thin films

The dynamic character of the magnetisation can be expressed by the Landau-Lifshitz equation [22]

$$\frac{1}{\gamma}\frac{d\mathbf{M}}{dt} = \mu_0 \mathbf{M}\times\mathbf{H} - \frac{\alpha\mu_0}{M_s}[\mathbf{M}\times(\mathbf{M}\times\mathbf{H})], \tag{A.11}$$

where γ is the gyromagnetic factor [Hz/T], **M** the magnetisation vector [A/m], **H** the *total* magnetic field vector [A/m], α the damping constant and M_s the saturation magnetisation [A/m]. The values for the damping constant reported in the literature range from 0.03 to 0.07 [21]. The gyromagnetic factor is the proportionality constant between the magnetisation and the angular momentum. It is defined by:

$$\gamma = g\frac{e}{2m_e}, \tag{A.12}$$

where g is the Landé splitting factor, e the electrical charge [C] of an electron and m_e its mass [kg]; $e/m_e = 1.759\cdot 10^{11}$ C/kg. For ferromagnetic iron and iron-based alloys the Landé splitting factor is equal to 2, which means that not the orbital angular momentum but the spin angular momentum is responsible for the observed ferromagnetism in iron. Using these values the gyromagnetic factor is determined to be 176 GHz/T.

The term on the left hand side in equation (A.11) represents the change in angular momentum. If we neglect the damping term the Landau-Lifshitz equation represents a precession around a certain field direction. The damping force acting on the precession gives rise to a motion in a

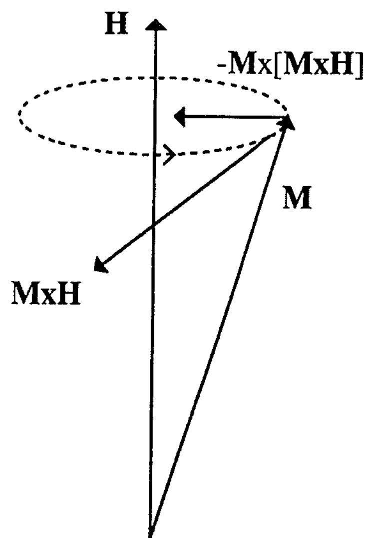

Figure A.3 Influence of a damping action on a precession motion.

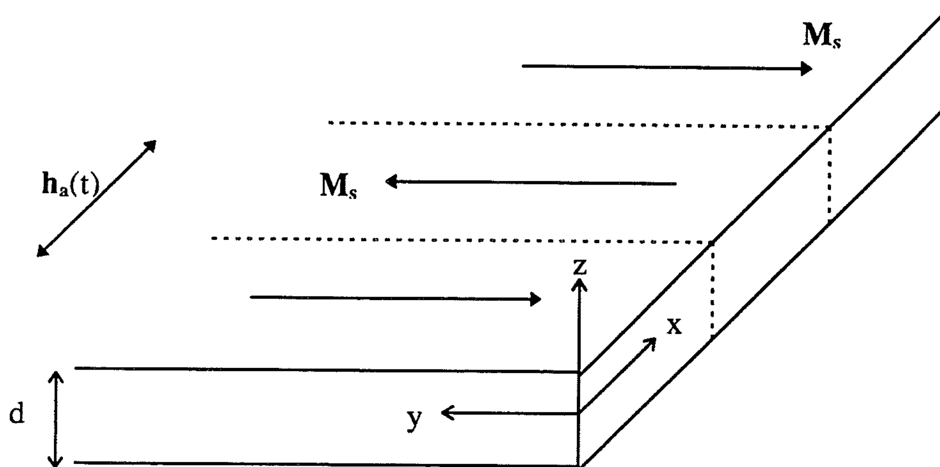

Figure A.4 Schematic representation of the magnetic structure. A small amplitude alternating magnetic field is applied along the x-axis. All domains are perfectly parallel to the y-direction.

direction perpendicular to -**M** and **M**×**H**, so the precession approaches the field direction (see figure A.3). Chikazumi [6] argues that the damping motion should act not only on the precession motion, but also on the motion induced by the second term at the right hand side of (A.11). Therefore the damping should act on the resultant motion of the magnetisation:

$$\frac{1}{\gamma}\frac{d\mathbf{M}}{dt} = \mu_0 \mathbf{M} \times \left[\mathbf{H} - \frac{\alpha}{\gamma\mu_0 M_s}\frac{d\mathbf{M}}{dt}\right] = \mu_0 \mathbf{M} \times \mathbf{H} - \frac{\alpha}{\gamma M_s}\mathbf{M} \times \frac{d\mathbf{M}}{dt}. \tag{A.13}$$

It can be seen that equations (A.11) and (A.13) are identical if $\alpha^2 \ll 1$.

We are interested in the solution of equation (A.13) when a small amplitude oscillating magnetic field (equation (A.1)) is applied in the x-direction to a soft magnetic film with uniaxial induced anisotropy in the y-direction (see figure A.4).
In that case the total magnetic field vector **H** contains the following contributions:

1. the applied field vector $\mathbf{h}_a(t)$,
2. the anisotropy field vector $\mathbf{H}_K$,
3. the demagnetising field vector $\mathbf{H}_{dem}$.

The preferential directions of the uniaxial anisotropy are induced by annealing ferromagnetic films in a static magnetic field parallel to the y-direction. Because of the annealing treatment all domains are aligned parallel to the y-direction. Therefore the anisotropy field vector is given by:

$$\mathbf{H}_K = \begin{pmatrix} 0 \\ H_K \\ 0 \end{pmatrix}, \tag{A.14}$$

where H_K is related to the uniaxial anisotropy constant K_u [J/m^3], according to equation (2.4). Again it is assumed that l,w » d, so the demagnetising factor in the z-direction N_z is equal to 1. The demagnetising field vector is:

$$\mathbf{H}_{dem} = -\mathbf{N}\mathbf{M} = -\begin{pmatrix} 0 & 0 & 0 \\ 0 & 0 & 0 \\ 0 & 0 & 1 \end{pmatrix}\begin{pmatrix} M_x \\ M_y \\ M_z \end{pmatrix} = -\begin{pmatrix} 0 \\ 0 \\ M_z \end{pmatrix}. \tag{A.15}$$

Because the amplitude of the oscillating field h_0 is small (typically 2.5 A/m) compared to the anisotropy field (typically 0.6 kA/m) the magnetisation **M**(t) may be taken as the sum of a large static component $\mathbf{M}_{stat}$ (in magnitude equal to the saturation magnetisation) and a small dynamic magnetisation component $\mathbf{m}_{dyn}(t)$ [20, 83]. For the small dynamic part of the magnetisation a harmonic approximation is used, so:

$$\mathbf{M}(t) = \mathbf{M}_{stat} + \mathbf{m}_{dyn}(t) = \begin{pmatrix} 0 \\ M_s \\ 0 \end{pmatrix} + \begin{pmatrix} m_x \\ m_y \\ m_z \end{pmatrix} e^{j\omega t}. \tag{A.16}$$

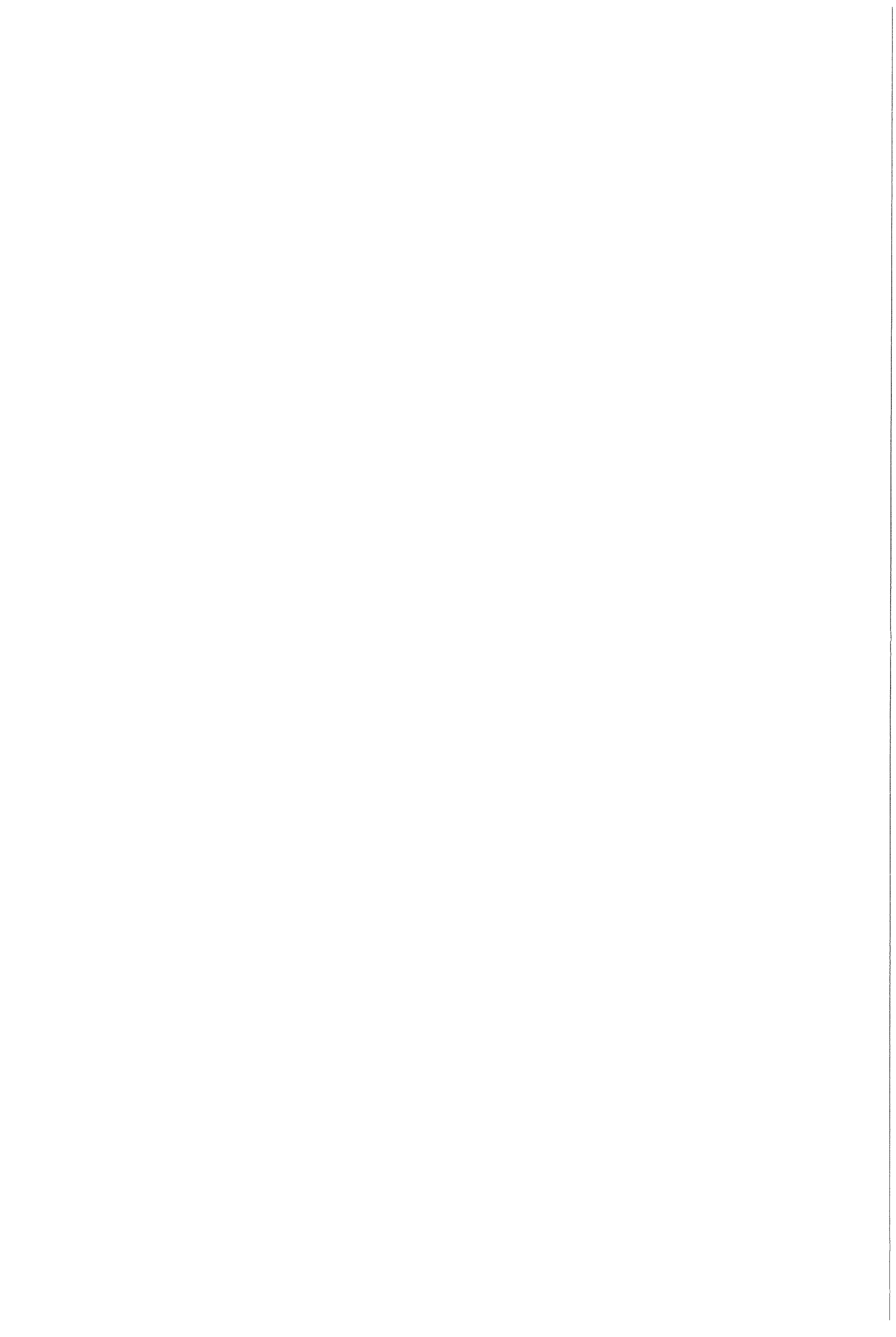

Substituting **M** and **H** into equation (A.13) and neglecting second order terms as m^2, mh and h^2, results in the following equations in the unknown parameters m_x, m_y and m_z:

$$\frac{j\omega}{\gamma}\begin{pmatrix} m_x \\ m_y \\ m_z \end{pmatrix} = \mu_0 \begin{pmatrix} -m_z(H_K + M_s) \\ 0 \\ m_x H_K - h_0 M_s \end{pmatrix} - \frac{j\omega\alpha}{\gamma}\begin{pmatrix} m_z \\ 0 \\ -m_x \end{pmatrix}. \tag{A.17}$$

The magnetic susceptibility χ connects the magnetisation vector to the magnetic field vector: $\mathbf{M} = \chi\mathbf{H}$. Because $\mathbf{B} = \mu_0(\mathbf{H} + \mathbf{M}) = \mu_0(1 + \chi)\mathbf{H} = \mu_0\mu\mathbf{H}$ one gets $\mu = \chi + 1$ or when both the relative permeability and the susceptibility are complex:

$$\hat{\mu} = \mu' - j\mu'' = \chi' + 1 - j\chi'' = \hat{\chi} + 1. \tag{A.18}$$

So $\mu' = \chi' + 1$ and $\mu'' = \chi''$. The complex magnetic susceptibility in the x-direction is now defined as m_x/h_x. Solving the set of equations (A.17) gives for the real and the negative of the imaginary part of the initial relative permeability in the x-direction gives:

$$\mu_f' = \mu_0^2 M_s \frac{\mu_0^2 H_K [M_s + H_K]^2 - \frac{\omega^2}{\gamma^2}[M_s + (1-\alpha^2)H_K]}{\left[\mu_0^2 H_K (M_s + H_K) - \frac{\omega^2}{\gamma^2}(1+\alpha^2)\right]^2 + \left[\frac{\omega}{\gamma}\alpha\mu_0(M_s + 2H_K)\right]^2} + 1 \tag{A.19^a}$$

and

$$\mu_f'' = \frac{\omega}{\gamma}\alpha\mu_0 M_s \frac{\mu_0^2 (M_s + H_K)^2 + \frac{\omega^2}{\gamma^2}(1+\alpha^2)}{\left[\mu_0^2 H_K (M_s + H_K) - \frac{\omega^2}{\gamma^2}(1+\alpha^2)\right]^2 + \left[\frac{\omega}{\gamma}\alpha\mu_0(M_s + 2H_K)\right]^2}. \tag{A.19^b}$$

The resonance frequency is defined as the frequency at which the real part of the permeability is zero. The ferromagnetic resonance frequency f_{res} [Hz] is now given by:

$$f_{res} = \frac{\mu_0\gamma}{2\pi}(M_s + H_K)\sqrt{\frac{H_K}{M_s + (1-\alpha^2)H_K}}. \tag{A.20}$$

These equations can be simplified, because $H_K \ll M_s$. I_s ($=\mu_0 M_s$) is typically 1 T, so the saturation magnetisation is $8\cdot10^5$ A/m, which is much larger than the anisotropy field (0.6 kA/m). Also $\alpha^2 \ll 1$. Now we can write:

$$\mu_f' = \mu_0^2 M_s^2 \frac{\mu_0^2 M_s H_K - \frac{\omega^2}{\gamma^2}}{\left[\mu_0^2 M_s H_K - \frac{\omega^2}{\gamma^2}\right]^2 + \left[\frac{\omega}{\gamma}\alpha\mu_0 M_s\right]^2} + 1, \tag{A.21^a}$$

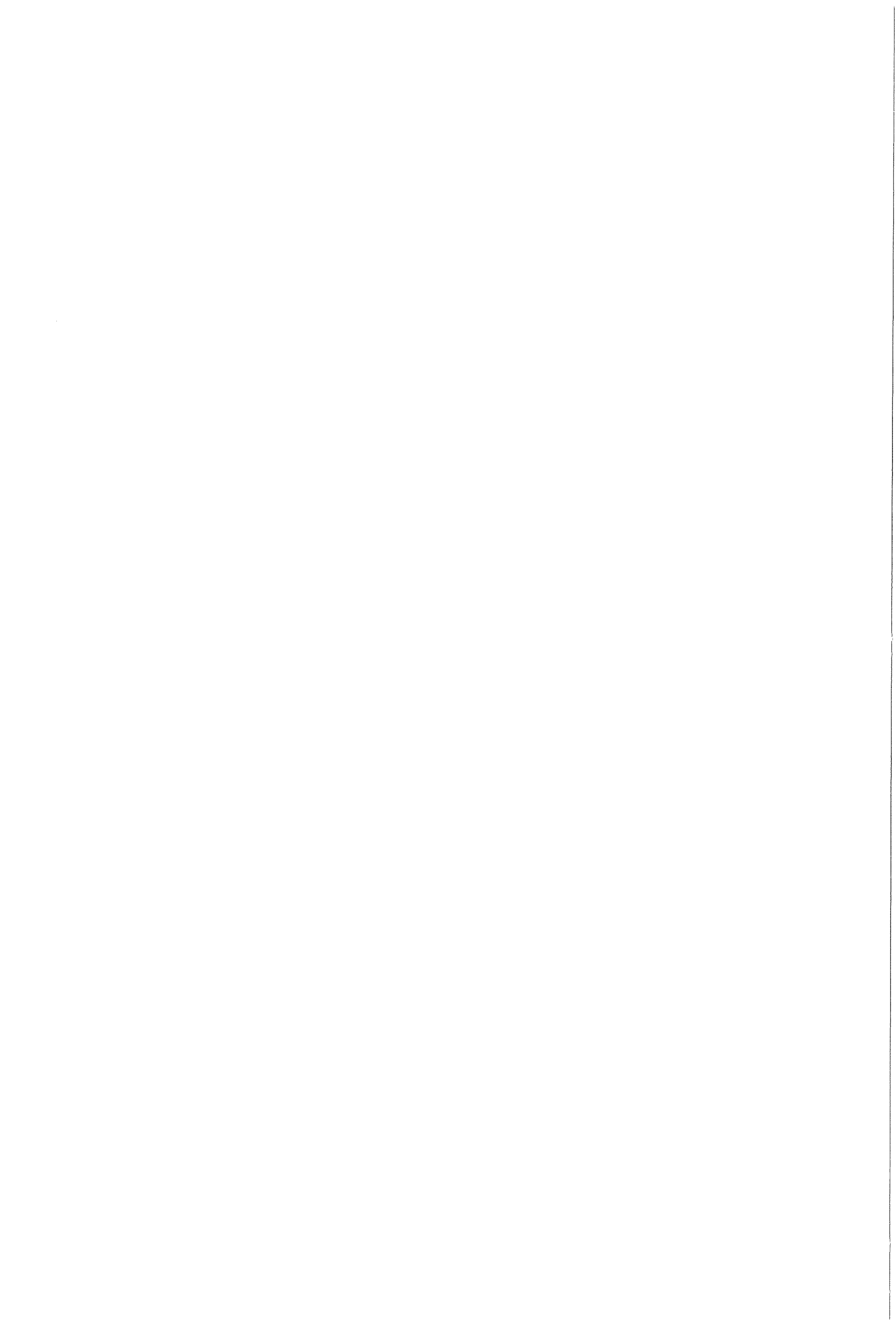

$$\mu_f'' = \frac{\omega}{\gamma}\alpha\mu_0 M_s \frac{\mu_0^2 M_s^2 + \frac{\omega^2}{\gamma^2}}{\left[\mu_0^2 M_s H_K - \frac{\omega^2}{\gamma^2}\right]^2 + \left[\frac{\omega}{\gamma}\alpha\mu_0 M_s\right]^2} \qquad \text{(A.21}^b\text{)}$$

and for the resonance frequency:

$$f_{res} = \frac{\mu_0 \gamma}{2\pi}\sqrt{M_s H_K} = \frac{\gamma}{2\pi}\sqrt{2\mu_0 K_u}\,. \qquad \text{(A.22)}$$

Substituting the mentioned values for γ, M_s and H_K shows that the resonance frequency is in the GHz range (f_{res} = 0.8 GHz).

A.3 Eddy current and resonance loss in ferromagnetic thin films

To obtain an expression that describes both eddy current and ferromagnetic resonance losses, the (complex) permeability for resonance loss is substituted for the permeability in the absence of eddy currents (the intrinsic permeability μ_i) in equation (A.9):

$$\hat{\mu}_f \rightarrow \mu_i\,. \qquad \text{(A.23)}$$

Then the skin depth and also k become complex quantities:

$$\hat{k} = \frac{d}{\hat{\delta}} = d\sqrt{\frac{\omega\mu_0\hat{\mu}_f}{2\rho}}\,. \qquad \text{(A.24)}$$

Now writing:

$$\hat{\mu}_f = \mu_f' - j\mu_f'' = |\hat{\mu}_f|\, e^{j\arg\hat{\mu}_x} = |\hat{\mu}_f|\left[\cos(\arg\hat{\mu}_f) + j\sin(\arg\hat{\mu}_f)\right] \qquad \text{(A.25)}$$

with

$$|\hat{\mu}_f| = \sqrt{(\mu_f')^2 + (\mu_f'')^2} \qquad \text{(A.26}^s\text{)}$$

and

$$\arg\hat{\mu}_f = -\arctan\left(\frac{\mu_f''}{\mu_f'}\right) \qquad \text{(A.26}^b\text{)}$$

gives in combination with equation (A.24):

$$\hat{k} = d\sqrt{\frac{\omega\mu_0|\hat{\mu}_f|}{2\rho}}\, e^{j\arg\hat{\mu}_f/2} \equiv k\left[\cos(\tfrac{1}{2}\arg\hat{\mu}_f) + j\sin(\tfrac{1}{2}\arg\hat{\mu}_f)\right], \qquad \text{(A.27)}$$

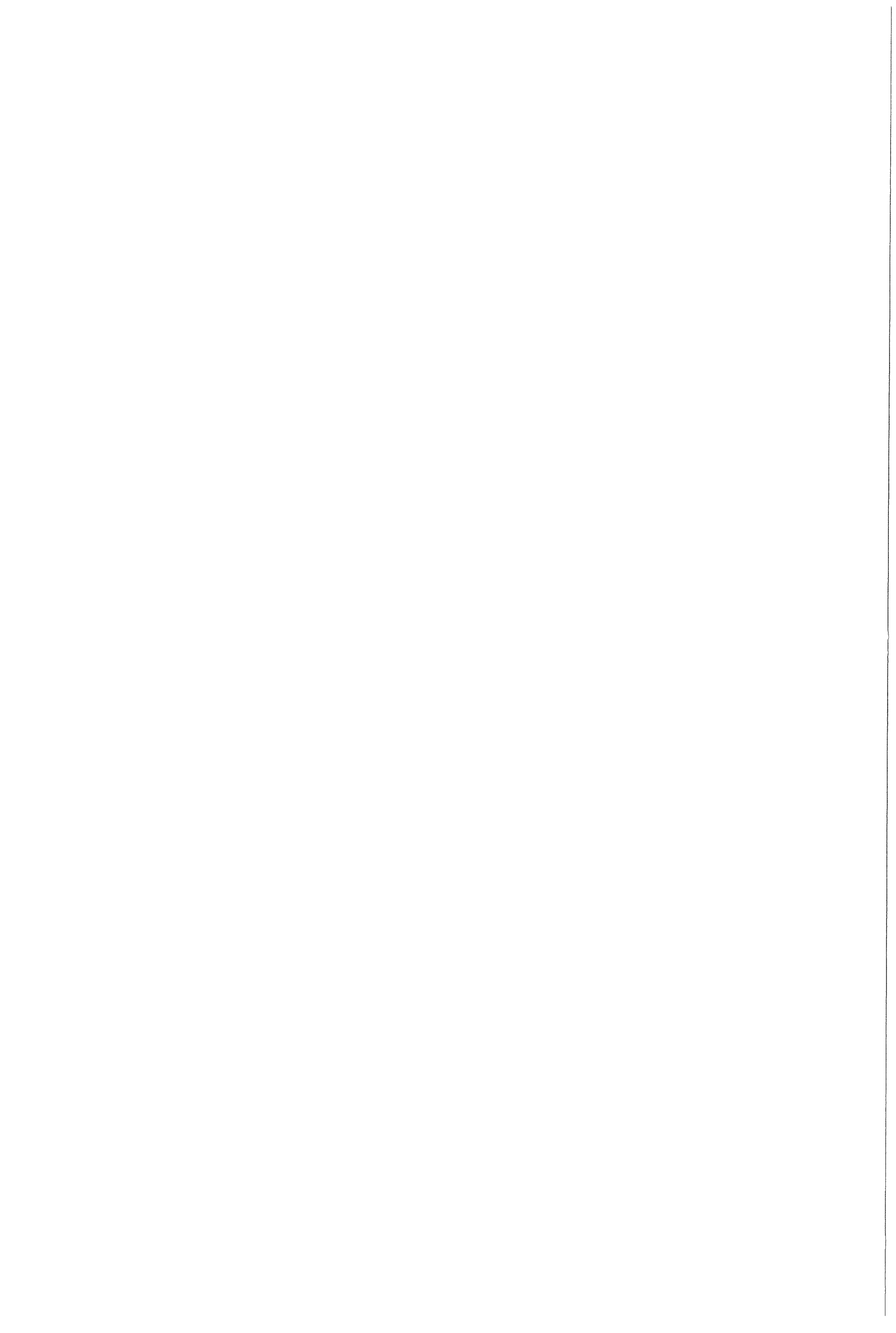

where the notation:

$$k = d\sqrt{\frac{\omega\mu_0|\hat{\mu}_f|}{2\rho}} \tag{A.28}$$

was introduced.
Rewriting equation (A.9) gives:

$$\hat{\mu} = (1-j)\frac{\hat{\mu}_f}{\hat{k}}\frac{e^{(1+j)\hat{k}}-1}{e^{(1+j)\hat{k}}+1}. \tag{A.29}$$

Applying straightforward mathematics results in the following expressions for the complex permeability due to eddy current and ferromagnetic resonance loss:

$$\mu' = \sqrt{2}\frac{|\hat{\mu}_f|}{k}\frac{(A^2-1)\cos C - 2A\sin B\sin C}{A^2+2A\cos B+1} \tag{A.30^a}$$

and

$$\mu'' = \sqrt{2}\frac{|\hat{\mu}_f|}{k}\frac{(A^2-1)\sin C + 2A\sin B\cos C}{A^2+2A\cos B+1}, \tag{A.30^b}$$

where the following constant were used:

$$A = \exp\{k[\cos(\tfrac{1}{2}\arg\hat{\mu}_f) - \sin(\tfrac{1}{2}\arg\hat{\mu}_f)]\}, \tag{A.31^a}$$

$$B = \exp\{k[\cos(\tfrac{1}{2}\arg\hat{\mu}_f) + \sin(\tfrac{1}{2}\arg\hat{\mu}_f)]\} \tag{A.31^b}$$

and

$$C = \tfrac{1}{2}\arg\hat{\mu}_f - \tfrac{1}{4}\pi. \tag{A.31^c}$$

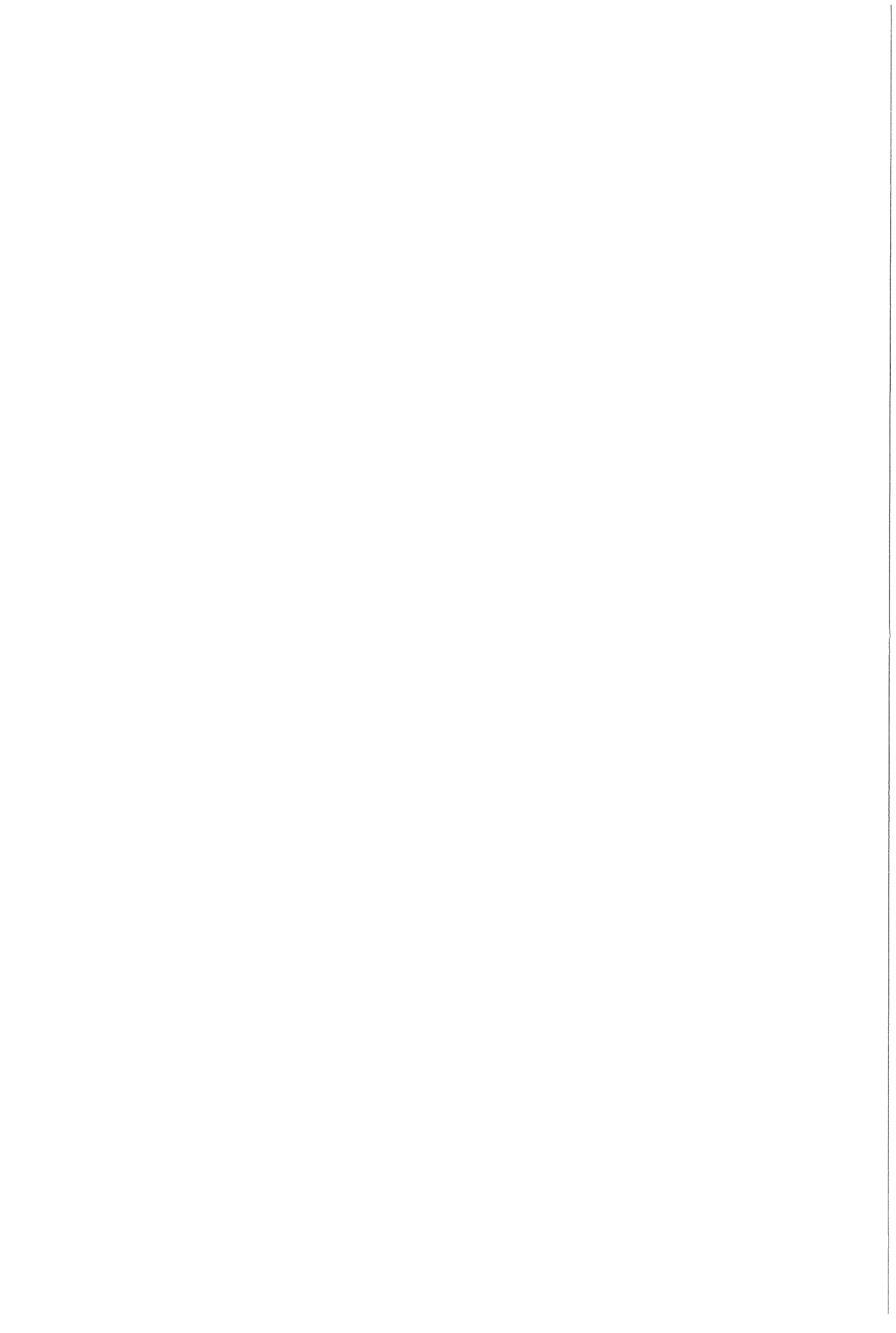

Appendix B. Non-isothermal crystallisation kinetics

Inserting equation (2.28),

$$\tau = \tau_0 \exp\left(\frac{Q_x}{RT}\right), \tag{B.1}$$

into equation (2.31),

$$\frac{df}{dt} = m\tau^{-1}(1-f)\left[-\ln(1-f)\right]^{\frac{m-1}{m}}, \tag{B.2}$$

while filling in the temperature profile $T(t) = T_0 + \phi t$ and integrating from fraction zero at time zero to fraction f at time t gives:

$$\int_{f'=0}^{f'=f} \left[-\ln(1-f')\right]^{\frac{1-m}{m}} \frac{df'}{1-f'} = \int_{t'=0}^{t'=t} m\tau_o^{-1} \exp\left[-\frac{Q_x}{R(T_0+\phi t')}\right] dt'. \tag{B.3}$$

The left side of this differential equation has to be integrated from $f' = 0$ to $f' = f$, while the right side has to be integrated from $t' = 0$ to $t' = t$. Before performing the integration, we use the following substitution:

$$x = \frac{Q_x}{R(T_0+\phi t)} \Rightarrow dt = -\frac{Q_x}{R\phi}\frac{dx}{x^2}. \tag{B.4}$$

Now $t = 0$ means $x = Q_x/RT_0$, which leads to:

$$m\left[-\ln(1-f)\right]^{\frac{1}{m}} = \frac{mQ_x}{R\phi\tau_0} \int_{x'=x}^{Q_x/RT_0} \frac{e^{-x'}}{x'^2} dx'. \tag{B.5}$$

Usually Q_x/RT_0 is large, so the integral can be taken from $x' = x$ to $x' = \infty$. By means of partial integration one can write:

$$\int_{x'=x}^{\infty} \frac{e^{-x'}}{x'^2} dx' = \frac{e^{-x}}{x} - \int_{x'=x}^{\infty} \frac{e^{-x'}}{x'^2} dx'. \tag{B.6}$$

The integral on the right hand side is equal to the exponential integral $E_1(x)$. This integral does not have an exact solution. However, it has the asymptotic expansion [84]:

$$E_1(x) = \frac{e^{-x}}{x}\left\{1 - \frac{1}{x} + \frac{2}{x^2} - \frac{6}{x^3} \dots\right\} = \frac{e^{-x}}{x}\sum_{n=0}^{\infty}(-1)^n \frac{n!}{x^n}. \tag{B.7}$$

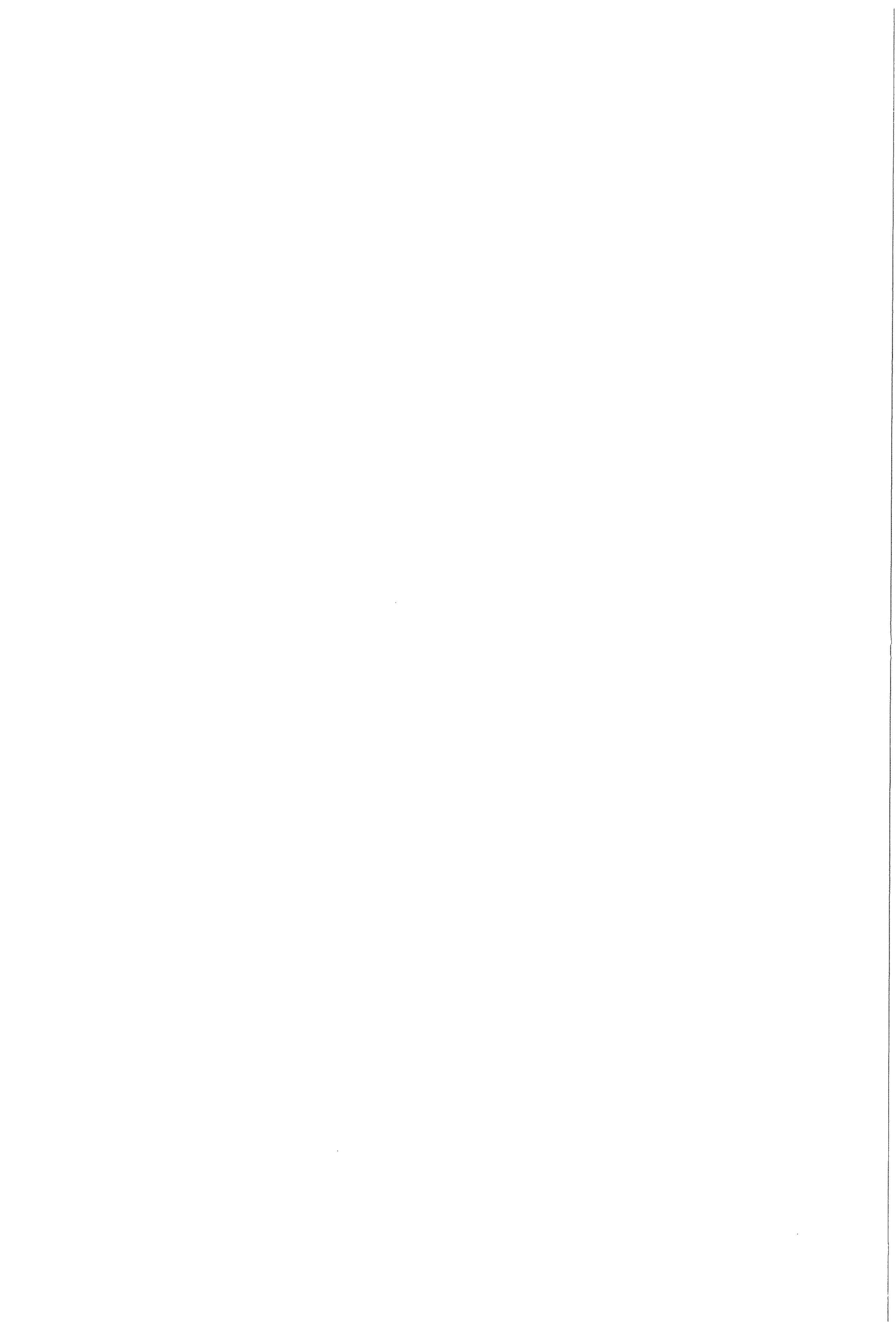

Combining the above results leads to the following expression for the fraction transformed:

$$f(t, x(t)) = 1 - \exp\left\{-\left[\frac{(T_0 + \phi t)g(x(t))}{\phi\tau_0}\right]^m\right\}, \tag{B.8}$$

where g(x) is defined as:

$$g(x) \equiv e^{-x}\sum_{n=1}^{\infty}(-1)^{n+1}\frac{n!}{x^n} = e^{-x}\left\{\frac{1!}{x} - \frac{2!}{x^2} + \frac{3!}{x^3} - \ldots\right\}. \tag{A.9}$$

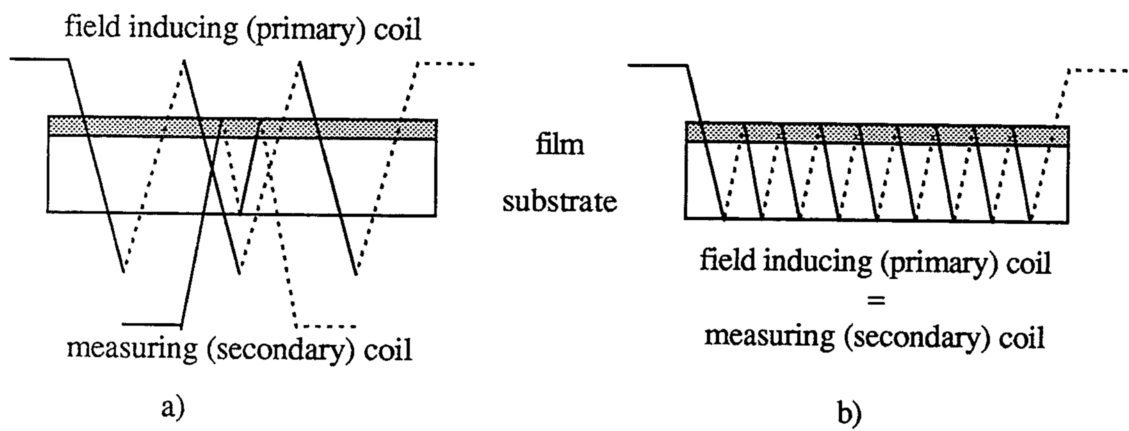

Figure C.1 Schematic representation of the permeability measurement set-ups:
a) low frequency (LF) set-up and
b) high frequency (HF) set-up.

Appendix C. Corrections for the magnetic permeability measurement

In this section the influence of the film geometry and experimental set-up is described [64,65]. The film dimensions are: length l [m], width w [m] and thickness d [m] ($l > w >> d$).
Two experimental set-ups are considered: a low frequency (LF) set-up and a high frequency (HF) set-up, as schematically shown in figure C.1. The first set-up (LF) consist of a primary (field inducing) coil and a secondary (measuring) coil. In the second set-up (HF) only one coil is used (field inducing coil = measuring coil). The set-up choice only influences the correction factors to be introduced, not on the measuring principle (section 3.6.1).
In the LF set-up the length of the primary (field inducing) coil l_1 [m] is larger than the sample length, whereas the length of the secondary (measuring) coil l_2 [m] is small compared to the film and primary coil dimensions, i.e. $l_1 > l > l_2$.
In the HF set-up the coil is larger than the sample length: $l_1 = l_2 > l$.

Field correction
The field produced by an electrical current i_1 [A] in a cylindrical (primary) coil with n_1 winding at its axis is given by [81]:

$$H_1(x) = \frac{n_1 i_1}{l_1}\left[\frac{l_1 + 2x}{2\sqrt{s_1 + (l_1 + 2x)^2}} + \frac{l_1 - 2x}{2\sqrt{s_1 + (l_1 - 2x)^2}}\right], \tag{C.1}$$

where x is the distance [m] from the centre of the coil and s_1 is the cross-sectional area [m^2] of the (primary) coil.
The field correction factor C_H is defined as:

$$C_H = \frac{1}{l_i}\int_{x=-l_i/2}^{x=l_i/2} \frac{H_1(x)}{H_1^{id}}\,dx = \frac{1}{2l_i}\left[\sqrt{s_1 + (l_1 + l_i)^2} - \sqrt{s_1 + (l_1 - l_i)^2}\right], \tag{C.2}$$

where l_i is equal to the length [m] of the measuring coil for the LF set-up or to the sample length for the HF set-up. The field correction factor C_H is determined to be 0.963 and 0.991 for a film length of 34 mm in the LF and HF set-up, respectively.

Demagnetising factor
The demagnetising field can be approximated by assuming that the film is ellipsoidal. In that case the demagnetising factor in the length direction of the film is:

$$N = \tfrac{1}{2} lwd \int_{t=0}^{t=\infty} \frac{dt}{\sqrt{(l+t)^2 + (w+t)^2 + (d+t)^2}}. \tag{C.3}$$

This elliptical integral can be solved numerically only. For example, the demagnetising factor of a film with dimensions l = 34 mm, w = 5 mm and d = 0.7 μm is equal to $7.072 \cdot 10^{-6}$. Additional calculations show that N increases linearly with increasing thicknesses up to 0.1 mm.

Missing flux
As mentioned in section 3.6.1, the field inside the sample is equal to the sum of the applied field H_a and the demagnetising field H_d. Because the tangential component of the field is continuous at any surface, it is reasonable to assume that the field is homogeneous and equal to $H_a + H_d$ within the (measuring) coil. Now the magnetic flux inside the (measuring) coil is given by

$$\Phi = \mu_0 n_2 \left[Ms + (H_a + H_d) s_i \right], \tag{C.4}$$

where s_i equals the cross-sectional area [m^2] of the measuring coil (LF set-up) or the area of the integrated measuring/field inducing coil (HF set-up). Note, that also the magnetic field flux outside the film measured; this flux should be subtracted. The corrected magnetic flux Φ_c is:

$$\Phi_c = \mu_0 n_2 \left[Ms + H_d s_i \right] = \mu_0 n_2 M \left[s - N s_i \right]. \tag{C.5}$$

The correction factor for the missing flux C_f is now defined as Φ_c/Φ_{id}, where Φ_{id} is the detected flux in the ideal case that only flux changes inside the sample are measured. So:

$$C_f = \frac{\Phi_c}{\Phi_{id}} = \frac{\mu_0 n_2 M \left[s - N s_i \right]}{\mu_0 n_2 M s} = 1 - N \frac{s_i}{s}. \tag{C.6}$$

The correction factor for the measured flux C_f of a film with dimensions $l = 34$ mm, $w = 5$ mm and $d = 0.7$ μm is determined to be 0.976 and 0.954 for the LF and HF set-up, respectively.

Now before calculating the relative permeability, an effective permeability μ_{eff} is introduced. This effective permeability is equal to the measured permeability corrected for the above described effects:

$$\mu_{eff} = \frac{\mu_{meas}}{C_H C_f}. \tag{C.7}$$

Finally the relative permeability itself is obtained:

$$\mu = \frac{B}{\mu_0 H} = \frac{\mu_0 (H_a + H_d + M)}{\mu_0 (H_a + H_d)} \approx \frac{M}{H_a - NM} = \frac{1}{1/\mu_{eff} - N}. \tag{C.8}$$

The approximation is justified because the applied field and demagnetising field are small compared to the induced magnetisation.

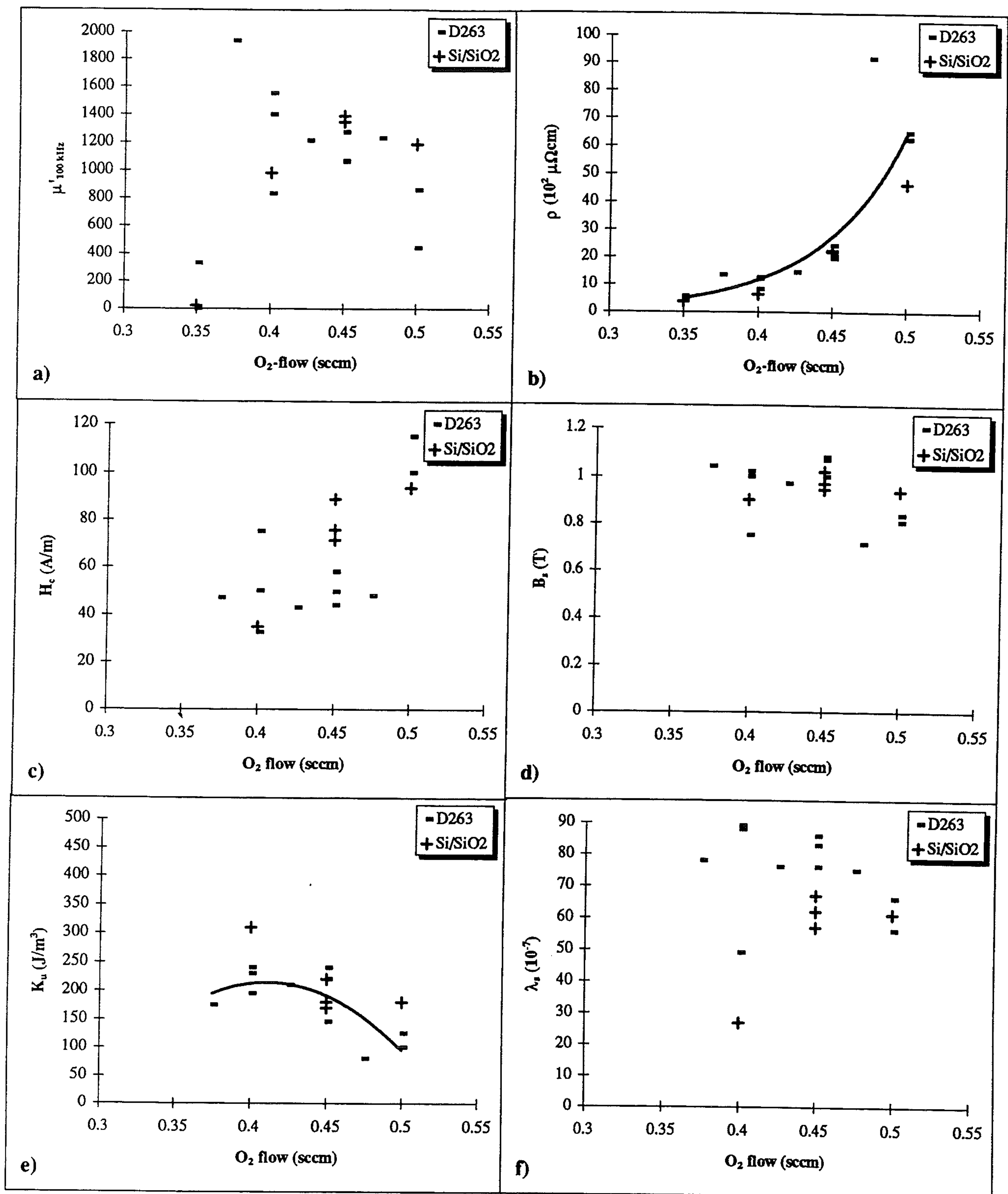

Figure D.1 Some magnetic properties of 0.70 μm thick FeHfO films deposited on D263 glass and single crystalline (100) Si with a 0.5 μm thick SiO_2 buffer layer after RTP for 5 seconds at 350°C:
a) the permeability at 100 kHz $\mu'_{100\,kHz}$,
b) the resistivity ρ [mΩcm],
c) the coercivity H_c [A/m],
d) the saturation magnetic induction B_s [T],
e) the uniaxial anisotropy constant K_u [J/m³] and
f) the saturation magnetostriction coefficient λ_s
as a function of the oxygen flow during sputter-deposition.

Appendix D. Results of optimisation procedure

In this appendix a more detailed description of the optimisation procedure than presented in section 4.1 is given. Here, not only the permeability at 100 kHz and the resistivity of 0.70 μm thick FeHfO films are considered, but also the saturation magnetisation, coercivity, uniaxial anisotropy constant (obtained from BH-loops) and the saturation magnetostriction coefficient. In the first section the results are given as a function of the oxygen flow during deposition; in the second section the annealing temperature will be varied. Both optimisation procedures are performed using either classical thermal processing or rapid thermal processing.

D.1 Optimising the oxygen flow

Several deposition runs are performed with different oxygen flows using D263 glass, Si/SiO_2 and GGG substrates. Oxygen flows between 0.35 and 0.50 sccm are used. The sputter time is one hour for all series, resulting in a film thickness of 0.70 μm. After deposition all films are annealed in a constant magnetic field in the width direction of the films, using RTP (5 seconds at 350°C) or CTP (2 hours at 325°C).
In figures D.1 (RTP) and D.2 (CTP) the measured permeability at 100 kHz $\mu'_{100\,kHz}$ (average of 20 measurements), resistivity ρ, coercivity H_c, saturation magnetic induction B_s ($\approx \mu_0 M_s$), uniaxial anisotropy constant K_u and saturation magnetostriction coefficient λ_s are shown as a function of the oxygen flow during sputter-deposition.
The first two plots in figure D.1 are discussed in section 4.1.2. No trend is observed in the coercivity data. No clear change in the saturation magnetic is found. It is approximately 1 T. The uniaxial anisotropy constant is about 0.2 kJ/m^3. The magnetostriction data obtained for Si/SiO_2 are signicantly lower than for films deposited on D263 glass. However, this may be caused by the fact that the Si/SiO_2 substrates are thicker that the D263 substrates, resulting in a smaller, and therefore more difficult to determine, deflections.
The first two plots in figure D.2 are discussed in section 4.1.2 as well. No clear change in the coercivity is observed. A maximum at 0.45 sccm O_2 is found in the saturation magnetic induction and, unfortunately, in the saturation magnetostriction coefficient as well. The uniaxial anisotropy decreases with the oxygen flow, in agreement with the increase in the permeability (in accordance with equation (2.18)).
Comparing both annealing procedures, it is found that RTP results in general better soft magnetic properties and a higher resitivities of the FeHfO films. The only parameter that shows a clear O_2 depence is the resistivity.

D.2 Optimising the annealing treatment

The optimisation procedure for the annealing treatment (RTP and CTP) is performed with films deposited on D263 glass, Si/SiO_2 and GGG substrates at an oxygen flow of 0.45 sccm (resulting in films of optimal composition $Fe_{55}Hf_{17}O_{28}$). The annealing times were 5 seconds (RTP) and 2 hours (CTP). All films are 0.70 μm thick.
In figures D.3 (RTP) and D.4 (CTP) the measured permeability at 100 kHz $\mu'_{100\,kHz}$ (average of 20 measurements), resistivity ρ, coercivity H_c, saturation magnetic induction B_s ($\approx \mu_0 M_s$), uniaxial anisotropy constant K_u and saturation magnetostriction coefficient λ_s are shown as a function of the annealing temperature T_a.
Again the two upper plots are not discussed here (see section 4.1.3). In figure D.3^c a minimum in coercivity of about 40 A/m can be recognised at approximately 400°C. Both the saturation

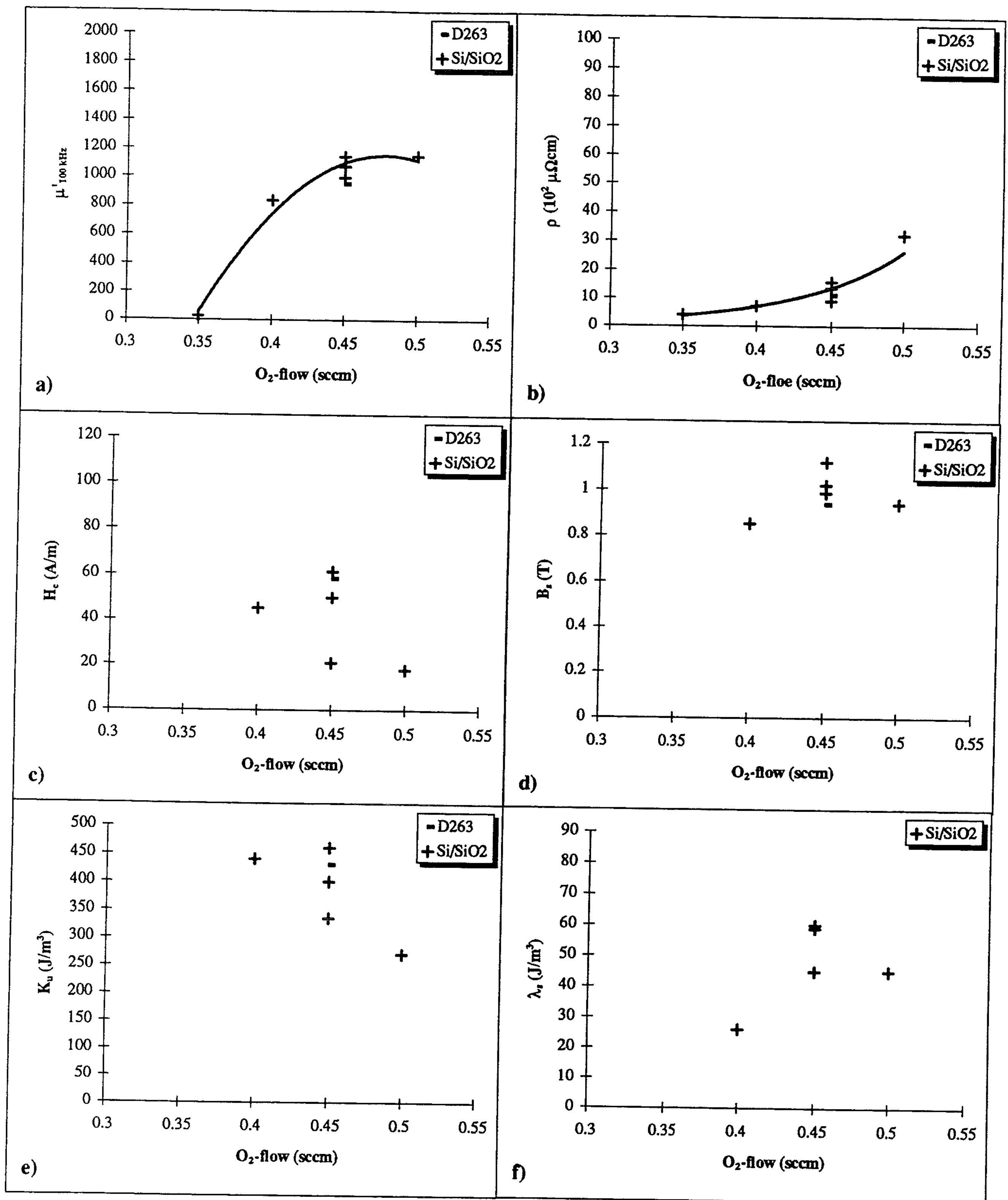

Figure D.2 Some magnetic properties of 0.70 μm thick FeHfO films deposited on D263 glass and single crystalline (100) Si with a 0.5 μm thick SiO_2 buffer layer after CTP for 2 hours at 325°C:

a) the permeability at 100 kHz $\mu'_{100\,kHz}$,

b) the resistivity ρ [mΩcm],

c) the coercivity H_c [A/m],

d) the saturation magnetic induction B_s [T],

e) the uniaxial anisotropy constant K_u [J/m^3] and

f) the saturation magnetostriction coefficient λ_s

as a function of the oxygen flow during sputter-deposition.

magnetic induction, the uniaxial anisotropy constant and the saturation magnetostriction coefficient do not change very much with the annealing temperature. The magnetostriction of films deposited on Si/SiO_2 is lower (which may be a result of the larger substrate thicknesses, see section D.1).
A continuous increase of the coercivity is seen in figure D.4[c]. The saturation magnetic induction is approximately 1 T for all temperatures and the uniaxial anisotropy constant is rather large. The saturation magnetostriction coefficient however, is much smaller using CTP than RTP. Also a significant decrease with annealing temperature is found.

In figure D.5 the change in the form of the hard axis BH-loops with annealing temperature (RTP: 5 seconds) and oxygen flow during deposition is shown. Small oxygen flows and low annealing temperatures result in a large hysteresis. Higher annealing temperatures at 0.45 sccm O_2 give the best results: small hysteresis and steep BH-loops (i.e. a large permeability).
It is concluded that the best set of magnetic and electrical properties is found by sputter-depositing at 0.45 sccm O_2 (resulting in the optimal composition $Fe_{55}Hf_{17}O_{28}$) and rapid thermal processing these films for 5 seconds at 400°C. However, the saturation magnetostriction coefficient of these films is large.

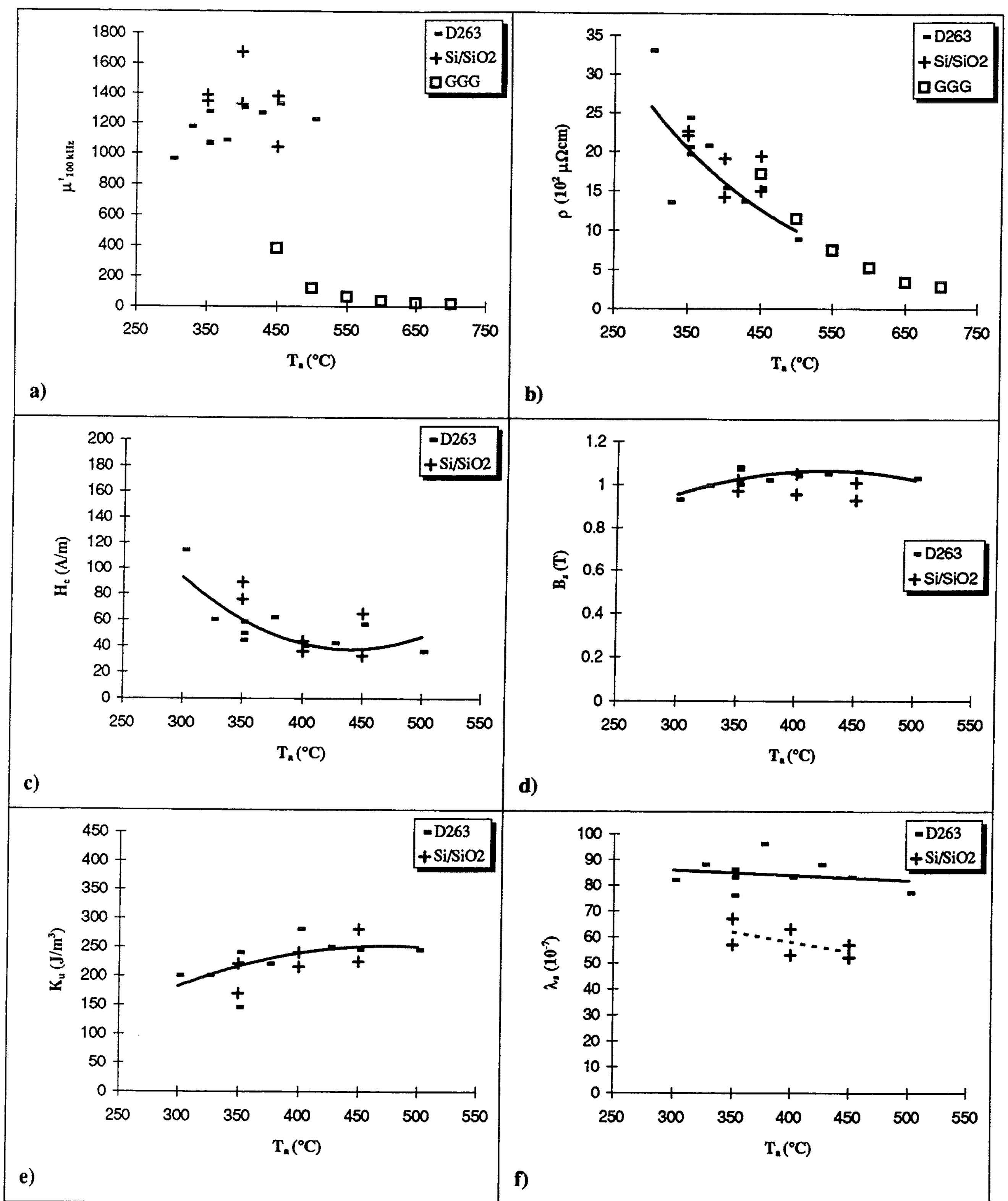

Figure D.3 Change upon annealing (RTP: 5 seconds) 0.70 μm thick $Fe_{55}Hf_{17}O_{28}$ films deposited on D263 glass, single crystalline (100) Si with a 0.5 μm thick SiO_2 buffer layer and GGG of:

a) the permeability at 100 kHz $\mu'_{100\ kHz}$,
b) the resistivity ρ [mΩcm],
c) the coercivity H_c [A/m],
d) the saturation magnetic induction B_s [T],
e) the uniaxial anisotropy constant K_u [J/m^3] and
f) the saturation magnetostriction coefficient λ_s

as a function of the annealing temperature T_a.

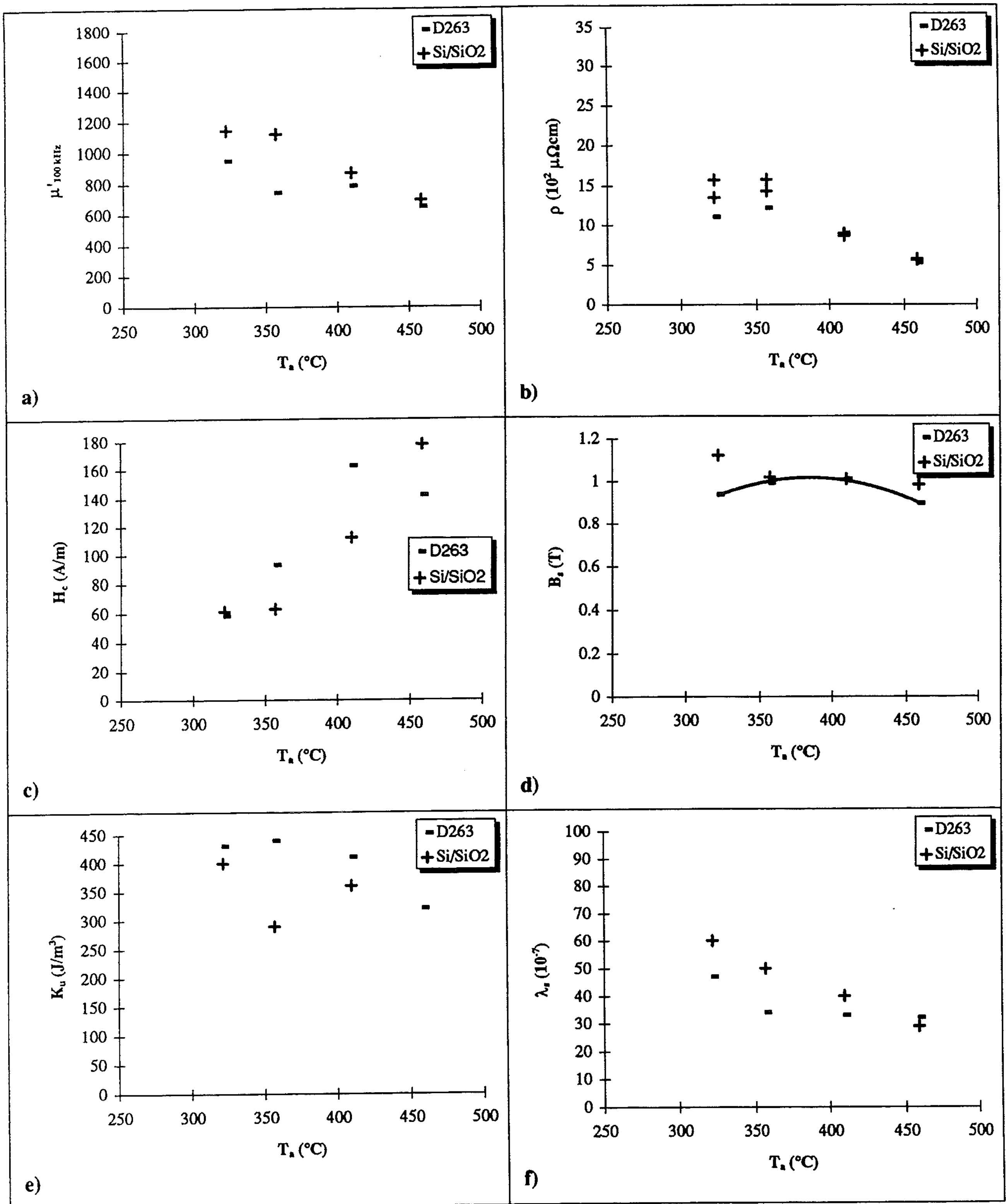

Figure D.4 Change upon annealing (CTP: 2 hours) 0.70 μm thick $Fe_{55}Hf_{17}O_{28}$ films deposited on D263 glass, single crystalline (100) Si with a 0.5 μm thick SiO_2 buffer layer and GGG of:
a) the permeability at 100 kHz $\mu'_{100\,kHz}$,
b) the resistivity ρ [mΩcm],
c) the coercivity H_c [A/m],
d) the saturation magnetic induction B_s [T],
e) the uniaxial anisotropy constant K_u [J/m^3] and
f) the saturation magnetostriction coefficient λ_s
as a function of the annealing temperature T_a.

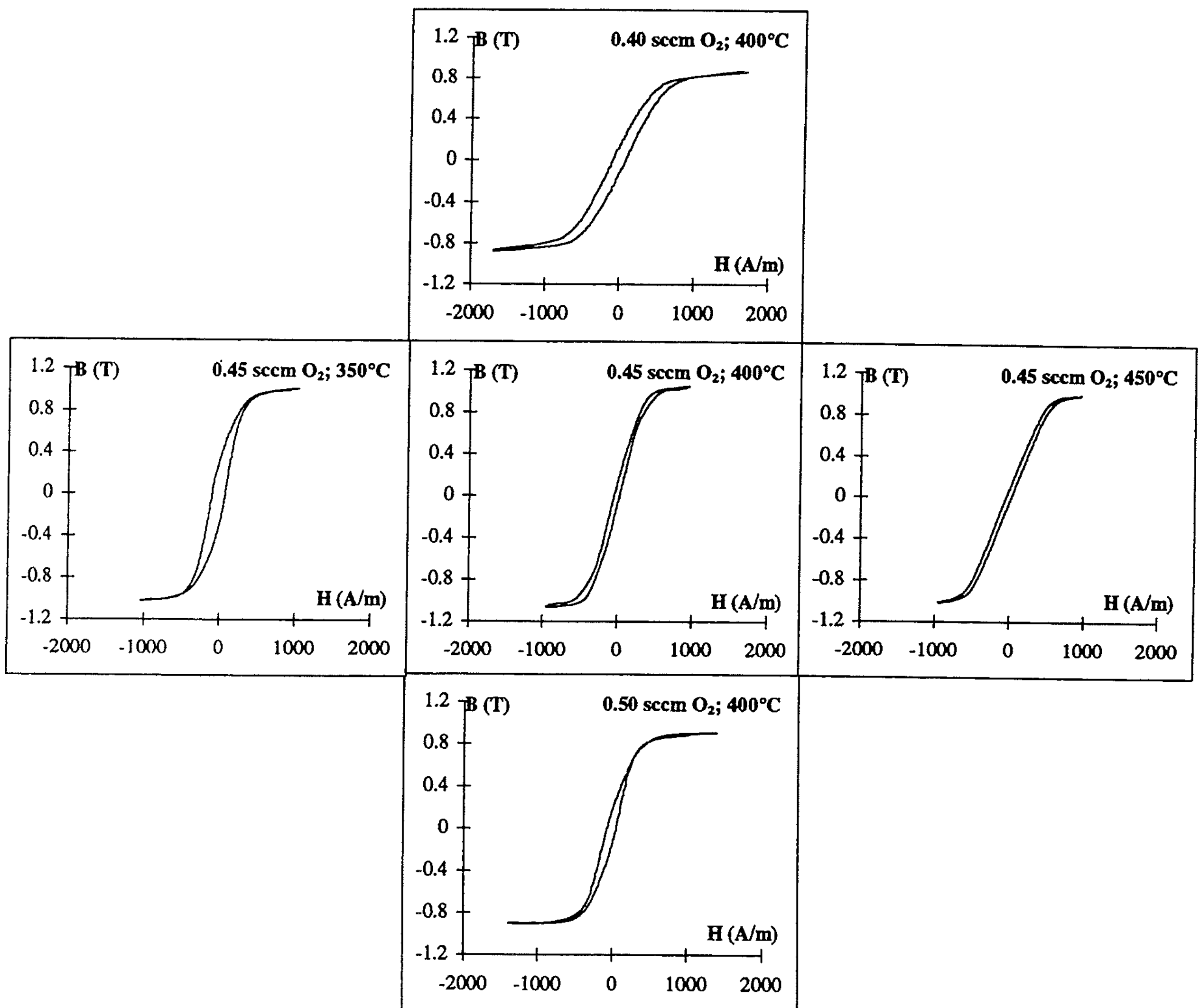

Figure D.5 Change upon annealing (RTP: 5 seconds at) of the hard axis BH-loops of 0.70 μm thick FeHfO films deposited on single crystalline (100) Si with a 0.5 μm thick SiO_2 buffer layer at different O_2 flows ():
vertical: variabel oxygen flow (0.40, 0.45 and 0.50 sccm O_2) and
horizontal: variabel annealing temperature (350, 400 and 450°C).

Appendix E. High frequency permeability measurements

In this appendix some additional high frequency permeability measurements and calculations are presented. In sections 4.4 and 5.3 only results obtained at films deposited on the model substrate D263 glass, single crystalline (100) Si with a 0.5 μm SiO_2 buffer layer and GGG were treated. Here the experimental and fitted curves for all substrates used(including several commercially available ones) are given.
The results are presented in figures E.1 to E.7. The experimental frequency dependence (measured with the HF set-up) is given in the upper and lower plot of each figure; the result determined with the LF set-up is only displayed in the lower plot (only μ' is given; μ'' did not differ much between the two set-ups).
Also some fitting results are displayed, assuming a combination of eddy current and resonance loss. The parameters in the fitting procedure are the uniaxial anisotropy constant K_u and the damping constant α. In the upper plots the results of the fitting procedure with respect to *both* μ' *and* μ'' are given (see table 5.8 for the best fit values of K_u and α); the lower plots contain the fitting results of the procedure where the theoretical expression is adjusted to μ'' *only* (see table 5.9 for the best fit values of K_u and α). The difference between the figures is the substrate material. These are:

- E.1: HCH,
- E.2: HCH with a 1 μm SiO_2 buffer layer,
- E.3: HTCS-II,
- E.4: HTCS-II with a 1 μm SiO_2 buffer layer,
- E.5: D263 glass,
- E.6: single crystalline Si with a 0.5 μm thick SiO_2 bufferlayer,
- E.7: single crystalline GGG.

The commercial substrates (HCH and HTCS-II) are used in two modifications: with and without 1 μm SiO_2. This buffer layer is used because the surface roughness of these polycrystalline substrate materials may be much larger than the roughness of the amorphous substrate D263 glass or the single crystalline substrates Si/SiO_2 and GGG.
It can be seen that depositing a SiO_2 buffer layer on HCH results in higher permeabilities. The highest permeabilities are obtained for HTCS (with and without SiO_2) and the model substrates. Permeabilities of 10^3 and more are found up to 30 MHz.
The results of the fitting procedure are discussed in section 5.3.

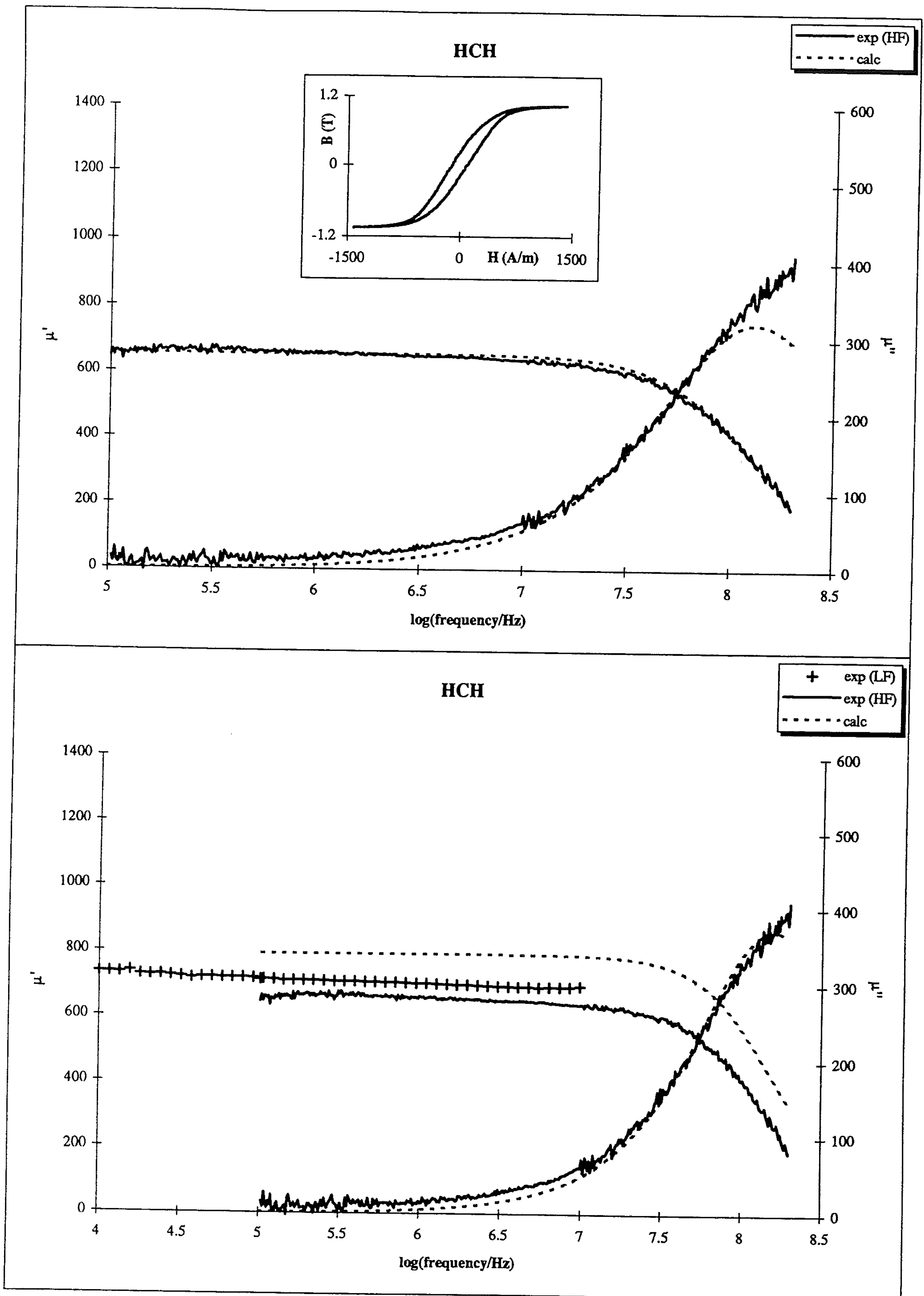

Figure E.1 Calculated (eddy currents and FMR) and experimental (LF and HF) frequency dependence of the complex permeability for the film on HCH:

- procedure A (both μ' and μ'')
- procedure B (only μ'')

See the text in appendix E for further explanation.

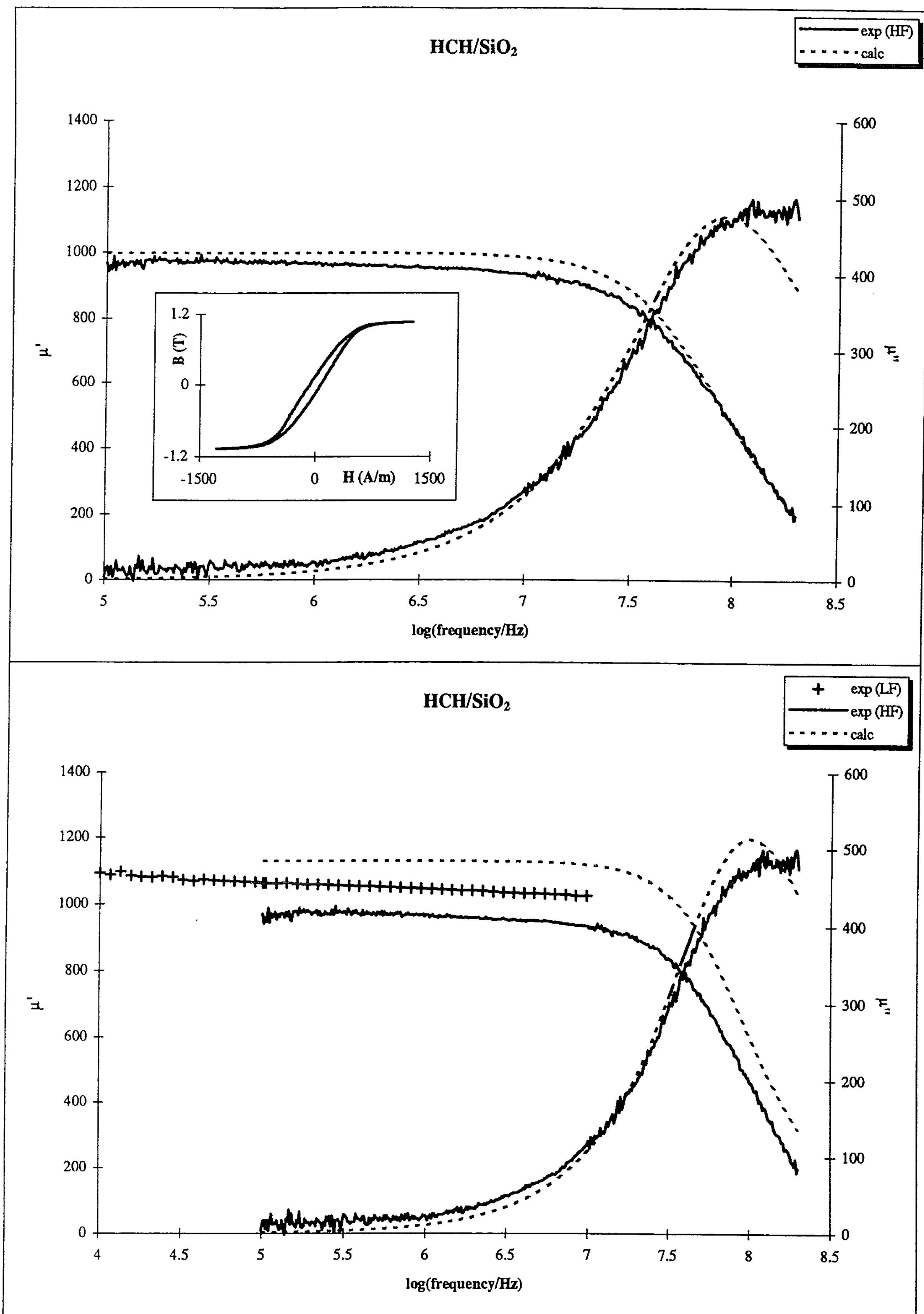

Figure E.2 Calculated (eddy currents and FMR) and experimental (LF and HF) frequency dependence of the complex permeability for the film on HCH\SiO$_2$:

- procedure A (both μ' and μ'')
- procedure B (only μ'')

See the text in appendix E for further explanation.

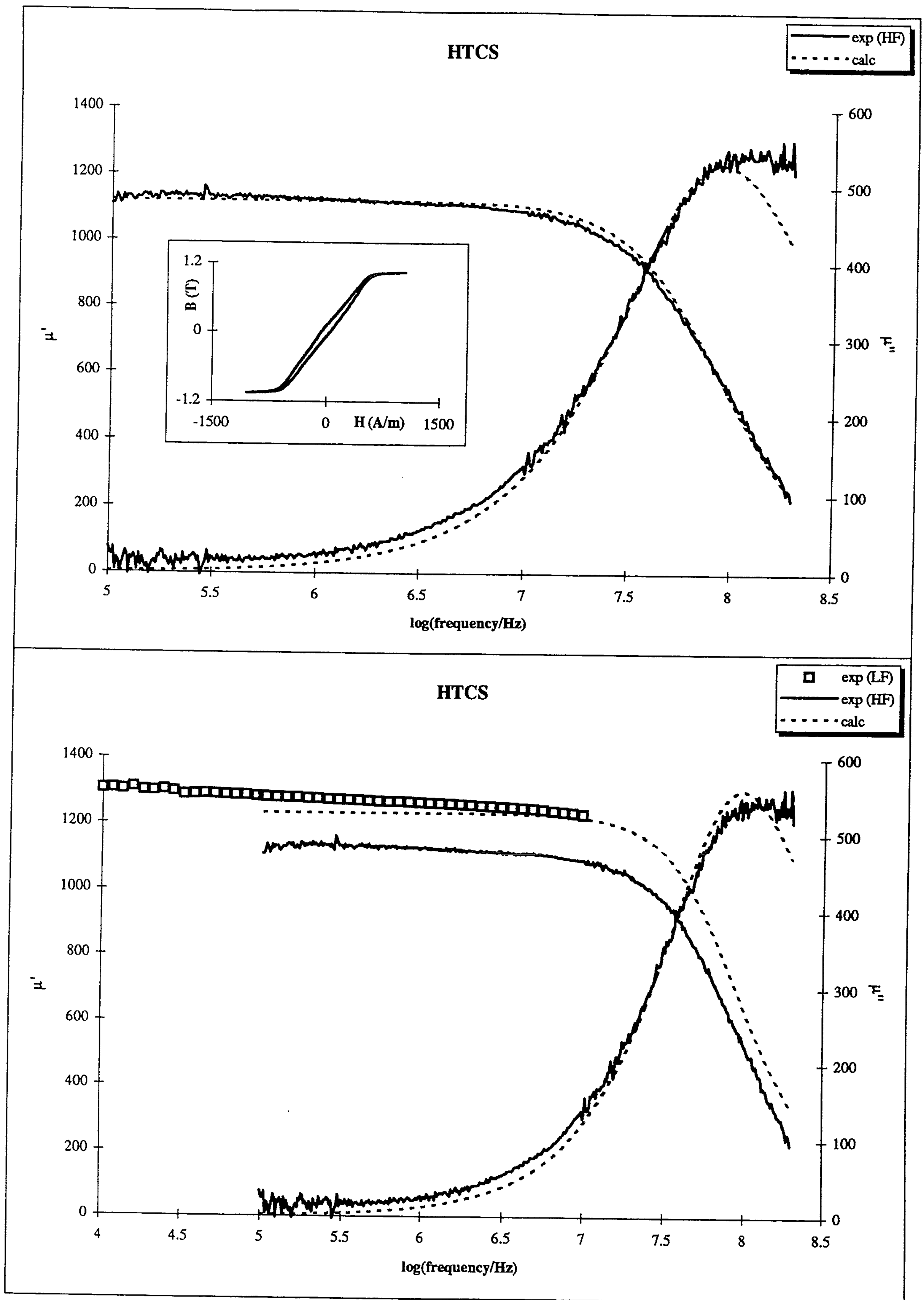

Figure E.3 Calculated (eddy currents and FMR) and experimental (LF and HF) frequency dependence of the complex permeability for the film on HTCS-II:

- procedure A (both μ′ and μ″)
- procedure B (only μ″)

See the text in appendix E for further explanation.

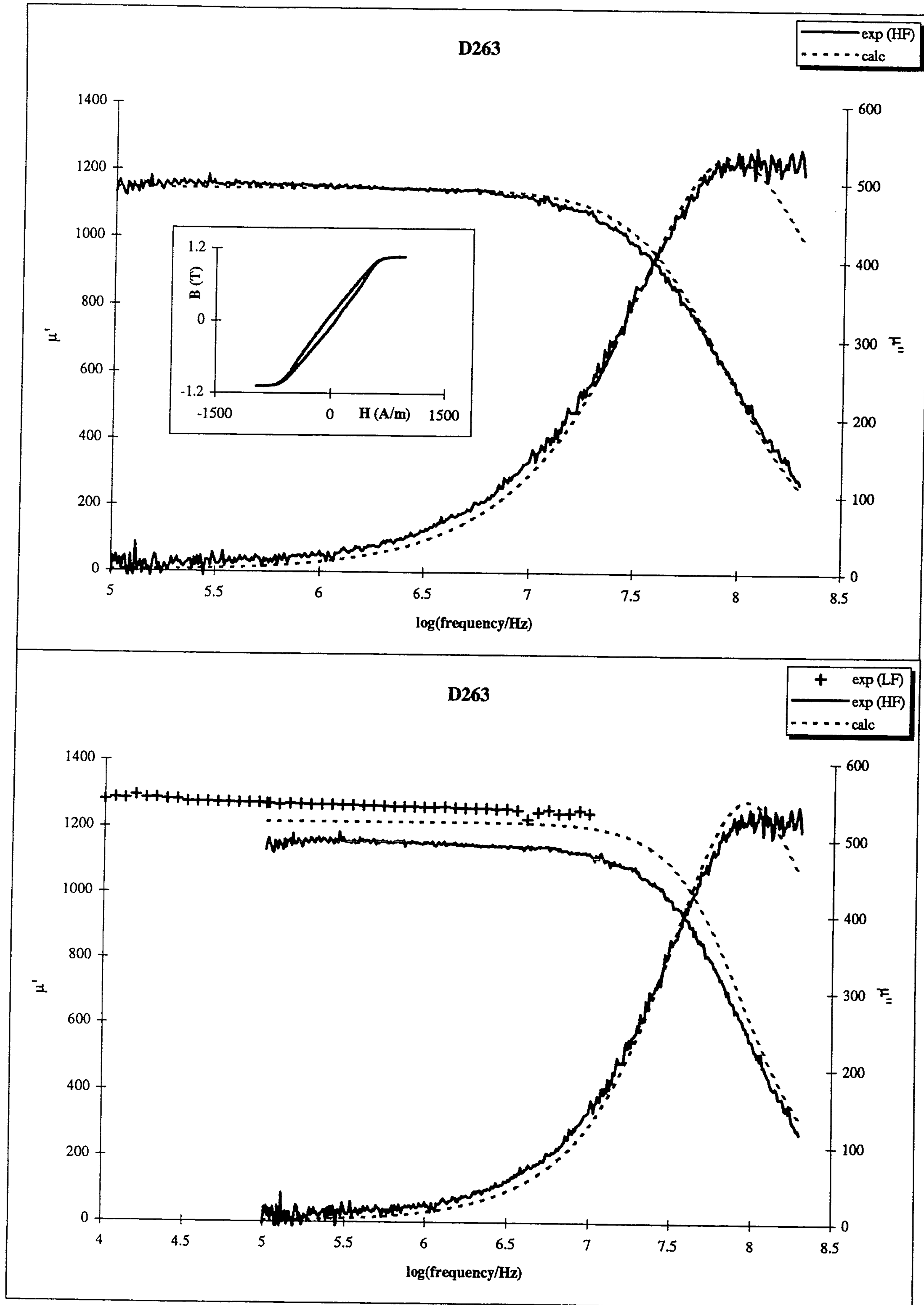

Figure E.5 Calculated (eddy currents and FMR) and experimental (LF and HF) frequency dependence of the complex permeability for the film on D263 glass:

- procedure A (both μ' and μ'')
- procedure B (only μ'')

See the text in appendix E for further explanation.

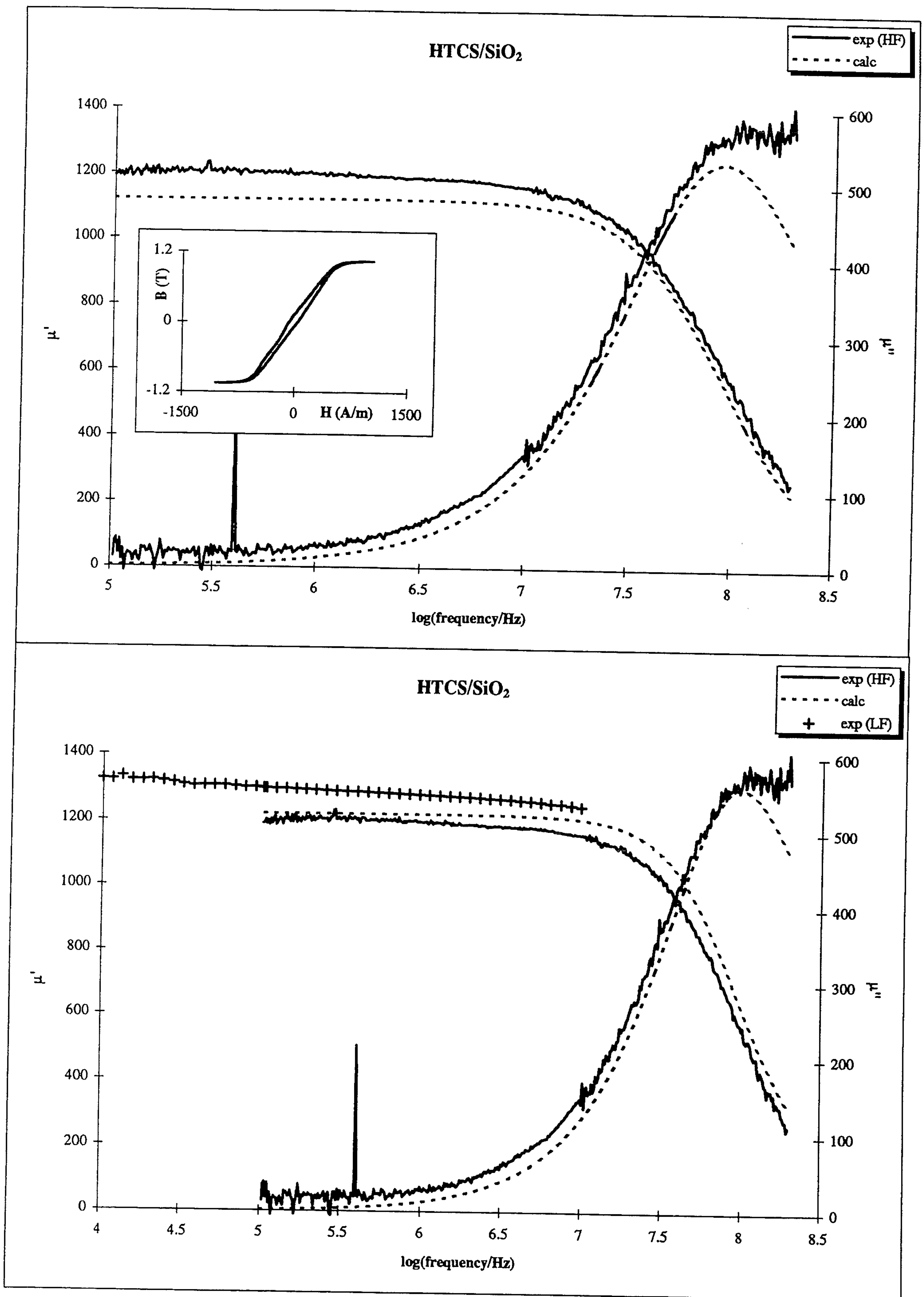

Figure E.4 Calculated (eddy currents and FMR) and experimental (LF and HF) frequency dependence of the complex permeability for the film on HTCS-II\SiO₂:

- procedure A (both μ' and μ'')
- procedure B (only μ'')

See the text in appendix E for further explanation.

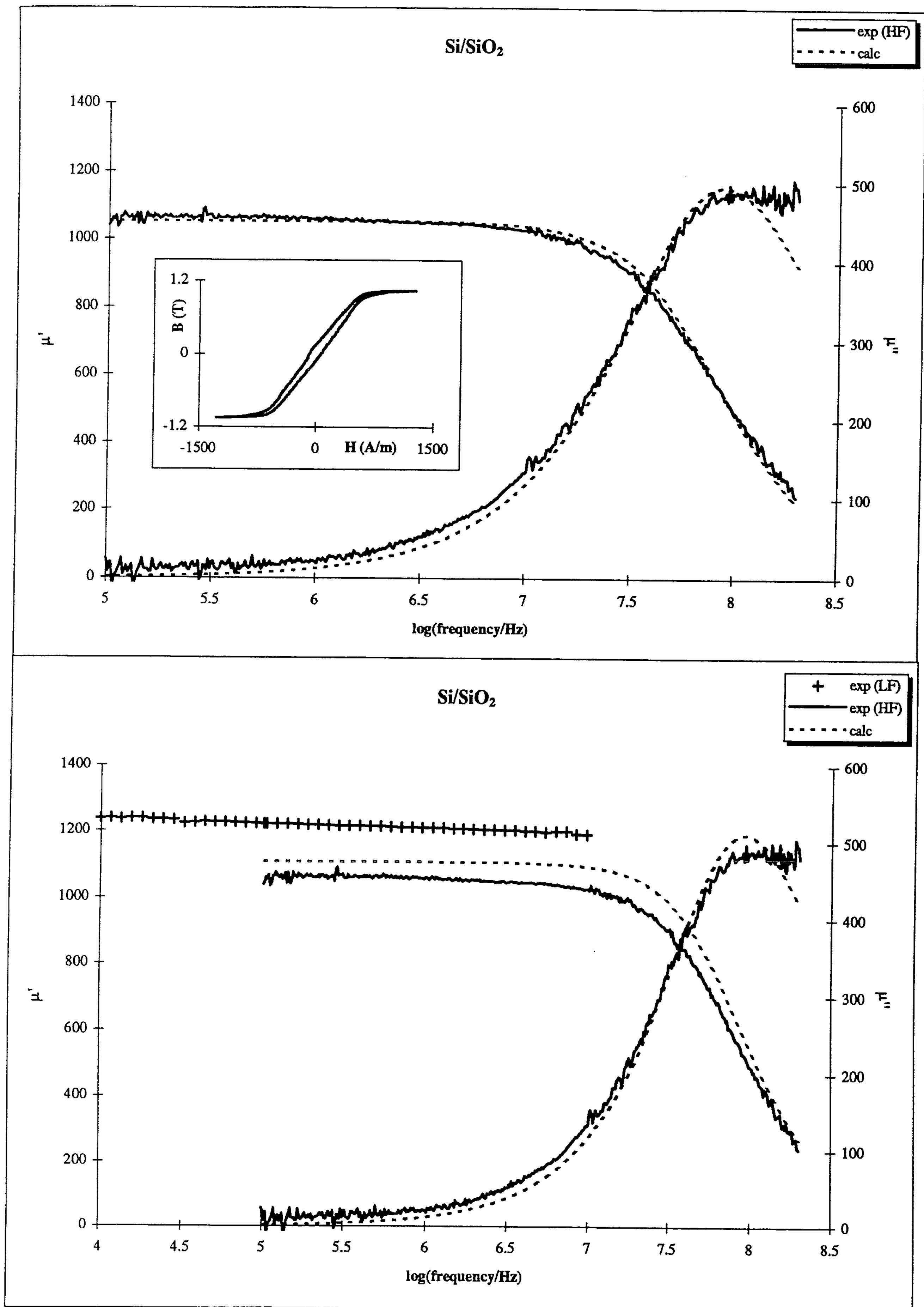

Figure E.6 Calculated (eddy currents and FMR) and experimental (LF and HF) frequency dependence of the complex permeability for the film on Si/SiO_2:

- procedure A (both μ' and μ'')
- procedure B (only μ'')

See the text in appendix E for further explanation.

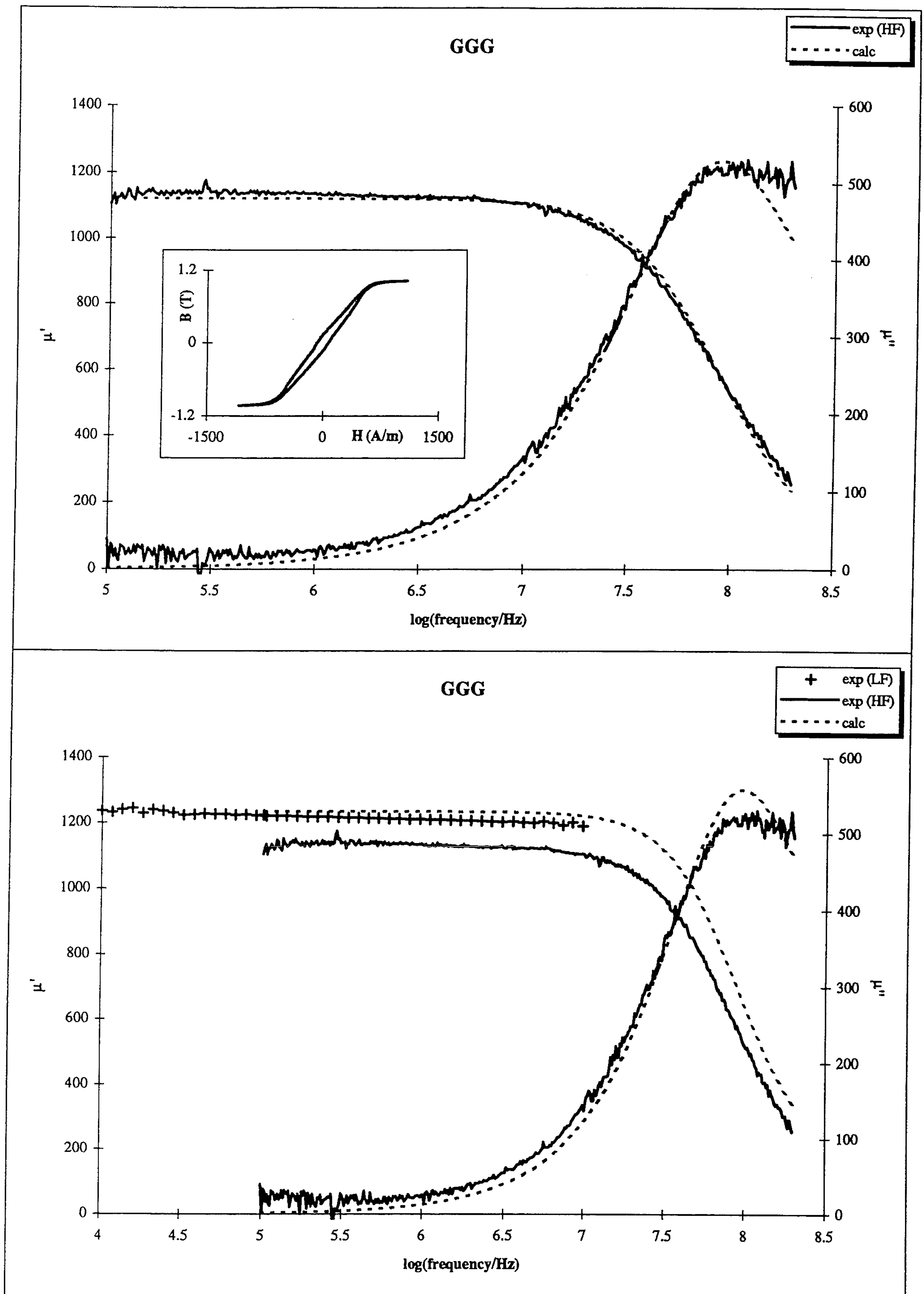

Figure E.7 Calculated (eddy currents and FMR) and experimental (LF and HF) frequency dependence of the complex permeability for the film on GGG:

- procedure A (both μ' and μ'')
- procedure B (only μ'')

See the text in appendix E for further explanation.